



**HAL**  
open science

# Cenozoic topography evolution in Southeast Tibet, focus on the Mekong and Yalong rivers

Xiong Ou

► **To cite this version:**

Xiong Ou. Cenozoic topography evolution in Southeast Tibet, focus on the Mekong and Yalong rivers. Tectonics. Université Grenoble Alpes [2020-..], 2022. English. NNT : 2022GRALU036 . tel-04658976

**HAL Id: tel-04658976**

**<https://theses.hal.science/tel-04658976>**

Submitted on 22 Jul 2024

**HAL** is a multi-disciplinary open access archive for the deposit and dissemination of scientific research documents, whether they are published or not. The documents may come from teaching and research institutions in France or abroad, or from public or private research centers.

L'archive ouverte pluridisciplinaire **HAL**, est destinée au dépôt et à la diffusion de documents scientifiques de niveau recherche, publiés ou non, émanant des établissements d'enseignement et de recherche français ou étrangers, des laboratoires publics ou privés.

## THÈSE

Pour obtenir le grade de

### DOCTEUR DE L'UNIVERSITÉ GRENOBLE ALPES

École doctorale : STEP - Sciences de la Terre de l'Environnement et des Planètes

Spécialité : Terre Solide (CETSOL)

Unité de recherche : Institut des Sciences de la Terre

## Évolution de la topographie du Sud-Est Tibet au Cénozoïque à partir de l'étude du Mékong et de la Yalong

## Cenozoic topography evolution in Southeast Tibet, focus on the Mekong and Yalong rivers

Présentée par :

**Xiong OU**

Thèse soutenue publiquement le **7 décembre 2022**, devant le jury composé de :

<b>Vincent GODARD</b> MAITRE DE CONFERENCE, Aix-Marseille Université	Rapporteur
<b>Yuntao TIAN</b> PROFESSEUR, Sun Yat-Sen University	Rapporteur
<b>Julia DE SIGOYER</b> PROFESSEURE DES UNIVERSITES, Université Grenoble Alpes	Présidente
<b>Laure GUERIT</b> CHARGÉE DE RECHERCHE, Université de Rennes 1	Examinatrice
<b>Xiaoping YUAN</b> PROFESSEUR, China University of Geosciences, Wuhan	Examineur
<b>Anne REPLUMAZ</b> CHARGÉE DE RECHERCHE, CNRS	Directrice de thèse
<b>Peter VAN DER BEEK</b> PROFESSEUR, Universität Potsdam	Co-directeur de thèse





# Preface

My PhD thesis is constructed on two neighbouring regions of southeast Tibet. I have chosen to present this work in form of three research articles, of which one is published, one is under review and one is being prepared to submit, following a general introduction of the whole region. A chapter of general description of methods has been cut off to avoid possible redundancy. I feel that it should be easier to read this work, when presented in a compact way with their own introduction and methods.

## 《致圣雅克》

亲爱的  
我困住在通往爱你的路上  
我无法前进也无法后退  
每一束阳光都像严苛的栅栏  
和风轻轻推我  
也无事于补  
痛苦在每个事物间发芽  
它们彼此冲撞  
以为能造就密集的幸福  
我的眼睛已无法容忍任何细微的季节  
一只狗横冲直撞般  
夺走了我最后一克灵魂  
我的忧愁 由内而外而神形具备  
它似有似无 似乎可以名状  
就像西天边的最后一抹秘色霞  
像自欺可以永久隐藏的秘密  
我将像骑士一样出发  
消失在荒芜的路上  
我要去寻求宝实般的无花果和葡萄  
这是我和西班牙夏天的共同约定  
就像上帝饱含果蜜的应许  
我不需要任何信仰  
只想要拜倒在你的脚下

---- 欧雄，2018年，踏上圣雅克之路前，巴黎

# Acknowledgements

---

The end is coming.

I can't tell how relieved and delighted I am right now. It has been a long journey to reach to this moment, after living through all the roundabout ways since my bachelor graduation, my first job, my miserable but eventually wonderful experiences in cinema community in Beijing and then my life in France. I, finally, finished my first 30 years of life by this PhD project, through which I am so lucky to have met so many people from science community or just daily life in Grenoble.

I would like to give my grateful thanks to my supervisors: **Anne Replumaz** and **Peter van der Beek** for passing knowledges and research methods during my PhD. Great thanks to **Marie-Luce Chevalier** and **Li Haibing** for organizing my filed mission in southeast Tibet in May, 2019, during which I have learned a lot and enjoyed the trip with **Philippe-Hervé Leloup**, **Paul Pitard**, **Bai Mingkun**, **Wang Shiguang**, **Li Kaiyu** and **Pan Jiawei**. Thanks to the help of **Matthias Bernet**, **Mélanie Balvay**, **Cécile Gautheron** and **Ed Sobel**, I could have applied the thermochronological dating in ISTERre and in Potsdam.

My dear parents, **OU Jianping** (欧建平) and **Jiang Manxiu** (姜满秀), have not always agreed with my life choices since my early 20s, until I decided to come to France to continue my studies after all my dramas back in China. But they have always been very supportive, mentally and more importantly financially during the early years (it's true). Without them, I can't imagine how hard life could be in the first two years in France. I love you guys, even though I have never spoken it out. And please forgive me for all the worries and sorrows I have caused to you in the past and probably in the future too.

Friends, yes, my best friends, **Wang Yuanyuan** (王圆圆), **Zhang Jiaojiao** (张娇娇) and **Wang Chao** (王超), our life has been so different since the college, but we have never been

different in sharing our friendship and wonderful discussion about our life, even we are in the four corners of the world nowadays. So many thanks to people from ISTerre, **Marion, Veleda, Paul, Jian, Yang, Marianna, Nicolas, Gino, Sonny, Raj, Dirhuba, Hester, Axel, Lara...**, we had great time together in all the lunch time and parties. Of course, I won't forget **Grégory Tissot**, for always being there to support.

OU Xiong 欧雄

October, 2022

# Résumé

---

Le Tibet du Sud-Est est caractérisé par des surfaces de faible relief à haute altitude avec de anciens âges thermochronologiques et très peu d'exhumation depuis au moins la collision Inde-Asie, et aussi par des vallées profondément incisées de grands fleuves (par exemple, Salween, Mékong, Yangtze et Yalong) avec de jeunes âges thermochronologiques et forte érosion. Ces surfaces de haute altitude à faible relief ont été interprétées comme des "surfaces reliques", et ont été proposé d'être formées à faible altitude et soulevées par l'écoulement de la croûte inférieure, puis encaissées par de grands fleuves depuis le Miocène Moyen. Le développement des précipitations de mousson pendant le Cénozoïque tend à entraîner la destruction des plateaux et une forte érosion dans les réseaux fluviaux, tandis que, face à ce forçage climatique, de forts soulèvements liés à des phases de compression importantes conduisent à préserver les surfaces hauts et plats dans les interfluves et en amont. Cependant, la manière dont cette interaction tectonique/climatique a conduit au développement de cette topographie particulière lors de la construction du plateau tibétain reste non résolue.

Dans mes travaux, je me concentre d'abord, à l'échelle locale, sur le massif de Baimaxueshan à faible relief (<600 m) et à altitude modérée (~4500 m), face au massif élevé de Kawagebo de l'autre côté du Mékong dans la région des Trois Rivières, adjacent au Syntaxe Est Himalayenne (SEH). La modélisation thermo-cinématique (Pecube) des données thermochronométriques à basse température montre que le Baimaxueshan a connu un soulèvement régional à une vitesse de 0,25 km/Myr depuis ~10 Ma, lié à l'indentation de l'SEH vers le nord-est, suivant une exhumation lente à un taux de 0,01 km/Myr depuis la collision Inde-Asie. L'incision estimée du Mékong représente un maximum de 30% de l'exhumation totale depuis 10 Ma et le paysage à faible relief du Baimaxueshan résulte en partie de processus glaciaires à haute altitude, renforçant depuis ~2 Ma. En revanche, le Kawagebo à haut relief et à haute altitude ont connu un fort soulèvement à un taux de 1,11-1,91 km/Myr entre 32 et ~15-10 Ma, lié à un chevauchement penchant vers l'ouest et parallèle au fleuve Mékong, pendant la

contraction régionale est-ouest. Cela a également été confirmé par une phase de soulèvement rapide Oligocène sur le plateau de Zuogong au nord, ainsi que par les preuves paléo-altimétriques, montrant un haut plateau existant depuis la fin de l'Éocène dans cette région. Une réactivation de ce chevauchement conduit à une deuxième phase de soulèvement rapide à une vitesse de 0,45–0,52 km/Myr depuis ~15–10 Ma, due à une structure « push-up » entre la faille dextre Parlung et Zhongdian.

À l'échelle régionale, nous avons appliqué une modélisation de l'évolution topographique (FastScape) dans le bassin versant de la rivière Yalong de la Région des Grands Coudes pour explorer l'influence des fortes précipitations de mousson, de forts chevauchements du YBT et son effet orographique imposé sur la réduction de précipitation sur la topographie particulière au Sud-Est du Tibet. Nous proposons qu'un couplage d'un fort soulèvement du Miocène sur le chevauchement Muli du YBT, d'un fort effet orographique sur les précipitations au-dessus de 3000 m et d'une augmentation supplémentaire de l'afflux dans la rivière pour simuler la capture de la zone endoréique du plateau intérieur, pourrait bien reproduire une topographie similaire de la Région des Grands Coudes. Mes travaux mettent l'accent sur le rôle dominant du forçage tectonique dans la construction de la haute topographie, depuis l'Oligocène ou le Miocène moyen dans deux régions au sud-est du Tibet, respectivement. Une combinaison d'une telle forte tectonique, de précipitations orographiques réduites sur le haut plateau et d'une capture potentielle de la zone endoréique est nécessaire pour inciser profondément les gorges de la rivière et préserver simultanément les surfaces de faible relief à haute altitude dans les interfluves et en amont.

**Mots clés:** Sud-Est du Tibet, Le Massif de Kawagebo, Exhumation, Thermochronologie de basses température, Modélisation thermal-cinématique (Pecube), Érosion, La Rivière de Yalong, Modélisation de l'évolution topographique (FastScape)

# Abstract

---

Southeast Tibet is characterized by low-relief surfaces at high-elevation with old thermochronological ages and very little exhumation since at least the India-Asia collision, and deeply incising valleys of large rivers (e.g., Salween, Mekong, Yangtze and Yalong) with young thermochronological ages and strong erosion. These low-relief high-elevation surfaces have been interpreted as “relict surfaces”, and been proposed to be formed at low elevation and uplifted by lower crust channel flow and then dissected by large rivers since middle Miocene. The development of large-scale monsoonal precipitation through the Cenozoic tends to result in plateau destruction and enhanced erosion in the river networks, while, competing with this climatic forcing, different uplift scenarios related to important thrusting phases leads to preserve the high and flat headwaters and interfluvial surfaces. However, how this tectonic/climatic interaction lead to the development of these peculiar topography during the building of the southeastern Tibetan Plateau remain unresolved.

In my work, I first, to a local scale, focus on the low-relief (<600 m), moderate-elevation (~4500 m) Baimaxueshan massif, facing the rugged and high Kawagebo massif across the Mekong river, in the Three Rivers Region, adjacent to the Eastern Himalayan Syntaxis (EHS). Thermo-kinematic modelling (Pecube) of low temperature thermochronometric data shows that the Baimaxueshan massif experienced a regional rock uplift at a rate of 0.25 km/Myr since ~10 Ma, linked to the continuous northward indentation of the EHS, which followed slow exhumation at a rate of 0.01 km/Myr since the India-Asia collision. Estimated Mekong River incision accounts for a maximum of 30% of the total exhumation since 10 Ma and low-relief landscape of the Baimaxueshan massif results from in part glacial “buzzsaw-like” processes at high elevation, enhancing since ~2 Ma. In contrast, the high-relief, high-elevation Kawagebo massif experienced a strong uplift at a rate of 1.11-1.91 km/Myr from 32 to ~15-10 Ma, link to a kinked westward-dipping thrust, striking roughly parallel to the Mekong River during the regional east-west contraction, contributing significantly to the high topography

(>5000 m) west to the Longmucuo–Shuanghu suture. This has also confirmed by a similar Oligocene rapid uplift phase on the Zuogong Plateau to the north to the south, as well as by the paleoaltimetric evidences, showing an existing high plateau since late Eocene in this region. A reactivation of this thrust result in a second rapid uplift phase at a rate of 0.42–0.52 km/Myr since ~15–10 Ma, due to a “push-up” structure between dextral Parlung and Zhongdian fault, continuing to locally generate high topography in the massif.

To a regional scale, I applied a landscape modeling (FastScape) in the Yalong River catchment of the Great Bends Region to explore the influence of strong monsoonal precipitation and the strong tectonics of the Yalong Thrust Belt (YBT) and its imposed orographic effect on reducing precipitation on sculpturing the peculiar topography in SE Tibet. I propose that a coupling of strong Miocene uniform uplift on the Muli thrust of the YBT, strong orographic effect on precipitation on the high plateau edge above 3000 m and supplementary increase of channel inflow to simulate capturing of upstream endorheic zone of inland plateau could well reproduce such a similar topography in Great Bends Region of SE Tibet. My work emphasizes the dominant role of tectonic forcing in constructing the high topography, since the Oligocene or the Mid Miocene in these two regions, respectively. A combination of such strong tectonics, reduced orographic precipitation on the high plateau and a potential capture of endorheic zone of the plateau is necessary to deeply incise the river gorges and simultaneously preserve the low-relief and high-elevation surfaces in the interfluves and headwaters.

**Key words:** Southeast Tibet, The Kawagebo massif, Exhumation, Low temperature thermochronology, Thermal-kinematic modelling (Pecube), Erosion, Yalong River, Landscape evolution modelling (FastScape)

# Material table

---

<b>List of figures</b>	<b>15</b>
<b>List of tables</b>	<b>18</b>
<b>Introduction: formation of the Tibetan Plateau</b>	<b>19</b>
1.1 Subduction and collision between India and Asia: formation of an orogenic plateau.....	19
1.2 General description of the Tibetan Plateau topography .....	21
1.3 Present-day deformation of the Tibetan Plateau.....	23
1.4 Models of the Tibetan Plateau growth .....	26
1.4.1 “Rigid blocks extrusion and continental subduction” model.....	26
1.4.2 “Soft Tibet” model (thin viscous sheet).....	30
1.4.3 “Channel flow” model .....	32
1.4.4 Proto-Tibetan Plateau” model.....	35
1.5 Tibetan Plateau geomorphology: evolution and mechanisms .....	38
1.5.1 Geomorphologic characteristics of Central, Northern and Eastern Tibet .....	39
1.5.1.1 Northern Tibetan Plateau: growing ranges and basins .....	40
1.5.1.2 Flatness of Central Tibetan Plateau and its mechanism.....	44
1.5.1.3 Deeply incising river valleys and low-relief remnant surfaces of southeast Tibet .....	45
1.5.1.4 Topographic evolution models of southeast Tibet:.....	55
(i) “Channel flow” model .....	55
(ii) “Negative topography” model .....	56
(iii) “Lateral shortening” model.....	58
1.5.2 Endorheic zone and exorheic zone.....	60
1.5.2.1 Extend of the paleo-endorheic zone of the Tibetan Plateau .....	61
1.5.2.2 Drainage evolution of the major rivers in exorheic southeast Tibetan Plateau: Salween, Mekong, Yangtze, Yalong and Dadu rivers.....	67

1.6	Paleoaltimetry of the southeast Tibetan Plateau .....	69
1.7	Present-day climate and paleoclimate of the southeast Tibetan Plateau .....	70
1.7.1	Monsoonal climate in southeast Tibet .....	70
1.7.2	Orographic effects on precipitation in southeast Tibet.....	72
1.7.3	Paleoclimate of southeast Tibet.....	75
1.7.3.1	Onset timing of a dominant monsoonal climate.....	75
1.7.3.2	Glaciation development in southeast Tibet .....	81
1.8	Interaction between tectonics, climate and landscape evolution of the orogenic mountain ranges and plateaux.....	83
1.9	Strategy and objects of thesis.....	86
<b>2</b>	<b>Exhumation, thrusting histories and relief development within the Three Rivers Region (Southeast Tibet)</b>	<b>89</b>
2.1	Contrasting exhumation histories and relief development within the Three Rivers Region (Southeast Tibet).....	91
2.1.1	Abstract.....	93
2.1.2	Introduction.....	94
2.1.3	Geologic setting .....	98
2.1.3.1	Cenozoic tectonic evolution of Southeast Tibet.....	98
2.1.3.2	Timing and quantification of exhumation and incision along the Mekong River....	101
2.1.4	Methods: thermo-kinematic modelling of multiple thermochronology data.....	102
2.1.5	Results .....	104
2.1.5.1	Baimaxueshan massif.....	105
2.1.5.2	Kawagebo massif.....	110
2.1.6	Discussion: tectonic and climatic forcing on exhumation .....	114
2.1.6.1	Tectonic and climatic forcing on the evolution of the low-relief Baimaxueshan massif .....	114
2.1.6.2	Dominant tectonic forcing on exhumation in the Kawagebo massif .....	117
2.1.7	Conclusion.....	120
2.1.8	Supplementary materials: low-temperature thermochronology data and thermo-kinematic modelling.....	122
2.1.8.1	Dataset.....	122
2.1.8.2	Thermo-kinematic modelling .....	125
2.1.8.3	Results.....	126

2.2 Eocene–Oligocene thrusting and exhumation within the Three Rivers Region (Southeast Tibet) (in preparation).....	129
2.2.1 Geological setting.....	131
2.2.2 Low-temperature thermochronological data at high elevation in the Kawagebo Massif, sampling strategy and method.....	135
2.2.2.1 Sampling strategy and analysis methods.....	135
2.2.2.2 Results: new low-temperature thermochronological ages of the Kawagebo Massif.....	138
2.2.2.3 Thermo-kinematic modelling method.....	140
2.2.3 3D thermal-kinematic modelling: timing and rate of exhumation in the Kawagebo massif.....	142
2.2.4 Discussion: Oligocene exhumation and tectonic deformation in the Kawagebo massif and its regional application.....	148
2.2.4.1 Regional exhumation patterns in the Three River Region since the Oligocene.....	148
2.2.4.2 Tectonic evolution in the Kawagebo massif: regional implication in the southeastern Tibetan Plateau.....	151
2.2.5 Conclusion.....	153
2.2.6 Supplementary materials: low-temperature thermochronology data and thermo-kinematic modelling.....	156
2.2.6.1 Dataset.....	156
<b>3 Topography and relief development in the Yalong River catchment, Southeast Tibet</b>	<b>167</b>
3.1 Topography and relief development in the Yalong River catchment, Southeast Tibet (under review).....	169
3.1.1 Abstract.....	171
3.1.2 Introduction.....	172
3.1.3 Regional Cenozoic geological setting and paleoclimate.....	175
3.1.3.1 Externally drained southeast Tibet: “Great Bends Region” versus “Three Rivers Region”.....	175
3.1.3.2 Cenozoic tectonic evolution and paleo-elevations of southeast Tibet.....	176
3.1.4 Method: Landscape evolution model (FastScape) and parametric studies.....	180
3.1.4.1 Landscape evolution modelling.....	180
3.1.4.2 Model setup.....	181
3.1.4.3 Basic parameter study.....	182
3.1.5 Landscape evolution under different climatic and tectonic scenarios.....	185
3.1.5.1 Climatic scenarios.....	185
3.1.5.2 Tectonic scenarios.....	186
3.1.5.3 Scenarios with orographic effect and/or reduced monsoon.....	188
3.1.5.4 Increasing upstream inflow scenario.....	189

3.1.6 Discussion .....	191
3.1.6.1 Effect of the monsoon on the topographic evolution of southeast Tibet .....	191
3.1.6.2 Implication of Oligocene (LMTB) versus Miocene (YTB) uplift on the resulting topography of the Yalong catchment.....	192
3.1.6.3 Competition between deeply incising rivers and interfluvial surfaces preservation of southeast Tibet.....	193
3.1.6.4 Potential gradual capture of upstream endorheic zone.....	194
3.1.6.5 Inefficiency of simple Stream Power Law to model plateau scale topography of southeast Tibet.....	195
3.1.7 Conclusion.....	196
<b>4 Conclusions and outlook</b>	<b>199</b>
4.1 Contrasting exhumation and topography development histories in the core of the Three Rivers Region .....	199
4.2 Regional crustal deformation and surface uplift in the Three Rivers Region during Cenozoic ..	201
4.3 Cenozoic topographic evolution in the southeastern Tibetan Plateau: exemplified by the Yalong River catchment .....	203
4.4 Perspectives for future works .....	205
<b>5 Annexes</b>	<b>209</b>
5.1 AFT age data by sample .....	209
References	215

# List of figures

---

Figure 1.1 – Topographic map and simplified tectonic structures of the Tibetan Plateau .....	20
Figure 1.2 – Topographic swath profiles across Tibetan Plateau .....	22
Figure 1.3 – GPS velocity field of the Tibetan Plateau.....	24
Figure 1.4 – GPS-measured movements of the Tibetan Plateau with focal mechanism solutions of earthquakes.....	25
Figure 1.5 – “Rigid block extrusion” model .....	27
Figure 1.6 – Simplified map of major tectonic boundaries and Tertiary faults in Tibet .....	29
Figure 1.7 – 3-D lithospheric diagram of the northeast Tibetan Plateau .....	30
Figure 1.8 – “Thin viscous sheet” .....	31
Figure 1.9 – “Channel flow” model.....	33
Figure 1.10 – Dynamically maintained topography across the Longmenshan.....	34
Figure 1.11 – “Outward plateau growth or proto-plateau” model .....	37
Figure 1.12 – Map of slopes in the Tibetan Plateau .....	38
Figure 1.13 – Local relief, elevation and local slope along two profiles .....	40
Figure 1.14 – Generation of plateau relief of Central and Northern Tibet.....	42
Figure 1.15 – Cenozoic relief, faults and basins in the northern Tibet.....	43
Figure 1.16 – Topography map of the southeast Tibetan Plateau .....	47
Figure 1.17 – Topography swath profiles of the Three Rivers Region and the Great Bends Region .	48
Figure 1.18 – 3D topography with surface remnants of southeast Tibet .....	50
Figure 1.19 – Daocheng and Jaggai massifs across the Yalong River.....	52
Figure 1.20 – Zoom-in relief map with higher resolution of southeast Tibet .....	54
Figure 1.21 – Topography evolution of southeast Tibet of the “Channel flow” model .....	56
Figure 1.22 – “Negative topography” of southeastern Tibet.....	58
Figure 1.23 – Divide and Capture (DAC) landscape evolution model.....	60
Figure 1.24 – Simplified tectonic structures and main basins of the Tibetan Plateau	

.....	63
Figure 1.25 – Map of lakes and lacustrine deposits of the central Tibetan Plateau until ~13.5 Ma .	64
Figure 1.26 – Morden drainage system of the central Tibetan Plateau.....	65
Figure 1.27 – Upstream Yellow River drainage evolution .....	67
Figure 1.28 – Proposed scenarios of drainage evolution in southeast Tibet .....	68
Figure 1.29 – Tibet topography map with Paleogene basins .....	70
Figure 1.30 – Distribution of the Asian monsoon and location of the studied region.....	72
Figure 1.31 – Annual precipitation and evapotranspiration of eastern part of the Tibetan Plateau....	74
Figure 1.32 – Precipitation and topography swath profiles across the Himalayasand the southeast Tibetan Plateau margin.....	75
Figure 1.33 – Compilation of paleoclimate change data of Tibet and its surroundings.....	76
Figure 1.34 – Sedimentary thicknesses in epicontinental marine basins in south and east Asia.....	79
Figure 1.35 – Compilation of physical erosion and chemical weathering proxies since 25 Ma at ODP Sites 1146 and 1148. ....	81
Figure 1.36 – Reconstructed minimum extent of maximum glaciation on the southeast and central Tibet .....	82
Figure 1.37 – Feedback loop among tectonics, climate, and erosion.....	85
Figure 2.1 – Kawagebo massif, viewed from Baimaxueshan massif .....	91
Figure 2.2 – Tectonic and geomorphic setting of Southeast Tibet.....	95
Figure 2.3 – Relief map of southeast Tibet .....	97
Figure 2.4 – Geological map of the Kawagebo area in the Three Rivers Region .....	100
Figure 2.5 – Thermo-kimematic model results for the Baimaxueshan massif.....	107
Figure 2.6 – Scatterplots of Pecube inversion misfits for the plateau scenario model of the Baimaxueshan massif.....	108
Figure 2.7 – Thermo-kimematic model results for the Kawagebo massif.....	112
Figure 2.8 – Scatterplots of Pecube inversion results of thrust model of the Kawagebo massif.....	113
Figure 2.9 – Exhumation since ~ 10 Ma for the Kawagebo and Baimaxueshan massifs.....	117
Figure 2.10 – Three–dimensional view of the Kawagebo.....	119
Figure 2.11 – Simplified geological structures of south–east Tibet, with GPS velocity field. ....	121
Figure 2.12 – Way to the location of the sample KS07 during the 2019 field mission.....	129
Figure 2.13 – Geological map of southeast Tibet.....	134
Figure 2.14 – Landsat image and simplified geological map of the Kawagebo Massif.....	137
Figure 2.15 – AHe (A) and ZHe (B) ages plotted as a function of eU content. ....	139
Figure 2.16 – Modelling results of steady–state scenarios of the Kawagebo massif .....	143
Figure 2.17 – Modelling results of tectonics scenarios with a thrust of the Kawagebo massif.....	145
Figure 2.18 – Scatterplots of Pecube inversion results for Model of the Kawagebo massif .....	146
Figure 2.19 – Topography and major tectonic structures of southeast Tibet.....	150
Figure 2.20 – Topography and major tectonic structures of the southeastern and eastern Tibet.....	155

Figure 3.1 – Topography of the Yalong River catchment and Yalong valley.....	169
Figure 3.2 – Large externally drained rivers and endorheic zone of the Tibet.....	174
Figure 3.3 – Topography of the central and eastern Tibetan Plateau.....	179
Figure 3.4 – Simple models testing the erosional parameters.....	184
Figure 3.5 – Model setting with different phases of uplift and precipitation .....	186
Figure 3.6 – Model settings with different phases of uplift and constant precipitation .....	187
Figure 3.7 – Model setting with different phases of uplift and precipitation of the “Orographic effect scenario” and “Reduced monsoon scenario” .....	189
Figure 3.8 – Model setting with different phases of uplift and precipitation .....	190
Figure 3.9 – Topography of southeast Tibet, divided into two zones, the Three Rivers Region to the west and the Great Bends Region to the east.....	196

Figure S. 2.1 – Pecube modelling result for the Baimaxueshan massif for a steady-state topography scenario of four exhumation phases.....	126
Figure S. 2.2 – Scatterplots of Pecube inversion misfits for the steady-state scenario of four exhumation phases.....	127
Figure S. 5.1 – Radial plot of the AFT age of sample KS01B .....	210
Figure S. 5.2 – Radial plot of the AFT age of sample KS02: .....	210
Figure S. 5.3 – Radial plot of the AFT age of sample KS03:.....	211
Figure S. 5.4 – Radial plot of the AFT age of sample KS04: .....	211
Figure S. 5.5 – Radial plot of the AFT age of sample KS05:.....	212
Figure S. 5.6 – Radial plot of the AFT age of sample KS06: .....	212
Figure S. 5.7 – Radial plot of the AFT age of sample KS07:.....	213
Figure S. 5.8 – Radial plot of the AFT age of sample KS08: .....	213
Figure S. 5.9 – Radial plot of the AFT age of sample KS09: .....	214
Figure S. 5.10 – Radial plot of the AFT age of sample KS10:.....	214

# List of tables

---

Table 2.1 - Thermal and flexural parameter values for Pecube modelling. ....	104
Table 2.2 - Inversion parameters for the different scenarios tested for the Baimaxueshan and Kawagebo massifs. ....	110
Table 2.3 - Synthesis of low-temperature thermochronology data from the Kawagebo Massif.....	141
Table 2.4 - Inversion parameters for the different scenarios tested for the Kawagebo massif.....	147
Table 3.1.....	182
Table S. 2.1 - Dataset of single-grain AHe, AFT and ZHe ages of the Kawagebo massif.....	123
Table S. 2.2 - Synthesis of <b>new AHe</b> data from high elevations of the Kawagebo Massif.....	157
Table S. 2.3 - Synthesis of <b>new AFT</b> ages from high elevations of the Kawagebo Massif .....	159
Table S. 2.4 - Synthesis of <b>new ZHe</b> ages from high elevations of the Kawagebo Massif.....	160
Table S. 2.5 - Synthesis of <b>existing AHe</b> ages from low elevations of the Kawagebo Massif .....	163
Table S. 2.6 - Synthesis of <b>existing AFT</b> ages from low elevations of the Kawagebo Massif.....	164
Table S. 2.7 - Synthesis of low-temperature thermochronology data from the Zuogong Plateau.....	165

## Introduction: formation of the Tibetan Plateau

---

### 1.1 Subduction and collision between India and Asia: formation of an orogenic plateau

The India-Asia continental collisional orogenic system is formed by the thickening of the Indian crust south of the Indus-Tsangpo suture, the southern part of it being the Himalayan range, and the thickening of Asian crust north of the suture mainly being the Tibetan Plateau, extending over an area of 2500 000 km<sup>2</sup> with an average elevation of ~5000 m above mean sea level, being the most extensive elevated surface and one of the most conspicuous physiographic features on earth (Fielding, 1994 <sup>[1]</sup>).

The Tibetan Plateau resulted from a gradual accretion of three terranes to the southern margin of Asia during the Paleozoic and Mesozoic periods, through diachronous closure of the Proto- to Neo-Tethys oceans (e.g., Dewey et al., 1988 <sup>[2]</sup>; Yin and Harrison, 2000 <sup>[3]</sup>; Metcalfe et al., 2021 <sup>[4]</sup>) (Figure 1.1B). From north to south, the Songpan-Ganzi terrane is separated from north Tibet, composed of the Kunlun range, the Qaidam basin and the Qilianshan, by the Kunlun suture and from the Qiangtang terrane in Central Tibet by the Jinsha suture. The Qiangtang terrane is divided by

Longmucuo–Shuanghu suture into two counterparts and is bounded by the Lhasa terrane in the south through the Bangong–Nujiang suture (e.g., Roger et al., 2000<sup>[5]</sup>) (Figure 1.1A).

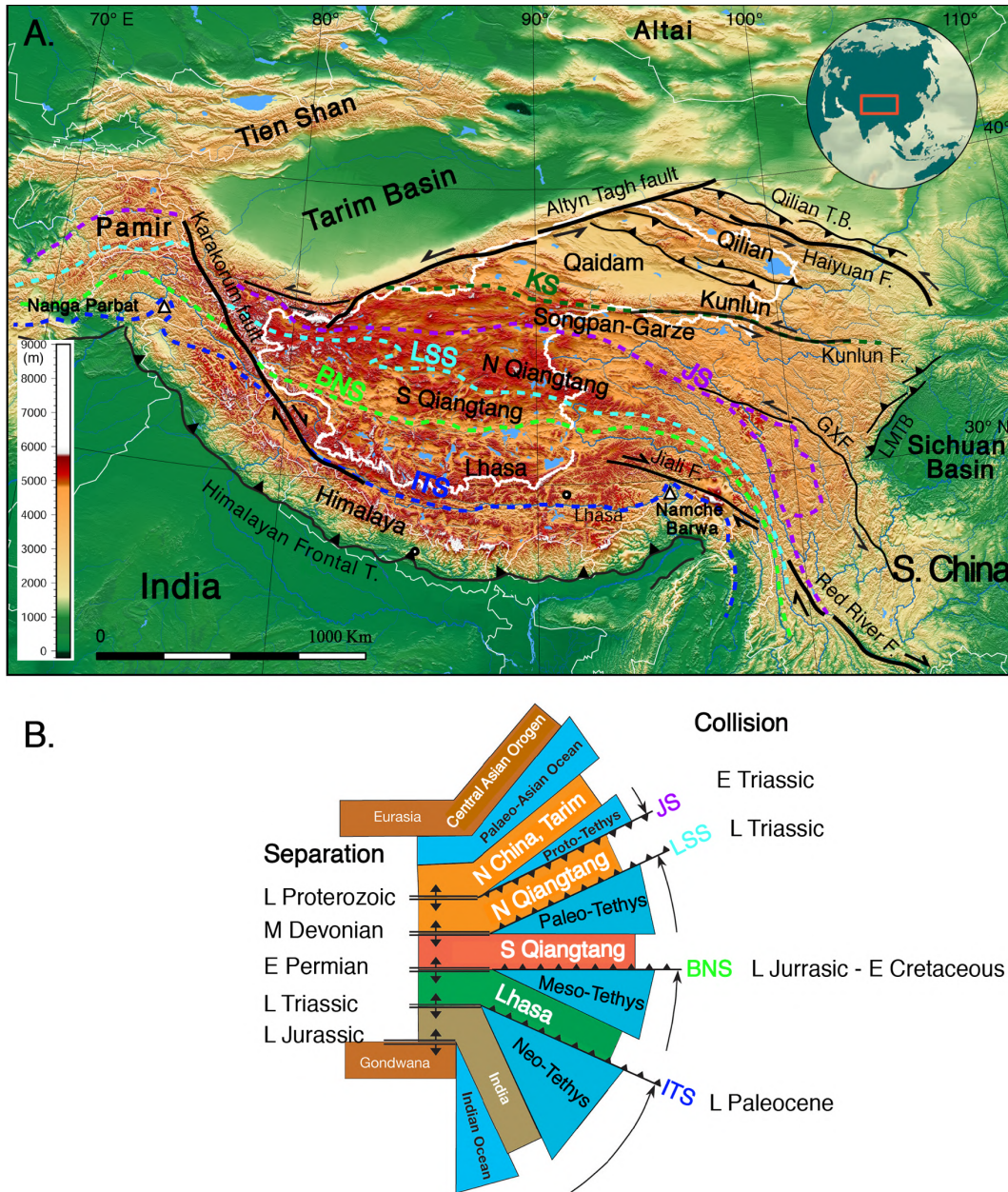


**Figure 1.1** – (A) Topographic map and simplified tectonic structures of the Tibetan Plateau and its surroundings, with accreted terranes delimited by sutures, marked by dash lines in different colors, modified from Roger et al., 2000<sup>[5]</sup>. Abbreviations: KS: Kunlun Suture; BNS: Bangong–Nujiang Suture; ITS: Indus–Tsangpo Suture; JS: Jinsha Suture; LSS: Longmucuo–Shuanghu Suture; GXF: Ganzi–Xianshuihe Fault; LMTB.: Longmenshan Thrust Belt. (B) Schema presenting separation and collision times of terranes by opening and closing oceans, but only in the Tibetan Plateau realm, modified after Metcalfe et al. (2021)<sup>[4]</sup>.

The rising of Tibetan Plateau from the sea level has been proposed to start briefly after the continental collision at ~55 Ma between Indian craton and Lhasa terrane along the Indus–Tsangpo suture (Molnar and Tapponnier, 1975<sup>[6]</sup>; England and Houseman, 1986<sup>[7]</sup>; Tapponnier et al., 2001<sup>[8]</sup>; Royden et al., 2008<sup>[9]</sup>). At the moment of collision, the paleo–geometry of the Indian continent’s northern boundary has been first estimated as linear between Sumatra and the Indus estuary (Tapponnier et al., 1986<sup>[10]</sup>), roughly following the positive anomalies of body wave beneath India (1000 to 1600 km at depth), interpreted as the oceanic Neo–Tethys slab, marking the paleo–position of colliding trench between India and Asia (Replumaz et al., 2014<sup>[11]</sup>). Based on such hypothesis, it has been estimated that the total amount of convergence was of ~2200 km, absorbed in India by ~900 km and in Asia by ~1300 km, of which at most 45% is accommodated by Asian continental subduction (Replumaz et al., 2013<sup>[12]</sup>, 2014<sup>[11]</sup>), with the rest of the convergence accommodated by a combination of shortening, extrusion and shallow subduction or underthrusting processes (Tapponnier et al., 2001<sup>[8]</sup>; Replumaz and Tapponnier, 2003<sup>[13]</sup>; Replumaz et al., 2010a<sup>[14]</sup>).

Other reconstruction has proposed the convergence amount to be around 2860–3600 km (from the western to eastern syntaxes), which should have been accommodated in the Himalayan–Tibetan orogen, with  $1100 \pm 560$  km partitioned into the Asian lithosphere and  $1700 \pm 560$  km consumed by the underthrusting Indian lithosphere (Lippert et al., 2014<sup>[15]</sup>), concluding to a significant crustal shortening deficit, estimated in Asia (<1000 km) and the Himalayas (<1000 km), compared to the total convergence between India and Asia (van Hinsbergen et al., 2011<sup>[16]</sup>, 2012<sup>[17]</sup>).

## 1.2 General description of the Tibetan Plateau topography

The Tibetan plateau lies at an average elevation of ~5000 m ( $\pm 200$  m), and surrounded by steep-sided margins, with abrupt elevation drawdown from ~5 km to <1 km over only 50–200 km, along the elevated Himalayan range in the south, the Altyn Tagh–Qilianshan in the north, and along the Longmenshan adjacent to the Sichuan Basin in the east (Clark and Royden, 2000<sup>[18]</sup>) (Figure 1.2B). While the southeast and northeast parts of the plateau exhibit gradually decreasing gradients in elevation, from ~5 km to ~1 km along the southeastern margin and from ~4.5 km to ~1.5 km along the northeastern margin both over a distance of ~2500 km.

Most northern and central Tibet is endorheic, with the low relief on both short and long wavelength; especially the central part shows an extraordinary flatness, with an average slope of  $\sim 5^\circ$  over 250 m windows (Fielding et al., 1994<sup>[11]</sup>). In contrast, the landscape of the externally drained area of the southeast Tibetan Plateau is strong dissected and enhanced topographic slopes are widely observed, except the upstream-most drainages of the large rivers, adjacent to the endorheic zone.

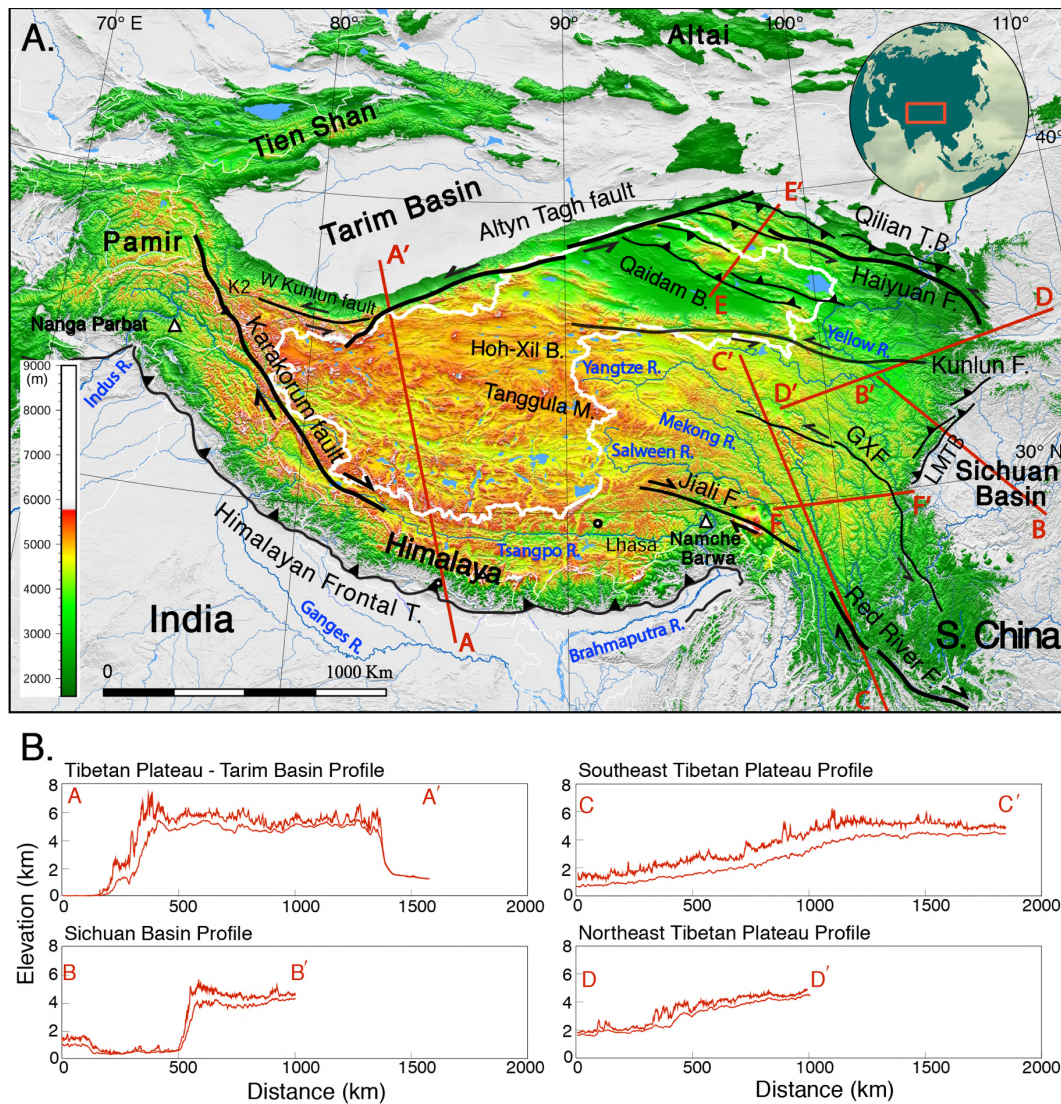


**Figure 1.2** – (A) Topographic map and simplified tectonic structures of the Tibetan Plateau B.: basin; M.: mountains; GXF: Ganzi–Xianshuihe Fault; LMTB.: Longmenshan Thrust Belt. The white thick line defines the endorheic zone (B) Topographic swath profiles across Tibetan Plateau (swath width is of 100–300 km), with locations marked in A. Profiles show the maximum and mean elevation, modified after Clark and Royden (2000)<sup>[18]</sup>.

### 1.3 Present-day deformation of the Tibetan Plateau

Detailed analyses of the Global positioning system (GPS) velocities in a Eurasia-fixed reference frame, measuring horizontal movements of crust, show a velocity decrease from the Himalayas front to the northern plateau margin from  $\sim 40$  mm/yr to  $\sim 5$ – $10$  mm/yr (Zhang et al., 2004<sup>[19]</sup>) (Figure 1.3A). More than 55% of the India-Asia convergence of present-day is accommodated by lithospheric deformation at the margins of the plateau and more than 33% of it is absorbed by internal shortening within the plateau, illustrated clearly in the middle to western part (Wang et al., 2001<sup>[20]</sup>) (Figure 1.3A, Figure 1.4A). The GPS measurements demonstrate also other remarkable crustal motions, such as eastward/southeastward extrusion of the plateau as well as clockwise rotation of southeast Tibet around EHS, which is clearly highlighted by the velocity field in a Tibetan Plateau-fixed reference frame (Figure 1.3B). This remarkable glacier-like flow zone around EHS is delimited by the large strike-slip faults of Jiali (dextral) and Ganzi-Xianshuihe (sinistral) from south to north (Gan et al., 2007<sup>[21]</sup>, 2021<sup>[22]</sup>).

Plateau margins (e.g., the Himalayas, the Qilianshan, and the Longmenshan) are dominated by thrusting with shortening rates of  $\sim 15$ – $20$ ,  $\sim 5.5$ – $6$ , and  $4$  mm/yr, respectively (Zhang et al., 2004<sup>[19]</sup>) (Figure 1.4A). The Altyn Tagh-Qilianshan also experiences significant strike-slip deformation at rate of  $\sim 5 \pm 2$  mm/yr, shown by focal mechanism solution of the earthquakes (Figure 1.4B). Strike-slip deformation is also observed dominant along the dextral Karakorum fault or in the eastern to southeastern part of the plateau, such as the sinistral Kunlun and Yushu-Ganzi-Xianshuihe-Xiaojiang fault system and the dextral Jiali-Zhongdian-Red River faults. In contrast, east-west extension at rate of  $\sim 22 \pm 3$  mm/yr is observed in south and central Tibet, most probably since 10–15 Ma (e.g., Molnar and Tapponnier, 1978<sup>[23]</sup>; Armijo et al., 1986<sup>[24]</sup>; Lyon-Caen and Molnar, 1989<sup>[25]</sup>; Wang et al., 2001<sup>[20]</sup>; Zhang et al., 2004<sup>[19]</sup>; Gan et al., 2007<sup>[21]</sup>; Elliott et al., 2010<sup>[26]</sup>; Ge<sup>[27]</sup> et al., 2015). Normal fault plane solutions of earthquakes are observed in south and central Tibet, but also in southeast Tibet in pull apart between strike-slip faults (Wang et al 2014<sup>[28]</sup>) (Figure 1.3B, Figure 1.4A, Figure 1.4B).

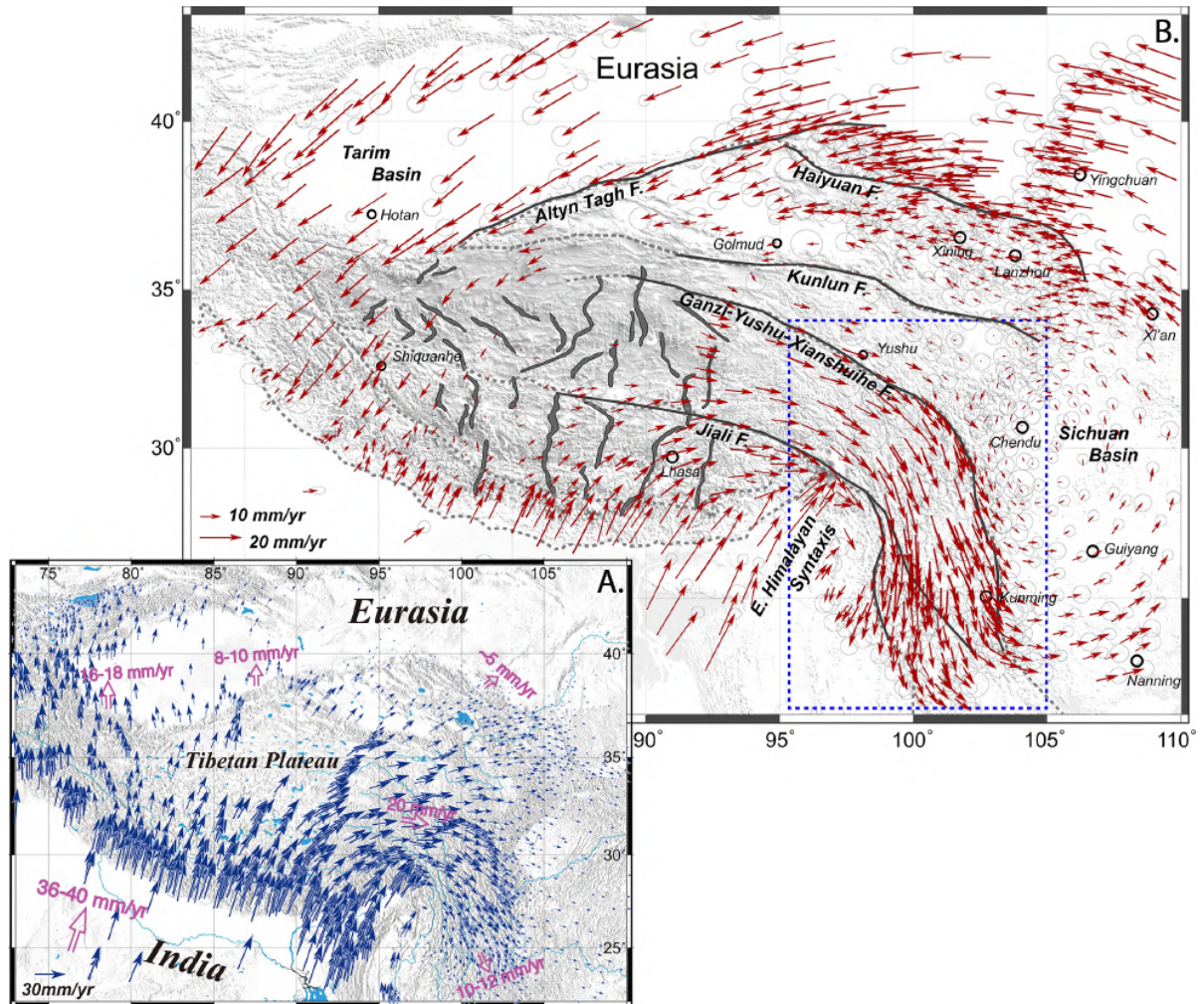
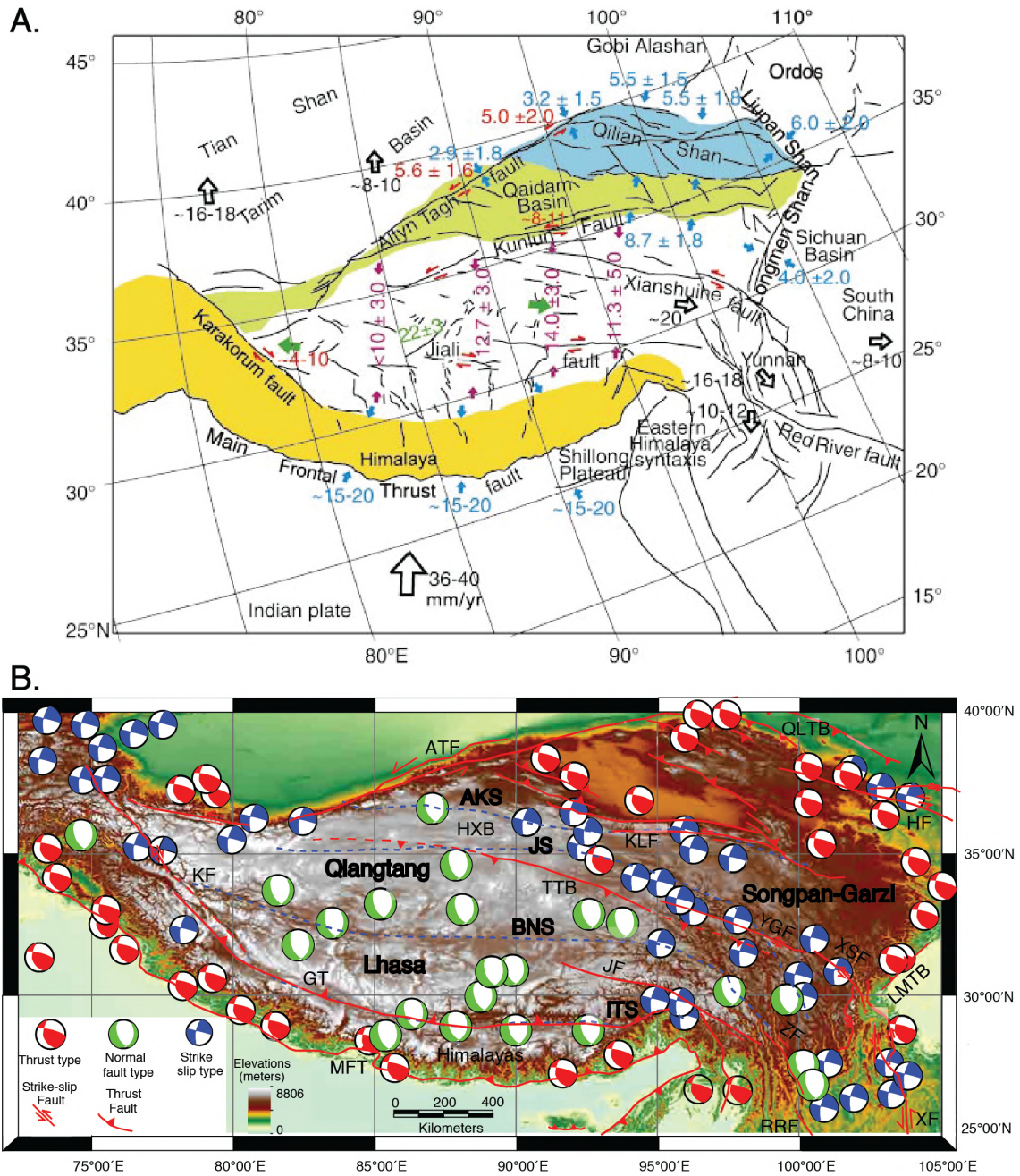


Figure 1.3 – (A) GPS velocity field of the Tibetan Plateau and its surroundings in a Eurasia-fixed reference frame, (GPS velocities from Zhang et al. 2004<sup>[19]</sup>). (B) GPS velocity field in Tibetan Plateau-fixed reference frame, with rifts and grabens, marked in dark grey belts, in central and southern Tibet under E-W extension tectonic regime. Adapted from Gan et al. 2021<sup>[22]</sup>.



**Figure 1.4** – (A) Simplified tectonic map illustrating active faults and GPS-measured movements of the Tibetan Plateau and its margins. Purple arrows show N20°E shortening in plateau interior. Blue/green/red arrows and numbers are shortening rates across plateau margins, extension rates in western and central Tibet and strike-slip rates. Black arrows show relative motion with respect to stable Eurasia. Modified after [Zhang et al. 2004](#)<sup>[19]</sup>. (B) Simplified tectonic map of the Tibetan Plateau, with focal mechanism solutions of earthquakes. Abbreviations: AKS: Ayimaqin–Kunlun Suture; ATF: Allyn Tagh Fault; BNS: Bangong–Nujiang Suture; GT: Gangdese Thrust; HF: Haiyuan Fault; HXB: Hoh–Xil Basin; ITS: Indus–Tsangpo Suture; JF: Jiali Fault; JS: Jinsha Suture; KF: Karakorum Fault; KLF: Kunlun Fault; LMTB: Longmenshan Thrust Belt; MFT: Main Front Thrust; QDB: Qaidam Basin; QLTB: Qilianshan Thrust Belt; RRF: Red River Fault; TTB: Tanggula Thrust Belt; XF: Xiaojiang Fault; XSF: Xianshuihe Fault; YGF: Yushu–Ganzi Fault; ZF: Zhongdian Fault. Modified after [Wang et al. 2014](#)<sup>[28]</sup>.

## 1.4 Models of the Tibetan Plateau growth

Several mechanisms have been invoked to explain the tectonic, topographic and geodynamic evolution of the Tibetan Plateau since the beginning of Tethyan oceanic subduction and subsequent continental/terrane collision, sometimes mutually exclusive, based on different lithospheric rheology or paleoaltitude data.

### 1.4.1 “Rigid blocks extrusion and continental subduction” model

In the lateral continental extrusion model (Tapponnier et al., 1982<sup>[29]</sup>), due to India’s relentless northward impingement, the migrating deformation re-invigorated the pre-existing and weakly welded sutures, inheriting from the Mesozoic subduction events. The horizontal collision force along the Himalaya eventually facilitated the generation of large-scale faults and localized intracontinental deformation at/near those sutures in Tibet. Analogue experiments of a solid indenter penetrating into a homogenous plasticine layers, materials capable to create faults, have been conducted to reproduce the indentation of the rigid India craton into the relatively weak Southern Eurasia margin, an agglomeration of terranes. A free east boundary was also imposed to represent the weak resistance of Pacific subduction east of the South China block (Figure 1.5A). Experiment results illustrated a successive extrusion of the Eurasian continental lithosphere to the east along the newly formed large strike-slip faults, away from the collision front (Tapponnier et al., 1982<sup>[29]</sup>; Peltzer and Tapponnier, 1988<sup>[30]</sup>). The lithosphere of the whole Indochina, as a rigid block, was firstly extruded southeastward along the sinistral Ailaoshan–Red River shear zone for over ~1000 km and rotated ~40° clockwise relative to Eurasia (Leloup et al., 1995<sup>[31]</sup>, 2001<sup>[32]</sup>). During later stages, continuous collision successively led to the extrusion of eastern part of the Qiangtang and Songpan–Ganzi terranes along the younger Ganzi–Xianshuihe and Kunlun sinistral strike-slip faults, and then the Qaidam–Kunlun–Qilian block along the Altyn Tagh and Haiyuan sinistral strike-slip faults in the north (Leloup et al., 2001<sup>[32]</sup>; Replumaz and Tapponnier, 2003<sup>[13]</sup>) (Figure 1.1A, Figure 1.5B). Regardless of its success in approximating the first-order strike-slip faults, the lateral extrusion model has been questioned for the fact that vertical strain or surface uplift in this analogue model was impeded rather than permitted, which necessitated a supplementary mechanism to explain the crustal shortening and thickening on a plateau-scale (e.g., Dewey et al., 1988<sup>[2]</sup>; van Hinsbergen et al., 2011<sup>[16]</sup>).

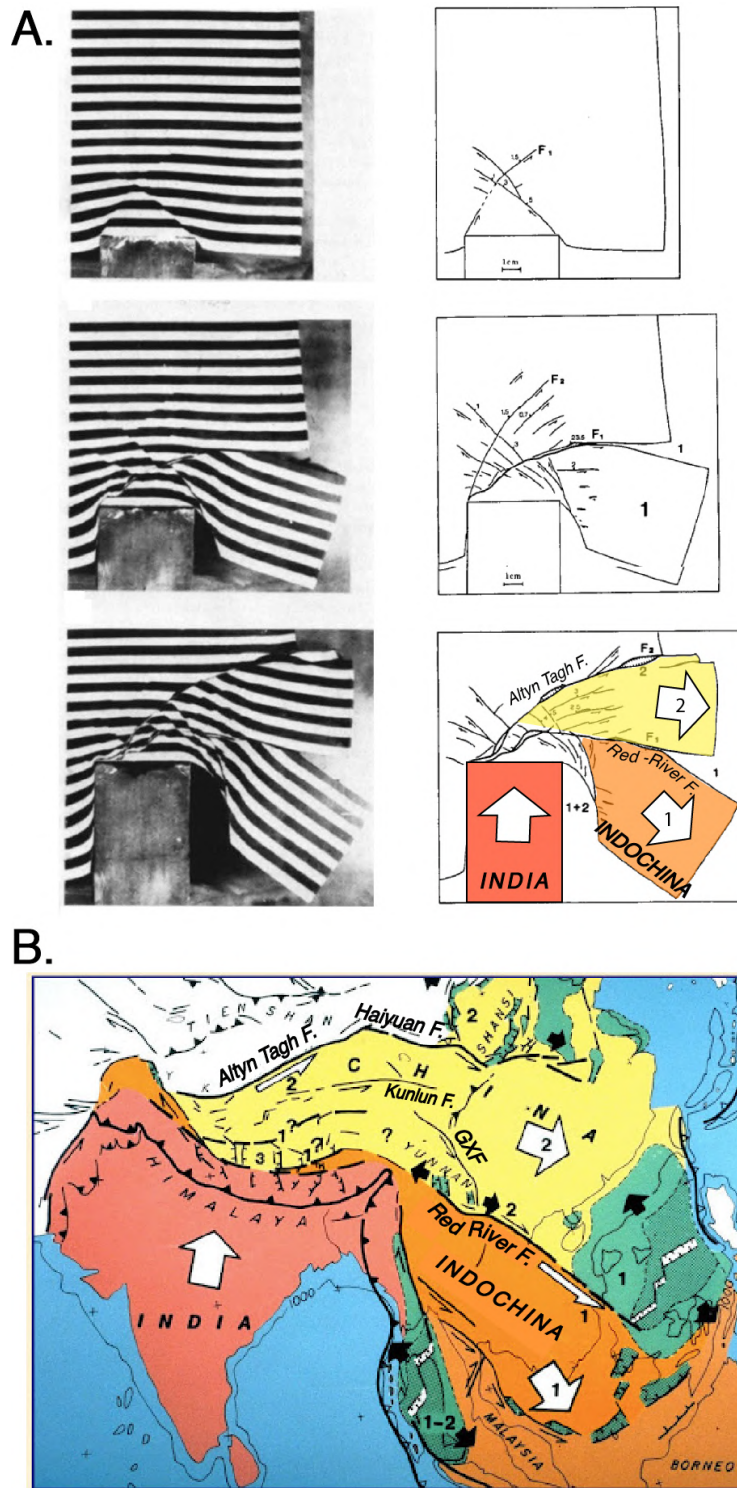


Figure 1.5 - (A) Analogue experiment of a rigid indentation (India craton) into a layered plasticine medium (Southern Eurasian Margin). The plasticine layers are vertically confined and have a free boundary on the east boundary. Successive extrusion of blocks to the east is delimited by large strike-faults and localize deformation (Tapponnier et al., 1982<sup>[29]</sup>). B) Schematic representation of the multi stages extrusion observed in the Southeast Asia, Eastern Tibet, due to Indian indentation (after Tapponnier et al. 1986<sup>[10]</sup>). GXF: Ganzi-Xianshuihe Fault.

While lately compiling Cenozoic deformation, magmatism and seismic structure, [Tapponnier et al. \(2001\)](#)<sup>[8]</sup> introduced internal shortening and successive intracontinental subduction of the Asian lithospheric mantle under the plateau ([Roger et al., 2000](#)<sup>[5]</sup>), a mechanism effectuating a geodynamic role on sustaining stepwise rise and growth of the plateau. Those authors formulated a time-dependent model for the continuous oblique growth of plateau in three main phases: the Eocene uplift of the south Tibet, the Oligocene–Miocene uplift of the central part and the most recent rising (Pliocene–Quaternary) of the northeast part. The southeastern Tibetan Plateau would be shortened and uplifted mostly before the Miocene, since it was extruded southeastward along the Red River and Xianshuihe faults ([Figure 1.6A](#)). As India continuously penetrated into Asia, sequential and northward reactivation of weakly welded sutures resulted in the thickening of the Asian lithosphere between these sutures due to the convergence force on the collision boundary ([Tapponnier et al., 2001](#)<sup>[8]</sup>; [Guillot and Replumaz, 2013](#)<sup>[33]</sup>). Successive, mantle subduction was then initiated ([Figure 1.6B](#)), contributing to the growth of crustal accretionary wedges, but decoupled by an intra-crustal décollement from the mantle (e.g., [Mattauer et al., 1986](#)<sup>[34]</sup>; [Tapponnier et al., 1990](#)<sup>[35]</sup>). Recent thermo-mechanical and analogue modelling suggested that the intracontinental subductions firstly took place through reactivation of the Jinsha suture due to the far-field tectonic force of the India–Asia collision, contrary to a simple northward migration of the deformation (e.g., [Replumaz et al., 2016](#)<sup>[36]</sup>; [Pitard et al., 2018](#)<sup>[37]</sup>; [Goussin et al., 2020](#)<sup>[38]</sup>).

The ongoing Pliocene–Quaternary growth of the northeast Tibetan Plateau illustrates the progressive “plateau rise and growth” and eastward block extrusion ([Meyer et al., 1998](#)<sup>[39]</sup>; [Tapponnier et al., 2001](#)<sup>[8]</sup>). Confined by the large Kunlun, Haiyuan, and northern Altyn Tagh sinistral faults, the Qaidam–Kunlun–Qilian block in the northeast plateau ([Figure 1.1A](#), [Figure 1.6A](#)) is thickened by multiple parallel thick-skinned thrusts, which are branched to the Altyn Tagh fault to the west. Those sinistral faults are decoupled from the mantle underneath on a gently south-dipping décollement, creating typical crustal accretionary wedges ([Figure 1.7](#)). The contrast and decrease of slip rate on different strike-slip faults favorize bloc extrusion and crustal thickening at the extremity of the faults over a tremendous region, as proposed in “rigid blocks extrusion and subduction” model ([Tapponnier et al., 2001](#)<sup>[8]</sup>).

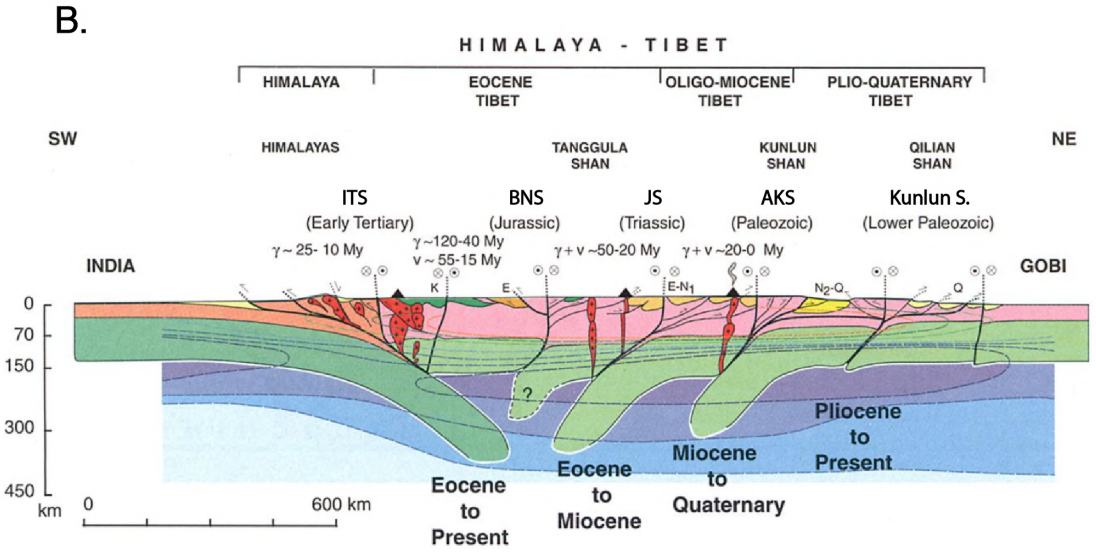
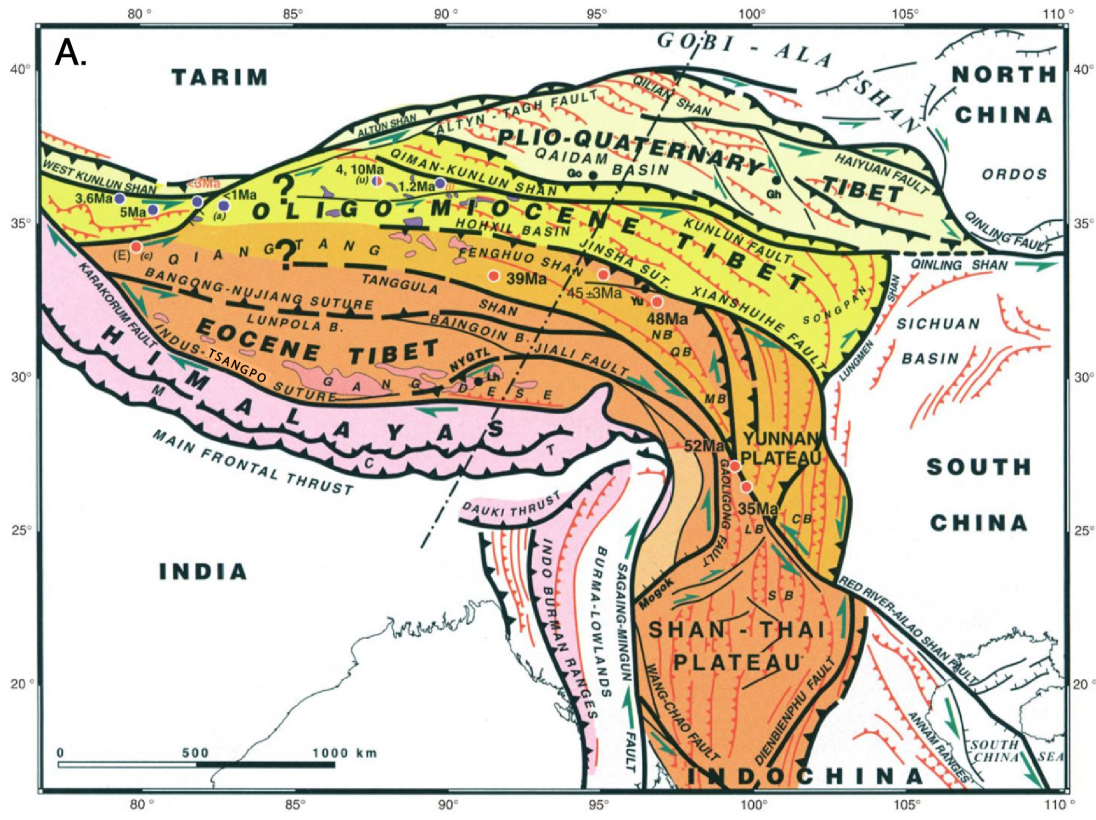


Figure 1.6 - (A) Simplified map of major tectonic boundaries and Tertiary faults in Tibet. Major thrusts and localized shear zones are shown in bold black lines and other crustal thrusts in red thin lines. Orange to pale yellow patches illustrate a northward younging of the plateau-building in Tibet. (B) NE-SW schematic section of lithosphere of Himalaya-Tibet orogen, showing a northward Cenozoic growing, as detailed in the renewed “Rigid blocks extrusion and subduction” model. Green patches are subducted Indian and Asian lithospheric mantle and yellow and dark green patches show somehow important sediment filling to create flatness. AKS: Ayimaqin-Kunlun Suture; BNS: Bangong-Nujiang Suture; ITS: Indus-Tsangpo Suture; JS: Jinsha Suture; LSS: Longmucuo-Shuanghu Suture; Modified from [Tapponnier et al. \(2001\)](#)<sup>[8]</sup>.

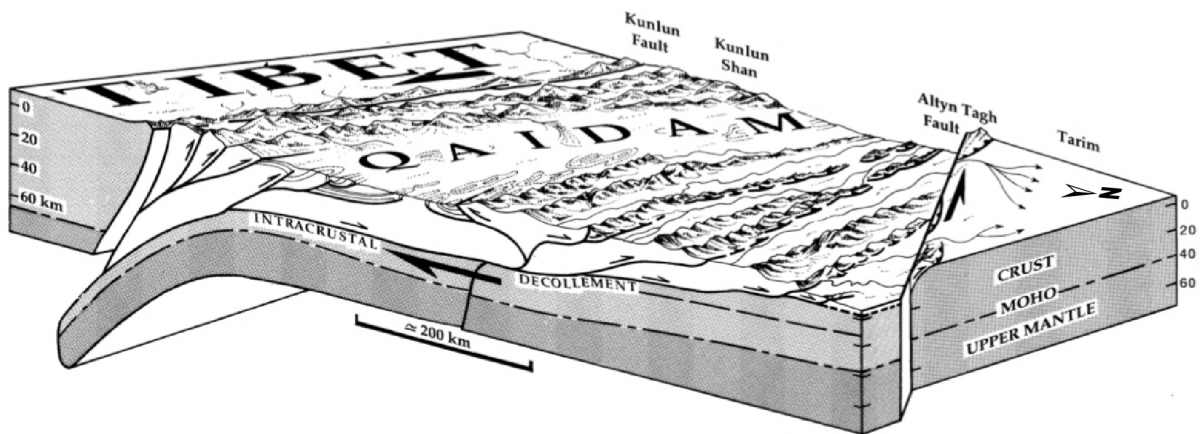


Figure 1.7 – 3-D lithospheric diagram of the northeast Tibetan Plateau. Northeastwards-migrating thrusts with sinistral motion branch in depth on a regional, shallow south-dipping décollement, which roots into the mantle subduction zone underneath the Kunlunshan (after Meyer et al., 1998<sup>[39]</sup>).

#### 1.4.2 “Soft Tibet” model (thin viscous sheet)

As inferred in the “rigid block extrusion” model, the assumption of solely considering plane horizontal strain arising from the convergence forces along the collision boundary (Molnar and Tapponnier, 1975<sup>[6]</sup>; Tapponnier and Molnar, 1976<sup>[40]</sup>; Molnar and Tapponnier, 1977<sup>[41]</sup>; Tapponnier et al., 1982<sup>[29]</sup>) might fail in regions with significantly thickened crust, where the resulting gravitational forces and vertical strain could remarkably influence the deformation regime (e.g. Richter and McKenzie, 1978<sup>[42]</sup>). Primarily motivated by general topographic features of the plateau, others authors proposed a “thin viscous sheet” model for the continental deformation, where the continental lithosphere is treated as a mechanical continuum medium, subject to a Newtonian or a power law rheology and shortening is almost homogenously distributed, without any vertical variation within the lithosphere (England and McKenzie, 1982<sup>[43]</sup>, 1986<sup>[44]</sup>; Houseman and England, 1986<sup>[45]</sup>).

Numerical experiments of a thin viscous sheet overlying an inviscid substrate illustrated that the viscous material first thickened homogenously in response to convergence forces along the Indian indentation front and then flowed and expanded simultaneously toward the surrounding edges due to its interior gravitational forces originating from gradients of crustal thickness contrasts (England and Houseman, 198<sup>[44]</sup>; Houseman and England, 1986<sup>[45]</sup>; Jiménez-Munt and Platt, 2006<sup>[46]</sup>). Thus the

horizontal divergence of such a flow established a time-dependent crustal thickening propagating outward from the central plateau, engendering a lateral movement of materials away from the region of thickest crust (Figure 1.8A). Moreover, the forces invoked by crustal thickness contrast are quantitatively sufficient to result in a pure extension regime in the core of the plateau, perpendicular to the convergence direction (Figure 1.8B). Those results corresponded well to the first-order observations of the flatness on the plateau, the active east-west extension of southern Tibet and the eastward motion of eastern Tibet, suggesting that the volume forces might exert a key role in the continents deformation.

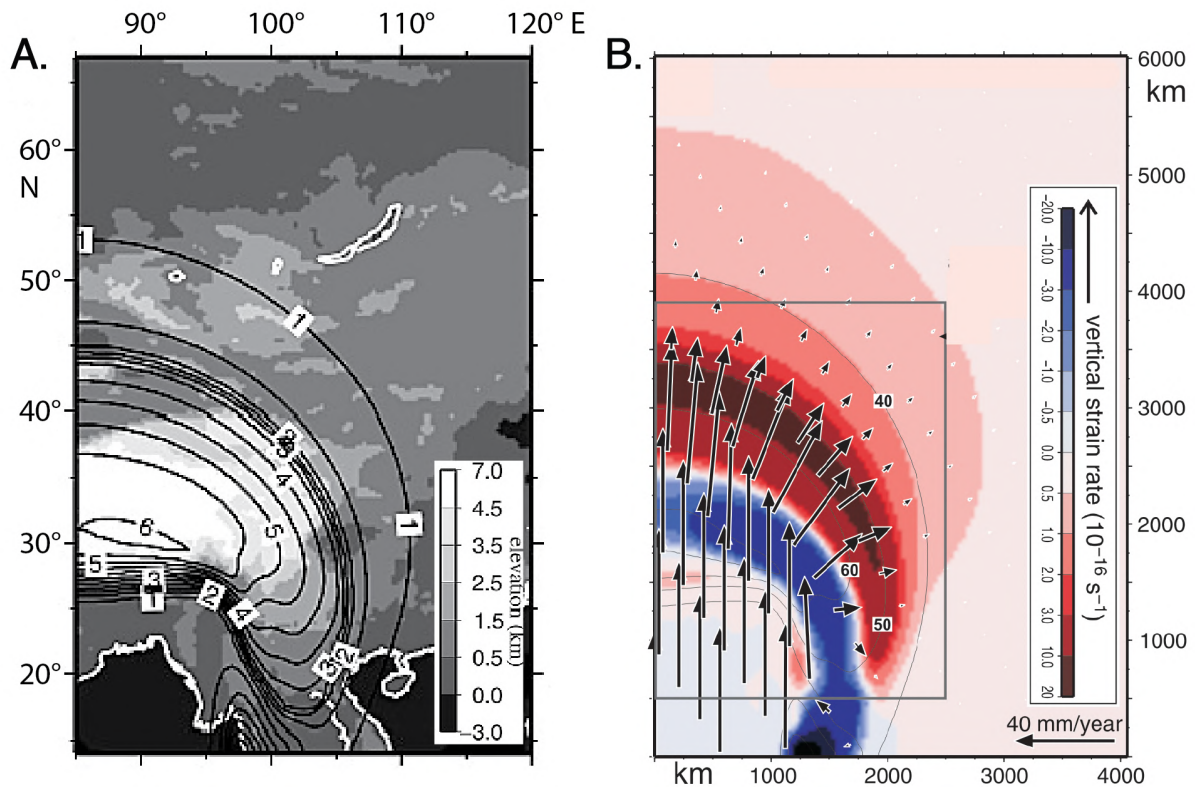


**Figure 1.8** – Results of a “thin viscous sheet” model of convergence at 50 mm/yr during 57 Ma and 7 Ma after the lithospheric mantle removal in regions with thickness passes 155 km. (A) Predicted elevation (contours) and measured (grey pattern) are shown. (B) Arrows present horizontal velocity field and vertical strain rate is shaded, positive for thickening and negative for thinning. Crustal thickness is delimited by thin gray contours of 10 km. Modified after Jiménez-Munt and Platt (2006)<sup>[46]</sup>.

However, such a ‘soft Tibet’ model cannot account for neither the regional discontinuous strain observed along the large deep-rooted shear zone and strike-slip faults, nor the basin development in the northern Tibetan Plateau. Additionally, later studies showed that such a continuum deformation could not uplift the Tibetan Plateau to reach its present average elevation of ~5000 m (e.g., [England and Houseman, 1989](#) <sup>[47]</sup>; [Molnar et al., 1993](#) <sup>[48]</sup>; [Jiménez-Munt and Platt, 2006](#) <sup>[46]</sup>). An introduction of mantle convection would trigger a thermal removal of cold/dense lower lithospheric mantle and then a lithospheric thinning after a certain degree of crustal thickening and eventually result in isostatic compensation ([Molnar et al., 1993](#) <sup>[48]</sup>). Such a process would lead to rapid isostatic rebound and significant surface uplift of Tibet being a single entity (e.g. from 3 to >5 km) only within a few million years since middle Miocene ([England and Houseman, 1988](#) <sup>[49]</sup>; [Platt and England, 1994](#) <sup>[50]</sup>), and strengthen the Indian monsoon at ~10–8 Ma ([Kroon et al., 1991](#) <sup>[51]</sup>; [Molnar et al., 1993](#) <sup>[48]</sup>).

### 1.4.3 “Channel flow” model

Crustal channel flow was first brought up to develop a new model with vertically heterogeneous rheology ([Kuhn, 1997](#) <sup>[52]</sup>), which was significantly different from conventional geodynamic models of finite homogeneous rheological layering within continental crust (e.g., “thin viscous sheet” model). A weak viscous lower crust, embedded by rigid upper crust and mantle, arising from partial melting in the thickened lithosphere with high radioactive heating, has been firstly introduced to suggest that Tibet was elevated hydraulically ([Burke and Dewey, 1973](#) <sup>[53]</sup>; [Zhao and Morgan, 1985](#) <sup>[54]</sup>) and its presence has been latterly evidenced by seismic reflection profiles of the first geophysical survey of Tibet (INDEPTH project) in 90s (e.g., [Jin et al., 1996](#) <sup>[55]</sup>; [Nelson et al., 1996](#) <sup>[56]</sup>; [Wei et al., 2001](#) <sup>[57]</sup>). In Tibet, the lower crustal layer attaining a critical viscosity could flow laterally at a constant rate from the central plateau toward the surrounding regions inside a 10–15 km thick channel, due to a horizontal gradient in lithostatic pressure. This pressure gradient is generated by the pronounced gravitational contrast between larger crustal thickness beneath the plateau center and smaller crustal thickness in the foreland ([Figure 1.9](#)) and could drive the viscous material to travel over ~1500 km, facilitating the outward gravitational expansion of the high plateau ([Royden, 1996](#) <sup>[58]</sup>; [Royden et al., 1997](#) <sup>[59]</sup>; [Clark and Royden, 2000](#) <sup>[18]</sup>; [Medvedev and Beaumont, 2006](#) <sup>[60]</sup>; [Royden et al., 2008](#) <sup>[9]</sup>). The velocity field of the flow could be qualitatively described by the Poiseuille flow between stationary boundaries where the pressure gradient leads to highest velocities in the middle of the channel ([Mancktelow, 1995](#) <sup>[61]</sup>; [Godin et al., 2006](#) <sup>[62]</sup>; [Klemperer, 2006](#) <sup>[63]</sup>) ([Figure 1.9](#)).

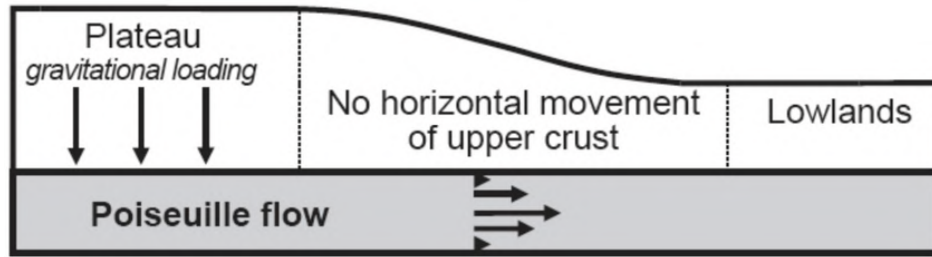
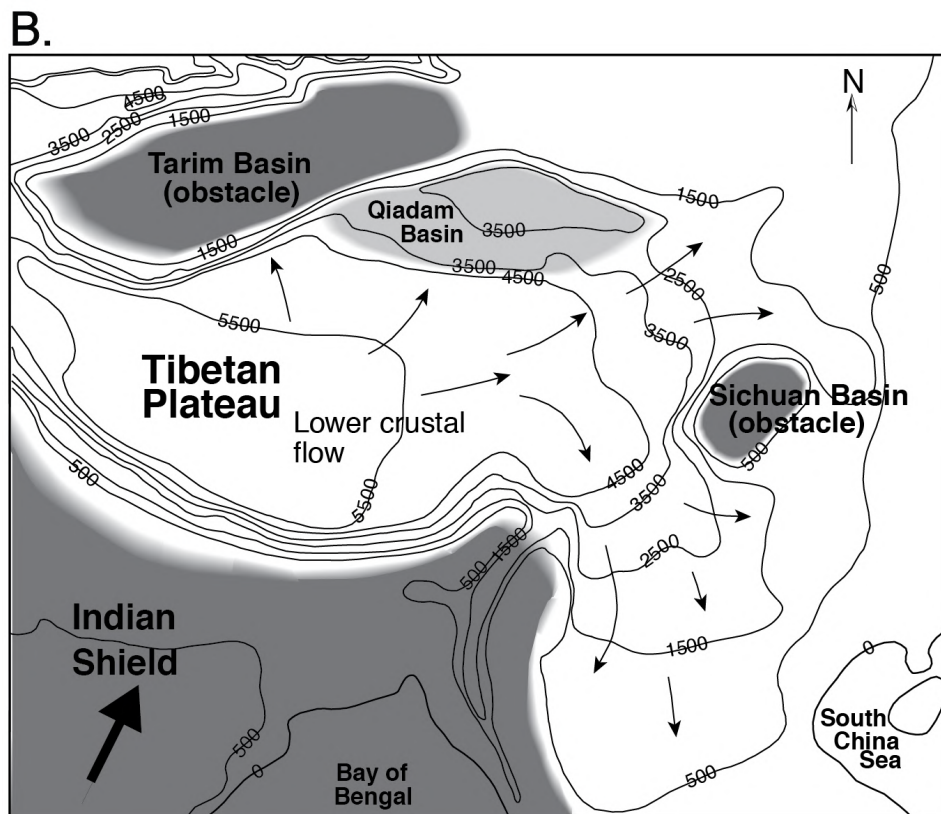
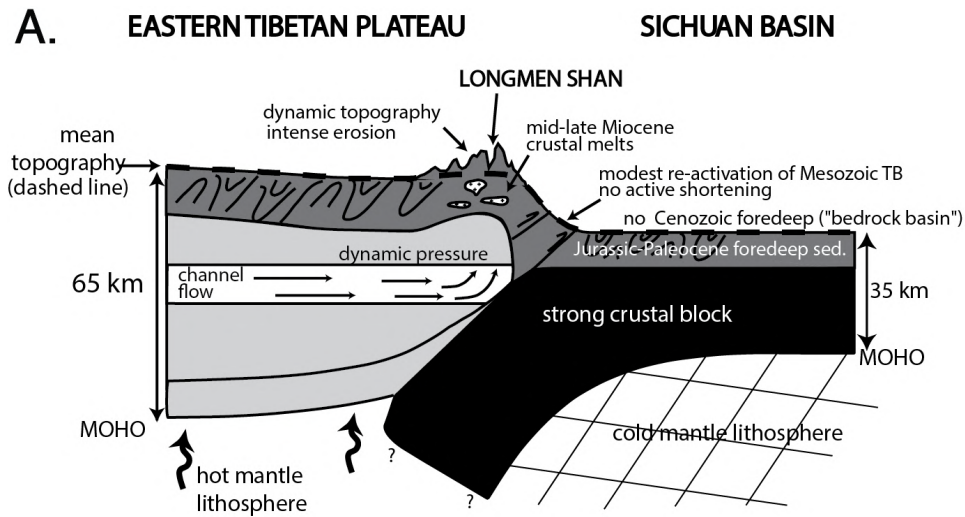


Figure 1.9 – Scheme of the channel flow model base on Clark and Royden, 2000<sup>[18]</sup>. Ductile lower crust migrates passively from the region of thickened crust towards foreland due to high lithostatic pressure gradient, modified from Klemperer (2006)<sup>[63]</sup>.

This approach was also developed to explain a broad regional uplift of the eastern Tibetan Plateau, terminated by an abrupt margin, by the Poiseuille flow of a Newtonian fluid through the lower crust channel (Royden et al., 1997<sup>[59]</sup>; Clark and Royden, 2000<sup>[18]</sup>). In this model, the presence of the cold, rigid lithosphere underneath the Sichuan Basin east to the Longmenshan acts as a barrier to inhibit the eastward flowing of viscous materials, dominantly contributing to surface uplift and enhanced topographic gradient between the eastern plateau and the Sichuan Basin foreland through the flexure of dynamic topography effect (Figure 1.10A). This model therefore minimized the contribution of upper-crustal deformation to surface uplift, in the context of slow convergence rate and relatively slow deformation, observed across the Longmenshan at present-day (Royden et al., 1997<sup>[59]</sup>; Clark and Royden, 2000<sup>[18]</sup>; Royden et al., 2008<sup>[9]</sup>; Burchfiel et al., 2008<sup>[64]</sup>). Low-velocity or low-resistivity zones in the middle-lower crust underneath the eastern Tibet have indeed been documented by magnetotelluric and seismic surveys, lending some support to the channel flow model (Zhang et al., 2009<sup>[65]</sup>; Zhao et al., 2012<sup>[66]</sup>). In southeast and northeast margins of the Tibetan Plateau, this process has been proposed to engender continuous surface uplift and gradually decreasing topographic gradients in those directions (Clark and Royden, 2000<sup>[18]</sup>, Clark et al., 2005a<sup>[67]</sup>) (Figure 1.10B).



**Figure 1.10** – (A) Simple cross-section of dynamically maintained topography across the Longmenshan, showing the interaction of the ductile lower crustal flow and the rigid crustal block, after [Clark et al. \(2005a\)](#)<sup>[67]</sup>. (B) Smoothed elevation contours of Tibetan Plateau and its surrounding regions. Dark gray to white shades represent areas with cold and rigid to weak crust, respectively. Lower crust materials escape from underneath thickened, high central plateau through the southeast and northeast Tibet with weak crust, after [Clark and Royden \(2000\)](#)<sup>[18]</sup>.

However, other evidences showed that lithospheric thickening here may largely, if not totally, stem from brittle crustal shortening accommodated by crustal-scale thrusting related to main tectonic structures of the Longmenshan (e.g., [Hubbard and Shaw, 2009](#)<sup>[68]</sup>; [Liu-Zeng et al., 2009](#)<sup>[69]</sup>; [Tian et al., 2013](#)<sup>[70]</sup>, [2016](#)<sup>[71]</sup>). The occurrence of Wenchuan earthquake of 7.9 magnitude in 2008 and Lushan earthquake of 7.0 magnitude in 2013 along the Longmenshan thrust belt has ruptured several thrusts, showing a clear compressive deformation regime and clearly active crustal shortening (e.g., [Zhang et al., 2009](#)<sup>[65]</sup>; [Xu et al., 2013](#)<sup>[72]</sup>). Moreover, this model attempted to illustrate an outward growth of the Tibetan Plateau, without considering a potential mechanism for initial lithospheric thickening in the central plateau and the onset of crustal flow. Several recent tomographic researches demonstrated that steps and relief of the Moho interface existed underneath the plateau, contrary to a continuous layering of lower crust in “channel flow” model ([Kind et al., 2002](#)<sup>[73]</sup>; [Vergne et al., 2002](#)<sup>[74]</sup>; [Wittlinger et al., 2004](#)<sup>[75]</sup>).

#### 1.4.4 “Proto-Tibetan Plateau” model

Hypothesis has emerged that part, if not most, of the crustal shortening, thickening and surface uplift of the plateau and its surroundings may have resulted from the collision between Qiangtang and Lhasa terranes and the continuous northward subduction of the Neo-Tethyan oceanic lithosphere below the Lhasa terrane since the Early Cretaceous, finally creating a “proto-plateau” similar to the Andes Altiplano probably at the Late Cretaceous (e.g., [Murphy et al., 1997](#)<sup>[76]</sup>; [Kapp et al., 2007](#)<sup>[77]</sup>; [Wang et al., 2008](#)<sup>[78]</sup>, [2014](#)<sup>[28]</sup>; [Searle et al., 2011](#)<sup>[79]</sup>). The idea of an outward growth of a ‘proto-Tibetan Plateau’ was firstly brought up by [Mulch and Chamberlain \(2006\)](#)<sup>[80]</sup>, arguing that the Tibet has probably evolved in piecemeal manner (e.g., [England and Searle, 1986](#)<sup>[7]</sup>; [Dewey et al., 1988](#)<sup>[2]</sup>; [Fielding, 1996](#)<sup>[81]</sup>; [Tapponnier et al., 2001](#)<sup>[8]</sup>; [Wang et al., 2008](#)<sup>[78]</sup>) and challenging the conventional concept of “the uplift of the Tibetan Plateau”, which implies that this tremendous and flat landscape unity rose as a coherent entity.

Based on a comprehensive synthesis of sedimentology/stratigraphy, structural geology, magmatism, exhumation and paleoaltimetry data, [Wang et al. \(2014\)](#)<sup>[28]</sup> proposed that surface uplift spread outwardly from an elevated Paleogene ‘proto-Tibetan Plateau’ toward its surrounding margins. In this model, the central core of plateau, including most part of Qiangtang and Lhasa terranes, was already highly elevated to >~4.5 km by middle Eocene (~40 Ma) ([Figure 1.11](#)), as demonstrated by stable isotope paleoaltimetry (e.g., [Burg and Chen 1984](#)<sup>[82]</sup>; [Rowley and Currie, 2006](#)<sup>[83]</sup>; [DeCelles et al., 2007](#)<sup>[84]</sup>;

Polissar et al., 2009<sup>[85]</sup>; Deng and Ding, 2015<sup>[86]</sup>) and low temperature thermochronology (e.g., Kapp et al., 2005<sup>[87]</sup>, 2007<sup>[77]</sup>; Rohrmann et al., 2012<sup>[88]</sup>). The southern edge of Tibet was proposed to be featured by a high Andean-type Gangdese range even before the India–Asia collision (e.g., Allégre et al., 1984<sup>[89]</sup>; Murphy et al., 1997<sup>[76]</sup>; Ding et al., 2014<sup>[90]</sup>). The subsequent expansion of surface uplift took place on the Hoh–Xil–Songpan–Ganzi terrane to the north earlier than early Neogene (e.g., Horton et al., 2002<sup>[91]</sup>, Dai et al., 2012<sup>[92]</sup>), the development of the Himalaya occurred no earlier than 15 Ma to the south (e.g., Molnar and Stock, 2009<sup>[93]</sup>; Gébelin et al., 2013<sup>[94]</sup>), as well as the eastward growth of plateau. To complete this model, some recent paleobotanic studies demonstrated that there might have been a lowland (<~2 km) (Figure 1.11A) during the middle–late Paleogene (45–35 Ma) based on plant megafossils of temperate wet climate from the Lunpola Basin (e.g., Wu et al., 2017<sup>[95]</sup>; Liu et al., 2019<sup>[96]</sup>; Su et al., 2019<sup>[97]</sup>; Tang et al., 2019<sup>[98]</sup>), before being uplifted at 38–29 Ma by detachment of lithospheric mantle of underneath the Lhasa Terrane (e.g., Xiong et al., 2022<sup>[99]</sup>).

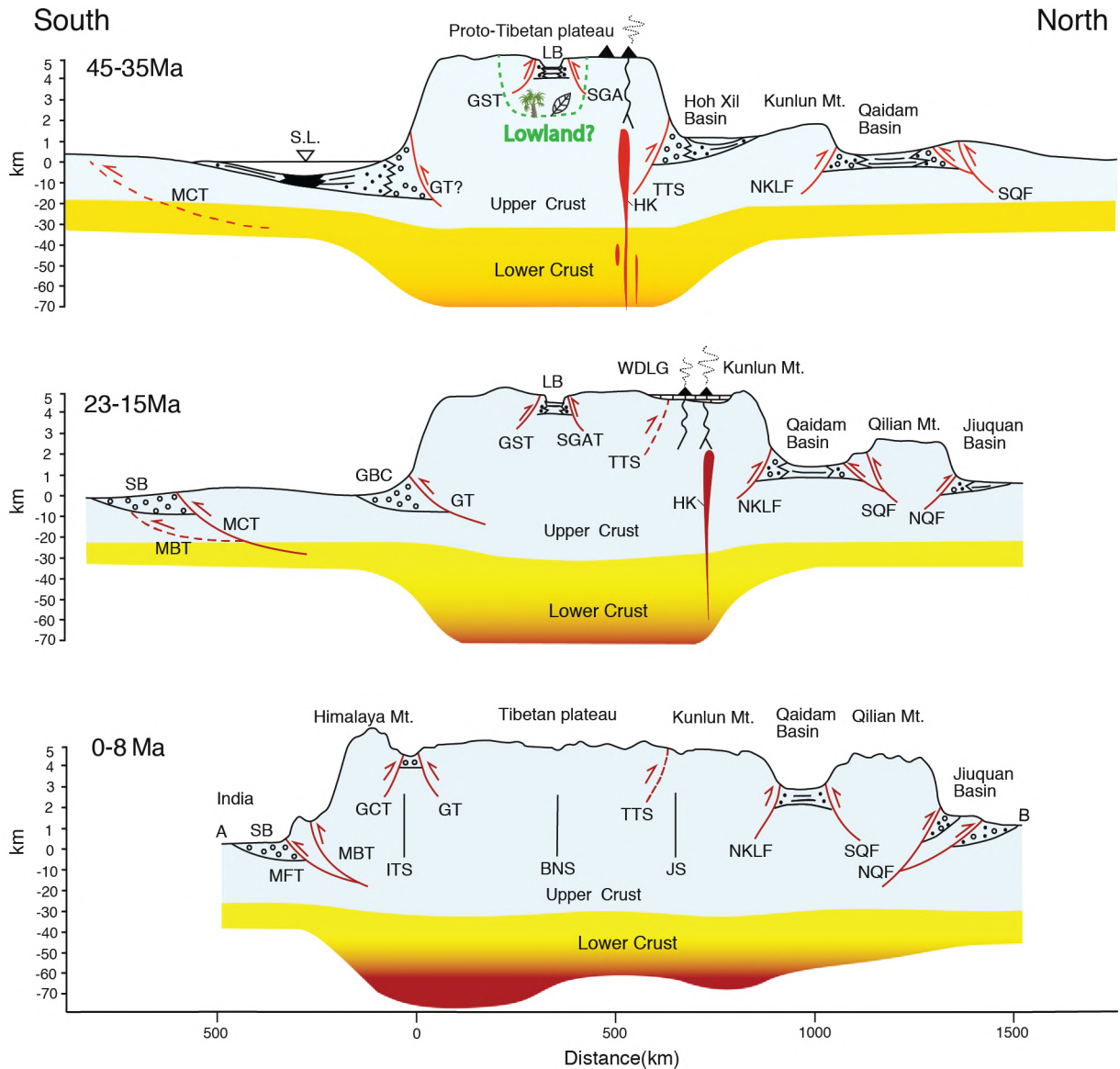


**Figure 1.11** – Outward plateau growth or proto-plateau model, based on Wang et al. (2014)<sup>[28]</sup> and Su et al. (2019)<sup>[97]</sup>. An elevated proto-plateau existed already during the Paleogene, with a potential lowland in the middle. Abbreviations: BNS: Bangong–Nujiang Suture; GCT: Great Counter Thrust; GBC: Gangrinboche conglomerate; GST: Gaize–Siling Tso Thrust; GT: Gangdese Thrust; HK: high–K calc–alkaline volcanic; JS: Jinsha Suture; LB: Lunpola Basin; MBT: Main Boundary Thrust; MCT: Main Central Thrust; MFT: Main Frontal Thrust; North Kunlun Fault; NQF: North Qilian Fault; NKLF: North Kunlun Fault; SB: foreland Siwalik Basin; SGAT: Shiquanhe–Gaize–Amdo Thrust; SL: sea level; SQF: South Qilian Fault; TTS: Tanggula Thrust System; WDLG: Wudaoliang Group; ITS: Indus–Tsangpo Suture.

## 1.5 Tibetan Plateau geomorphology: evolution and mechanisms

As aforementioned, the elevated and tremendous Tibetan Plateau results from a protracted collaboration of geodynamic/surface processes, tectonics and climate, linked to the Tethyan oceanic subduction and the India-Asia continental collision. Various topography characteristics, linked with different tectonic and climate regime, have been long recognized across the different regions of plateau. The plateau is devised into a vast endorheic zone and an exorheic zone (Fielding et al., 1994<sup>[1]</sup>, Liu-Zeng et al., 2008<sup>[100]</sup>) (Figure 1.2A, Figure 1.12), the latter is often referred to as the “Water Tower” of Asia (Viviroli et al., 2007<sup>[101]</sup>; Immerzeel et al., 2020<sup>[102]</sup>), where the large Yellow, Yangtze, Red, Mekong, Salween, Tsangpo-Brahmaputra, Indus and Ganges rivers flow out of the plateau.

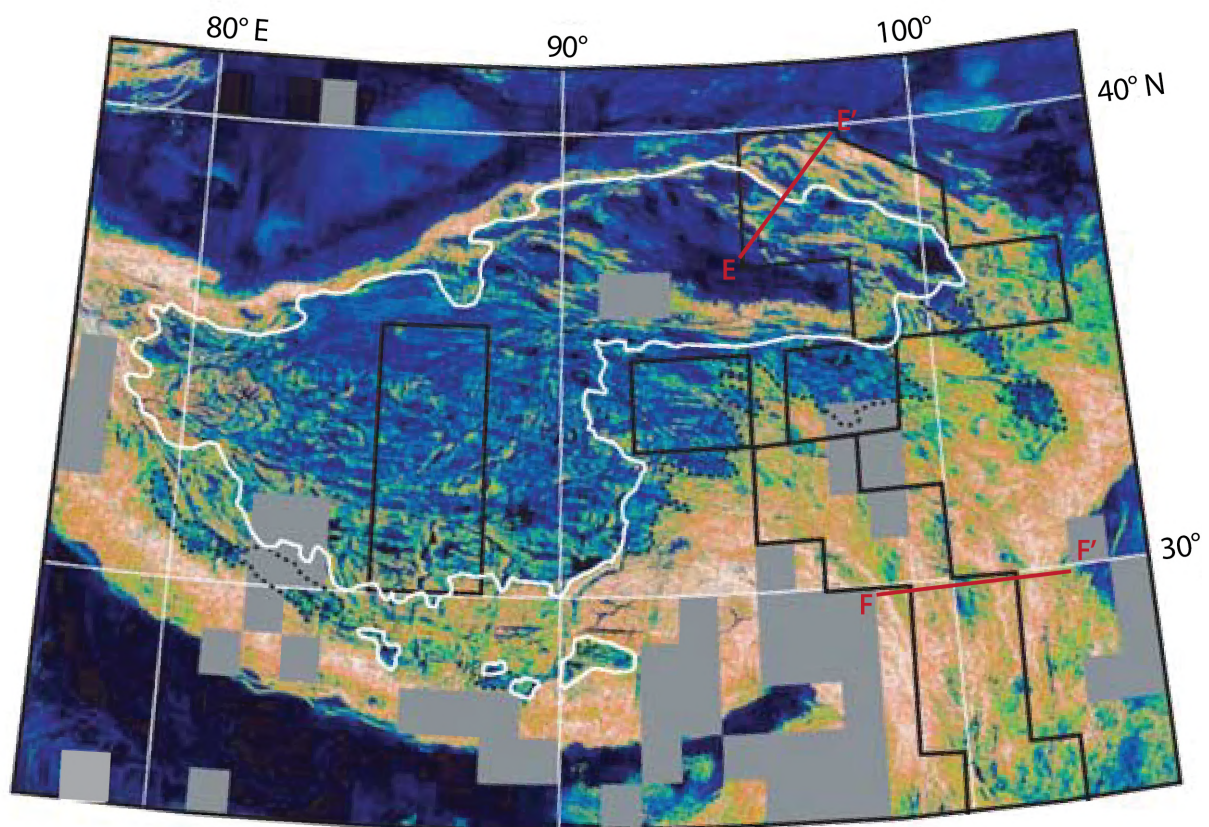
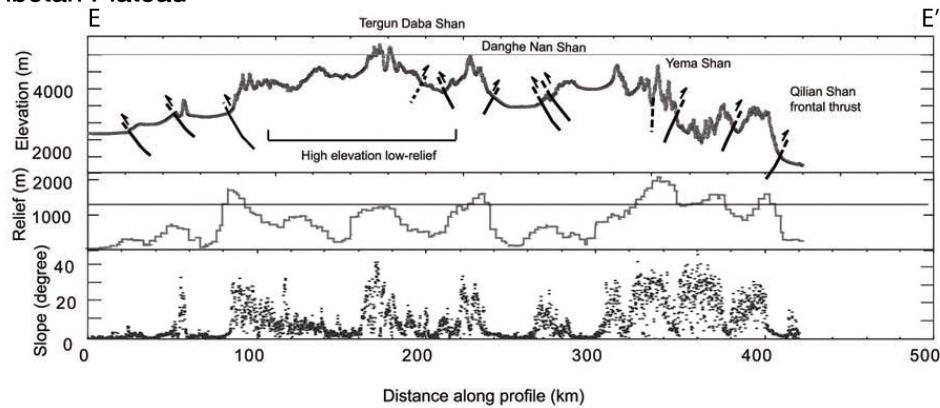


**Figure 1.12** – Map of slopes in the Tibetan Plateau (from Fielding et al., 1994<sup>[1]</sup> and Liu-Zeng et al., 2008<sup>[100]</sup>). Slopes are calculated within 250 m window and samples at a resolution of ~1 km. The white thick line delimits the extent of the endorheic zone and the dashed black line separates the high topographic slope downstream from the low slope upstream in the southeast Tibetan Plateau.

## 1.5.1 Geomorphologic characteristics of Central, Northern and Eastern Tibet

Former geomorphology analysis and quantitative descriptions of Tibetan topography clearly exhibit different patterns of the bulk landscape characteristics in different regions (e.g., [Fielding et al., 1996](#)<sup>[81]</sup>; [Liu-Zeng et al., 2008](#)<sup>[100]</sup>). The central and northern regions of the plateau, with vast low-relief surfaces, are bounded and intervened by narrow, linear, and parallel mountains slightly higher than the plateau's average elevation. They have been described as a “positive topography” ([Figure 1.13A](#)), which means local relief/slope and elevation demonstrate a positive correlation, with high relief/steep slopes at high elevation and low relief/shallow slopes at low elevation. Whereas the eastern part of the plateau is characterized by a contrary “negative topography” ([Figure 1.13B](#)), where local relief/slope and elevation demonstrate an inverse correlation, with low relief/shallow slopes at high elevation and high relief/steep slopes at low elevation. The transition of the contrasting “positive and negative topography” roughly corresponds to the boundary between the internally drained central-northern plateau and the externally drained eastern part of the plateau. It has been proposed that a combination of the continuously evolving fluvial systems, drainage efficiency, hydraulic capacity of transporting sediments out of the orogen, together with tectonic uplift, climatic variations and even lithospheric geodynamics, influenced how the geomorphology and relief were sculptured in different regions across the plateau through time ([Liu-Zeng et al., 2008](#)<sup>[100]</sup>).

### A. North Tibetan Plateau



### B. Southeast Tibetan Plateau

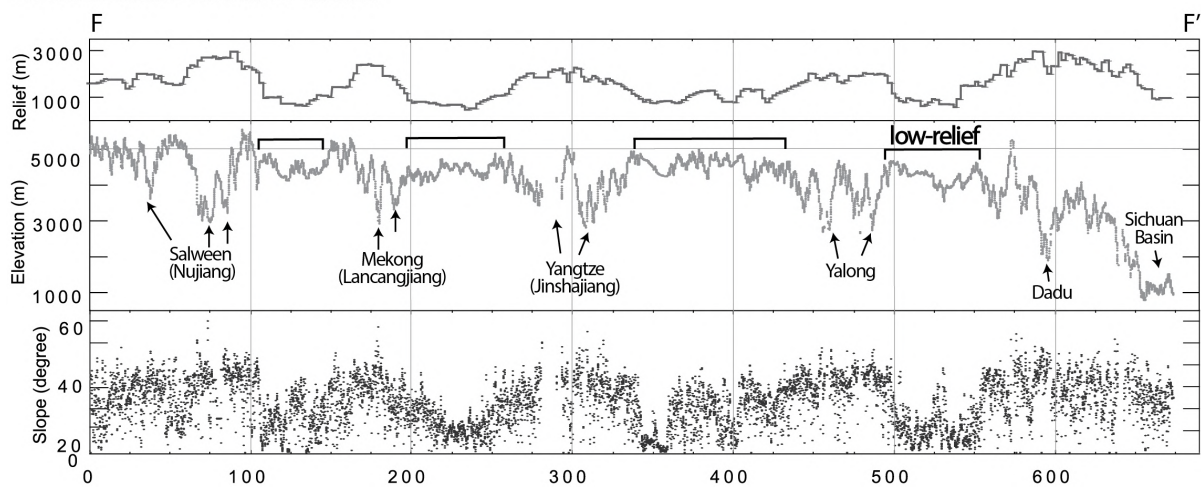


**Figure 1.13** – Local relief, elevation and local slope along two profiles, locations given in [Figure 1.2A](#), [Figure 1.12](#), modified from [Liu-Zeng et al. \(2008\)](#) <sup>[100]</sup>. (A) Profile E–E’ illustrates the “positive topography” across Qilianshan region of the Northern Tibetan Plateau, with low relief/shallow slopes at low elevation and high relief/steep slopes at high elevation. Highest relief is generally associated with active faults. (B) W–E directed profile F–F’ across the southeastern plateau, showing the topographic characteristics of “negative topography”, with low relief/ shallow slopes at high elevation and high relief and steep slopes at low elevation.

#### 1.5.1.1 Northern Tibetan Plateau: growing ranges and basins

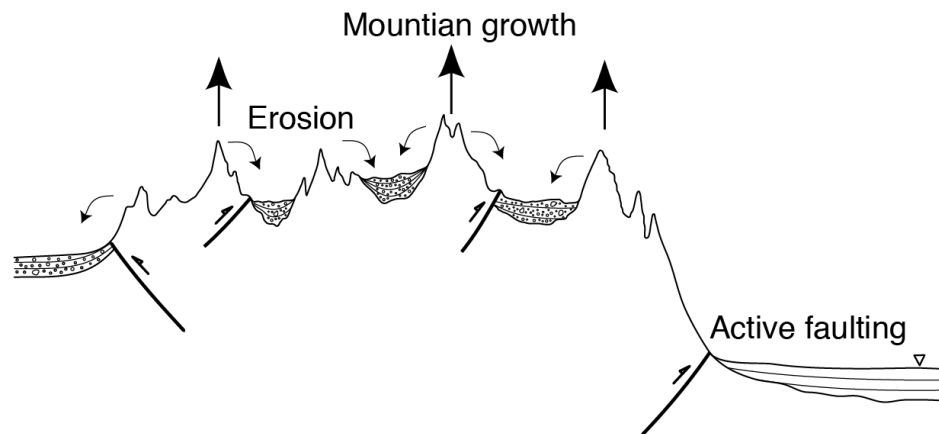
The northern part of the Tibetan Plateau is confined by the Qilian Thrust Belt and the sinistral Haiyuan fault in the north, the sinistral Altyn–Tagh fault to the west and the sinistral Kunlun fault to the south ([Figure 1.2A](#), [Figure 1.12](#)), it could also be defined as “positive topography”. The landscape of northern part of this region is characterized by small, elongated and externally drained basins with tens of kilometers of width (at 3000–4000 m high), bounded by rugged linear subparallel mountain ranges ([Meyer et al., 1998](#) <sup>[39]</sup>; [van der Woerd et al., 2001](#) <sup>[103]</sup>). The strongest relief at high elevation,

with slopes  $10^\circ$  greater than the central plateau's one, could be found along the ranges along the plateau's topographic rim, which are generally delimited by still active thrust faults (Figure 1.2A, Figure 1.12), dominating the local growing relief. The incising stream power in rivers of those basins has kept pace with the growth of the mountain barriers. The southern part of this region is internally drained and occupied by extensive rhomboidal basins (e.g., the Qaidam Basin) at an average elevation of  $\sim 3000$  m, representing a transition zone of topographic features towards the plateau interior (Liu-Zeng et al., 2008<sup>[100]</sup>). Those basins have experienced defeat of their fluvial systems and final outpacing of incision by tectonic uplift, which eventually resulted in a disconnection with the foreland base-level. Similar to the plateau interior, the northern part of the Tibetan Plateau is dominated by a semi-arid to arid climate.

One mechanism for the topographic evolution of the northern plateau is the stepwise intermontane “bathtub sediment infilling” (as in the “rigid block” model), which is an integral process of active elevation gain and relief smoothing (Meyer et al., 1998<sup>[39]</sup>; Métivier et al., 1998<sup>[104]</sup>; Tapponnier et al., 2001<sup>[8]</sup>; Liu-Zeng et al., 2008<sup>[100]</sup>), similar to the landscape evolution in central Tibet in terms of “eroding-high, filling-low” (Figure 1.14). The difference is that the ongoing northward propagation of crustal deformation in the northern plateau have progressively activated the thrusts and strike-slip faults since at least Late Miocene, which led to a damming of rivers by fast tectonic uplift of the ranges and cut off catchment outlets from the foreland (e.g., Meyer et al., 1998<sup>[39]</sup>; Sobel et al., 2003<sup>[105]</sup>). And eventually isolated, internally drained rhomb-shaped basins younging to the northeast have formed behind these rising tectonic barriers and erosion of the local highland started to infill and flatten those endorheic basins, generating a certain flatness at low elevation (Figure 1.15A, B). Those topographic analysis in the central and northern Tibet strongly proposed that the low-relief surfaces of those regions were generated by diachronous beveling at high elevation, rather than being formed at low elevation and successively being uplifted to present-day elevation (e.g., Métivier et al., 1998<sup>[104]</sup>).

## A. Northern Tibet

*Positive topography due to actively growing mountains*  
*Steep slopes and large relief at highlands*  
*Small slopes and relief at intermountane basins*  
*Narrow ranges and basins*



## B. Central Tibet

*Positive but smoothed topography due to local internal deposition*  
*Steep slope and large relief at highlands, and flat at lowlands*  
*Large range and wide basins*

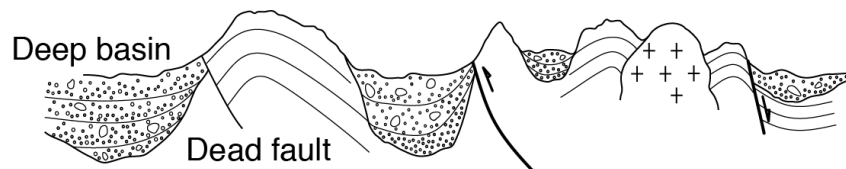
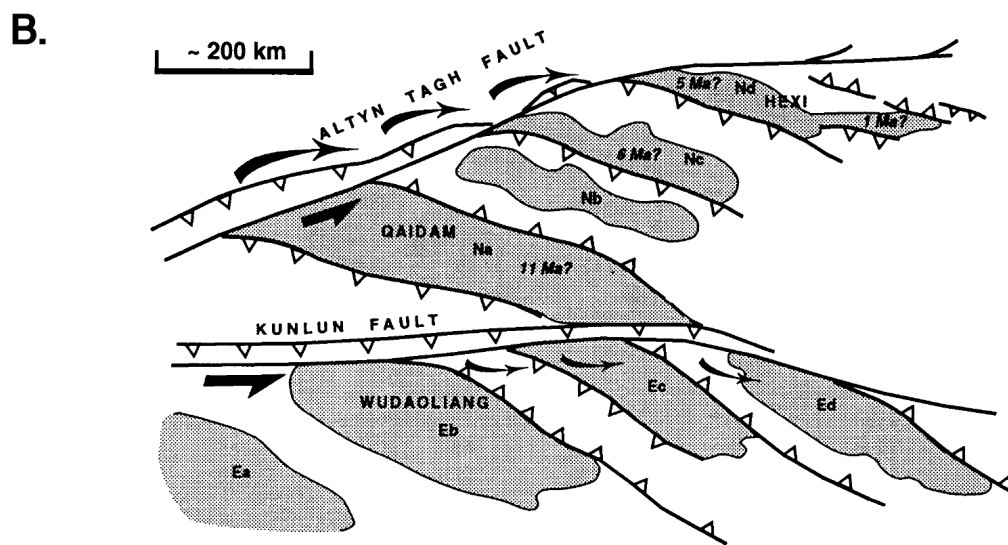
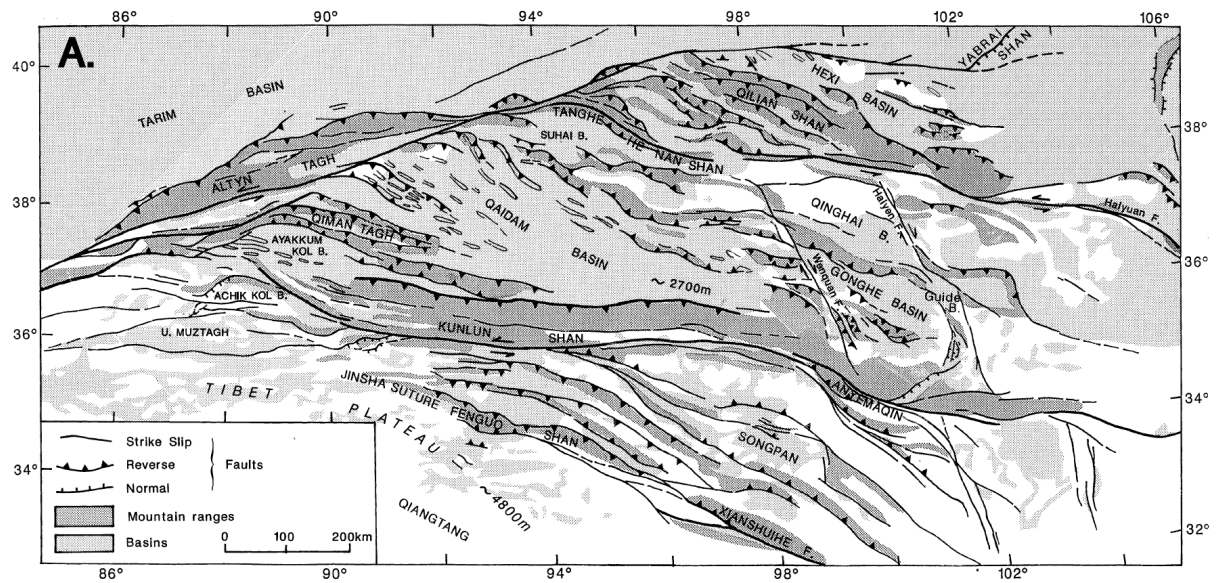


Figure 1.14 – Cartoons representing the generation of plateau relief of Central (A) and Northern Tibet (B), illustrating interaction and collaboration between sedimentation, drainage efficiency and crustal shortening, modified after Liu-Zeng et al. (2008) <sup>[100]</sup>.



**Figure 1.15** – (A) Sketch map of Cenozoic relief, faults and basins in the northern Tibet. High topography and basin flats are controlled by faulting. (B) Schematic mode of the strike-slip-controlled growth of northern Tibet, summarizing the morpho-tectonic map A. Most Cenozoic thrusts branch southeastwards from the Altyn Tagh and Kunlun faults, reflecting crust-scale slip-partitioning. The onset of basin sedimentation south of the Altyn Tagh fault youngs towards the northeast, concurrent with the northeastward propagation of active faulting and relief growing. Modified after Meyer et al. (1998)<sup>[39]</sup>.

### 1.5.1.2 Flatness of Central Tibetan Plateau and its mechanism

The most intriguing characteristic of the Central Tibetan Plateau, described as “positive topography”, is the great flatness at an elevation of ~4000–4500 m over a tremendous surface (Figure 1.12), corresponding to low-relief piedmonts and basins of tens to several hundreds of kilometers wide, intervening between linear mountain ranges. The plateau interior is divided into more than hundreds of small internal drainages, in which the lowlands, usually covered by huge saline lakes, serve as local base levels. The erosion, despite its limited capacity under an arid climate, attempts to wipe out any strong tectonic relief, flood the basins with unneglectable amount of sediments and eventually submerge to some extent the existing strong relief. This unceasing process leads to average slopes of generally  $<7^\circ$  in the basins, accounting for 63–65 % of the total surface area of the plateau interior (Figure 1.12). Generally, the mean slope increases with elevation, up to  $\sim 15^\circ$  on average approaching the mountain ranges. Only the presence of enhanced glacier erosion and grabens due to the active extension in some areas of the central/southern plateau results in some steepen slopes of  $>30^\circ$  (e.g., Armijo et al., 1986<sup>[24]</sup>; Liu-Zeng et al., 2008<sup>[100]</sup>).

In the endorheic plateau, the landscape generation is dominated by a competition between tectonic activities and concurrent or subsequent relief reduction through basin filling (Meyer et al., 1998<sup>[39]</sup>). While, the tectonic events in the central Tibet in response to the India-Asia collision have been evidenced to take place mainly in the early Cenozoic, as exemplified by the reactivated uplift of the elevated and high-relief Tangula mountain range during the early Tertiary (Roger et al., 2000<sup>[5]</sup>; Tapponnier et al., 2001<sup>[8]</sup>; Kapp et al., 2005<sup>[87]</sup>, 2007<sup>[77]</sup>; Rohrmann et al., 2012<sup>[88]</sup>). The lack of crustal shortening in the late Cenozoic has left enough time for the surface processes, despite the long-lasting low denudation rate, to smooth the existing highlands in the endorheic plateau interior and fill progressively the piedmont basins, for example, the 5-km thick sediments in the Hoh-Xil Paleogene foreland basin to the north of Tangula mountains (Wang et al., 2008<sup>[78]</sup>) (Figure 1.2A, Figure 1.12). The first comprehensive geomorphological studies of Tibet (Fielding et al., 1994<sup>[1]</sup>; Fielding, 1996<sup>[81]</sup>) pointed out that very low precipitations and cool temperatures on the plateau should result in minimal erosion and they denied the important role played by surface processes in generating the flatness of central Tibet. But, Liu-Zeng et al. (2008)<sup>[100]</sup> argued that even a slow denudation rate in such an arid environment during a protracted period of tectonic quiescence, combined with very limited drainage efficiency in internal drainages, could be effective in erasing relief at higher elevation (Figure 1.14B), similar to the “high-altitude peneplanation” (e.g., Babault et al., 2005<sup>[106]</sup>, 2007<sup>[107]</sup>; Garcia-Castellanos et al., 2007<sup>[108]</sup>). Similarly, Sobel et al. (2003)<sup>[105]</sup> demonstrated a good spatial correlation of low-relief

topography with aridity in the Puna plateau interior of the Andes, emphasizing the capacity of slow erosion in unroofing relief.

Several previous studies also referred to viscous flow in the lower crust as a mechanism to smooth out irregularities in topography based on the observation of the interior flatness of the highest part of the Tibet plateau (Bird, 1991 <sup>[109]</sup>; Fielding et al., 1994 <sup>[1]</sup>; Fielding, 1996 <sup>[81]</sup>; Shen et al., 2001 <sup>[110]</sup>; McKenzie and Jackson, 2002 <sup>[111]</sup>). Such a geodynamic process, combined with a passive sediment infilling, has been proposed to interpret the subdued relief in the Altiplano plateau (Lamb and Hoke, 1997 <sup>[112]</sup>). But the shortage of the lower crust channel flow model in terms of not being capable to explain the viscous material source and the presence of Moho relief and steps beneath the Tibetan Plateau (Kind et al., 2002 <sup>[73]</sup>; Vergne et al., 2002 <sup>[74]</sup>; Wittlinger et al., 2004 <sup>[113]</sup>) makes it still not universally appreciated.

### 1.5.1.3 Deeply incising river valleys and low-relief remnant surfaces of southeast Tibet

Located in between the rigid Sichuan Basin and the northward indenting EHS of Namche Barwa, the southeastern Tibetan Plateau is externally drained by several large rivers, including Salween (Nujiang in Chinese), Mekong (Lancangjiang), Yangtze (Jinshajiang) and Yalong rivers, flowing southeastward nearly parallelly on the southeast plateau margin of gentle topographic gradient (Figure 1.2A). The narrow spacing between the large rivers is remarkably reduced to several tens to hundreds of kilometers (Figure 1.16A), probably due to the enhanced lateral advection related to the Indian impingement during the collision (e.g., Koons, 1995 <sup>[114]</sup>; Brookfield, 1998 <sup>[115]</sup>; Hallet and Molnar, 2001 <sup>[116]</sup>; Yang et al., 2015 <sup>[117]</sup>) or the topographic descent on the southeastern plateau away from the plateau center (e.g., Clark et al., 2004 <sup>[118]</sup>; Yuan et al., 2021 <sup>[119]</sup>). A concurrent geomorphologic characteristic is that the attenuated width of the subparallel drainage basins of wasp-like shape clearly differ from the teardrop-shaped drainages of dendritic rivers developed on the undeformed continental cratons, such as the Mississippi River or Amazon River (Hallet and Molnar, 2001 <sup>[116]</sup>; Clark et al., 2004 <sup>[118]</sup>).

The landscape of the Southeastern Tibetan Plateau is typically defined by a “negative topography”, where the deeply incising gorges of large rivers with the strongest relief are neighbored by low-relief surfaces perched at high-elevation, exempted from the large-scale regressive erosion (Liu-Zeng et al., 2008 <sup>[100]</sup>). The regional relief map illustrates clearly the spatial distribution of this topographic characteristic, with the moderate to high local relief constrained in the river valleys, marked in yellow, and shallow relief in blue patches on the interfluvial spaces (Figure 1.16B). The strongest relief in the

river valleys are observed in the middlestream, roughly located between 25° and 31°N latitudes, with gradual decreases toward both upstream region with little strong fluvial incision or downstream of low-lying foreland. One thing to notice is that some local high relief could be also linked to the faults activities, such as the Gongga Shan at an elevation of 7556 m or Kawagebo at an elevation of 6740 m, uplifted in a restraining bend of sinistral Xianshuihe strike-slip fault or Parlung–Zhongdian faults, respectively. In the Three Rivers Region (Figure 1.16A, B), where the subparallel Salween, Mekong and Yangtze rivers flows southeastward in a narrowed space, the strongest relief stems from river incision due to the northward continuous indentation of the EHS, which also forced the river courses to curve along the indenting direction (Yang et al., 2015<sup>[117]</sup>). To the east, in the Great Bends Region, where the lower part of Yangtze middlestream, Yalong and Dadu river flow across the Yulong–Yalong thrust belt, consisting of the Jiulong, Muli, Jinhe–Qinghe and Yulong thrusts, the largest relief results from enhanced river down-cutting related to the diachronous tectonic activities of those structures since late Eocene (Wang et al., 2012<sup>[120]</sup>; Zhang et al., 2016<sup>[121]</sup>; Cao et al., 2020<sup>[122]</sup>; Pitard et al., 2021<sup>[123]</sup>; Zhu et al., 2021<sup>[124]</sup>). Intriguingly, the courses of the Yangtze and Yalong rivers both shift to the northeast, generating hairpin-shaped bends over >100 kilometers before flowing back to south, which was assumed as a result of the river captures (Clark et al., 2004<sup>[118]</sup>) or due to the thrusting or strike-slip motion along the thrust, if any (Burchfiel and Chen, 2012<sup>[125]</sup>).

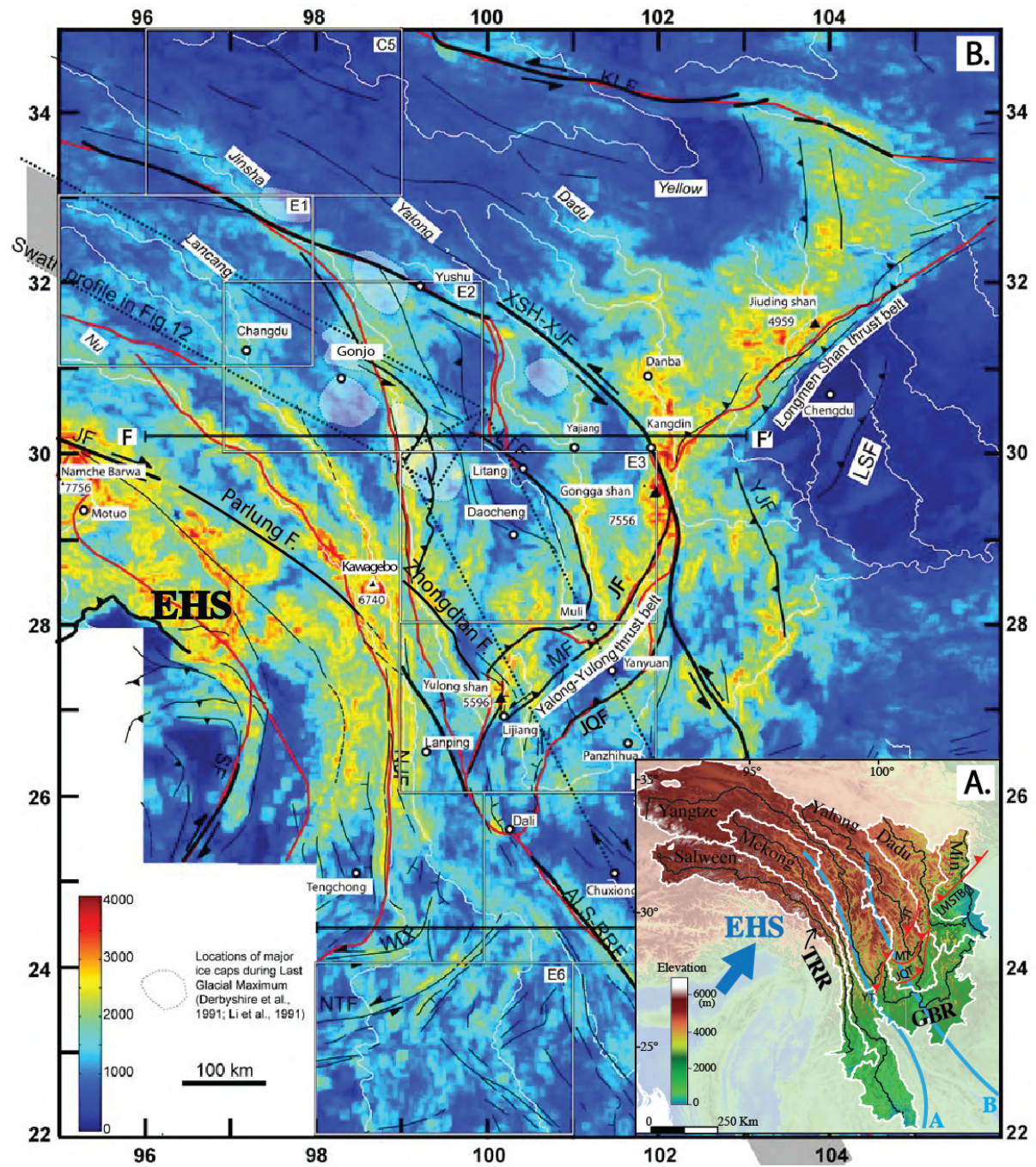


**Figure 1.16** – (A) Topography map of the southeast Tibetan Plateau, white lines delimit the drainage boundaries of large rivers in black. Simplified thrusts are marked in red in the Great Bends Region (GBR). Thick cyan lines are topography swath profiles in [Figure 1.17](#). EHS: Eastern Himalayan Syntaxis; JQT: Jinhe–Qinghe Thrust; JT: Jiulong Thrust; LMSTB: Longmenshan Thrust Belt; MT: Muli Thrust; TRR: Three Rivers Region. YT: Yulong Thrust; (B) Relief map of southeast Tibetan Plateau. Thick white lines are major river courses. Dark lines indicate major active faults. The strongest relief mainly located in the deeply incising rivers and also along major active faults. XSH-XJF: Xianshuihe–Xiaojiang Faults; ALS-RRF: Ailaoshan–Red River Fault. Modified after [Liu-Zeng et al. \(2008\)](#)<sup>[100]</sup>.

The gentle topographic gradient across southeast Tibet has been previously considered as being continuous, gradual and decreasing southeastward from ~4.5 km to 1–2 km over a distance of >1500 km (Clark et al., 2005a<sup>[67]</sup>). However, as illustrated on the topographical swath profile (profile A in Figure 1.17), this might be true only in the Three Rivers Region, where the pervasive thrusts strike parallelly along the large rivers (Burchfiel and Chen, 2012<sup>[125]</sup>). While the topographic swath profile in the Great Bends Region (profile B in Figure 1.17) undoubtedly demonstrates an evident elevation dropdown from 4–5 km to ~2 km, across a northeast-trending zone of approximately 200–250 km wide, which roughly corresponds to the Yalong Thrust Belt (Figure 1.16A). A clear topographic step and “slope break”, across several subparallel Cenozoic thrusts (e.g., Jiulong, Muli, Jinhe–Qinghe and Yulong thrusts), unambiguously delimit the southeastern margin of the high Tibetan Plateau and appear to mark an eroded plateau rim in the Great Bends Region (Liu–Zeng et al., 2008<sup>[100]</sup>). Such a topographic characteristic in this region seemed to have been overlooked in previous studies (e.g., Clark et al., 2005a<sup>[67]</sup>; Clark et al., 2006<sup>[126]</sup>). The average elevation of the region southeast of this thrust belt is majorly between 1 and 3 km, meanwhile no distinctive inverse correlation between elevation and local relief/slope, as defined in “negative topography”, is observed in this foreland–alike region (Liu–Zeng et al., 2008<sup>[100]</sup>).

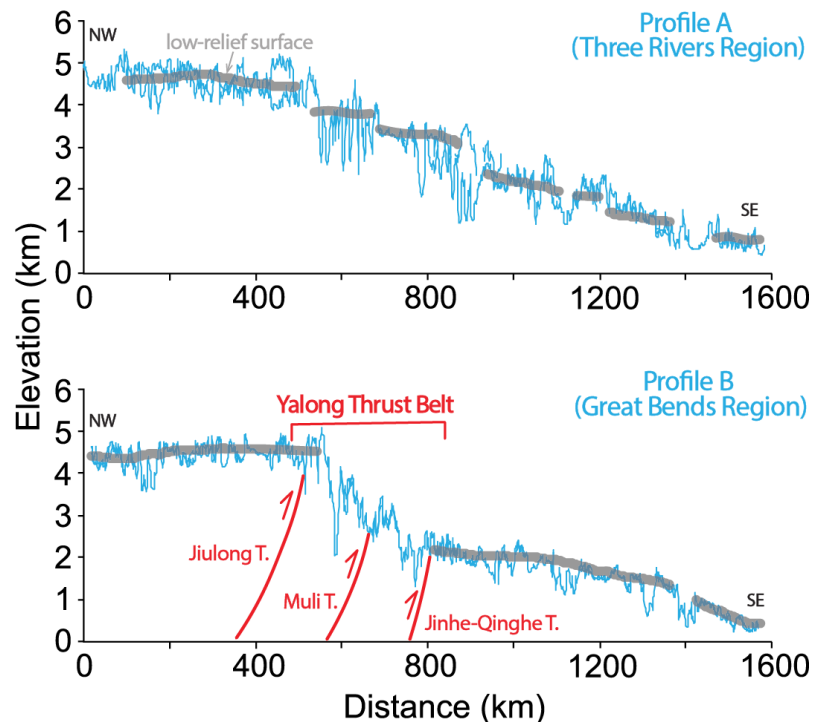
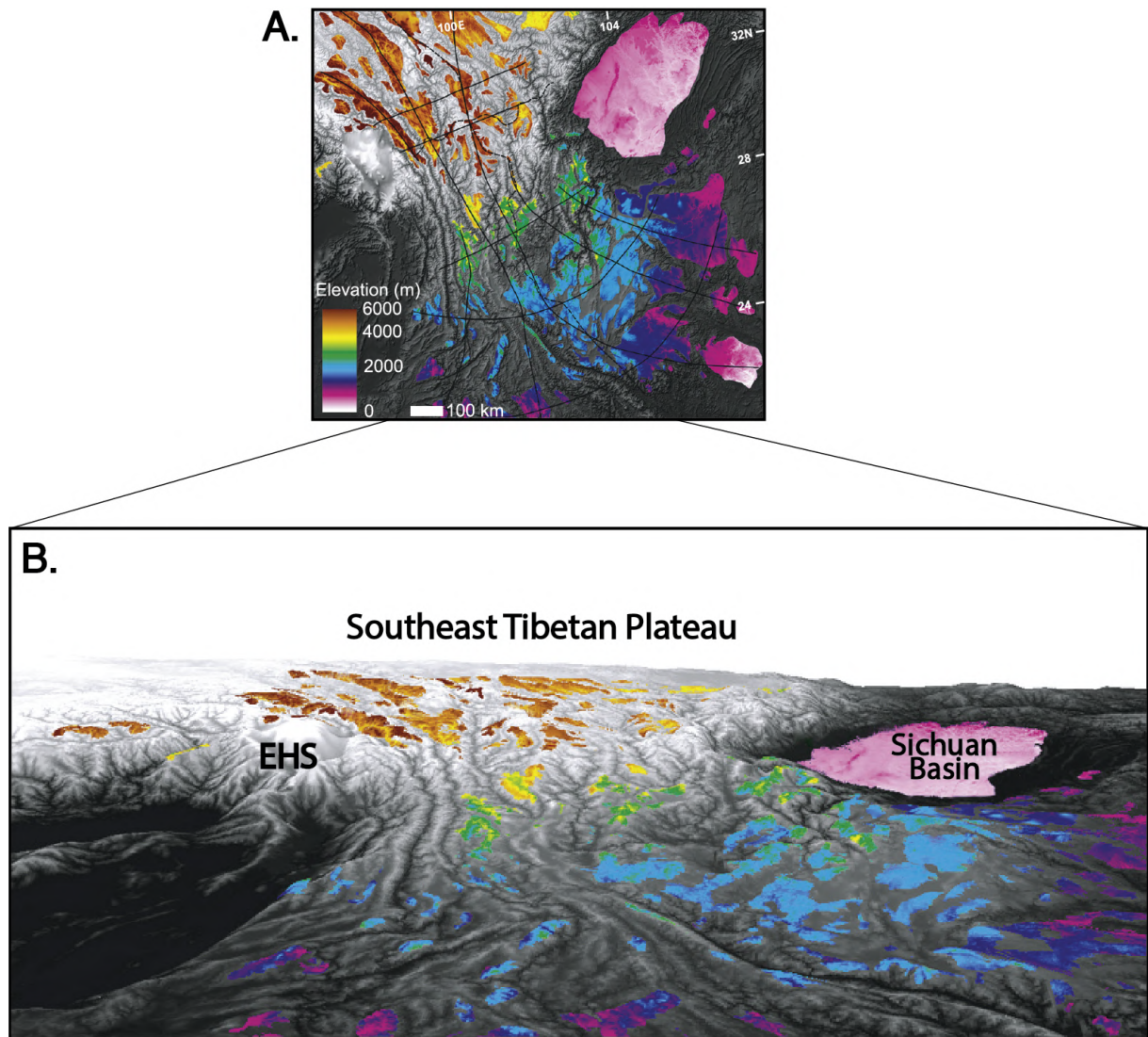


Figure 1.17 – Topography swath profiles parallel to regional topographic gradient across the Three Rivers Region (profile A), and the Great Bends Region (profile B), crossing the Yalong Thrust Belt. Locations are shown in Figure 1.16A. Real topography along the profiles is in cyan solid lines. Thick shaded lines give elevation of interpolated fit (spline) to remnant surfaces, with local relief <1 km, modified after Clark et al. (2006)<sup>[126]</sup>.

In the high southeast Tibetan Plateau with typical “negative topography”, the deeply dissected landscape of low-lying river valleys with highest relief (~1000–4200 m relief) and slopes (~>20°) has been defined as “active landscape”, where the topography evolves actively to respond to the enhanced fluvial incision rates and mass wasting in the major bedrock rivers and principal tributaries. While, the elevated upstream portions of tributary and headwaters of major rivers with low-relief (<600 m relief) and shallow slope (>10°) has been described as “relict landscape”, where the strong river incision in the “active landscape” due to new erosional conditions has not yet propagated into tributary upstream and affected the upland low-relief surfaces (Clark et al., 2006<sup>[126]</sup>). Those low-relief surfaces, without yet complete adjustment to the new erosional conditions, occupy generally the headwaters of numerous tributary rivers that transform from alluvial to bedrock rivers toward downstream. By applying certain criteria of local elevation/relief/slope, active structures and surface processes, those authors have recognized and correlated such non-incised areas adjacent to the deep river gorges to eventually identify a discontinuous, regional “remnant surface”. This collective surface defines the maximum elevation across the plateau margin and spreads from the Tibet interior to coastal plains adjacent to the South China Sea over a distance of thousands kilometers (Clark and Royden, 2000<sup>[18]</sup>; Clark et al., 2006<sup>[126]</sup>) (Figure 1.18). Such a regional “remnant surface” has been presumed to be a once regionally continuous, low-relief landscape at low elevation, which was initially of erosional or depositional origin with different ages and experienced a protracted erosion. Those low-relief surfaces at present-day have areas of typically several tens to hundred square kilometers, with reduced relief generally less than 1 kilometer averaged over a pixel window of 5-kilometers-width (Clark et al., 2006<sup>[126]</sup>; Fox et al., 2021<sup>[127]</sup>), as observed on the regional topographic swath profiles (Figure 1.13B, Figure 1.17). By minimizing the late Cenozoic upper crustal deformation in the southeast Tibet, those authors further used the modern altitude of a reconstructed “remnant surface” on a regional scale to calculate the minimum vertical displacement of the plateau surface due to crustal thickening and successive erosion during the Tibetan Plateau grew laterally.



**Figure 1.18** – (A) Gray scale topographic map of southeast Tibetan Plateau, draped by remnant surfaces with different colors at different elevations. (B) 3D close-up of topography with surface remnants (color). Modified from Clark et al. (2006) <sup>[126]</sup>.

Some of the best examples of such low-relief “remnant surfaces” are the exhaustively studied Jaggai massif and Daocheng granite massif with different origins and ages, located on the west and east side of the Yalong River, respectively (Figure 1.19, Figure 1.20). Inside the Jaggai massif, there is a clear transition of the river physiology from wide, braided alluvial stream with local relief of approximately 500 m to a narrow, boulder-armed bedrock river valley, separated by an abrupt knickpoint (sudden changes in the river’s channel slope) (Clark et al., 2006 <sup>[126]</sup>). The lithology outcrops of the Jaggai massif are mainly thick sequences of middle and upper Triassic flysch deposited in the gradually

closing Proto–Tethyan ocean. As part of the Songpan–Ganzi tecto–lithological unity, the deposits on the Jaggai massif have subsequently been extensively faulted, folded, metamorphosed to low or intermediate degree. Important post–orogenic plutonism have taken place in the region during the late Triassic to Jurassic age, intruding into the flysches in small to intermediate bodies on the massif (Burchfiel et al., 1995 <sup>[128]</sup>; Huang et al., 2003 <sup>[129]</sup>; Harrowfield and Wilson, 2005 <sup>[130]</sup>; de Sigoyer, 2014 <sup>[131]</sup>). One of the flattest landscape of the Tibetan Plateau has also developed in the realm of the bedrock of the Late Triassic Daocheng granite, generated by melting of thickened continental crust due to the collision between the Yidun Arc and the Songpan–Ganze terrane (Liu et al., 2006 <sup>[132]</sup>; Reid et al., 2007 <sup>[133]</sup>). The Daocheng massif is connected and evacuated by a secondary tributary to the Yangtze River, but the flat surface is far away from being affected by the enhanced incision in the lowermost downstream, contributing to the formation of a great flatness on the tremendous granite body. Geologic maps show that there are very limited and local early Tertiary, Neogene and Quaternary sedimentary deposits on those two massifs (Bureau of Geological and Mineral Resources of Sichuan Province (BGMRS), 1991 <sup>[134]</sup>), implying that those two flat surfaces are of erosional origin. Isotopic ages and low–temperature thermochronology across the Songpan–Ganzi terrane both indicate that those two massifs also experienced a regional slow cooling (1–3 °C/Myr) and slow exhumation (0.01–0.02 mm/yr) from late Jurassic time until at least Late Miocene time, generally showing apatite (U–Th)/He (AHe) ages >50 Ma and apatite fission track (AFT) ages >100 Ma (Xu and Kamp, 2000 <sup>[135]</sup>; Kirby et al., 2002 <sup>[136]</sup>; Huang et al., 2003 <sup>[129]</sup>; Reid et al., 2005b <sup>[137]</sup>; Clark et al., 2005b <sup>[138]</sup>; Tian et al., 2014 <sup>[139]</sup>) (Figure 1.20).

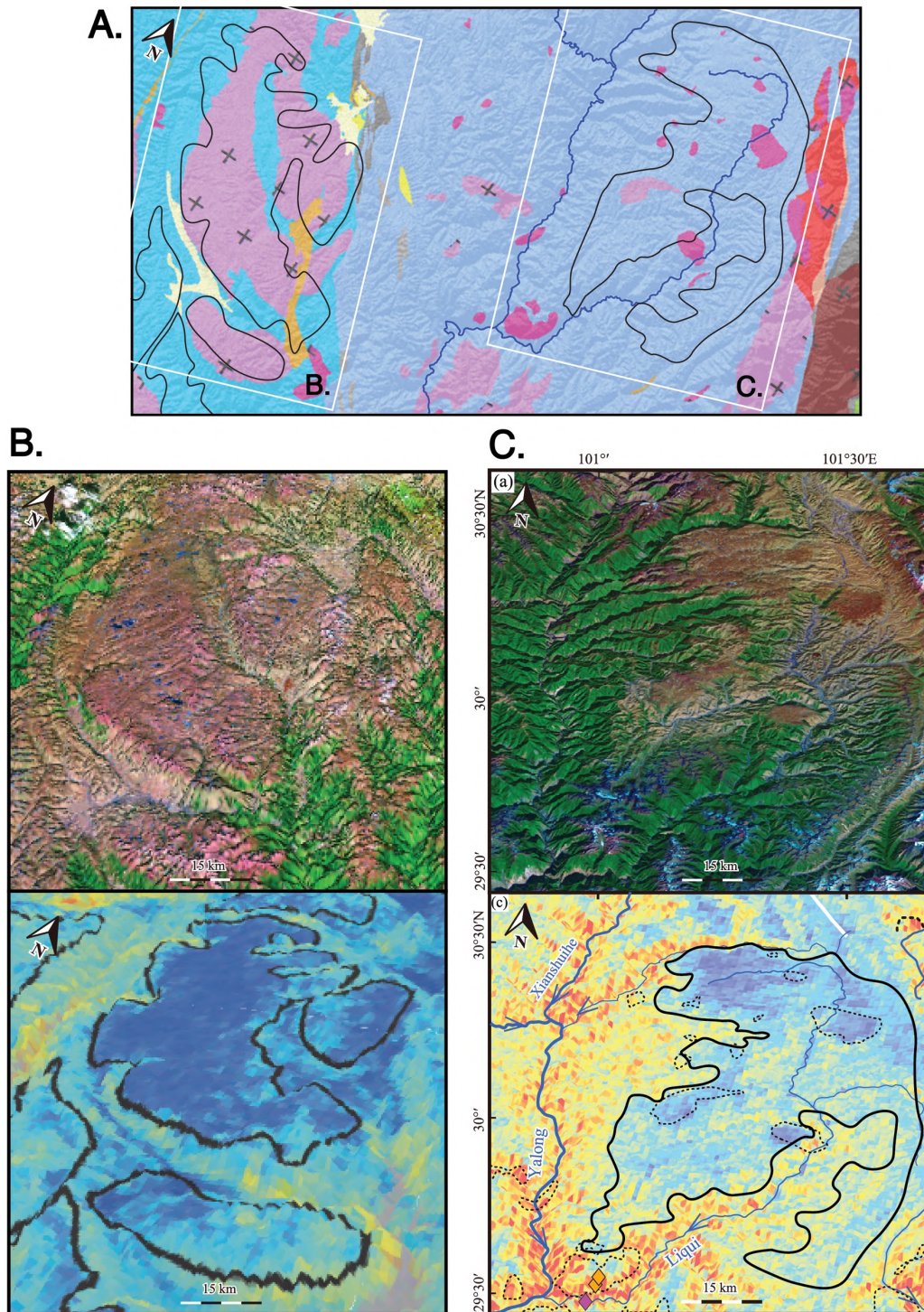


**Figure 1.19** – Geology (A), topography in Landsat images (B) and relief (C) maps of the Daocheng and Jaggai massifs across the Yalong River. The warm colors represent high relief, the cold colors low relief, with black lines delimiting the “relict surfaces” of Clark et al. 2006 <sup>[126]</sup>. Modified from Zhang et al. (2017) <sup>[140]</sup>.

Just as the low-relief Daocheng and Jaggai massifs, even though the elevated southeast Tibetan Plateau is externally drained by several large rivers, yet it has experienced quite limited erosion in total during Cenozoic, most of which took place in deep gorges formed by the major rivers and their principal tributaries (Wang et al., 1998<sup>[141]</sup>). Low temperature thermochronological ages of samples collected from the large river valleys generally show AHe ages <15 Ma and AFT ages <50 Ma (Figure 1.20). A relatively synchronous incision of large rivers strengthening since middle Miocene across the eastern plateau margin has been recorded through exhumation deduced from various thermochronometry on bedrock channels (e.g., Clark et al., 2005b<sup>[138]</sup>; Godard et al., 2010<sup>[142]</sup>; Ouimet et al., 2010<sup>[143]</sup>). To the east, major rivers of the Longman Shan show an enhanced incision occurring simultaneously with surface uplift since middle-late Miocene (12–8 Ma), such as Min River (Godard et al., 2010<sup>[142]</sup>; Wilson and Fowler, 2011<sup>[144]</sup>) and Dadu River (Clark et al., 2005b<sup>[138]</sup>; Ouimet et al., 2010<sup>[143]</sup>; Tian et al., 2015<sup>[145]</sup>; Yang et al., 2020<sup>[146]</sup>). A stronger incision either during 13–9 Ma (Clark et al., 2005, Zhang et al., 2016) or since >14 Ma (Ouimet et al., 2010<sup>[143]</sup>) or even older (28–12 Ma, Wilson et Fowler, 2011<sup>[144]</sup>) has been experienced in the middle Yalong River, of which a tributary to the west experienced an earlier rapid erosion phase (~24–18 Ma, Tian et al., 2014<sup>[139]</sup>). To the west in the Three Rivers Region, the onset of accelerated incision of Yangtze River varied from 15–10 Ma (Ouimet et al., 2010<sup>[143]</sup>), 12–6 Ma (Wilson et Fowler, 2011<sup>[144]</sup>) in the upstream to 18–9 Ma (McPhillips et al., 2016<sup>[147]</sup>) or during the Miocene–early Oligocene (Lacassin et al., 1996<sup>[148]</sup>; Shen et al., 2016<sup>[149]</sup>) in the lower part near the big bend of the Yangtze River. Along Mekong and Salween rivers near the EHS, Yang et al. (2016)<sup>[150]</sup> modelled an increasing erosion rate since at least 10 Ma, confirmed by later studies for Mekong River (Replumaz et al., 2020<sup>[151]</sup>; Ou et al., 2021<sup>[152]</sup>), though a rapid erosion since ~17 Ma in both upstream and/or downstream of them has been proposed (Dai et al., 2013<sup>[153]</sup>; Nie et al., 2018<sup>[154]</sup>). The modelling results of erosion rate from detrital thermochronometry, averaged over upstream catchments of major rivers in southeast Tibet (e.g. Salween, Mekong, Yangtze, Yalong rivers), showed a significant increase between 11 and 4 Ma after a protracted slow erosion phase (Duvall et al., 2012<sup>[155]</sup>). This apparent synchronicity in accelerated erosion in both upstream and downstream of large rivers in the southeast Tibet, rather than a spatial or temporal northward progression, led those authors to appeal an uniform surface uplift due to a Mid–Miocene lower crust channel flow. While, a succedent revise casted doubts on such a simultaneous regional Mid–Miocene erosion acceleration across the southeast Tibet, based on their thermochronometry study of bed rock samples from the same catchment (Dai et al., 2013<sup>[153]</sup>).

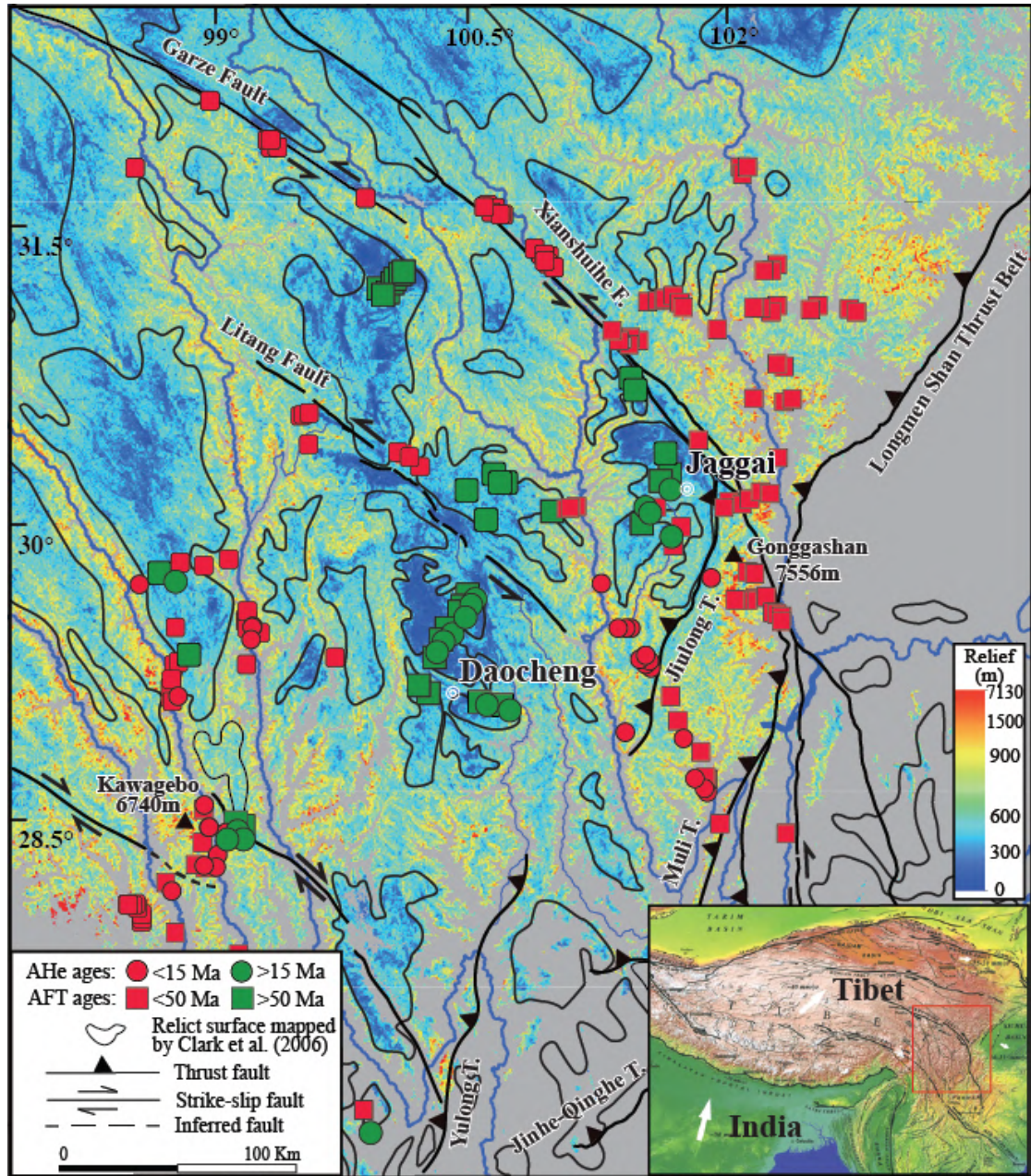
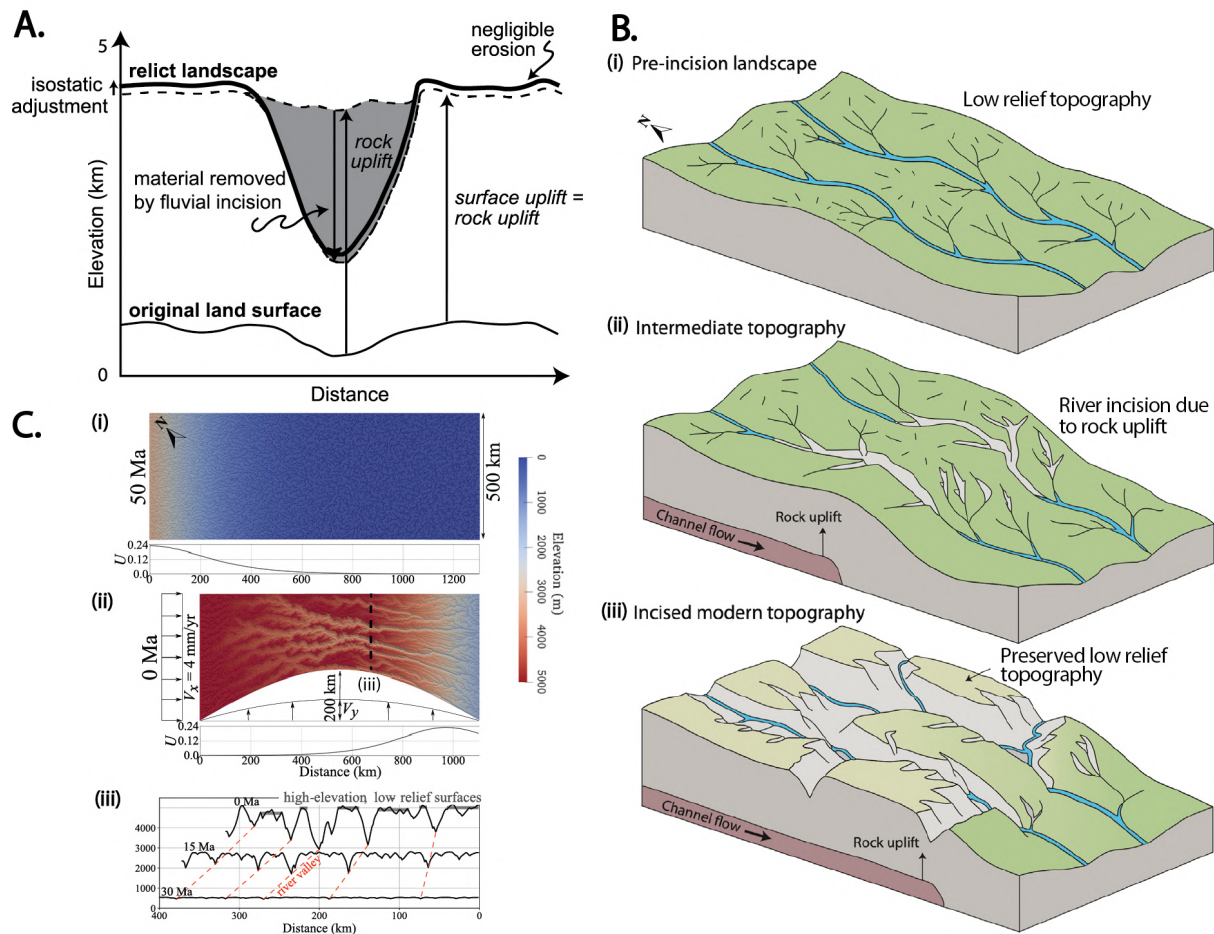


Figure 1.20 - Zoom-in relief map with higher resolution (after Zhang et al., 2015<sup>[156]</sup>) of southeast Tibetan Plateau, centered on the plateau fringe. The relief is calculated over a domain with radius of 1 km for elevations >3500 m. Relict surfaces, identified by Clark et al. (2006)<sup>[126]</sup>, is represented in black outlines. The inset topography map is from Tapponnier et al. 2001<sup>[8]</sup>. Thermochronometric data are from: [1] Yang et al. (2016)<sup>[150]</sup>, [2] Liu-Zeng et al. (2018)<sup>[157]</sup>, [3] Replumaz et al. (2020)<sup>[151]</sup>, [4] Ouimet et al. (2010)<sup>[143]</sup>, [5] Clark et al. (2005b)<sup>[138]</sup>, [6] Zhang et al. (2016)<sup>[121]</sup>, [7] Tian et al. (2014)<sup>[139]</sup>, [8] Nie et al. (2018)<sup>[154]</sup>, [9] Godard et al. (2009)<sup>[158]</sup>, [10] Wang et al. (2012)<sup>[120]</sup>, [11] Xiao et al. (2015)<sup>[159]</sup>, [12] Zeitler et al. (2014)<sup>[160]</sup>, [13] Gourbet et al. (2019)<sup>[161]</sup>, [14] Cao et al. (2020)<sup>[122]</sup>, [15] Shen et al. (2016)<sup>[149]</sup>, [16] Wang et al. (2018)<sup>[162]</sup>, [17] Zhang et al. (2015)<sup>[156]</sup>, [18] Reid et al. (2005)<sup>[163]</sup>, [19] Wilson and Fowler (2011)<sup>[144]</sup>, [20] Lai et al. (2007)<sup>[164]</sup>, [21] Lei et al. (2006)<sup>[165]</sup>, [22] Zhang et al. (2017)<sup>[140]</sup>, [23] Dai et al. (2013)<sup>[153]</sup>, and [24] Xu and Kamp (2000)<sup>[135]</sup>.

#### 1.5.1.4 Topographic evolution models of southeast Tibet:

##### (i) “Channel flow” model

The aforementioned channel flow of viscous lower crust has been specifically exploited to explain the lateral plateau growth and topographic evolution in the southeastern Tibetan Plateau (Royden et al., 1997<sup>[59]</sup>; Clark and Royden, 2000<sup>[18]</sup>; Clark et al., 2005a<sup>[67]</sup>). In such model, recent and ongoing lower crustal channel flow would cause the southeastern plateau to be rapidly uplifted from an extensive low-relief “relict surface” at low elevation near the sea level throughout the late Cenozoic to present-day (Clark and Royden, 2000<sup>[18]</sup>; Clark et al., 2005a<sup>[67]</sup>, 2006<sup>[126]</sup>). Recognition of this paleolandscape and the low-relief remnant surfaces at present-day potentially enables a measure of surface uplift and/or rock uplift in response to crustal thickening and allows to map the responsible geodynamic processes (Figure 1.21A). In response to the rock uplift, rivers steepen and incise deeply into the rocks, gradually propagating the strong erosion into slowly eroding upstream areas without strongly destroying the elevated low-relief “relict surface”. Those “relict surfaces” are preserved thanks to the incomplete adjustment of tributaries on those surfaces to new erosion conditions, contrary to the deeply incised canyons in river stems (Figure 1.21B). Limited isostatic adjustment occurred due to the material evacuation of the river gorges and only a minimal erosion of the “relict surface” linked to surface processes is considered in this model to finally shape the modern landscape (Clark et al., 2006<sup>[126]</sup>). This model apparently contradicts earlier concepts that low-gradient, regional topography stemmed from regional elevation reduction by intense fluvial dissection of large southeastward flowing rivers (Fielding, 1996<sup>[81]</sup>; Tapponnier et al., 2001<sup>[8]</sup>; Liu-Zeng et al., 2008<sup>[100]</sup>). A recent study of landscape evolution of the southeast Tibet has been conducted in the Three Rivers Region, with an uplift scenario of a simple propagating Gaussian wave of strong surface uplift from the central plateau toward southeast, similar to the “Channel flow” model, to well reproduce the deep river valleys and high flat surfaces (Yuan et al., 2021<sup>[119]</sup>). This study also implied a spatially varying lateral shortening to simulate the intending India craton, of which the contribution to the drainage development and topographic evolution is not important (Figure 1.21C). While, a new inversion scheme of geomorphological characteristics to investigate the initial channel steepness within paleolandscape revealed that large variations in channel steepness were required along the trunk channels on a regional scale. This is clearly not consistent with a low-relief paleo-surface before being uplifted and undermines the credibility of a simple interpolation of modern “relict surfaces” to explain the landscape evolution in southeastern Tibetan Plateau (Fox et al., 2020<sup>[127]</sup>).



**Figure 1.21** – (A) Schematic cross section of topography evolution of the southeast Tibetan Plateau of the “Channel flow” model, after [Clark et al. \(2006\)](#) <sup>[126]</sup>. (B) Carton illustration of the “Channel flow” model, after [Fox et al. \(2020\)](#) <sup>[127]</sup>. (i) A low-relief landscape with low erosion rates, before the onset of rock uplift across SE Tibet. (ii) Lower-crustal channel flow uplifted the surface and rivers incised into the low-relief landscape. (iii) Low-relief remnant surfaces are preserved with little erosion. (C) Landscape evolution model (FastScape) of the southeast Tibetan Plateau due to propagating uplift to southeast and lateral shortening, after [Yuan et al. \(2021\)](#) <sup>[119]</sup>. (i), (ii) Elevation and river network of model at 50 Ma and 0 Ma, with vertical rock uplift rate  $U$  (mm/yr) and later shortening rate  $V$  (mm/yr) plotted below panels. (iii) Topography cross-section perpendicular to the rivers at 30 Ma, 15 Ma, and 0 Ma located at dashed lines in (ii), showing the well reproduced deep valleys and elevated low-relief surfaces.

## (ii) “Negative topography” model

Based on the quantitative comparison and geomorphic characterization of different regions of the Tibetan Plateau, this model speculated an evolutionary sequence of plateau landscape development ([Liu-Zeng et al., 2008](#) <sup>[100]</sup>). The drainage efficiency and drainage evolution from internal to external have played an important role during this process ([Liu-Zeng et al., 2008](#) <sup>[100]</sup>). The landscape evolution

of southeast Tibet started with a phase of the active thrusting with internal intermontane basins (like in northeastern plateau, [Figure 1.14A](#)), followed by a continuous smoothing of topography during tectonic quiescence (like in central plateau, [Figure 1.14B](#)), then terminated by the demise of flat highlands by external fluvial erosion (“negative topography”, [Figure 1.22A](#)). It has been also pointed out by those authors that the elevated southeast plateau surface was formed at high-elevation and terminated along the Yalong-Yulong Thrust belts, generating a 200 km wide, northeast trending topographic edge of ~2 km high, which was a residual of a former higher plateau rim ([Figure 1.16](#)). A former disconnection with the external drainage networks has preserved such elevated surfaces, before the recent phase of aggressive headward invasion of the large rivers into a plateau interior. Enhanced fluvial down-cutting by external drainages attacked and dismembered the elevated and smoothed plateau surface long protected by hydraulic isolation. An introduction of smoothing of highlands by efficient glacial and periglacial erosion could additionally help to yield the low-relief plateau landscape at high elevation ([Zhang et al., 2016](#) <sup>[121]</sup>). This concept of fluvial incision into a preexisted high plateau was clearly contrary to a continuous “relict surface” formed at low elevation and expanding to the coast before a late Miocene uplift ([Clark et al., 2006](#) <sup>[126]</sup>). Some other evidences have been referred to challenge the channel flow model, such as the Paleogene sedimentation in the Yanyuan and Chuxiong foreland basins in the foot of the Yalong-Yulong Thrust Belt ([Bureau of Geology and Mineral Resources of Sichuan Province \(BGMRS\), 1991](#) <sup>[134]</sup>), the diachronous ages of the “high-elevation low-relief” remnant surface described in [Clark et al. \(2006\)](#) <sup>[126]</sup> and the first high peak of sedimentation rate in off-shore basins at 24–10 Ma in favor of a pre-Miocene uplift ([Metivier et al., 1999](#) <sup>[166]</sup>; [Clift, 2006](#) <sup>[167]</sup>; [Clift and Sun, 2006](#) <sup>[168]</sup>). Such a preexisting high plateau has also been invoked in some recent models to explain the topographic evolution in the Three Rivers Region. For example, [Nie et al. \(2018\)](#) <sup>[154]</sup> promoted the key role of a strengthening summer monsoon in dissecting the already-high plateau since the Mid-Miocene Climate Optimum (~17–14 Ma). While [Rohrmann et al. \(2018\)](#) <sup>[169]</sup> proposed a drainage-area expansion of the external large rivers into the paleo-endorheic zone of an elevated plateau, without invoking any tectonic or climatic forcing ([Figure 1.22B](#)).

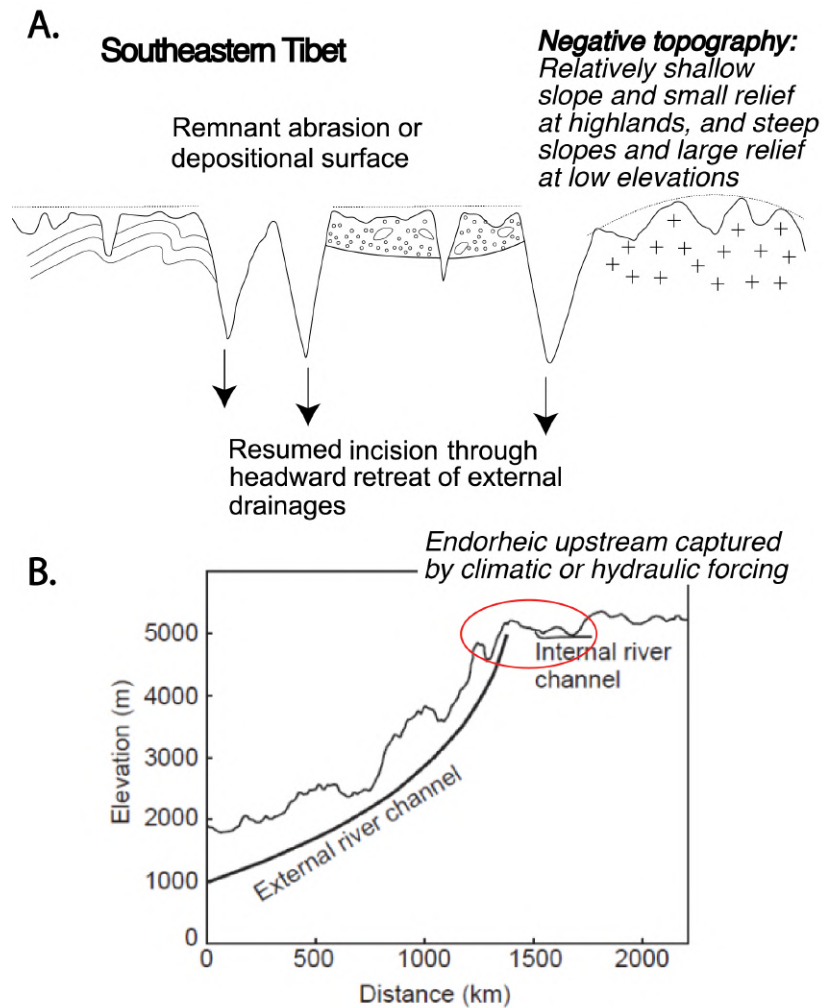


**Figure 1.22** – (A) Cartoons representing the generation of plateau relief of southeastern Tibet of “negative topography”, illustrating regressive fluvial erosion of external drainage into an elevated plateau, modified after [Liu-Zeng et al. \(2008\)](#) <sup>[100]</sup>. (B) Schematic cross-section of model invoking a capture of endoreic upstream by a wetter climate ([Nie et al., 2018](#)) <sup>[154]</sup> or a pure hydraulic expansion into upstream drainage area ([Rohrmann et al., 2018](#)) <sup>[169]</sup>.

### (iii) “Lateral shortening” model

A calculation of  $\chi$  (i.e. a transformed horizontal coordinate measured from the outlet of a basin, [Willett et al., 2014](#) <sup>[170]</sup>) and  $\chi$ -elevation plots across numerous low-relief surfaces at high-elevation in the southeast Tibet, recognized in [Clark et al. \(2006\)](#) <sup>[126]</sup>, showed no common uplift history that could explain the aggregate set of river profiles on those surfaces ([Yang et al., 2015](#) <sup>[117]</sup>). They observed

significant deviation in river profile steepness (i.e. the slope of the  $\chi$ -elevation plot), where the  $\chi$  profiles of interior rivers of the low-relief surface plot below the trunk river and rivers around the surface are steeper and plot above the trunk river. After excluding the influence of differences in rock erodibility, uplift rate or precipitation rate on the river steepness variation across different surfaces, they concluded that changes in drainage area through river capture should be responsible for the variation in the  $\chi$ -elevation plot (Willett et al., 2014<sup>[170]</sup>). Indeed, drainage area loss will result in a higher  $\chi$ , a lower steepness and therefore lower erosion rates, which in return contributes to higher elevation and lower relief of the shrinking drainage. Conversely, drainage area gain would decrease  $\chi$  of the surrounding rivers, aggressively advancing into the shrinking drainage basins (Figure 1.23A). A numerical model of a landscape, incorporating the Indian indentation into Asia (Figure 1.23A), has been applied to demonstrate a lateral shortening could lead to capture events and then drainage gain/loss to eventually generate low-relief surfaces at high-elevation in the Three Rivers Region (as illustrated by cartons in Figure 1.23B), immediately east to the indenting EHS (Yang et al., 2015<sup>[117]</sup>). This implication illustrated that such low-relief surfaces with low erosion rate could be developed in situ due to drainage reorganization, not necessarily preserving a remnant of a low-relief paleolandscape (Clark et al., 2006)<sup>[126]</sup>, although this implication has been immediately challenged with observational and theoretical arguments (Whipple et al., 2017)<sup>[171]</sup>.

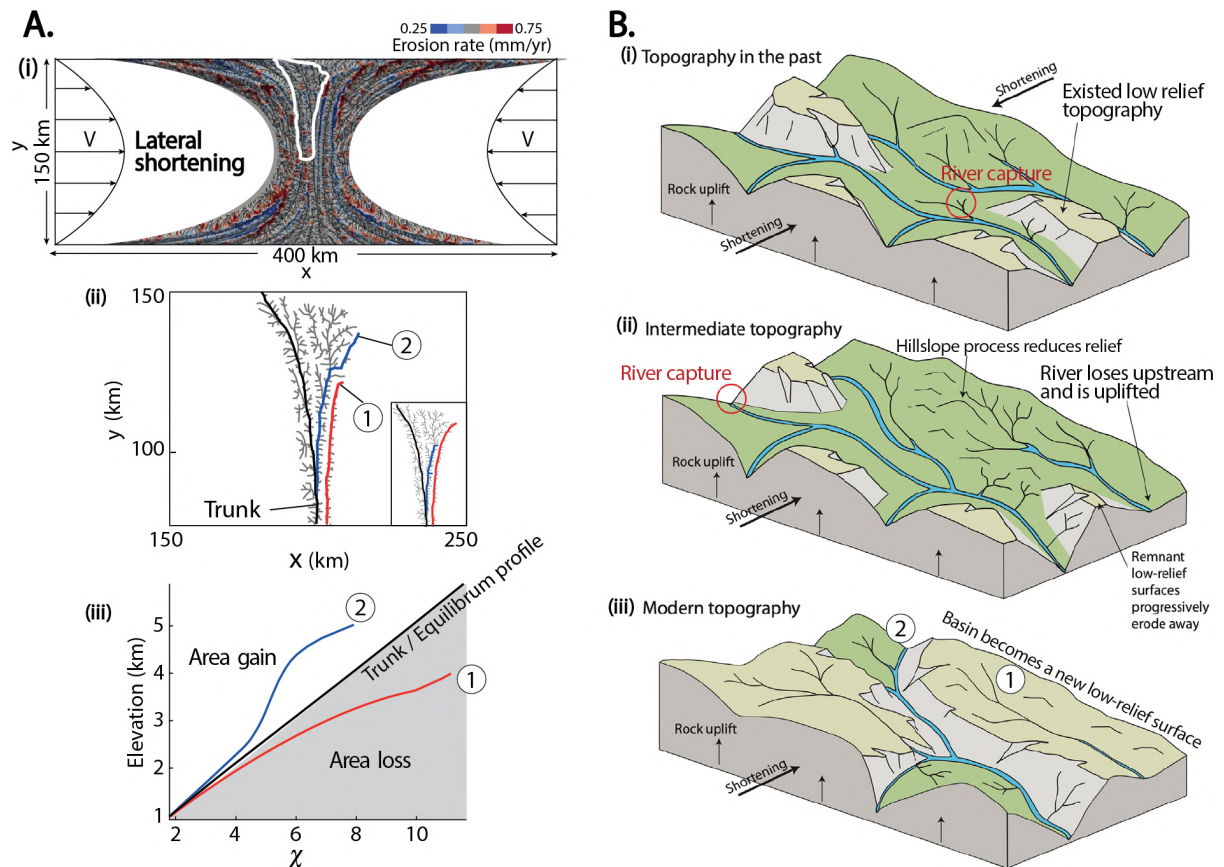


**Figure 1.23** – (A) Numerical model using the Divide and Capture (DAC) landscape evolution model from “Lateral advection” model, after [Yang et al. \(2015\)](#) <sup>[117]</sup>. (i) Final river network configuration and erosion rate, with constant vertical rock uplift rate at 0.5 mm/yr and a various lateral shortening. (ii) A select drainage basin (white polygon in (i)). The inset shows the initial drainage basin configuration before the blue river captured the red one. (iii) Graph of  $\chi$ -elevation plot of river basin selected in b, with higher  $\chi$  in tributaries losing drainage area and lower  $\chi$  in tributaries gaining area. (B) Carton illustration of the “Lateral advection” model, after [Fox et al. \(2020\)](#) <sup>[127]</sup>. (i) Some preexisting low-relief landscapes due to drainage reorganization. (ii) Lateral advection resulted in river capture and drainage reorganization. Loss in upstream drainage area reduces the erosion rate and topographic relief. (iii) The basin losing upstream drainage area formed in-situ gradually a low-relief surface at high elevation. Rivers 1 and 2 correspond to the (iii) in A.

## 1.5.2 Endorheic zone and exorheic zone

The interior part to the west of the Tibetan Plateau at an elevation of ~5000 m, together with the Qaidam Basin in the north at ~3500 m high, is characterized by an extensive endorheic zone, occupied by an extremely arid climate, in contrast with the surrounding wet outer margins that feeds all the major external Asian rivers ([Figure 1.2A](#), [Figure 1.12](#)). The present-day endorheic drainage basin has only ephemeral short-course rivers, which generally flow into the numerous saline alpine lakes on the plateau interior. Limited structural relief creation since at least early Neogene and inefficient

drainage evacuation of eroded sediments inside the internal basins contribute to the appearance of large-scale flatness, which potentially favors a gradual drainage capture by the large external rivers from the east, even though the climatic aridity could slow down this process (Fielding et al., 1994<sup>[1]</sup>, 1996<sup>[81]</sup>). The relief map (Figure 1.12) illustrates clearly that the limit of the flat plateau interior is located up to several hundred kilometers east of the internal drainage divide, which stands as a proof of a potential larger paleo-endorheic zone extending further to the east, prior to the headward conquest by the large rivers from the east (Liu-Zeng et al., 2008<sup>[100]</sup>).

### 1.5.2.1 Extend of the paleo-endorheic zone of the Tibetan Plateau

Between the Jinsha and Longmucuo-Shuanghu sutures, an arcuate belt of Cretaceous-Paleogene intermontane basins (e.g., Hoh-Xil, Nangqian-Yushu, Gonjo, Markam and Jianchuan basins) spans from central Northern Qiangtang to the southeast plateau edge (Li et al., 2020<sup>[172]</sup>) (Figure 1.24). Complex studies of the sedimentologic, stratigraphic and structural data of the elongate basins on the plateau, located near the headwaters or the upstream of the Mekong and Yangtze Rivers could assist to illuminate the extend evolution of the endorheic and exorheic zone of the Tibetan Plateau. To the west, a continuous sedimentation since ~80 Ma to ~27 Ma in the Hoh-Xil Basin is composed of fluvial to fan delta mudstone, sandstone, and conglomerate, with a minor lacustrine carbonate and subordinate gypsum layers, related to the activities of the Tanggula and Fenghuoshan thrust belts (e.g., Leeder et al., 1988<sup>[173]</sup>; Li et al., 2012<sup>[174]</sup>; Staisch et al., 2014<sup>[175]</sup>). In the Nangqian-Yushu basins to the southeast, sedimentary deposits consist of mud and carbonate accumulation in lacustrine environments and sand to gravel in fan-delta or alluvial-fan environments, contemporaneous with motion on fold-thrust structures during ~51-37 Ma (e.g., Horton et al., 2002<sup>[91]</sup>; Spurlin et al., 2005<sup>[176]</sup>). Similarity, the basin infilling of the Gonjo Basin is dominated by continental sediments of predominantly alluvial fan, fan-delta, floodplain, and lacustrine deposition since ~53 Ma to at least late Tertiary (e.g., Studnicki-Gizbert et al., 2008<sup>[177]</sup>; Zhang et al., 2018<sup>[178]</sup>). Deposited sediments in the Markam Basin from Lower Cretaceous to early Oligocene are predominantly reddish sandstones, siltstones and mudstones with gypsum interbeds (Li et al., 2015<sup>[179]</sup>; Su et al., 2018<sup>[180]</sup>). Deposition of alluvial-fan and braided-river sediments, with important overlapping layers of lacustrine carbonate in the Jianchuan basin has been evidenced by eastward and northeastward paleo-flows and terrestrial clasts derived from the hanging wall of bounding thrusts during ~50-39 Ma (Gourbet et al., 2017<sup>[181]</sup>; Cao et al., 2020<sup>[122]</sup>). Those studies all showed a sediment source proximity and some certain stratigraphic variability among the sub-basins, which indicated independent evolution of each basin

filled with materials derived from relatively small internal drainage areas. Detailed sedimentologic and provenance evidence analyses also revealed relatively limited unroofing and low average sedimentation rates in these syn-contractual basins, where internal short-course rivers and shallow regional slopes defined the landscape during the Paleogene (e.g., Horton et al., 2002<sup>[191]</sup>; Staisch et al., 2014<sup>[175]</sup>, 2016<sup>[182]</sup>). Such similar geomorphic characteristics are observed in the low-relief Tibetan plateau interior of present-day, encouraging those authors to presume an emplacement of the deeply incised Mekong and Yangtze rivers later than the regional scale development of those Paleogene basins.

The widely distributed Wudaoliang Formation, composed of layers of lacustrine carbonate and sandstones with organic rich shales, were described as early to middle Miocene age (~23.0–13.5 Ma) by dating interbedding volcanic deposits (Yi et al., 2000<sup>[183]</sup>; Liu and Wang, 2001<sup>[184]</sup>; Liu et al., 2001<sup>[185]</sup>; Wu et al., 2008<sup>[186]</sup>). Such a predominantly lacustrine carbonate deposit were recognized in the Wudaoliang, Beiluhe, Tuotuohe, Tongtianhe, Ando, Naqu, Bangoin, Lunpola and Shuanghu Basins from north to south across the central plateau (Wu et al., 2008<sup>[186]</sup>) (Figure 1.25). This extensive distribution of carbonate delimited the extend of numerous immense lakes from ~23.5 to ~13.5 Ma, which were linked by water passages between mountain ranges, forming a huge lake complex of >100 000 km<sup>2</sup> in the north-central plateau and another one >50,000 km<sup>2</sup> in the south-central plateau. The persistence of those internal huge lakes and lacustrine deposits implied an much larger endorheic drainage zone further to the east compared to present-day's endorheic-exorheic divide until at least ~13.5 Ma (Figure 1.26). A climatic shift from the warm, dry conditions during the Oligocene to moderately cool and wet ones at early Miocene, followed by progressive cooling and drying, has also been revealed by the fossils in these basins and could be related to the paleo-lakes' expansion (e.g., Wu et al., 2008<sup>[186]</sup>; Zhao et al., 2022<sup>[187]</sup>). To summary, the upstream drainages of the modern external Yangtze, Mekong, and Salween rivers haven't reached into the plateau interior as far as present-day, the Tibetan Plateau formed with limited dissection of external rivers until the middle Miocene (Liu-Zeng et al., 2008<sup>[100]</sup>, Wu et al., 2008<sup>[186]</sup>). This view contrasts radically the previous hypothesis which presumed the antecedence of these large rivers since long (e.g., Hallet and Molnar, 2001<sup>[116]</sup>, Clark et al., 2005a<sup>[138]</sup>, 2006<sup>[126]</sup>).

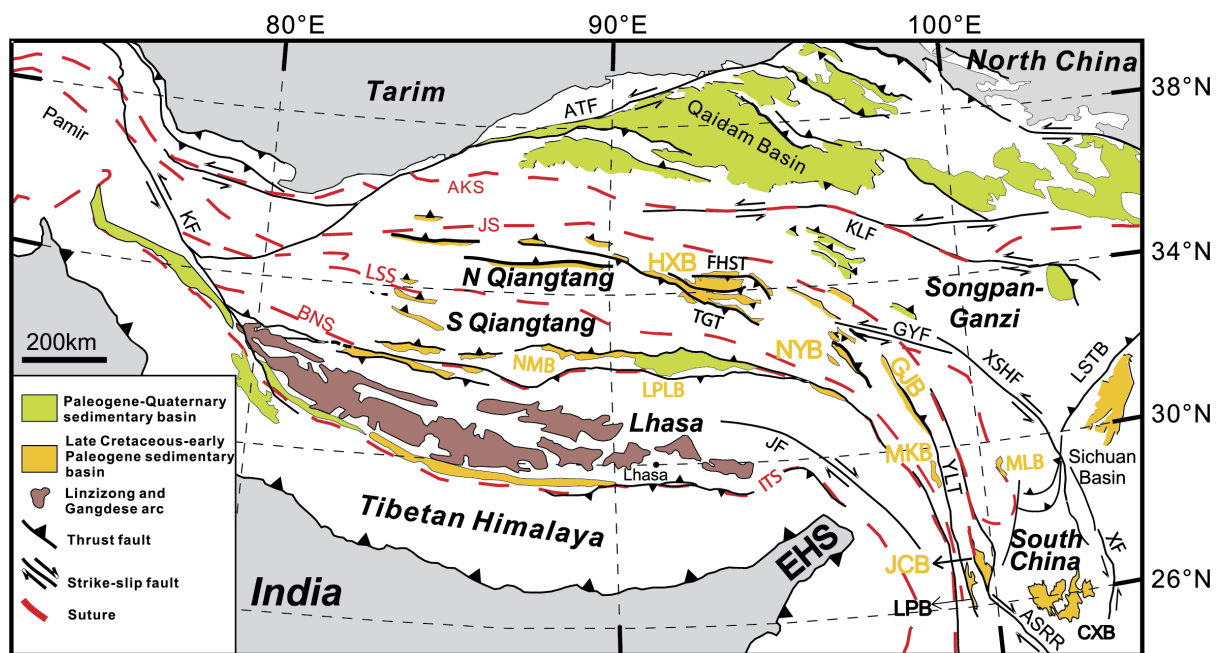


**Figure 1.24** – Simplified tectonic structures and main basins of the Tibetan Plateau. Abbreviations: AFT: Altyn Tagh Fault; AKS: Ayimaqin–Kunlun suture; ASRR: Ailaoshan–Red River fault; BNS: Bangong–Nujiang suture; CXB: Chuxiong Basin; EHS: Eastern Himalaya Syntaxis; FHST: Fenghuoshan Thrust; GJB: Gonjo Basin; GYF: Ganzi–Yushu Fault; HXB: Hoh–Xil Basin; ITS: Indus–Tsangpo suture; JCB: Jianchuan Basin; JF: Jiali Fault; JS: Jinsha Suture; KF: Karakorum Fault; KLF: Kunlun Fault; LPB: Lanping Basin; LPLB: Lunpola Basin; LSS: Longmucuo–Shuanghu Suture; LSTB: Longmenshan Thrust Belt; MLB: Mula Basin; NYB: Nangqian–Yushu Basin; NMB: Nima Basin; TGT: Tanggula Thrust; XF: Xiaojiang Fault; XSHF: Xianshuihe Fault; YLT: Yangla Thrust. Modified after [Li et al. \(2020\)](#) <sup>[172]</sup>.

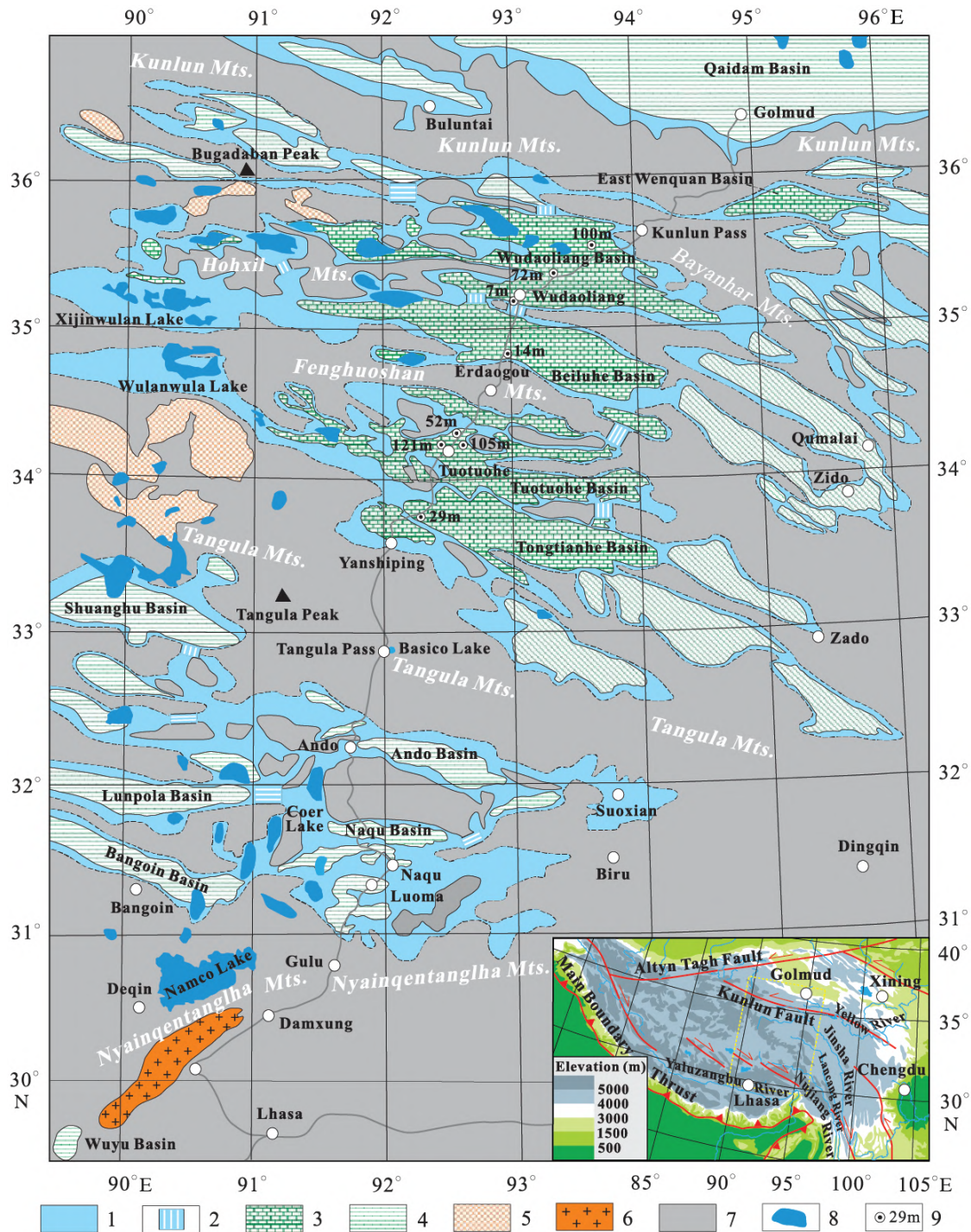


**Figure 1.25** – Map showing lakes and lacustrine deposits of the central Tibetan Plateau until at least ~13.5 Ma. 1: early Miocene lake cover; 2: passages linking lakes; 3: lower Miocene carbonate deposits; 4: lower Miocene clastic deposits; 5: Miocene basalts; 6: Miocene granite; 7: area of early Miocene erosion; 8: present lakes; 9: boreholes and thickness of lower Miocene strata penetrated. Thin grey line is the Golmud-Lhasa Railway. The inset shows the plateau topography and study area in [Wu et al. \(2008\)](#) [186].

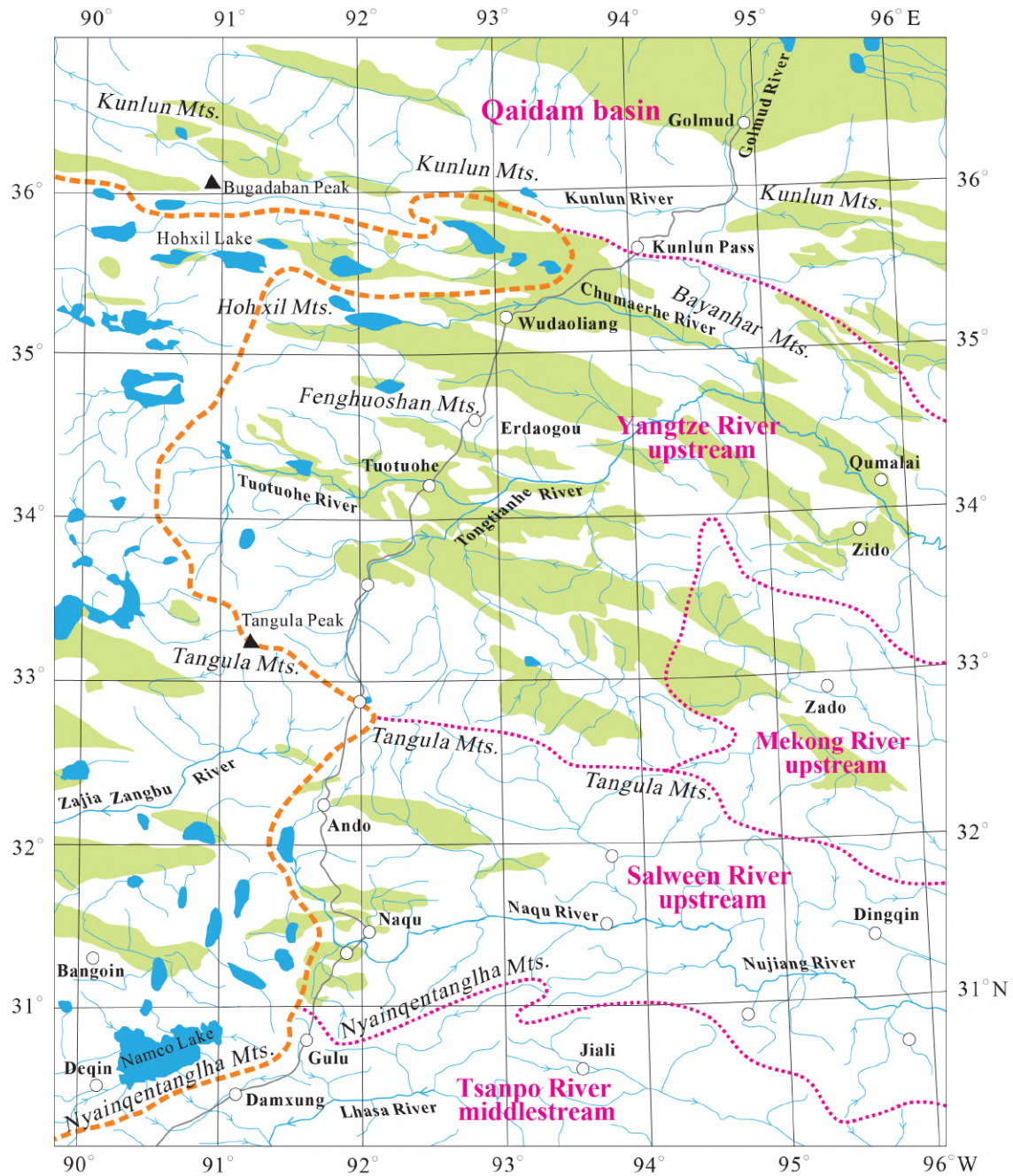
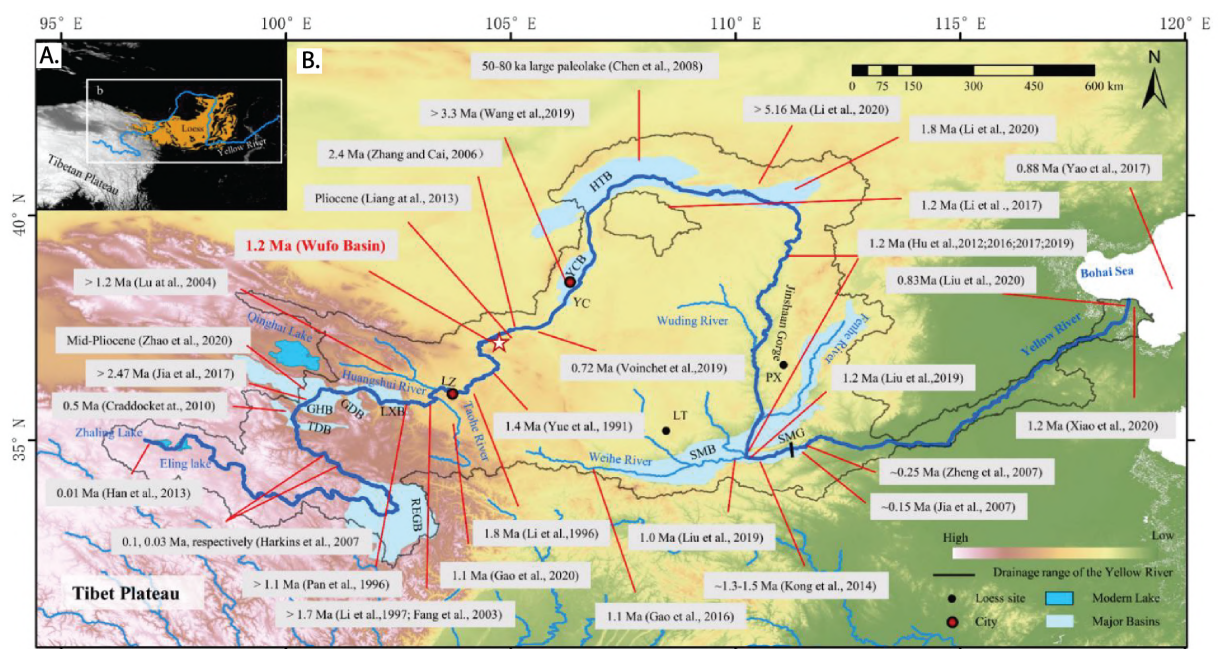


Figure 1.26 – Modern drainage system of the central Tibetan Plateau. Green area is the cover of lower Miocene lacustrine strata. Thin grey line is the Golmud-Lhasa Railway. Orange dashed line is modern boundary between endorheic and exorheic zones. Red dotted line represents the drainage divide between river drainages, modified after Wu et al. (2008) [186].

One of the best studied drainage expansion into the paleo-endorheic zone of the Tibetan Plateau is the upstream of the Yellow River, which drains the northeast growing plateau rim of Tibet (Figure 1.27). Most studies exploiting sediments composition analyses, fluvial terraces dating, sediment provenance in the basins and detrital thermochronological data proposed an emplacement of the modern Yellow River no earlier than the Quaternary, regardless of the significant difference of the precise timing of incision onset into the plateau (e.g., Harkins et al., 2007<sup>[188]</sup>; Craddock et al., 2010<sup>[189]</sup>; Perrineau et al., 2011<sup>[190]</sup>; Li et al., 2021<sup>[191]</sup>) (Figure 1.27). A Quaternary enhanced incision along the upstream of the Yellow River substantially lagged the onset of mountain building and surface uplift in the northeast plateau margin, which has been recognized to mainly take place at ~14–8 Ma (e.g., Garzione et al., 2005<sup>[192]</sup>; Lease et al., 2007<sup>[193]</sup>). The rise of ranges bounding different isolated basins resulted in pronounced sediment accumulation and eventually basins ponding (Métivier et al., 1998<sup>[104]</sup>; Sobel et al., 2003<sup>[105]</sup>), which in the end hosted numerous shallow lakes before the regional scale upstream drainage capture across the Quaternary. The mechanism of integration of those internal lakes into downstream fluvial incision remains undefined yet. Some proposed that cooler climates since the onset of Northern Hemisphere glaciation (Molnar et al., 2004<sup>[194]</sup>) possibly favored lake expansion and spillover, which led to downstream fluvial incision and generation of the modern course of the Yellow River (Craddock et al., 2010<sup>[189]</sup>). Alternatively, enhanced headward erosion could possibly cut through alternating basin–mountain structures, capturing and interconnecting the endorheic drainage of lakes by the lower Yellow River (Hu et al., 2019<sup>[195]</sup>; Bridgland et al., 2020<sup>[196]</sup>).



**Figure 1.27** – (A) Localisation of the Yellow River relative to the Tibetan Plateau, with the Loess Plateau in yellow shade. (B) Yellow River drainage marked in thin black line and major basins, with river incision studies in grey box. Light blue polygons represent basins that were once occupied by paleolakes. GHB: Gonghe Basin; GDB: Guide Basin; HTB: Hetao Basin; LXB: Linxia Basin; REGB: Ruoergai Basin; SMB: Sanmen Basin; SMG: Sanmen Gorge; TDB: Tongde Basin; YCB: Yinchuan Basin, after [Li et al. \(2021\)](#) <sup>[191]</sup>.

### **1.5.2.2 Drainage evolution of the major rivers in exorheic southeast Tibetan Plateau: Salween, Mekong, Yangtze, Yalong and Dadu rivers**

The topographic evolution of the southeast Tibetan Plateau is closely related to the erosion pattern of the continental-scale fluvial systems, of which the establishment and dynamics are in return predominantly controlled by the topography history during the Cenozoic collision of India and Asia. As aforementioned, the attenuated geometries of the subparallel drainage basins in the southeast Tibet, as well as the shapes of longitudinal or transverse river profiles, could loyally record the regional tectonic and uplift history (e.g., [Jackson and Leeder, 1994](#) <sup>[197]</sup>; [Hallet and Molnar, 2001](#) <sup>[116]</sup>). A good understanding of the drainage systems evolution in this region could shed light on perceiving how the landscape evolved. A regional compilation of geomorphic observations suggested that the southeast Tibetan Plateau margin was once drained by a single, southward flowing and Mississippi-like river system into the South China Sea ([Clark et al., 2004](#) <sup>[118]</sup>; [Wang et al., 2019](#) <sup>[198]</sup>) (**Figure 1.28A**). In this scenario, disruption of the paleo-drainage by river capture and reversal was proposed to have happened on a low-relief paleolandscape, coeval with or prior to the middle Miocene surface uplift, which has occurred over long wavelengths (>1000 km), contributing to the low-gradient topographic slope of present-day. Later geochemistry researches, based on major and trace element proxies, bulk Nd and single K-feldspar grain Pb isotope, showed a connection between the middle Yangtze and the paleo-Red River until 24 Ma, and also a probable connection with tributary rivers eroding the Songpan Ganzi terrane prior to 12 Ma (e.g., [Clift et al., 2006](#) <sup>[167]</sup>, [2008](#) <sup>[199]</sup>, [2020](#) <sup>[200]</sup>). However, their results didn't support any former connection of the paleo-Red River with the upper Yangtze, Mekong or Salween rivers (**Figure 1.28B**) and speculated that drainage capture events have occurred during the whole Cenozoic, in correspondence to southeastward gradual propagation of surface uplift. Recent results of petro-stratigraphy, detrital zircon U-Pb dating and heavy-mineral analysis from late Cretaceous-early Paleogene sedimentary basins along the southeast plateau margin ([Deng et al., 2018](#) <sup>[201]</sup>, [Zhao et al., 2021](#) <sup>[202]</sup>) showed some similarities in the provenance signatures and speculated a continental-scale fluvial system once drained southwestward into the Neo-Tethyan Ocean (**Figure 1.28C**). However, such a purported south-flowing river network has been questioned by others, due

to few presence of fluvial landscapes and a lack of links in terms of some key geochemistry proxies among drainages (e.g., [Wissink et al., 2016](#) <sup>[203]</sup>; [Zhang et al., 2017](#) <sup>[204]</sup>) ([Figure 1.28D](#)).

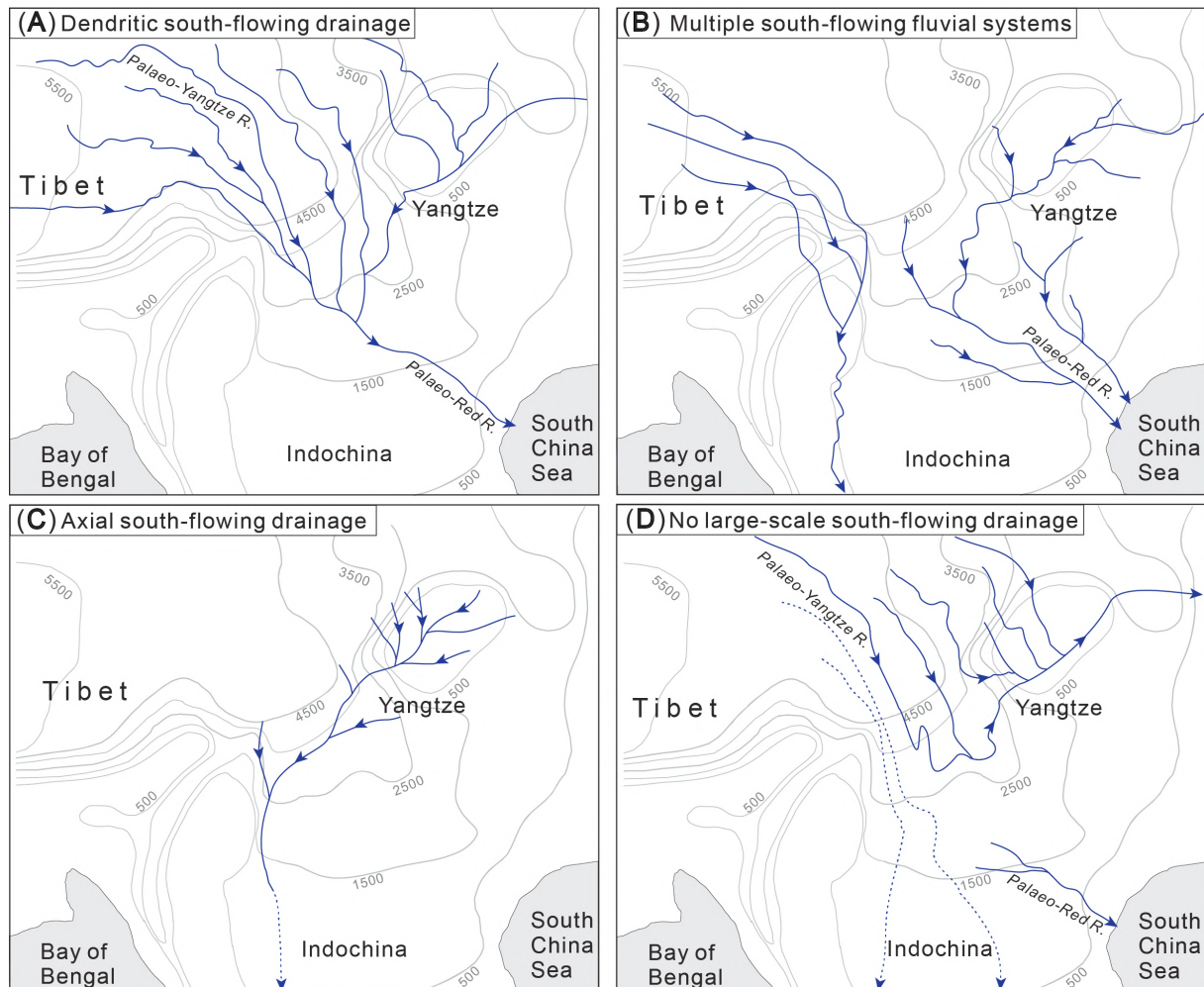


**Figure 1.28** - Proposed scenarios of drainage evolution in southeast Tibet. (A) Dendritic, continental-scale river network, drained by the paleo-Red River southward into the South China Sea ([Clark et al., 2004](#) <sup>[118]</sup>; [Wang et al., 2019](#) <sup>[198]</sup>). (B) Multi south-flowing river networks draining the western Yangtze terrane to the South China Sea and the southeast Tibet to the Indian Ocean ([Clift et al., 2006](#) <sup>[167]</sup>, [2008](#) <sup>[199]</sup>, [2020](#) <sup>[200]</sup>). (C) An axial transcontinental drainage flowing to the Neo-Tethyan Ocean of the time from the western South China Block ([Deng et al., 2018](#) <sup>[201]</sup>, [Zhao et al., 2021](#) <sup>[202]</sup>). (D) A long-standing Yangtze River network, with no connection with any south-flowing rivers ([Wissink et al., 2016](#); [Zhang et al., 2017](#) [Wissink et al., 2016](#) <sup>[203]</sup>; [Zhang et al., 2017](#) <sup>[204]</sup>). Modified after [Zhao et al. \(2021\)](#) <sup>[202]</sup>.

## 1.6 Paleoelevation of the southeast Tibetan Plateau

One good constraint of surface uplift comes from the paleoelevation estimates across the southeast plateau, regardless of their spatial sparsity and large uncertainties (>1000 m) related to paleoelevation techniques (Quade et al., 2011<sup>[205]</sup>). Stable-isotope paleoelevation exploits variations of the isotopic composition in precipitation (usually  $\delta^{18}\text{O}$ ) with respect to elevation to calculate the paleoelevation (e.g., Rowley et al., 2001<sup>[206]</sup>). Most of the paleoelevation studies in southeast Tibet are concentrated in the Three Rivers Region (e.g., Gonjo, Markam and Jianchuan basins) and several locations in the upstream of the Yangtze River (e.g., Fenghuoshan basin), while in the Great Bends Region to the east, paleoelevation data are relatively rare (Figure 1.29A, B). On the plateau, the paleoelevation estimates of the Fenghuoshan basin based on oxygen isotope was less than 2 km (Cyr et al., 2005<sup>[207]</sup>) and was uplifted to present elevation at ~4500 m near 22 Ma (Polissar et al., 2009<sup>[85]</sup>; Dai et al., 2012<sup>[92]</sup>). Carbonate clumped isotope paleoelevation suggested that the Nangqian basin have arisen to a mean elevation of ~3.0 km by ~37 Ma, nearly 1.1-1.2 km lower than their modern counterparts (Li et al., 2018<sup>[208]</sup>). The paleoelevation of the Gonjo-Markam Basin derived from leaf fossil physiognomy suggested that the basin had reached its near-present elevation at ~4500 m since at least near 40 Ma (Li et al., 2015<sup>[179]</sup>; Tang et al., 2017<sup>[209]</sup>; Su et al., 2018<sup>[180]</sup>; Xiong et al., 2020<sup>[210]</sup>). Southeast of the plateau margin, oxygen isotope paleoelevation indicated that the Jianchuan basin has risen to their present elevation at ~3300 m by ~35 Ma, the Lanping basin used to reach ~3300  $\pm$  450 m near 15 Ma, higher than present-day's elevation of 2700 m; the Yanyuan basin in the footwall of the Muli thrust and Eryuan basin located in the south reached their present elevation at ~2300 m by the early Pliocene near 5 Ma, while the Chake Basin to the south remained near sea level throughout the Eocene, until being uplifted to ~2000 m at ~11 Ma (Hoke et al., 2014<sup>[211]</sup>; Li et al., 2015<sup>[179]</sup>). These results indicated that Tibetan orography has expanded southeastwards since the Eocene. However, careful revising of sedimentary age and paleoelevation of Jianchuan basin (Gourbet et al. 2017<sup>[181]</sup>; Wu et al. 2018<sup>[212]</sup>) reassigns a significantly lower altitude (1200  $\pm$  1200 m.a.s.l) than precedent evaluation at late Eocene (Hoke et al., 2014<sup>[211]</sup>; Li et al., 2015<sup>[179]</sup>). To the east, Xu et al. (2016)<sup>[213]</sup> suggest a lower bound for the elevation of the Longmenshan in the late Miocene of ~3000 m (present-day at 2800-3700 m).

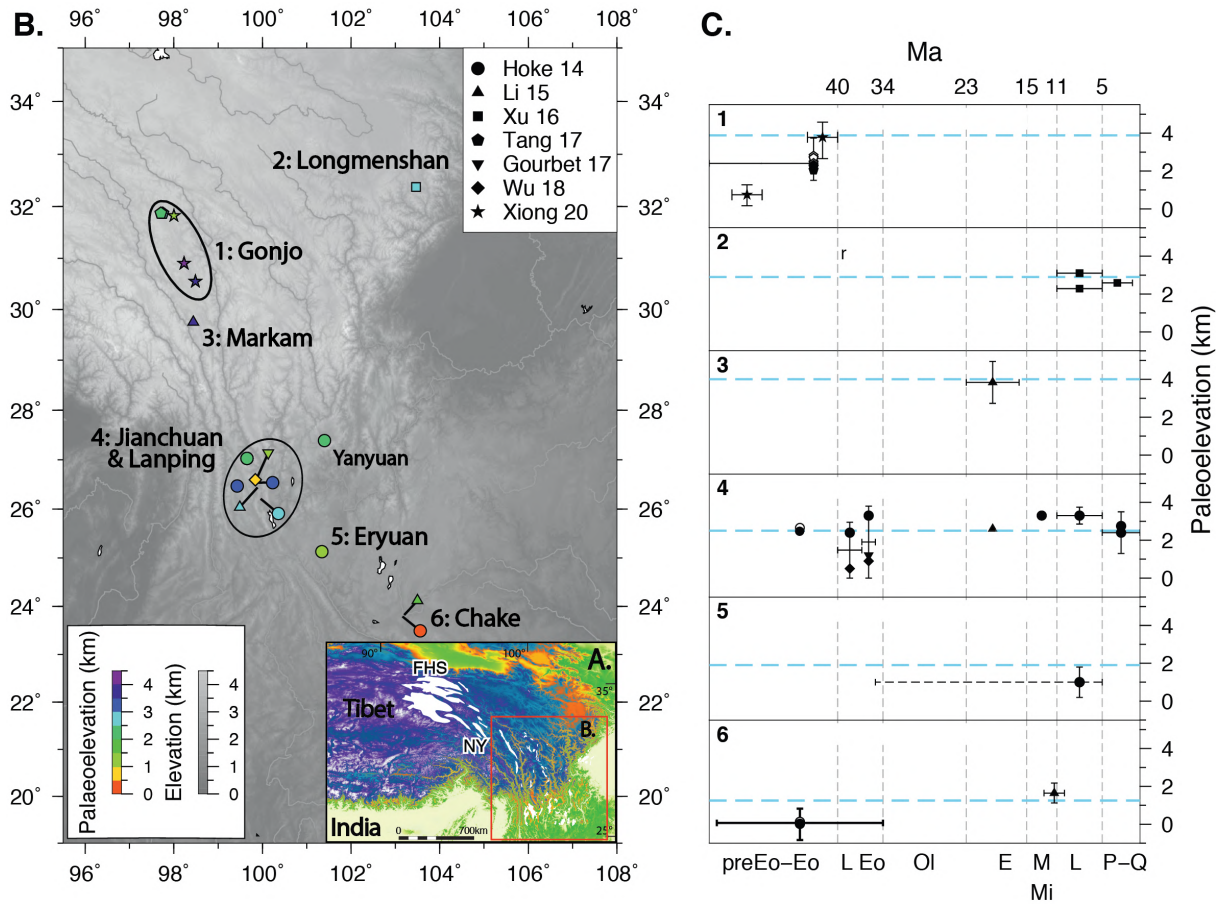


**Figure 1.29** – (A) Tibet topography map with Paleogene basins marked in white patches. FHS: Fenghuoshan Basin; NY: Nangqian–Yushu Basin. (B) Sample locations from Hoke et al. (2014)<sup>[211]</sup>; Li et al. (2015)<sup>[179]</sup>; Xu et al. (2016)<sup>[213]</sup>; Gourbet et al. (2017)<sup>[181]</sup>; Tang et al. (2017)<sup>[209]</sup>; Wu et al. (2018)<sup>[212]</sup> and Xiong et al. (2020)<sup>[210]</sup> are colored by paleoelevation. (C) Paleoelevations and ages plot of each studies. Mean present-day elevation of samples are shown by dashed blue lines. Only a single error bar is plotted to represent samples from same site. Filled and open symbols represent paleoelevation estimates using a modern temperature–elevation relationship and a higher Eocene temperature, respectively.

## 1.7 Present-day climate and paleoclimate of the southeast Tibetan Plateau

### 1.7.1 Monsoonal climate in southeast Tibet

Different from most places of same latitude on earth, which are dominated by a dry and hot condition under the subtropical high pressure, the South and East Asia are mainly characterized by

seasonal wind reversion and heavy summer precipitation, namely the monsoon climate (Allen and Armstrong, 2012<sup>[214]</sup>). Monsoon is an unique metrological phenomenon of global weather and stems from unequal distribution of “hot” land masses and the differential specific heat capacity between land and oceans (e.g., Webster and Chou, 1980<sup>[215]</sup>; Molnar et al., 1993<sup>[48]</sup>; An et al., 2001<sup>[216]</sup>; Boos and Kuang, 2010<sup>[217]</sup>). The Intertropical Convergence zone (ITCZ) represents the area where the northeast and the southeast trade winds converge and it encircles the Earth near the thermal equator, though its specific position varies seasonally, depending on the exposition towards the sun (e.g. Webster and Chou, 1980<sup>[215]</sup>) ( Figure 1.30A). The Indian monsoon (IM) and East Asian monsoon (EAM) are regarded as a northward migration (further to ~50°N) of the global tropical monsoon system, which is confined to low latitudes (<20°–23°N and S) and driven by the ITCZ (Wang, 2006<sup>[218]</sup>; Kitoh et al., 2013<sup>[219]</sup>). The southeast Tibetan Plateau and its surroundings are strongly influenced by both the IM and EAM (Fang et al., 2021<sup>[220]</sup>) (Figure 1.30B). The air masses originate from the Indian and Pacific oceans from southwest and southeast, respectively, penetrate the Birman terrane and the South China craton to the southeast margin of the Tibetan Plateau. The arrival of vapor-carrying airflow collides with the high topography, causing strong upward air movement and heavy convective monsoonal precipitation in front of the southeast plateau margin (Bookhagen et al., 2005<sup>[221]</sup>; Barros et al., 2006<sup>[222]</sup>). Peak rainfall is from June to September for the IM and arrives somehow earlier for the EAM, showing a strong seasonality. The emplacement and evolution of monsoon was principally attributed to the uplift of the Himalayan–Tibetan complex (Ramstein et al., 1997<sup>[223]</sup>; Guo et al., 2002<sup>[224]</sup>, 2008<sup>[225]</sup>). For example, numerical modelling showed that a high Tibetan plateau with half of present average altitude was sufficient to drive the tropical IM into the middle–latitude temperate zones (Boos and Kuang, 2010<sup>[217]</sup>; Liu et al., 2019<sup>[96]</sup>).

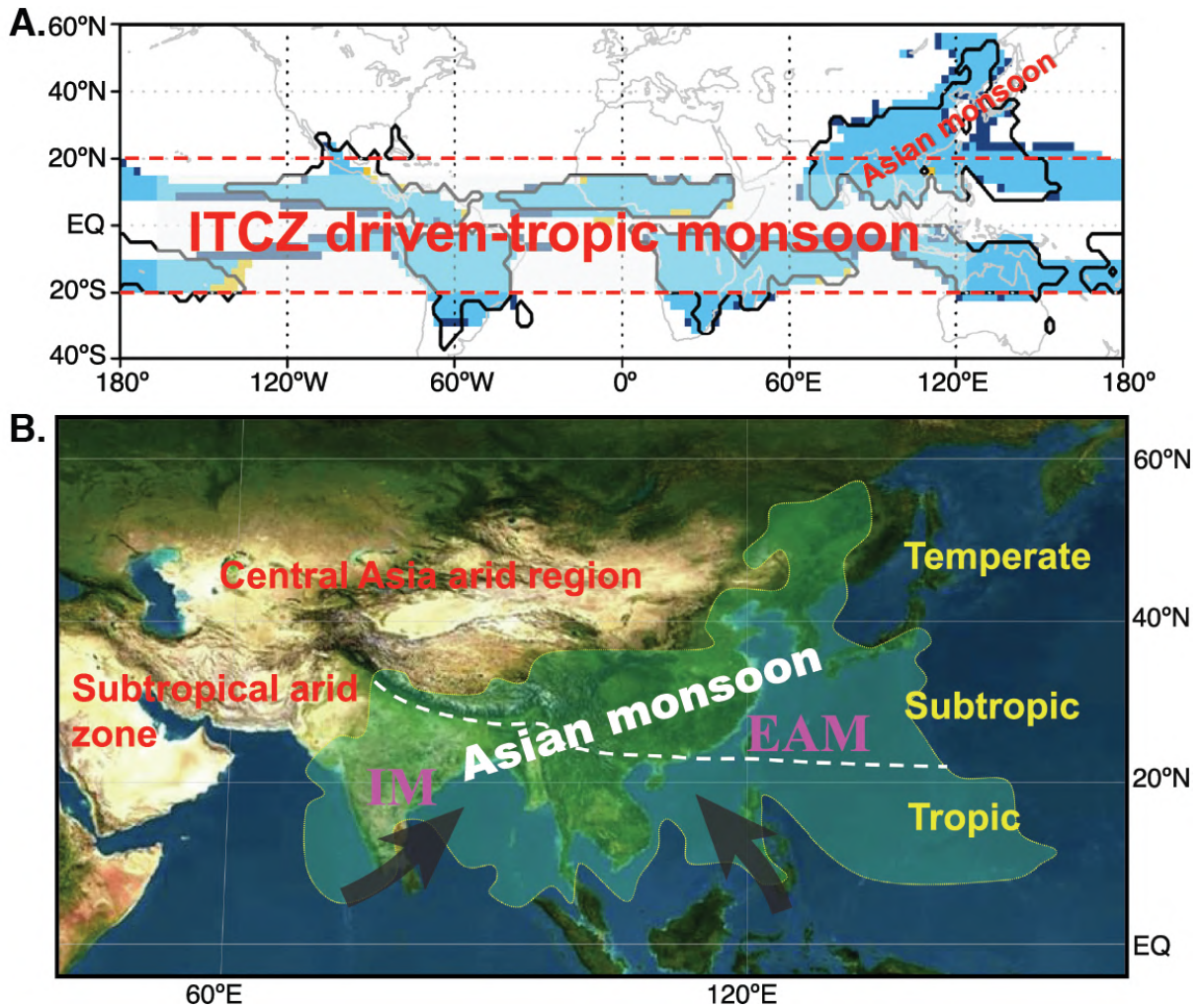


**Figure 1.30** – Distribution of the Asian monsoon and location of the studied region. (A) Observed (thick contour) and simulated (shading) global monsoon domain showing an exceptional extension of the Asian monsoon from tropics up to the middle latitude of  $\sim 55^{\circ}\text{N}$  in East Asia (modified from Kitoh et al. 2013<sup>[219]</sup>). (B) The Asian monsoon range (taken from (a)) with respect to the TP and Asian inland and subtropical dry regions. In (b), the white broken line shows the boundary between modern tropical and subtropical monsoons. IM and EAM mean the Indian monsoon and East Asia monsoon, respectively. Modified from Fang et al. 2021<sup>[220]</sup>.

## 1.7.2 Orographic effects on precipitation in southeast Tibet

“Orographic effects” represent complex physical processes, which cause enhanced and/or reduced precipitation through the interaction of earth surface and atmosphere (Roe, 2003<sup>[226]</sup>, 2005<sup>[227]</sup>). The presence of orography leads to dynamic responses of the vapor-carrying airflow, when its partial pressure outpaces the saturation pressure, water starts to condensate to generate precipitation.

Concretely, when the underlying topography forces moisture-bearing airflow to rise, partial pressure will largely increase due to continuous cooling and diabatic expansion, approaching the saturation pressure, and lead to moisture condensation (Roe, 2005<sup>[227]</sup>; Smith, 2006<sup>[228]</sup>). Once the condensed water droplets gain enough mass and gravity larger than the buoyancy of the rising air, the droplets will fall as rain or snow. A continuous growing of surface elevation along the orogenic mountain ranges and plateaus would result in significant rainfalls in the windward side of high topography, as in the Himalayas or in the foreland of southeast Tibet, and also the leeward decent of dry and warm air masses generates a distinct “rain shadow” area and much slighter rainfall, as on the southeast plateau margin (Figure 1.31A). Therefore, the incorporation of orographic rainfall gradients is important to evaluate the spatial distribution of precipitation, also to model river incision and topographic evolution.

In southeast Tibet at present-day, a sharp contrast of monsoonal precipitation exists between on the plateau and in the foreland due to a strong orographic effect of high topography, which means much less moisture could be transported to the highland plateau >~3000 m of elevation, blocking the southward arrival of the wet monsoonal air masses, as similarly observed across the Himalayas (Bookhagen and Burbank 2010<sup>[229]</sup>) (Figure 1.32). Precipitation of less than 500 mm/yr (Figure 1.31A) and strong evapotranspiration of an order of several hundreds of millimeter per year (Figure 1.31B) is generally recorded on the high plateau of southeast Tibet, making the net precipitation collected in the river network of ~200 mm/yr (e.g., Lin et al., 2021<sup>[230]</sup>; Ma and Zhang, 2022<sup>[231]</sup>). The heavy rainfall >1000 mm/yr is observed in the foreland region at low <1000 m, with intense moisture penetrating into the plateau interior through the deeply incised large river valleys of the Yangtze, Yalong and Dadu rivers, while the Mekong and Salween rivers are more characterized by dry condition. One thing worthy noting is that even though the net precipitation is relatively low on the plateau, the total quantity of water collected in these vast upstream drainages could be tremendous.

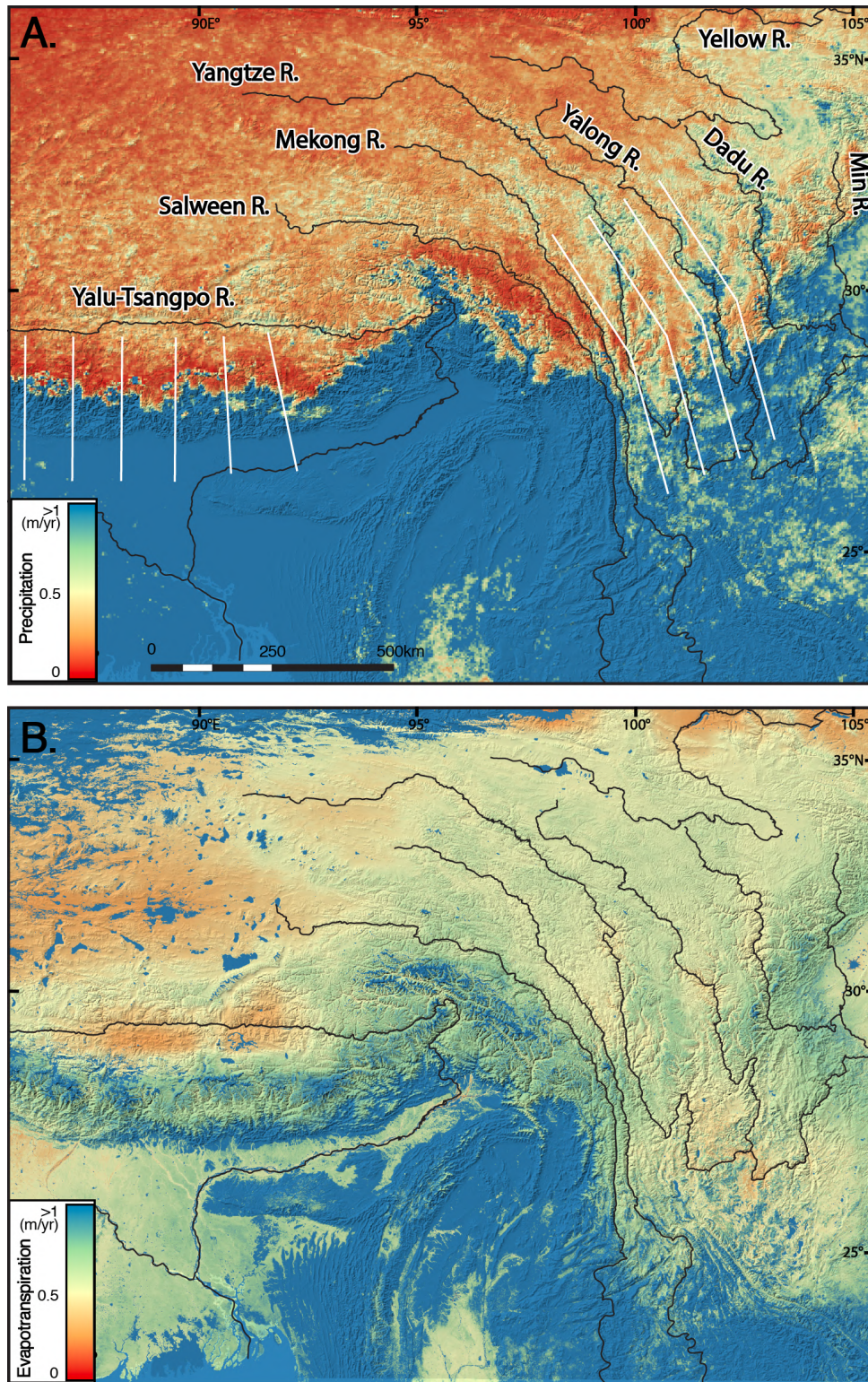
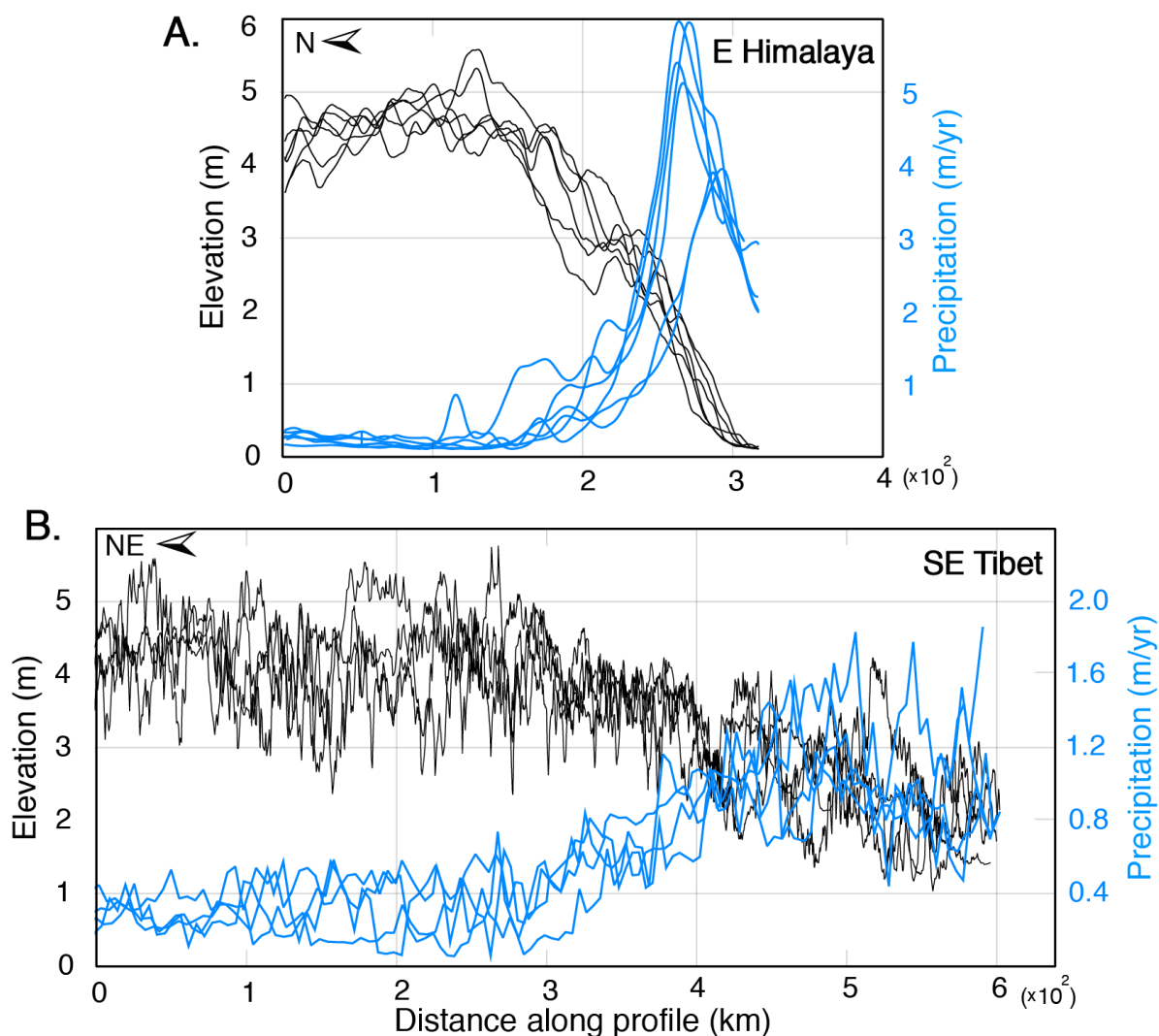


Figure 1.31 – Spatial distribution of the annual precipitation (A) and evapotranspiration (B) across the eastern part of the Tibetan Plateau, based on TRMM 2B31 (1998–2009) dataset.



**Figure 1.32** – Precipitation and topography swath profiles across the Himalayas (A) (modified from [Bookhagen and Burbank 2010](#)<sup>[229]</sup>) and the southeast Tibetan Plateau margin (white lines in [Figure 1.31](#)), showing a gradual increase of topography and a sharp decrease of precipitation when elevations pass ~3000 m.

## 1.7.3 Paleoclimate of southeast Tibet

### 1.7.3.1 Onset timing of a dominant monsoonal climate

The timing of initiation of Asian monsoon is still a heatedly debated issue based on numerous studies ([Allen and Armstrong, 2012](#)<sup>[214]</sup>) ([Figure 1.33](#)). Former estimates of the onset timing of monsoon varies from the late Miocene (~11–8 Ma) to the early Miocene (~23–20 Ma) (e.g. [Quade et al., 1989](#)

[232]; Kroon et al., 1991 [51]; Prell et al., 1992 [233]; Rea et al., 1998 [234]; Qiang et al., 2001 [235]; Sun and Wang, 2005 [236]; Clift, 2006 [167]; Clift et al., 2008 [199], 2014 [237]; Guo et al., 2002 [224], 2008 [225]; Xu et al., 2009 [238]). An increase of  $\delta^{13}\text{C}$  and  $\delta^{18}\text{O}$  in the pedogenic carbonate in northern Pakistan and in the Himalayan foreland basin in Nepal and India at ~10–8 Ma and in the Bengal fan at ~7.4 Ma has been interpreted as a significant expansion of C4 type vegetation (grassland) in place of C3 type (forest), indicating of strengthening of Indian monsoon at that time (Harrison et al., 1993 [239]; Quade et al., 1989 [232], 1995 [240]; Sanyal et al., 2004 [241]; Galy et al., 2010 [242]). A peak of aeolian dust in the North Pacific at 8 Ma was documented in deep-sea sediments from ODP site 885/886, which was interpreted as an enhanced production of dust in the northern China and transported by a strengthened westerlies during the winter monsoon (Rea et al., 1998 [234]).

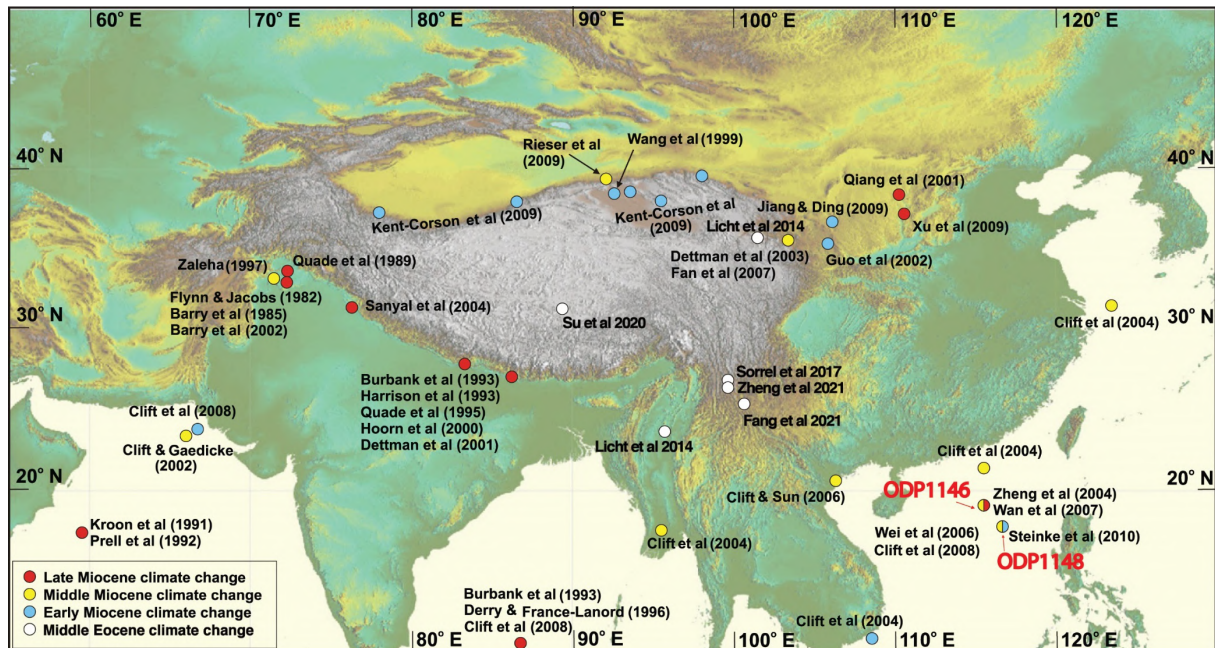


Figure 1.33 – Compilation of paleoclimate change data of Tibet and its surroundings, modified from Allen and Armstrong (2012) [214].

In contrast, some later studies propose that the continental eastern Asia was dominated by a W–E zonal arid to semi-arid environment during Paleogene, before the significant shift at early Miocene to a monsoon dominated wet climate like present-day (Sun and Wang, 2005 [236]; Guo et al., 2008 [225];

Quan et al., 2012 <sup>[243]</sup>, 2014 <sup>[244]</sup>). This transition is probably due to the combination of Himalayan–Tibetan uplift and the shrinkage of the epicontinental Paratethys sea in the central Asia (Ramstein et al., 1997 <sup>[223]</sup>; Guo et al., 2002 <sup>[224]</sup>, 2008 <sup>[225]</sup>). Based on the total sedimentation rate in epicontinental sea basins around the east or southeast Asia (Clift, 2006 <sup>[167]</sup>), an early Miocene onset of monsoon has been speculated from some evidences: e.g., enhanced sedimentation rates offshore of the Mekong drainage system (Clift et al., 2004 <sup>[245]</sup>), high sediment flux rates for the Indus fan with detritus from the Himalayan/Tibetan orogen (Clift and Gaedicke, 2002 <sup>[246]</sup>; Clift et al., 2008 <sup>[199]</sup>). Those results predicted an onset timing of monsoon at least 14 million years earlier than previous model of the coupling of convective mantle dynamics, Tibet surface uplift and monsoon development (e.g. Quade et al., 1989 <sup>[232]</sup>; Kroon et al., 1991 <sup>[51]</sup>; Molnar et al., 1993 <sup>[48]</sup>). Additionally, palaeomagnetic measurements and fossils analyses of nearly continuous aeolian deposits on the inland Loess Plateau (Guo et al., 2002 <sup>[224]</sup>, 2008 <sup>[225]</sup>) and  $\delta^{13}C$  and  $\delta^{18}O$  estimates in sediments along the northern slope of Tibetan plateau (Kent–Corson et al., 2009 <sup>[247]</sup>) revealed the existence of a large source areas of aeolian dust (the central Asian desertification) and energetic winter monsoon winds since ~22 Ma. A shift to wetter conditions near the Oligocene–Miocene boundary was also inferred based on pollen assemblages, with an increase of deciduous broad-leaved trees and a decrease in the proportion of xerophytes (Wang et al., 1999 <sup>[198]</sup>; Jiang and Ding, 2009 <sup>[248]</sup>).

Enhanced sedimentation rates since ~33 Ma was revealed in the offshore fans (e.g., the Mekong River in Clift et al., 2004 <sup>[245]</sup> and Indus River in Clift and Gaedicke, 2002 <sup>[246]</sup> and Clift et al., 2008 <sup>[199]</sup>), as firstly documented and described by Métivier et al. (1999) <sup>[166]</sup> (Figure 1.34A). Sedimentation rate acceleration was related to the strong Himalayan/Tibetan orogen and gradual global cooling. A strengthened monsoon was also invoked to partially explain this accelerating sedimentation rate since at least ~23 Ma (Clift et al., 2006 <sup>[167]</sup>) (Figure 1.34B). Also, continuous global cooling eventually led to the occurrence of vast Holocene glaciation, strengthening further the erosion on the plateau (Owen et al., 2009 <sup>[249]</sup>; Fu et al., 2013a <sup>[250]</sup>). Clift et al. (2008 <sup>[199]</sup>, 2014 <sup>[237]</sup>) also pointed out a drawdown of precipitation during since ~10 Ma until the reinforcement of summer precipitation and intensification of seasonality from Pliocene (Allen and Armstrong, 2012 <sup>[214]</sup>) (Figure 1.34B). Based on sediments recovered at Ocean Drilling Program (ODP) Sites 1146 and 1148 in the continental margin in the northern South China Sea (positions seen in Figure 1.33), some most robust proxies of physical erosion and chemical weathering, apart from the sedimentation rate evidences, demonstrate clearly a weakening summer monsoon since at least 10 Ma to ~5 Ma (e.g., Clift et al., 2014 <sup>[237]</sup>) (Figure 1.35).

Some recent studies from Jianchuan basin proposed a much older onset of ITCZ-induced tropical monsoon by revealing a transition at ~36 Ma from a precedent arid aeolian sedimentation context (Zheng et al., 2021<sup>[251]</sup>) to a wetter lacustrine/palustrine condition (Sorrel et al., 2017<sup>[252]</sup>). New Eocene paleoenvironmental records from central Yunnan (~26°N) also demonstrated a sudden switch from a dry environment to a seasonally wet condition at 41 Ma (Fang et al., 2021<sup>[220]</sup>), due to northward expansion of ITCZ-induced tropical monsoon. Plant fossil taxa discovered in the Lunpola basin of the Central Tibetan Plateau suggested a Middle Eocene (~47 Ma) humid subtropical ecosystem in a lowland valley between highland Gangdese and Tangula mountains (e.g., Su et al., 2020<sup>[97]</sup>). Oxygen isotope study in gastropod shells and mammal teeth from Myanmar, and aeolian dust deposition in northwest China revealed modern-like Eocene monsoonal rainfall, also supported by climate simulations (Licht et al., 2014<sup>[253]</sup>). Modelling showed that the previous idea of zonal-like arid desert/steppe climate band from northwest to southeast across the whole Chinese continent has been proposed to in presence in the Early Eocene, rather than until Oligocene–Miocene transition, and the zonal arid band probably disappeared in the Late Eocene due to increased precipitation over East China (Li et al., 2018<sup>[208]</sup>).

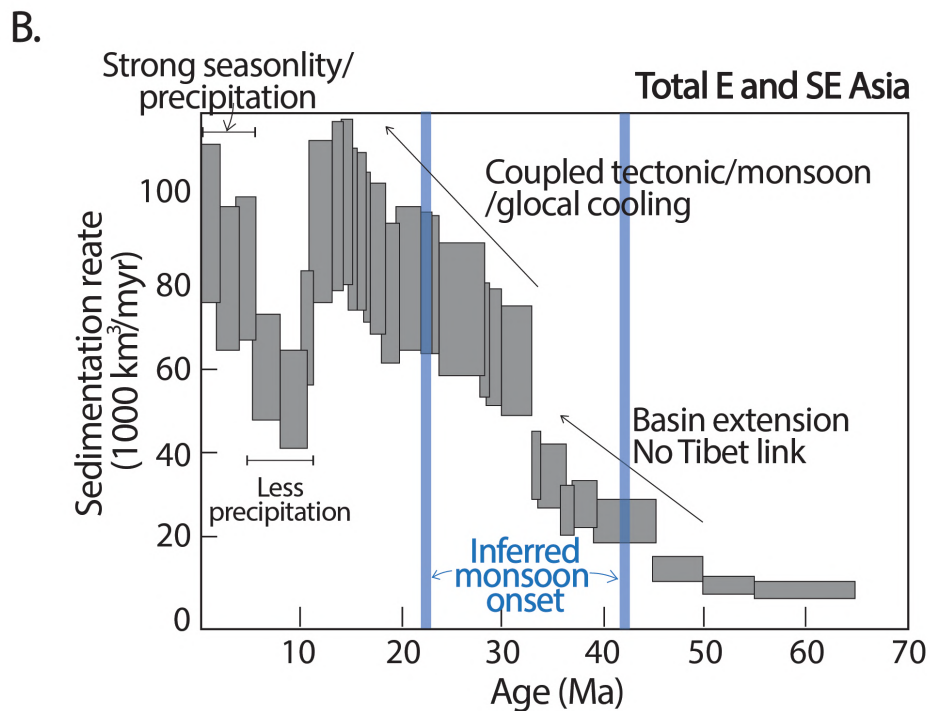
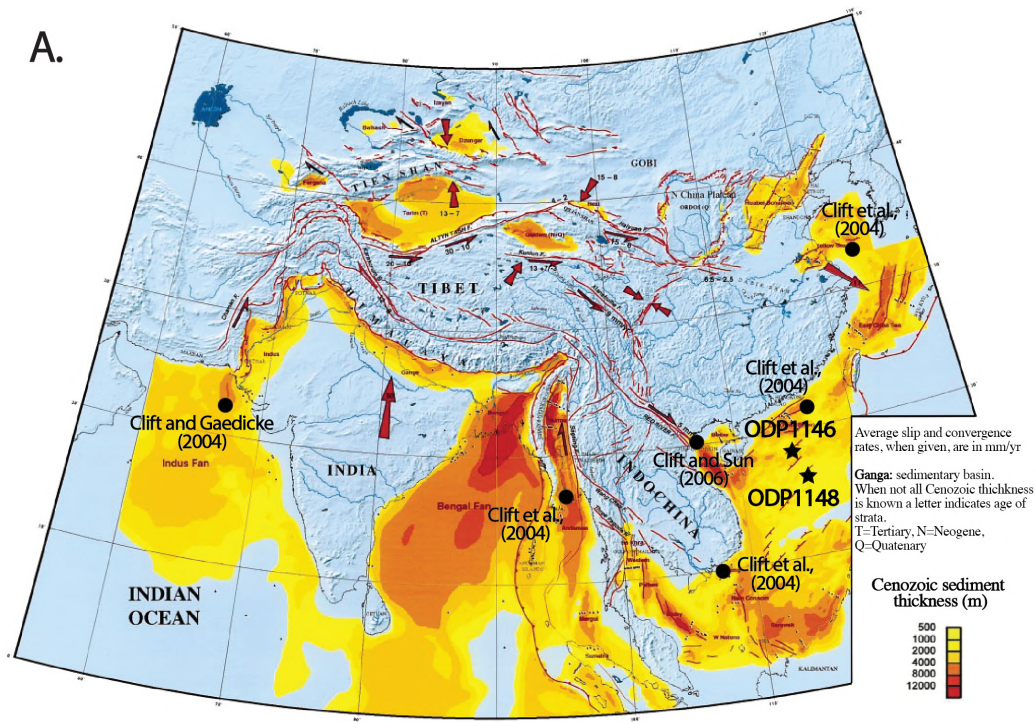


**Figure 1.34** - (A) Sedimentary thicknesses in epicontinental marine basins in south and east Asia. Arrows indicate present-day (India/Siberia, Shanghai) rates of displacement and shortening. Modified from [Métivier et al. 1999](#) <sup>[166]</sup>. (B) Integrated sediment budget and inferred total sedimentation rates for Mekong/Nam Con Son Basin, Gulf of Thailand/Pattani, Malay, West Natuna Basins, South China margin/Pearl River Mouth Basin, Red River/Yinggehai-Song Hong Basin, Indus Fan, revealing the net flux of material from Asian continent into the marginal marine basins, modified from [Clift et al. 2006](#) <sup>[167]</sup>.

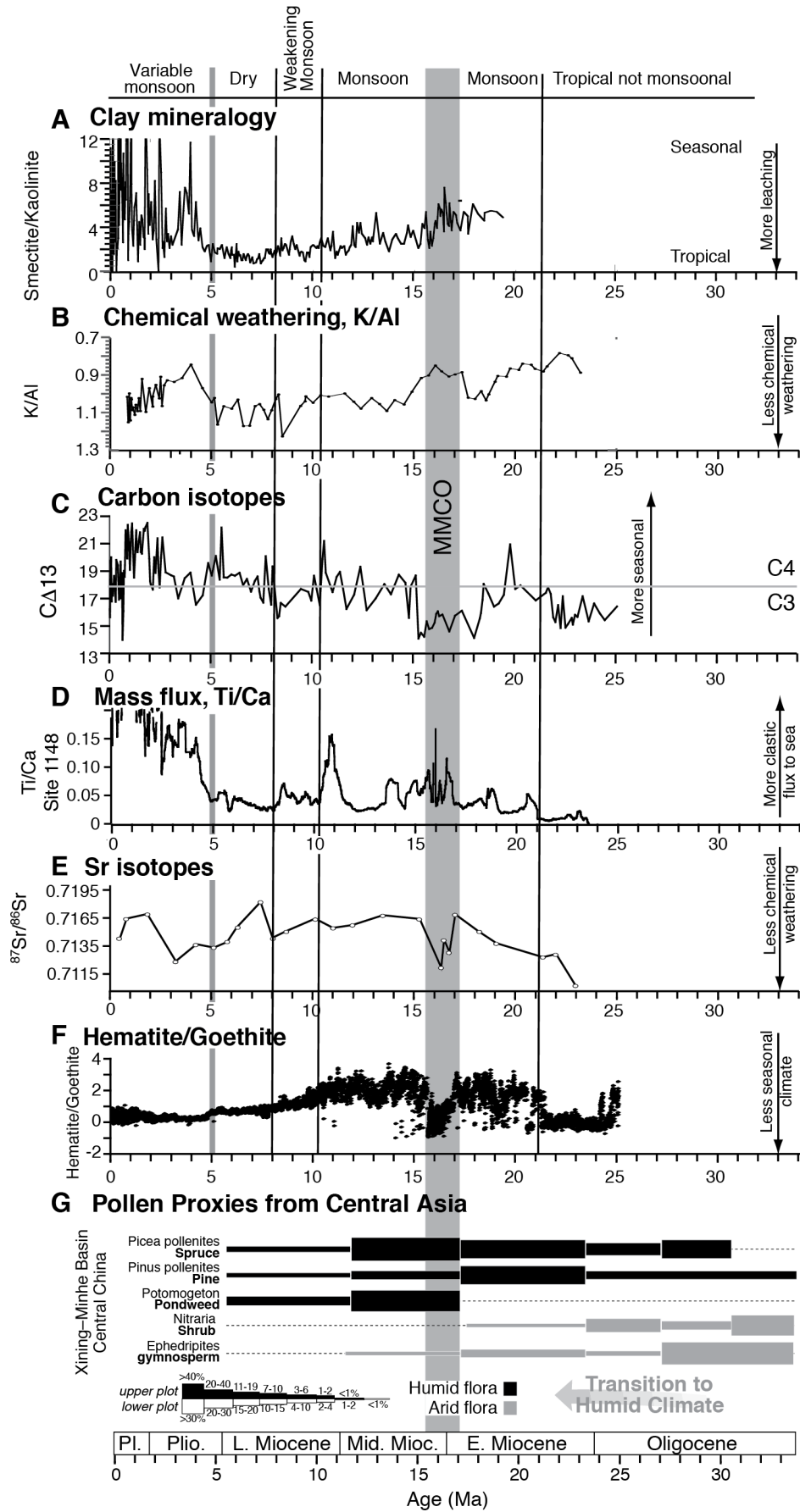


**Figure 1.35** – Compilation of physical erosion and chemical weathering proxies since 25 Ma at ODP Sites 1146 and 1148. (A) Kaolinite/(illite + chlorite). (B) K/Rb as a measure of chemical weathering intensity. (C) Carbon isotopes from black carbon from ODP Site 1148 representing regional terrestrial biomass. (D) Scanned Ti/Ca from ODP Site 1148. (E) Sr isotopes from ODP Site 1148. (F) the CRAT proxy (ratio of hematite/goethite) tracking the relative influence of chemical weathering versus physical erosion. (G) Pollen proxies from central Asia. All those proxies show a clear weakening monsoon between ~10–5 Ma. MMCO: Middle Miocene Climate Optimum (~15.5–17.2 Ma). Taken from [Cilft et al. 2014](#) <sup>[237]</sup>.

### 1.7.3.2 Glaciation development in southeast Tibet

Glacial erosion and related periglacial processes have been proposed to strongly modulate plateau landscapes, through erosive processes related to gravitational movements of ice caps, trellis valley glaciers and piedmont glaciers ([Brozovic et al., 1997](#) <sup>[254]</sup>; [Hales and Roering, 2009](#) <sup>[255]</sup>). High mountainous topography or outermost zone of ice caps are characterized by strongly eroded glacial valleys, generating significant topographic reliefs, as observed in Gonggashan and Kawagebo massifs ([Figure 1.16B](#), [Figure 1.36A](#)). Erosion of rocks underneath glaciers is favored by temperatures close to zero and sufficient ice thickness, through plucking or quarrying underlying rocks, subglacial meltwater or abrasion by rocks embedded in ice. Meanwhile regions covered by ice caps are generally flat at high elevation, with scoured terrain surfaces, suggesting that ice flows across the broad plateau with plucking and abrasion on rock surfaces and reduces local topographic relief, as observed in Daocheng and Jaggai massif ([Figure 1.19](#), [Figure 1.36B](#)), albeit with less important glacial erosion when compared to valley glaciers ([Heyman et al., 2009](#) <sup>[256]</sup>; [Fu et al., 2012](#) <sup>[257]</sup>, [2013a](#) <sup>[250]</sup>). The glaciation is extremely sensitive to the climate fluctuation. When greenhouse progresses, icemelts introduce river discharge of high amplitude, which intensely enhances downstream fluvial incision and sediment transport. Furthermore, as ice masses and glaciers repeatedly advance and retreat during the glacial and interglacial alternating, glacial landscapes shall be significantly enhanced ([Menzies, 2018](#) <sup>[258]</sup>).

Although extent and impact of glacial and periglacial erosion within the southeast Tibetan Plateau prior to the Quaternary is rarely clarified, it's widely recognized today that this region has experienced extensive glaciation since at least the late Pliocene, as demonstrated by erosional and depositional evidences originating from ice caps and valley glaciers during global Last Glacial Maximum ([Shi et al., 1986](#) <sup>[259]</sup>; [Owen et al., 2002](#) <sup>[260]</sup>, [2005](#) <sup>[261]</sup>; [Zheng et al., 2002](#) <sup>[262]</sup>; [Heyman et al., 2009](#) <sup>[256]</sup>, [2011a](#) <sup>[263]</sup>, [2011b](#) <sup>[264]</sup>; [Morén et al., 2011](#) <sup>[265]</sup>; [Fu et al., 2012](#) <sup>[257]</sup>; [2013a](#) <sup>[250]</sup>, [2013b](#) <sup>[266]</sup>). Previously, a large ice cap in Daocheng massif during the maximum glaciation, covering a surface of 3600 km<sup>2</sup> with a thickness up to 800 m, has been also reconstructed, corresponding to the most exemplary low-relief surface of southeast Tibet ([Li et al., 1996](#) <sup>[267]</sup>) ([Figure 1.36B](#)). A former coexistence of a small-scale of ice cap and

valley glaciers could be observed from present-day geomorphology in Baimaxueshan massif, facing the strongly glacially eroded Kawagebo massif across the Mekong River. The most effective glacial erosion is present near the glacial equilibrium line altitudes (ELAs), where net ice production and melting are roughly balanced, with a maximum ice sliding velocity (Kessler et al., 2006 [268]). Mean ELAs in southeast Tibet were suggested to lie near elevations of ~4400–4500 m, close to the mean elevation of plateau surface (Fu et al., 2012 [257], 2013a [250]; Zhang et al., 2016 [121]). Although the most striking landscapes generated by vigorous glacial erosion are the sharp topographic contrast between towering peaks and U-shaped valleys, evidences also demonstrated the capacity of glaciation to smooth topography and reduce relief (Egholm et al., 2009 [269]; Oskin and Burbank, 2005 [270]). In southeast Tibet, “buzzsaw-like” glacial erosion have been suggested to smooth *in-situ* the local relief of formerly mountainous landscapes, and participate significantly in the development of low-relief surfaces on the high-elevation plateau (Liu-Zeng et al., 2008 [100]; Zhang et al., 2016 [121]), which were not necessarily uplifted from a flat lowland as previously proposed (Clark et al., 2006 [126]).

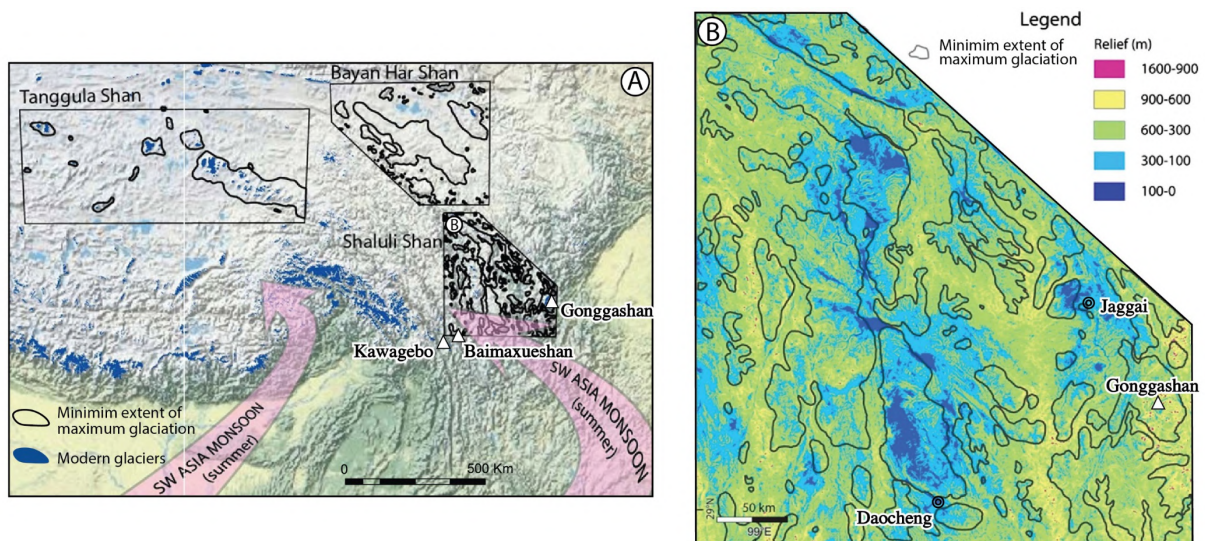


**Figure 1.36** – (A) Reconstructed minimum extent of maximum glaciation on the southeast and central Tibet, with Tanggula Shan taken from Morén et al. (2011) [265]; Bayan Har Shan taken from Heyman et al. (2009) [256] and Shaluli Shan taken from Fu et al. (2012) [257]. (B) Minimum extent of maximum glaciation in Shaluli Shan (southeast Tibet), wrapped on relief map. Modified from Fu et al. (2013a) [250].

## 1.8 Interaction between tectonics, climate and landscape evolution of the orogenic mountain ranges and plateaux

The most significant surface uplift and topography gain take place principally in the convergent tectonic context, which also demonstrates the strongest erosion and exhumation, exposing deep metamorphized materials (Willett, 1999<sup>[271]</sup>). Therefore, physical interactions between the tectonic growth of topography, erosional destruction of topography and climatic influence on erosion patterns and rates influence fundamentally the landscape evolution of mountain belts, orogenic plateau and continental interiors (Willett et al., 2006<sup>[272]</sup>; Molnar, 2003<sup>[48]</sup>; Reiners et al., 2003<sup>[273]</sup>; Whipple, 2009<sup>[274]</sup>). Enhanced relief created by tectonic processes (Figure 1.37A, B) would increase river channel gradients and subsequently strengthen erosion rates. Additionally, high topography would generate orographically enhanced precipitation on the windward side of ranges, contributing to larger discharge in the river networks and stronger fluvial erosion (Reiners et al., 2003<sup>[273]</sup>) (Figure 1.37C). High topography creates a “rain shadow”, when moistures could not successfully travel above a certain elevation (Barry, 1981<sup>[275]</sup>), significantly reducing precipitation on the leeward side. When mountains or plateau grows above a certain altitude threshold (e.g., equilibrium limit altitude), glaciation will efficiently erode and remarkably modulate surface landscapes (e.g., Brozovic et al., 1997<sup>[254]</sup>; Hales and Roering, 2009<sup>[255]</sup>; Zhang et al., 2016<sup>[121]</sup>) (Figure 1.37D). Expanding drainage area of a catchment and increasing river discharges would strengthen the channel incision (Figure 1.37E). Since the elevation of river channels defines local base level for hillslope processes, enhanced downward incision of channels increases apparently possibility of hillslope failure (Figure 1.37F). Although bedrock channel incision has been long recognized to dominate the landscape evolution in response to tectonic or climatic variation (Howard et al., 1994<sup>[276]</sup>; Whipple and Tucker, 1999<sup>[277]</sup>; Sklar and Dietrich, 2001<sup>[278]</sup>; Hartshorn et al., 2002<sup>[279]</sup>), hillslope processes in hilly and mountainous regions, including landslide, soil creep, debris flow, solifluction and rock fall, could play a nonnegligible role in governing landscape evolution through time (Burbank et al., 1996<sup>[280]</sup>; Hovius et al., 1997<sup>[281]</sup>). Hillslope erosion processes generate and deliver sediments to channels, which serve as tools for erosion, as in “detachment-limited” rivers, or as a cover protecting the underlying bedrock from erosion, as in “transport-limited” rivers.

Erosional feedback on tectonic deformation and topography construction, especially in orogenic mountains and plateaux, is principally influenced by gravitational stresses, which vary largely with

respect to redistribution of near-surface mass through erosion (Figure 1.37H). Meanwhile, the tectonic response to erosion is very complex in different circumstances. Small scale orogenic belts, such as the arc-continent collision in Taiwan (e.g., Suppe, 1980<sup>[282]</sup>; Barr and Dahlen, 1991<sup>[283]</sup>), the Southern Alps in New Zealand (Adams, 1980<sup>[284]</sup>; Norris et al., 1990<sup>[285]</sup>; Koons, 1989<sup>[286]</sup>) and Cascadia forearc high (Brandon et al., 1998<sup>[287]</sup>), where strong erosion rates due to high precipitation balance the convergence-induced surface uplift, nearly reaching to a steady-state and dominantly sculpting the size and physiology of the orogenic mountains (Willett, 1999<sup>[271]</sup>). In contrast, limited erosion due to strengthened aridity and tectonic quiescence inside continent or plateau interior would reduce the topographic relief and sustain a steady-state landscape for several tens million years, as in the Altiplano and central Tibet (e.g., Sobel et al., 2003<sup>[105]</sup>; Liu-Zeng et al., 2008<sup>[100]</sup>). If erosional fluxes outpace tectonic crustal deformation and thickening, mean elevation of orogenic belts or plateaus will be progressively reduced, leading to erasing of constructed tectonic topography (Figure 1.37I). Meanwhile, enhanced surface erosion potentially leads to nonnegligible isostatic rebound of continental crust and eventually flexural surface uplift and/or topographic reliefs, without requiring tectonic forcing (Molnar and England, 1990<sup>[288]</sup>).

Large scale tectonics growth could modify global climate, for example, the Tibetan Plateau growth gives birth to strong monsoonal precipitation in neighboring regions and aridification in the others (e.g., Boos and Kuang, 2010<sup>[217]</sup>; Farnsworth et al., 2019<sup>[289]</sup>; Tardif et al., 2020<sup>[290]</sup>). By feedback, resulting strong erosion could also affects global climate, through perturbation on the carbon cycle, when physical erosion exposes fresh rock and promotes chemical weathering of Mg and Ca silicate rocks, (e.g., Pagani et al., 2005<sup>[291]</sup>; Maher and Chamberlain, 2014<sup>[292]</sup>; Torres et al., 2014<sup>[293]</sup>) (Figure 1.37G).

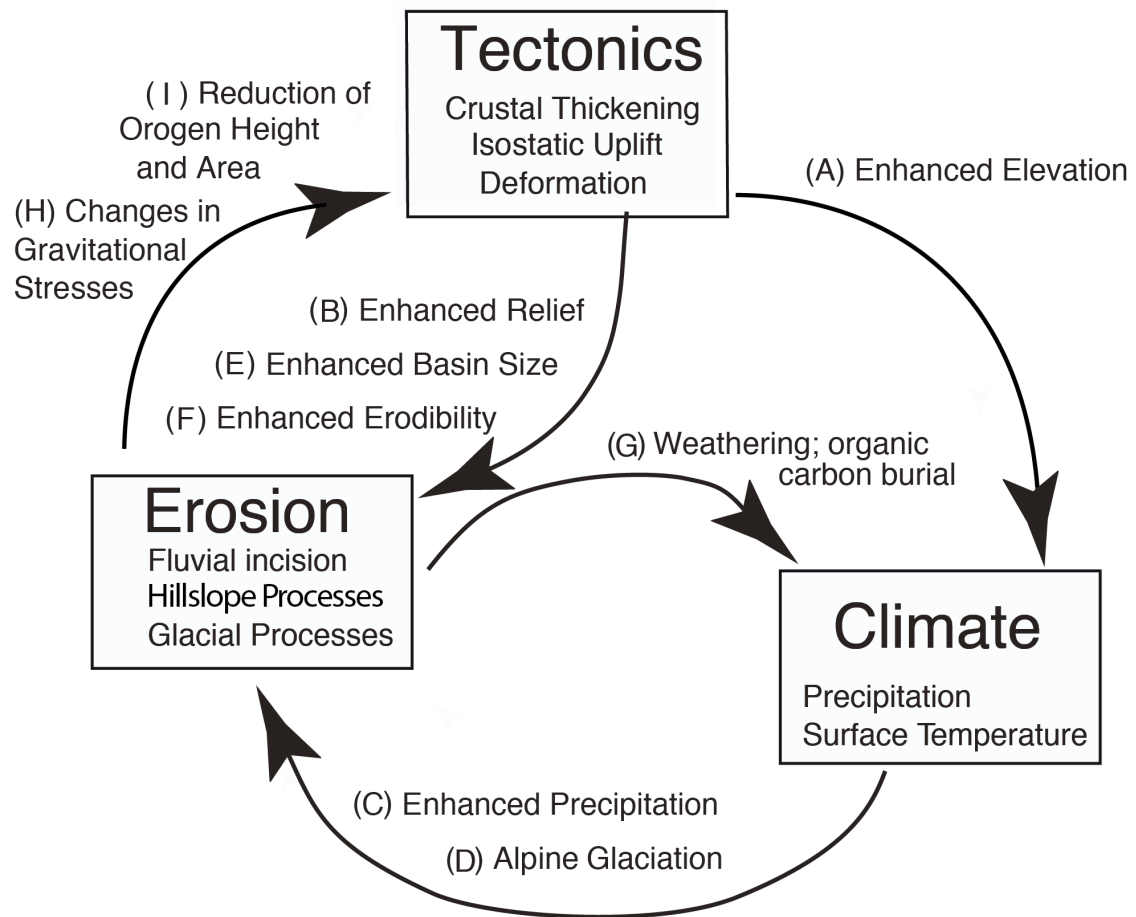


Figure 1.37 - Illustration of the feedback loop among three fundamental surface processes: tectonics, climate, and erosion, modified from Willett et al. (2006)<sup>[272]</sup>.

## 1.9 Strategy and objects of thesis

Significant topographic contrasts are present between the central interior, plateau margins and southeastern region, where different tectonics and climate regimes operate together to shape this characteristic landscape (Fielding, 1994<sup>[11]</sup>; Liu-Zeng et al., 2008<sup>[100]</sup>). Along southern margin of the Himalayas, remarkable reliefs with an elevations rising from ~200 m to >8000 m over less than 250–km-distance and strong uplift rates of several millimeters per year (e.g. Lavé and Avouac, 2001<sup>[294]</sup>; Bettinelli et al., 2006<sup>[295]</sup>; Blythe et al., 2007<sup>[296]</sup>) are observed with precipitations up to several thousands of millimeters per year in its foreland (Bookhagen and Burbank, 2006<sup>[221]</sup>, 2010<sup>[229]</sup>). Strong uplift rates along main tectonic structures prohibit powerful rivers to cross through the Himalayas and force them to remain short courses, deeply downcutting the range. The Longmenshan range demonstrates less significant uplift rates and precipitation (annual rainfall of ~1500 mm/yr), larges rivers are strong enough to penetrate into the hinterland of the range, generating dendritic river networks and lowering the regional averages elevations. The southeast Tibetan Plateau is, to the first order, characterized by a regional coexistence of deeply incising large rivers and neighboring low-relief surfaces at high elevation in the interfluves and headwaters, which is remarkably different from flat plateau interior and highly mountainous plateau rims with abrupt topographic drops. Although different models have been proposed (section 1.5.1.4), the generation of this peculiar topography in southeast Tibet remains still highly debated.

Attempting to contribute to this debate, my works focus on the southeastwardly flowing Mekong and Yalong rivers of southeast Tibet. **Firstly**, I investigate the exhumation histories, on a local scale, of the high-relief (>2000 m) and high-elevation (~6740 m) Kawagebo massif and the low-relief (<600 m), moderate-elevation (~5200 m) Baimaxueshan massif, straddling across the Mekong River in the core region of Three Rivers Region, adjacent to the EHS, in order to answer following questions:

- (1) How was the low-relief topography of the Baimaxueshan massif formed and is it part of the previously defined “relict surfaces”, which were proposed to be formed at low elevation and then uplifted to present-day’s elevation with little denudation (Clark et al., 2005<sup>[138]</sup>)?
- (2) What roles do the regional or local tectonics and river incision play in exhumation histories of both massifs and their contribution to the topography development on a local scale?

- (3) How the tectonics influenced exhumation inside the large knickzone in the middlestream of the Mekong River, locating closely east to the EHS ? or is climatic forcing dominant on exhumation due to strengthened monsoon since Middle Miocene (e.g., [Nie et al., 2018](#)<sup>[154]</sup>)?
- (4) How the exhumation history of the Kawagebo massif reveals a regional west–east compression linked to the indenting EHS, generating important topography in the Three Rivers Region during Eocene–Oligocene, when combined with more regional data?

To answer all these questions, I applied the 3D thermal–kinematic modelling (Pecube, [Braun, 2003](#)<sup>[297]</sup>, [Braun et al., 2012](#)<sup>[298]</sup>) on the existing data of both massifs and combined with our newly collected low temperature thermochronological data during the field mission in 2019 at high elevation of the Kawagebo massif. Several scenarios, including different forcing of tectonic and river incision, have been effectuated to well reconstruct exhumation histories of both massifs.

**Secondly**, in order to better understand the topographic evolution on a large scale of continental plateau in southeast Tibet, we applied a landscape evolution model (FastScape, [Braun and Willett, 2013](#)<sup>[299]</sup>), to the Yalong River catchment as an example. We collected the existing low temperature thermochronology data along the Yalong Thrust Belt, crossing the downstream of the Yalong River, to extract reliable data of tectonic uplift rates. Paleoclimatic data were also carefully compiled to rebuild the climate evolution of southeast Tibet. A collective input of those parameters has then been exploited in different scenarios of the landscape evolution modelling, in order to investigate:

- (5) Whether the previously proposed climatic forcing either by a monsoonal strengthening since the Mid–Miocene Climate Optimum (~17–14 Ma, [Nie et al., 2018](#)<sup>[154]</sup>) or by an enhanced runoff through a drainage–area expansion into the paleo–endorheic zone (since ~15 Ma, [Rohrmann et al., 2018](#)<sup>[169]</sup>) on a pre–existing high plateau, could explain the coexisting deeply incising rivers and neighboring flat surfaces?
- (6) How the tectonic uplift related to different scenarios of thrusting and the temporal and spatial variation in precipitation due to orographic effect on a plateau or monsoon evolution could regulate the topography? Or a combination of both is necessary, together with potential capture of the endorheic zone of the plateau, to explain such a coexistence of deeply incising rivers and neighboring flat surfaces?

The landscape evolution model FastScape, which resolves the fluvial erosion and hillslope processes, could help us to test those different scenarios, imposing all the mentioned important factors during the landscape development.

## CHAPTER 2

# Exhumation, thrusting histories and relief development within the Three Rivers Region (Southeast Tibet)



## 2.1 Contrasting exhumation histories and relief development within the Three Rivers Region (Southeast Tibet)

Ou, X., Replumaz, A., van der Beek, P., 2021. Contrasting exhumation histories and relief development within the Three Rivers Region (south-east Tibet). *Solid Earth* 12, 563–580. <https://doi.org/10.5194/se-12-563-2021>.



Figure 2.1 – The towering Kawagebo massif, viewed from the Baimaxueshan massif across the Mekong River.



### 2.1.1 Abstract

The Three Rivers Region in Southeast Tibet represents a transition between the strongly deformed zone around Eastern Himalayan Syntaxis (EHS) and the less deformed southeast Tibetan plateau margin in Yunnan and Sichuan. In this study, we compile and model published thermochronometric ages for two massifs facing each other across the Mekong River in the core of the Three Rivers Region (TRR), using the thermo-kinematic code Pecube to constrain their exhumation and relief history. Modelling results for the low-relief (<600 m), moderate-elevation (~4500 m) Baimaxueshan massif, east of the Mekong River, suggest regional rock uplift at a rate of 0.25 km/Myr since ~10 Ma, following slow exhumation at a rate of 0.01 km/Myr since at least 22 Ma. Estimated Mekong River incision accounts for 30% of the total exhumation since 10 Ma. We interpret exhumation of the massif as a response to regional uplift around the EHS and conclude that the low relief of the massif was acquired at high elevation (>4500 m), probably in part due to glacial “buzzsaw-like” processes active at such high elevation, and particularly efficient during Quaternary glaciations. Exhumation of the Baimaxueshan is significantly higher (2.5 km since ~10 Ma) than that estimated for the most emblematic low-relief “relict” surfaces of Eastern Tibet, where apatite (U-Th)/He (AHe) ages >50 Ma imply only a few hundreds of meters of exhumation since the onset of the India-Asia collision. The low-relief Baimaxueshan massif, with its younger AHe ages (<50 Ma) that record significant rock uplift and exhumation, thus cannot be classified as a “relict surface”. Modelling results for the high-relief, high-elevation Kawagebo massif, to the west of the Mekong, imply a similar contribution of Mekong River incision (25%) to exhumation, but much stronger local rock uplift at a rate of 0.45 km/Myr since at least 10 Ma, accelerating to 1.86 km/Myr since 1.6 Ma. We show that the thermochronometric ages are best reproduced by a model of rock uplift on a kinked westward-dipping thrust striking roughly parallel to the Mekong River, with a steep shallow segment flattening out at depth. Thus, the strong differences in elevation and relief of two massifs are linked to variable exhumation histories due to strongly differing tectonic imprint.

#### Highlight points:

- Thermo-kinematic modelling of a compiled low-temperature thermochronology dataset shows rapid Quaternary exhumation in the Mekong River knickzone, Southeast Tibet

- Both the amount of Quaternary exhumation and the pattern of river steepness point to a tectonic origin of the knickzone
- The exhumation history and topography around the knickzone are related to localized tectonic uplift associated with a restraining overstep between the Zhongdian and Parlung faults

## 2.1.2 Introduction

Despite its high mean elevation of ~5000 m, Tibet is mainly characterized by low relief (<1 km), with an average slope of ~5° (Fielding et al., 1994<sup>[1]</sup>). However, topographic characteristics vary throughout the Tibetan Plateau. Central and North Tibet are characterized by extensive low-relief surfaces, with narrow, linear, and parallel mountain ranges that rise slightly above the mean elevation of the plateau, defining “positive topography” where elevation is positively correlated with relief and mean slope (Liu-Zeng et al., 2008<sup>[100]</sup>). In those regions, structural relief that was tectonically generated during the collision between India and Asia has been smoothed out locally by internal drainages, which transport sediments from the nearby ranges to fill local intermontane basins, but cannot evacuate sediments out of Tibet (Meyer et al., 1998<sup>[39]</sup>). In contrast, Southeast Tibet is characterised by “negative topography”, where deeply incised valleys are separated by patches of low-relief surfaces at a mean elevation of ~4500 m, slightly lower than the average plateau height (Figure 2.2A). Although only scattered remnants of these surfaces occur in the Three Rivers Region of Southeast Tibet, they gradually become more continuous northward and eventually integrate into the extensive low-relief surfaces of the plateau interior (Figure 2.2B, Figure 2.3A). The most emblematic surface with remarkable low relief occurs on the Triassic Daocheng granite (Figure 2.3A, B), located between the Yangtze and the Yalong rivers draining the southeastern plateau margin in Yunnan/Sichuan (Figure 2.3A). These low-relief surfaces, with <600 m relief in a radius of 5 km, have previously been interpreted as “relict surfaces”; i.e., remnants of a paleo-landscape that was formed at low elevation and subsequently uplifted (Clark et al., 2005a<sup>[138]</sup>; 2006<sup>[126]</sup>). No such low-relief relict surfaces are observed further west, between the Salween River and the Eastern Himalayan syntaxis (Figure 2.2B, Figure 2.3A).

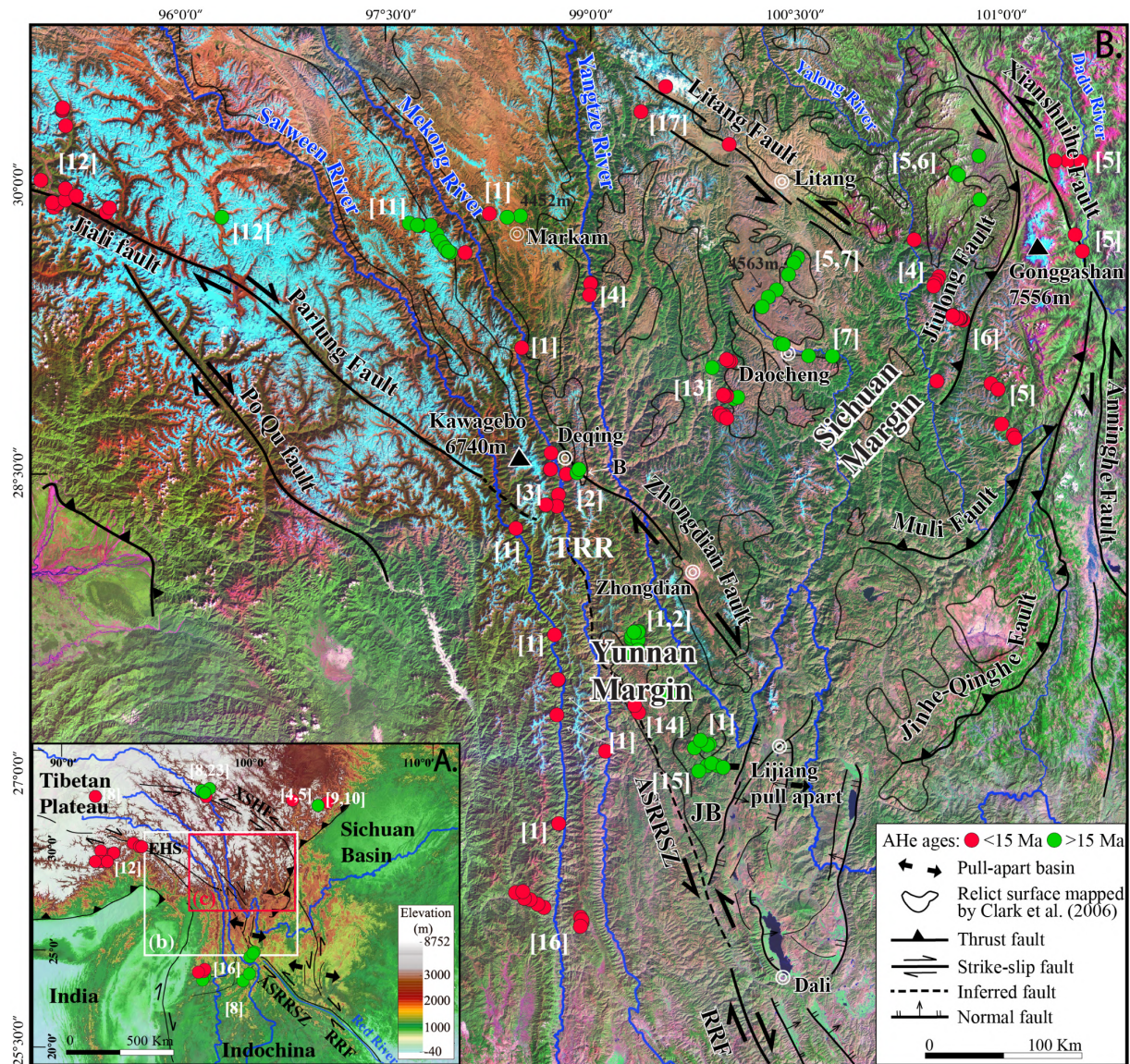


**Figure 2.2** – Tectonic and geomorphic setting of Southeast Tibet. (A) Topography and tectonic framework of the central and eastern Tibetan Plateau, based on GTOPO30 Digital Elevation Model (DEM). White box shows extent of Figure 2.2A; red box shows extent of Figure 2.3A. (B) Main faults, rivers, relict surfaces and Apatite (U-Th)/He (AHe) data, overlain on Landsat image mosaic of Southeast Tibet (USGS). Apatite (U-Th)/He (AHe) are from [1] Yang et al. (2016) [150], [2] Liu-Zeng et al. (2018) [157], [3] Replumaz et al. (2020) [151], [4] Ouimet et al. (2010) [143], [5] Clark et al. (2005a) [138], [6] Zhang et al. (2016) [121], [7] Tian et al. (2014) [139], [8] Nie et al. (2018) [154], [9] Godard et al. (2009) [158], [10] Wang et al. (2012) [120], [11] Xiao et al. (2015) [159], [12] Zeitler et al. (2014) [160], [13] Gourbet et al. 2019 [161], [14] Cao et al. (2020) [122], [15] Shen et al. (2016) [149], [16] Wang et al. (2018) [162], [17] Zhang et al. (2015) [156]. Abbreviations: ASRRSZ: Ailaoshan-Red River Shear Zone, B: Baimaxueshan, EHS: Eastern Himalaya Syntaxis, JB: Jianchuan Basin, RRF: Red River fault, TRR: Three Rivers Region, XSHF: Xianshuihe fault.

Samples collected from these low-relief surfaces in southeast Tibet show much older thermochronometric ages than samples from the deep river valleys that dissect them (Figure 2.2B). The Daocheng plateau and other low-relief surfaces of the Yunnan/Sichuan margin are characterized by apatite (U-Th)/He (AHe) ages >50 Ma and apatite fission track (AFT) ages >100 Ma, whereas samples collected from the gorges of the Dadu, Yalong and Yangtze rivers show AHe ages <15 Ma and AFT ages <50 Ma (e.g., Clark et al., 2005a<sup>[138]</sup>; Ouimet et al., 2010<sup>[143]</sup>). These data have been interpreted as recording a regional rapid incision phase starting between ~13 and 9 Ma in Eastern Tibet, which was considered a proxy for widespread plateau uplift shortly preceding this incision (Clark et al., 2005a<sup>[138]</sup>; Ouimet et al., 2010<sup>[143]</sup>). However, the direct link between river incision and regional tectonic uplift has been challenged by others, who argued for a delay between crustal shortening, occurring mostly in the Eocene, and significant incision mostly during the Miocene in southeast Tibet (Liu-Zeng et al., 2008<sup>[157]</sup>). A purely climatic forcing on river incision by intensified monsoonal precipitation at ~17 Ma was proposed by Nie et al. (2018)<sup>[154]</sup>. Other thermochronologic studies have also provided evidence for earlier phases of rapid exhumation, the timing of which varies regionally between 30–20 Ma in the Longmenshan (Godard et al., 2009<sup>[161]</sup>; Wang et al., 2012<sup>[120]</sup>; Tian et al., 2013<sup>[70]</sup>, 2015<sup>[145]</sup>; Tan et al., 2014<sup>[300]</sup>), to 40 – 30 Ma in the Yalong thrust belt (Zhang et al., 2016) and ~60–~40 Ma in the Baimaxueshan massif (Liu-Zeng et al., 2018<sup>[157]</sup>). The latter has been linked to uplift of the Southeast Tibetan plateau, consistent with paleo-elevation data implying that the plateau has been close to its present-day elevation since the Late Eocene – Oligocene (Hoke et al., 2014<sup>[211]</sup>; Li et al., 2015<sup>[179]</sup>; Wu et al., 2018<sup>[212]</sup>).

An inherent problem with thermochronology data is that they do not provide direct information on (either rock- or surface-) uplift (Molnar and England, 1990<sup>[288]</sup>; Reiners, 2007<sup>[301]</sup>). However, such data do potentially provide constraints on paleo-relief (Braun, 2002<sup>[302]</sup>; Reiners, 2007<sup>[301]</sup>) and careful thermo-kinematic modelling of thermochronological datasets may allow differentiating between regional exhumation, presumably related to rock uplift, and relief change through valley incision (e.g., Valla et al., 2010<sup>[303]</sup>; 2011<sup>[304]</sup>). Spatial patterns of thermochronological ages also potentially allow constraining the kinematics of rock exhumation and the underlying fault geometry at depth (e.g., Robert et al., 2011<sup>[305]</sup>; Braun et al., 2012<sup>[298]</sup>).

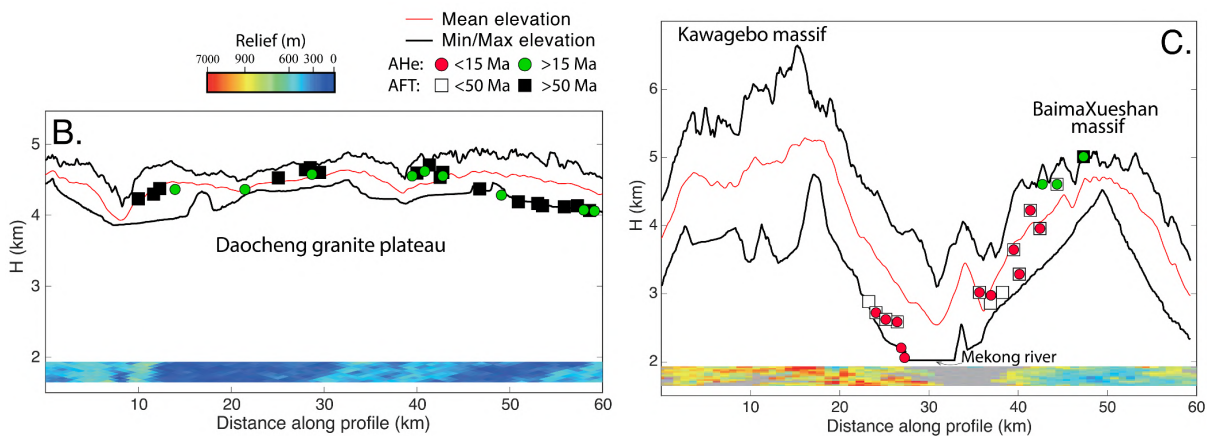
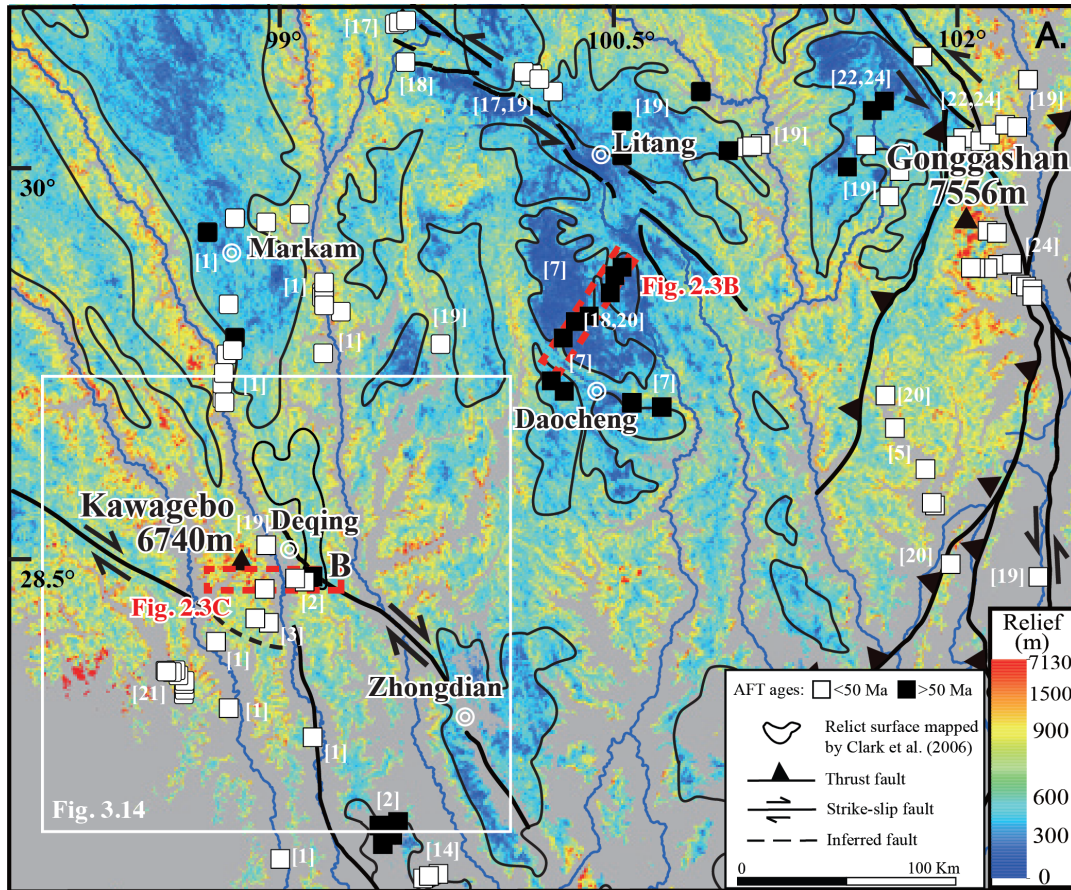


**Figure 2.3** – (A) Relief map (modified from Zhang et al., 2015<sup>[156]</sup>), derived from 30-m resolution DEM; 1-km radius relief is shown for pixels at elevations >3500m above sea level. Black outlines delimit low-relief relict surfaces with relief <600 m, as mapped by Clark et al. (2006)<sup>[126]</sup>. Note that some averaging of the relief across the relict surface and active landscape occurs at the edges of the relict surface. In these areas local relief can be as high as 1 km. Two red rectangles represent topographic profile and relief shown in B, C. Apatite Fission track (AFT) ages are from [1] Yang et al. (2016)<sup>[150]</sup>, [2] Liu-Zeng et al. (2018)<sup>[157]</sup>, [3] Replumaz et al. (2020)<sup>[151]</sup>, [4] Ouimet et al. (2010)<sup>[143]</sup>, [5] Clark et al. (2005a)<sup>[138]</sup>, [7] Tian et al. (2014)<sup>[139]</sup>, [17] Zhang et al. (2015)<sup>[156]</sup>, [18] Reid et al. (2005a)<sup>[163]</sup>, [19] Wilson and Fowler (2011)<sup>[144]</sup>, [20] Lai et al., (2007)<sup>[164]</sup>, [21] Lei et al. (2006)<sup>[165]</sup>, [22] Zhang et al. (2017)<sup>[140]</sup>, [24] Xu and Kamp (2000)<sup>[135]</sup>. (B), (C) Topographic profiles across Daocheng granite plateau, Kawagebo and Baimaxueshan massifs, respectively, showing local topography and relief with available thermochronometric ages. Note that these two panels share the same legend.

In this paper, we use the thermo-kinematic modelling code Pecube (Braun et al., 2012<sup>[298]</sup>) to quantify both river incision and structurally controlled rock exhumation, based on a dense thermochronologic dataset from the Three Rivers Region. The Three Rivers Region forms the transition between the Eastern Himalayan syntaxis and the southeast margin of the Tibetan plateau in Yunnan/Sichuan, where the Salween (Nu), Mekong (Lancang) and Yangtze (Jinsha) rivers run closely parallel to each other over hundreds of kilometers and deeply dissect the plateau margin (Figure 2.2B). The narrow spacing between the rivers has been interpreted as resulting from strong lateral shortening in response to indentation of the Indian-plate corner (Hallet and Molnar, 2001<sup>[116]</sup>; Yang et al., 2015<sup>[117]</sup>). This transition region, separating areas without low-relief surfaces to the west and southwest from areas with extensive low-relief surfaces to the east and north, is key to better understand plateau-growth mechanisms and the geodynamic processes operating both within the high strain zone around the syntaxis and within the lower strain zone of the Yunnan/Sichuan margin (Figure 2.2B).

In the core of this region, the Mekong River separates the Kawagebo massif (max. elevation 6740 m) to the west from the Baimaxueshan massif (max. elevation ~5400 m) to the east. The Baimaxueshan massif corresponds to the southern prolongation of the elongated low-relief surface of Markam (mean elevation ~4500 m), located upstream between the Yangtze and the Mekong rivers; both were mapped as relict surfaces by Clark et al. (2006)<sup>[126]</sup> (Figure 2.3A, C). The Kawagebo massif is thought to have been rapidly exhumed recently (<10 Ma) due to motion on a local thrust fault in a restraining bend between two regional-scale strike-slip faults (Replumaz et al., 2020<sup>[151]</sup>) (Figure 2.2B, Figure 2.3A). Here, we quantify the exhumation history of the low-relief Baimaxueshan massif during the collision period to identify the different roles played by regional rock uplift and river incision and we compare it with the exhumation history of the high-relief Kawagebo massif, while constraining the geometry of the crustal fault responsible for uplifting the latter.

## 2.1.3 Geologic setting

### 2.1.3.1 Cenozoic tectonic evolution of Southeast Tibet

At the regional scale, the mean elevation between the Eastern Himalayan syntaxis and the Mekong River (>5000 m) is higher than the mean elevation of the low relief surfaces east of the river (~4500 m), suggesting stronger shortening and crustal thickening around the syntaxis (Figure 2.2A, B).

Within this zone, the Kawagebo massif, near the city of Deqing, peaks at 6740 m and towers over the plateau by more than 1700 m. Across the Mekong River in this area, a remarkable topographic and geomorphologic contrast is observed between the Kawagebo massif to the west, showing a high topography, high-relief and rugged landscape (Figure 2.3A, Figure 2.4C), and the Baimaxueshan massif to the east, characterised by an elevation close to the mean plateau elevation (~4500 m) and low relief (Figure 2.3C, Figure 2.4B). Furthermore, deeper and larger U-shaped glacial valleys are observed in the Kawagebo massif than in the Baimaxueshan.

From the late Eocene to the early Miocene, the dominant driver of deformation in southeast Tibet was the extrusion of the Indochina block along the left-lateral AilaoShan-Red River shear zone following the Red River (Figure 2.2A), subsequently inverted along the right-lateral Red River fault since ~5–10 Ma (Leloup et al., 1995<sup>[31]</sup>, 2001<sup>[32]</sup>; Replumaz et al., 2001<sup>[306]</sup>; Fyhn and Phach, 2015<sup>[307]</sup>) (Figure 2.2B). High-temperature thermochronology data from southeast Tibet shear zones show ages mainly between ~34 and ~17 Ma, along the Red, the Salween and the Mekong rivers, which have been linked to this extrusion process (Leloup et al., 2001<sup>[32]</sup>; Wang et al., 2016<sup>[308]</sup>, 2018<sup>[162]</sup>). Compared to the timing of extrusion, no clear estimate for the timing of plateau uplift in the Three Rivers Region has been obtained. Rapid sediment filling of the Jianchuan basin (Figure 2.2B), located downstream of the Three Rivers Region, around 37–35 Ma demonstrates significant erosion and suggests uplift in the source region just predating extrusion (Gourbet et al., 2017<sup>[181]</sup>). The Jianchuan basin subsequently experienced significant exhumation along thrust faults between ~28 and 20 Ma (Cao et al., 2019<sup>[309]</sup>), suggesting regional uplift at that time.

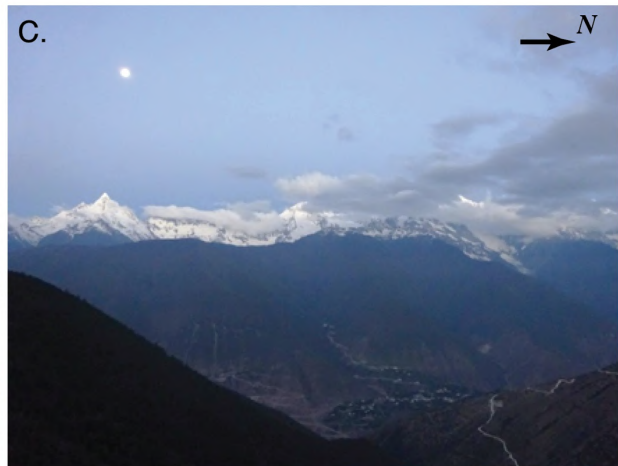
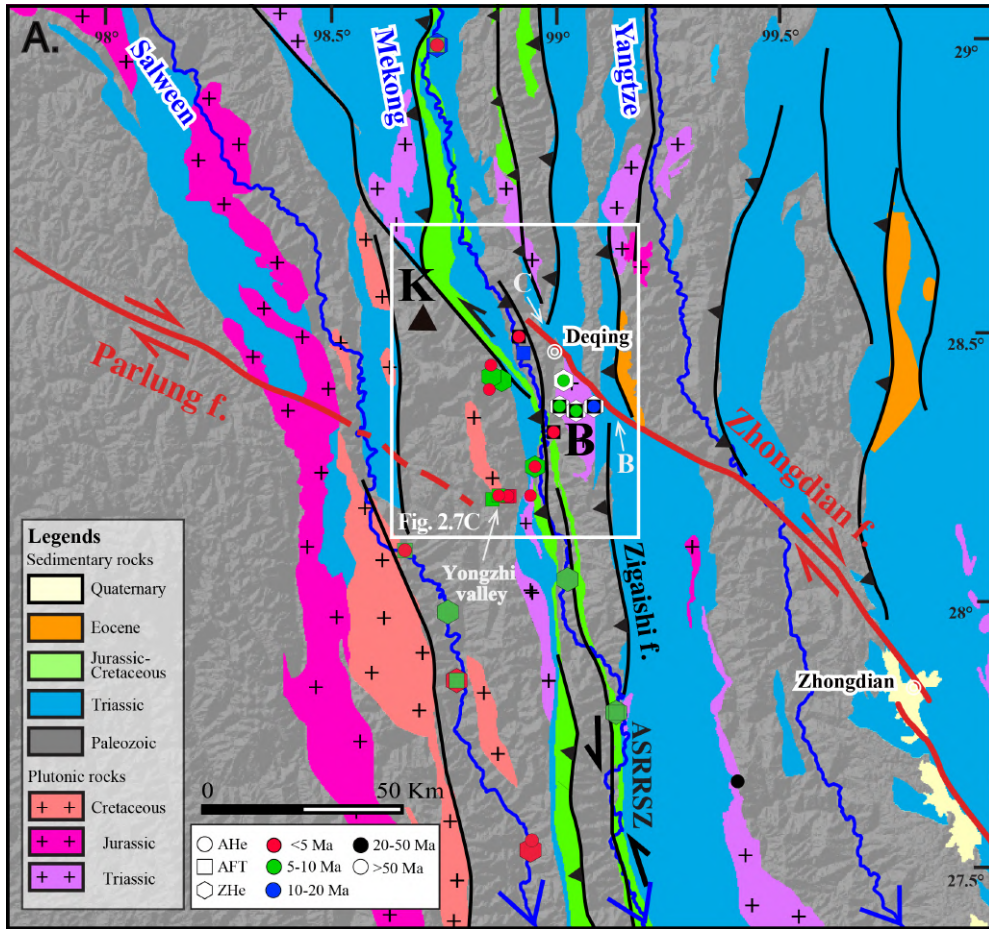


**Figure 2.4** - (A) Geological map of the Kawagebo area in the Three Rivers Region. Active faults are in red, other major faults in black. Thermochronology data are shown with colour according to age and symbol according to method. ASRRSZ: Ailaoshan-Red River Shear Zone, K: Kawagebo massif, B: Baimaxueshan massif. (B) View of the low-relief Baimaxueshan massif at ~4500 m mean elevation, with summits peaking at ~5400 m visible at the background. (C) View of high-relief Kawagebo massif, with summit peaking at 6740 m, while the Mekong River valley lies at ~2000 m elevation, creating almost 5000 m of relief.

In the Three Rivers Region, the AilaoShan–Red River shear zone is prolonged along a distinctive and intensively sheared Jurassic red–wine colored clastic formation, following the Mekong River (Figure 2.2A, Figure 2.4A). Intense shear and deformation is attested by mostly steep to subvertical stratification and fault planes along the Mekong River, particularly in the Jurassic unit (Replumaz et al., 2020<sup>[151]</sup>). Mostly right–lateral sub–horizontal striations have been recognized, incompatible with either motion along the left–lateral AilaoShan–Red River ductile shear zone or thrusting. Parallel to this shear zone along the Mekong River, several thrusts affecting Eocene basins have been observed, but the timing and amount of exhumation related to activity on these thrusts have not been fully quantified (Liu–Zeng et al., 2018<sup>[157]</sup>; Replumaz et al., 2020<sup>[151]</sup>). The roughly north–south trending thrusts and shear zones have been left–laterally offset by regional strike–slip faults, with the most prominent offset occurring north of the Kawagebo massif (Figure 2.4A). Some of these left–lateral strike–slip faults have been reactivated as right–lateral faults, such as the Zhongdian fault crossing the Baimaxueshan massif near Deqing.

Present–day deformation of southeast Tibet is dominated by active right–lateral strike–slip faults, such as the Jiali fault, splitting eastward into the Parlung and PoQu faults (Figure 2.2B), which accommodate overall clockwise rotation around the Eastern Himalayan syntaxis (Gan et al., 2007<sup>[21]</sup>; Bai et al., 2018<sup>[310]</sup>). In the Three Rivers Region, the Parlung fault jumps north–eastward to the Zhongdian fault, uplifting the Kawagebo massif in a restraining overstep since at least ~10 Ma (Figure 2.4A), then jumps south–eastward to the Red River fault, opening the Lijiang pull–apart basin (Replumaz et al., 2020<sup>[151]</sup>).

### **2.1.3.2 Timing and quantification of exhumation and incision along the Mekong River**

In the upper and lower reaches of the Mekong River, AHe ages from the valley bottom cluster around 20–15 Ma and have been interpreted as recording >700 m of river incision in the interval ~17–14 Ma, linked to intensification of monsoonal precipitation (Nie et al., 2018<sup>[154]</sup>). However, Oligocene or earlier (>34 Ma) entrenchment of the lower reach of the Mekong River has previously been proposed, based on river offsets by structures related to the extrusion of Indochina in Burma (Lacassin et al., 1998<sup>[311]</sup>). Regionally, a northward increase in erosion rate along the Mekong River and a westward increase toward the syntaxis since ~10 Ma have been proposed (Yang et al., 2016<sup>[150]</sup>).

In the Baimaxueshan massif, located east of the Mekong River in its middle reach, AHe ages between 5 and 16 Ma, AFT ages between 20 and 60 Ma, and zircon (U-Th)/He (ZHe) ages between ~80 and 120 Ma have been reported by [Yang et al. \(2016\)](#) <sup>[150]</sup> and [Liu-Zeng et al. \(2018\)](#) <sup>[157]</sup>. Age-elevation profiles have been interpreted as recording two rapid phases of exhumation, one between 60 and 40 Ma, interpreted as being linked to the main regional uplift and crustal thickening phase, the other since ~20 Ma, speculated to be linked to regional Miocene river incision ([Liu-Zeng et al., 2018](#) <sup>[157]</sup>). However, quantitative time-temperature modelling of these age-elevation profiles using the 1D QTQt model ([Gallagher, 2012](#) <sup>[312]</sup>) suggests a different scenario, with rapid exhumation only starting at 10 Ma, and no indication of a previous phase of rapid exhumation ([Replumaz et al., 2020](#) <sup>[151]</sup>).

In the Kawagebo massif, also along the middle reach but to the west of the Mekong River, all thermochronometric ages are much younger: AHe ages between 1 and 4 Ma, AFT ages between 3 and 7 Ma, and a single ZHe age at ~8 Ma have been reported from the Mekong valley and its tributary Yongzhi valley ([Yang et al., 2016](#) <sup>[150]</sup>; [Replumaz et al., 2020](#) <sup>[151]</sup>). Quantitative time-temperature inversion of the Kawagebo data suggests rapid exhumation since at least 8 Ma, with no clear estimate of the onset timing, and an acceleration after ~1.5 Ma ([Replumaz et al., 2020](#) <sup>[151]</sup>). Rapid exhumation of the Kawagebo massif has been interpreted to be linked to tectonic uplift along a local thrust fault located along the Mekong River, in a restraining stepover between the Parlung and Zhongdian strike-slip faults ([Replumaz et al., 2020](#) <sup>[151]</sup>) ([Figure 2.4](#)). However, this local thrust fault, inferred to be related to reactivation of regional north-south trending thrusts, has not been documented in the field. Therefore, additional work is needed in this region to resolve the exhumation history of the low-relief mean-elevation Baimaxueshan and the high-relief high-elevation Kawagebo massifs during the India-Asia collision period, in order to distinguish the effects of regional plateau uplift, incision of the Mekong River, and uplift along local tectonic structures.

#### **2.1.4 Methods: thermo-kinematic modelling of multiple thermochronology data**

We synthesized published AHe, AFT and ZHe ages in the Three Rivers Region around Deqing ([Table S. 2.1](#), Supplementary Material) to constrain our thermo-kinematic modelling using Pecube ([Braun et al., 2012](#) <sup>[298]</sup>). This model is designed to solve the three-dimensional heat-transport equation in a crustal block undergoing lateral and vertical rock-particle transport, exhumation, and surface change. The flexural response to surface change is also taken into account, leading to additional rock

uplift and exhumation. Default thermal and flexural parameters are shown in [Table 2.1](#); some of these are optimized during the inversion. In forward mode, this set of model parameters together with a tectonic/geomorphic scenario (exhumation rates, transition times, fault geometry, surface evolution) results in rock–particle paths and an evolving 3D crustal temperature field through time, which are used to predict cooling ages for different thermochronometers. These predicted cooling ages are then compared to measured ages, defining a misfit value  $\phi$  for this set of parameters as expressed by:

$$\phi = \sqrt{\frac{\sum_{i=1}^N \frac{(\alpha_{i,obs} - \alpha_{i,pre})^2}{\sigma_i^2}}{N}} \quad (1)$$

where  $N$  is the number of data points,  $\alpha_{(i,obs)}$  and  $\alpha_{(i,pre)}$  are the observed and predicted ages for data point  $i$ , respectively, and  $\sigma_i$  is the uncertainty on the age for data point  $i$ . Inversion using the Neighbourhood Algorithm is employed to search for a best-fitting geological scenario, i.e., the set of model parameters leading to the minimum misfit value, as well as to define the resolution with which these parameter values can be constrained ([Braun et al., 2012<sup>\[298\]</sup>](#)). Modelling results are represented in scatter plots for different parameter couples and as 1D or 2D marginal probability density functions (pdf's) of each parameter ([Braun et al., 2012<sup>\[298\]</sup>](#)).

Geological scenarios in Pecube take into account temporal variations in exhumation rates and in paleo-topography, separately or combined. Different transition times mark the timing of exhumation or topographic changes between any two different phases. Here, we define a “steady-state topography scenario” as a scenario considering only spatially and temporally varying rock exhumation rates, but sustaining the modern topography without any evolution through time. In contrast, we define an “incision scenario” as a scenario considering a simple topographic evolution from a plateau at a prescribed elevation to the modern topography, with possibly different phases separated by transition times. In order to explore the influence of incision of the Mekong River, we set up an initial plateau at 4500 m elevation, which corresponds to the average elevation of low-relief surfaces in southeast Tibet (e.g. Markam and Daocheng surfaces), evolving toward the present-day topography characterized by the deeply incised Mekong River valley ([Figure 2.4C](#)). A combined scenario starting with a plateau but allowing additional rock exhumation is defined as a “plateau scenario”, where transition times mark the onset timing of river incision from the initial plateau as well as of different exhumation

phases. For the Kawagebo massif, in order to model spatial variations of uplift above a crustal-scale fault rooting at a mid-crustal depth, a 3D fault geometry is implemented following [Robert et al. \(2011\)](#) <sup>[305]</sup>, defining a “tectonic scenario”. In this scenario, the topography is in steady state, and rock exhumation is due to motion along the fault. The fault trace at the surface and the number of segments at depth are fixed parameters in this inversion. The geometry of the fault is represented by different segments, separated by several inflection points, which are defined by their coordinates (r, s), corresponding to the depth and distance relative to the surface trace of fault, respectively. Those coordinates and velocities are inverted to constrain the fault geometry and exhumation history best fitting the thermochronology dataset.

Thermal parameters	Value	Reference	Plate Flexural Parameters	Value	Reference
Crustal thickness	50 km	<a href="#">Yao et al. (2010)</a> <sup>[313]</sup>	Crustal density	2700 kg/m <sup>3</sup>	<a href="#">Braun et al. (2012)</a> <sup>[298]</sup>
Thermal diffusivity	25 km <sup>2</sup> /Ma	<a href="#">Braun et al. (2012)</a> <sup>[298]</sup>	Mantle density	3200 kg/m <sup>3</sup>	<a href="#">Braun et al. (2012)</a> <sup>[298]</sup>
Sea level temperature	25 °C	<a href="#">Bermúdez et al. (2011)</a> <sup>[314]</sup>	Young’s modulus	1.10 <sup>11</sup> Pa	<a href="#">Braun et al. (2012)</a> <sup>[298]</sup>
Atmospheric lapse rate	4 °C/km	<a href="#">Bermúdez et al. (2011)</a> <sup>[314]</sup>	Poisson ratio	0.25	<a href="#">Braun et al. (2012)</a> <sup>[298]</sup>
Crustal heat production	10 °C/Ma	<a href="#">Braun et al. (2012)</a> <sup>[298]</sup>	Equivalent elastic thickness	23 km	<a href="#">Chen et al. (2014)</a> <sup>[316]</sup>
Model basal temperature	900 °C	<a href="#">Wang et al. (2012)</a> <sup>[315]</sup>			

**Table 2.1** – Thermal and flexural parameter values for Pecube modelling.

## 2.1.5 Results

The strong contrasts in elevation, relief, and thermochronological ages between the Baimaxueshan and Kawagebo massifs on the two flanks of Mekong River led us to model their exhumation histories separately. We tested “steady-state”, “incision”, and “plateau” scenarios for both massifs, to resolve the influence of Mekong River incision on their exhumation history ([Table 2.2](#)). For the Kawagebo massif, we additionally tested a “tectonic” scenario implementing a thrust fault with a surface trace along the Mekong River, as recently suggested by [Replumaz et al. \(2020\)](#) <sup>[151]</sup>, aiming to determine its geometry and the contribution of its activity to exhumation in the massif.

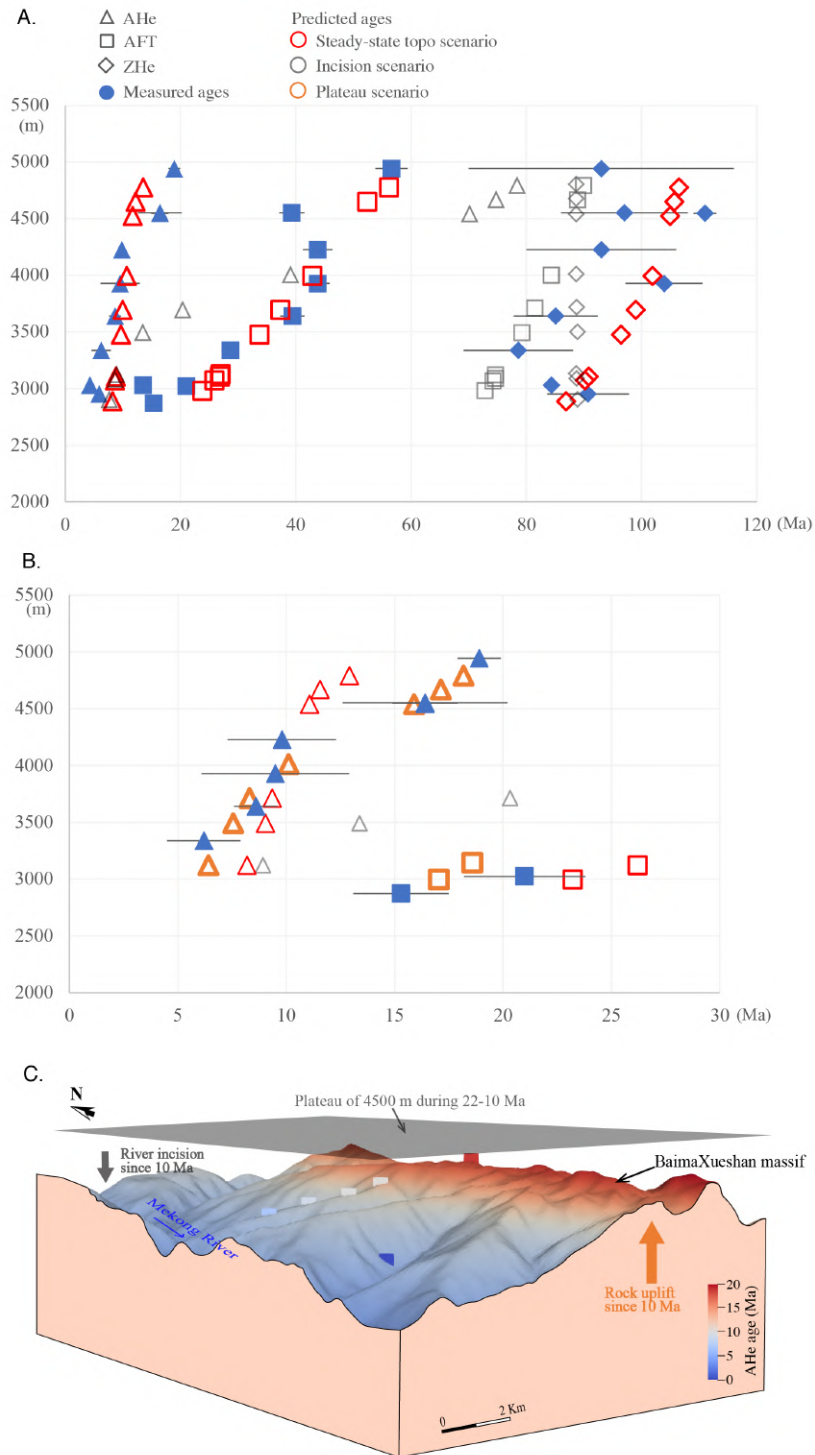
### 2.1.5.1 Baimaxueshan massif

The exhumation history of the Baimaxueshan massif has been modelled using the available data for three thermochronometers (AHe, AFT, ZHe) (Figure 2.5A, Table S. 2.1) from Yang et al. (2016)<sup>[150]</sup> and Liu-Zeng et al. (2018)<sup>[157]</sup>. Models were run for 110 Ma to encompass the full history recorded by these data. We initially ran steady-state topography scenarios (Table 2.2). A model with two exhumation phases, with protracted slow exhumation at a rate of 0.04 km/Myr from 110 to 7 Ma followed by rapid exhumation at a rate 0.42 km/Myr since 7 Ma, fits the entire dataset with a relatively low misfit (3.29). However, the break-in-slope in AFT ages around 40 Ma, marked by three ages at elevations between ~4000 and ~4700 m and interpreted by Liu-Zeng et al. (2018)<sup>[157]</sup> as recording a rapid phase of exhumation, is not reproduced (Figure 2.5A). Moreover, AHe ages >10 Ma, marking a subtle break-in-slope around 4500 m elevation, and AFT ages <25 Ma are not well modelled either in this steady-state topography scenario (Figure 2.5A, B). To test the existence of a rapid exhumation phase around 40 Ma, as proposed by Liu-Zeng et al. (2018)<sup>[157]</sup>, we modelled more complex scenarios with three or four exhumation phases and specified transition times. The best-fitting of these models comprises a four-phase scenario (Table 2.2, Figure S. 2.1), resulting in a slightly lower misfit (3.13) than the previous two-phase scenario. However, none of the more complex models resolve a rapid exhumation phase around 40 Ma; they all result in best-fit models characterized by slow exhumation that accelerated in the last few Myr (<10 Ma), very similar to the two-phase exhumation scenario (Table 2.2). We conclude that the data do not require rapid exhumation prior to the last few Myr and we do not further consider these more complex scenarios.

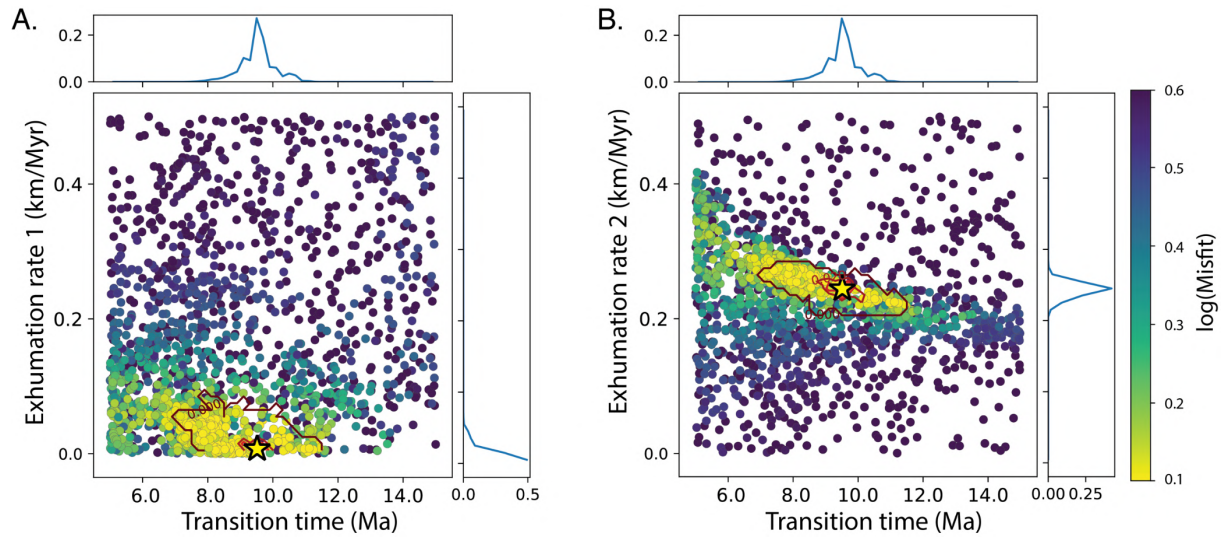
Second, we ran an incision scenario, comprising a plateau at an elevation of 4500 m at the beginning of the model (110 Ma), which linearly evolves toward the present-day topography after a transition time. The best-fitting model shows a transition time at ~10 Ma (Table 2.2). For this end-member incision scenario, only the lowest-elevation AHe and ZHe ages are relatively well predicted, while the predicted AHe ages at > ~3300 m elevation and the AFT ages do not fit the observed ages (Figure 2.5A), as expressed by a high overall misfit of 12.6. The high misfit and over-prediction of all but the lowest-elevation ages imply that the total amount of exhumation is underestimated in this scenario.

We finally tested a plateau scenario, including both regional rock uplift and incision, fitting only the AHe and AFT ages younger than 22 Ma to concentrate on the Neogene history, considering that the steady-state models, including the old ZHe ages, adequately predict the early history. The best-fit model includes initial protracted slow exhumation at a rate of 0.01 km/Myr, a transition time at ~10

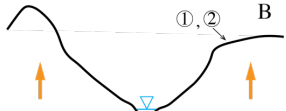
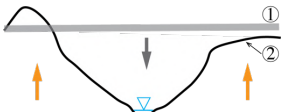
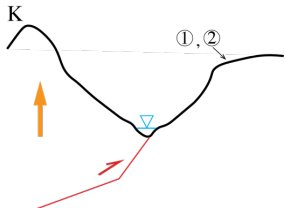
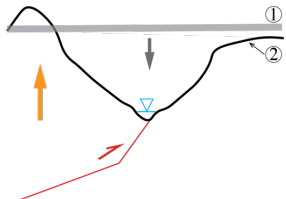
Ma, marking the onset time of river incision, and more rapid exhumation at a rate of 0.25 km/Myr since ~10 Ma. This model has the lowest misfit (1.16), with well resolved parameter values (Figure 2.6). Note that this lowest misfit (1.16) cannot be directly compared to the misfit of the best steady-state scenario (3.29), which models a longer time-scale (110 Ma) with more data (AFT ages > 22 Ma and ZHe ages). However, this plateau scenario better reproduces the AHe and AFT age-elevation trends, including the slope break around ~10 Ma in the AHe age-elevation plot (Figure 2.5B). Maximum river incision in this scenario from a plateau of 4500 m is 2.5 km for the Mekong Valley bottom (currently at 2000 m elevation); the average contribution of river incision to exhumation of the modelled samples in the valley (average elevation 3500 m) is ~1 km, accounting for ~30% of the total exhumation of ~3.5 km (~1 km topographic change and 2.5 km of rock uplift) since 10 Ma (cf. Figure 2.9).



**Figure 2.5** – Model results for the Baimaxueshan massif. (a) Age–elevation profiles of measured (solid blue symbols; triangles, squares and diamonds corresponding to AHe, AFT and ZHe ages respectively) and predicted (open symbols colored according to scenario) ages for the steady–state topography and incision scenarios. (b) Age–elevation profile of measured AHe and AFT ages (<22 Ma) and predicted ages for the plateau scenario, and predictions of the scenarios shown in (a) for comparison. (c) 3D view of the present–day topography (at resolution of 90 m) of the Baimaxueshan massif above the Mekong River, colored according to predicted AHe ages for the plateau scenario, the best–fit model for Baimaxueshan transect (orange symbols in b). Note that the plateau is shown slightly higher than its real elevation for clarity. The squares indicate the sample locations.



**Figure 2.6** – Scatterplots of Pecube inversion misfits for the plateau scenario model of the Baimaxueshan massif. Coloured dots represent individual forward-model runs plotted in 2-dimensional projections of the parameter space, with colours corresponding to misfit values, shown on a log scale. Posterior probability density functions for parameter values are plotted along the axes. The best-fit solution is represented by a yellow star with  $2\sigma$  (dark red) and  $1\sigma$  (light red) confidence contours. (a) Transition time (between first and second exhumation phase) versus exhumation rate during the first phase. (b) Transition time versus exhumation rate during the second phase.

Massifs	Scenarios	Parameter range	Annotation	Best-fit parameter	Misfit
<b>Baimaxueshan</b> 	<b>Steady-state topography scenario (2 phases)</b> (1): initial topography (2): modern topography B: Baimaxueshan)	E1: 0–1 km/Myr T: 0–40 Ma E2: 0–1 km/Myr T <sup>o</sup> : 900°	Exhumation rate of 1 <sup>st</sup> phase Transition time Exhumation rate of 2 <sup>nd</sup> phase Model basal temperature	0.04 km/Myr 7 Ma 0.42 km/Myr	3.29
	<b>Steady-state topography scenario (4 phases)</b>	E1: 0–0.5 km/Myr T1: 70–40 Ma E2: 0–1 km/Myr T2: 40–20 Ma E3: 0–0.5 km/Myr T3: 20–0 Ma E4: 0–1 km/Myr T <sup>o</sup> : 900°	Exhumation rate of 1 <sup>st</sup> phase 1 <sup>st</sup> Transition time Exhumation rate of 2 <sup>nd</sup> phase 2 <sup>nd</sup> Transition time Exhumation rate of 3 <sup>rd</sup> phase 3 <sup>rd</sup> Transition time Exhumation rate of 4 <sup>th</sup> phase Model basal temperature	0.04 km/Myr 64 Ma 0.04 km/Myr 25 Ma 0.06 km/Myr 3 Ma 0.72 km/Myr	3.13
	<b>Plateau scenario</b> (1): initial plateau (2): modern topography)	Plateau: 4500 m high E1: 0–0.5 km/Myr T: 0–20 Ma E2: 0–1 km/Myr T <sup>o</sup> : 900°	Exhumation rate of 1 <sup>st</sup> phase Transition time Exhumation rate of 2 <sup>nd</sup> phase Model basal temperature	0.01 km/Myr 10 Ma 0.25 km/Myr	<b>1.16</b>
	<b>Kawagebo</b> 	<b>Tectonic scenario</b> (1): initial topography (2): modern topography red line: fault K: Kawagebo)	r <sub>1</sub> : 22.5 km s <sub>1</sub> : -50–0 km r <sub>2</sub> : 0–22.5 km s <sub>2</sub> : -50–0 km E1: -1–0 km/Myr T: 0–10 Ma E2: -2–0 km/Myr T <sup>o</sup> : 900°	Coordinates of fault inflection points Fault-slip rate of 1 <sup>st</sup> phase Transition time Fault-slip rate of 2 <sup>nd</sup> phase Model basal temperature	-16.9 km 8.4 km -15.1 km -0.69 km/Myr 1.5 Ma -1.84 km/Myr
	<b>Tectonic+Plateau scenario</b> (1): initial plateau (2): modern topography red line: fault)	Plateau: 4500 m high r <sub>1</sub> : 22.5 km s <sub>1</sub> : -16.9 km r <sub>2</sub> : 8.4 km s <sub>2</sub> : -15.1 km E1: -1–0 km/Myr T: 0–10 Ma E2: -2–0 km/Myr T <sup>o</sup> : 900°	Coordinates of fault inflection points Fault-slip rate of 1 <sup>st</sup> phase Transition time Fault-slip rate of 2 <sup>nd</sup> phase Model basal temperature	-0.45 km/Myr 1.6 Ma -1.86 km/Myr	<b>0.66</b>

**Table 2.2** – Inversion parameters for the different scenarios tested for the Baimaxueshan and Kawagebo massifs. The best-fit scenario, with the lowest misfit for each massif, is in bold. A range of exhumation rates is explored for different phases, separated by transition times. Coordinates of the fault inflection points define the geometry of the fault plane, with  $r_i$  and  $s_i$  (in km) corresponding to the depth and distance relative to the surface trace of fault, respectively. Note that the tectonic scenario includes a slip rate on the fault rather than a vertical exhumation velocity, and that upward slip on a thrust is indicated by negative values (see [Braun et al., 2012](#) <sup>[298]</sup> for more detail).

### 2.1.5.2 Kawagebo massif

Published thermochronology data from the Kawagebo massif are dispersed over more than 40 km along the Mekong River valley ([Figure 2.4](#)). To the north, several samples yield ages with large error bars, with AHe ages clustering between 2 and 5 Ma, AFT between 5 and 30 Ma, and ZHe ages between 7 and 50 Ma ([Wilson and Fowler, 2011](#) <sup>[144]</sup>; [Liu-Zeng et al., 2018](#) <sup>[157]</sup>; [Replumaz et al., 2020](#) <sup>[151]</sup>). To the south, near the village of Yongzhi, along a west-bank tributary incising the Kawagebo massif, samples show more coherent ages, with AHe ages between 1 and 4 Ma, AFT ages between 3 and 7 Ma, and a single ZHe age at ~8 Ma ([Yang et al. 2016](#) <sup>[150]</sup>; [Replumaz et al., 2020](#) <sup>[151]</sup>). We use this dataset from the Yongzhi valley to constrain thermo-kinematic modelling of the massif evolution since 10 Ma. The steady-state topography scenario predicts a transition at 1.2 Ma between slower exhumation (0.54 km/Myr) and rapid exhumation (1.75 km/Myr), fitting the data reasonably well (misfit = 1.05). However, this scenario does not reproduce the increasing AFT ages with elevation, nor the observed slope break in AHe ages in the age-elevation plot ([Figure 2.7A](#)). As the high-elevation samples were collected toward the core of the massif, farther from the Mekong River, these characteristics of the age-elevation plot could potentially be explained by spatially varying exhumation rates due to a curved fault at depth and/or incision of the Mekong River. To explore these possibilities, we include tectonic particle transport along a thrust fault striking along the Mekong River and incision in the following inversions.

A tectonic scenario with a simple planar (one-segment) fault converges to a similar misfit (1.08) as the steady-state topography scenario (1.05). The best-fit model shows a fault dipping 85° to the west and a transition time at 1.3 Ma, with a slow slip rate of 0.58 km/Myr before and a faster rate of 1.87 km/Myr after. Due to the steep dip of this reverse fault, this tectonic scenario is very similar to the steady-state topography scenario considering purely vertical motion ([Figure 2.7A](#)).

A more complex tectonic scenario with a kinked (two-segment) thrust fits the data slightly better (misfit = 0.96) but much better reproduces the observed age-elevation relationships ([Figure 2.7B](#)). In

this scenario, the best-fit fault geometry is a thrust with a steep shallow segment (dipping at 65°) and a near-horizontal (1.5° dip) deeper segment, below 15 km (Figure 2.7C). The transition time is 1.5 Ma, with a slip rate of 0.69 km/Myr before, increasing to 1.84 km/Myr after. The velocity field predicted by this model implies decreasing exhumation rates away from the Mekong valley, as high exhumation rates above the steep shallow segment of the thrust give way to lower rates above the deep flat segment (Figure 2.7C). The low slope in the AFT age/elevation plot and the slope break in AHe ages are reproduced due to this spatial variation in exhumation rates. Input parameters of this scenario are relatively well constrained, as shown by the misfit scatterplots and the posterior pdf's of parameter values (Figure 2.8).

For consistency with the modelling results of the Baimaxueshan massif across the Mekong River, we also ran a “tectonic+plateau” scenario, adding the incision of a 4500 m high plateau to the tectonic scenario (two-segment thrust). This “tectonic+plateau” scenario converges to the lowest misfit (0.66), with a similar transition time (1.6 Ma), but somewhat smaller fault-slip rates (0.45 km/Myr until 1.6 Ma, 1.86 km/Myr after) than the tectonic scenario with two thrust segments (Figure 2.7B). The average contribution of river incision from a plateau of 4500 m to exhumation of the modelled samples (average elevation 2500 m) is ~2 km or ~25% of the total exhumation of ~8 km (~2 km topographic change and 6.1 km of rock uplift) since 10 Ma (Figure 2.9), a proportion similar to that of Baimaxueshan. The similarity between scenarios with and without topographic change suggest that river incision plays a minor role in the exhumation history of the Kawagebo massif, characterised mainly by tectonic forcing.

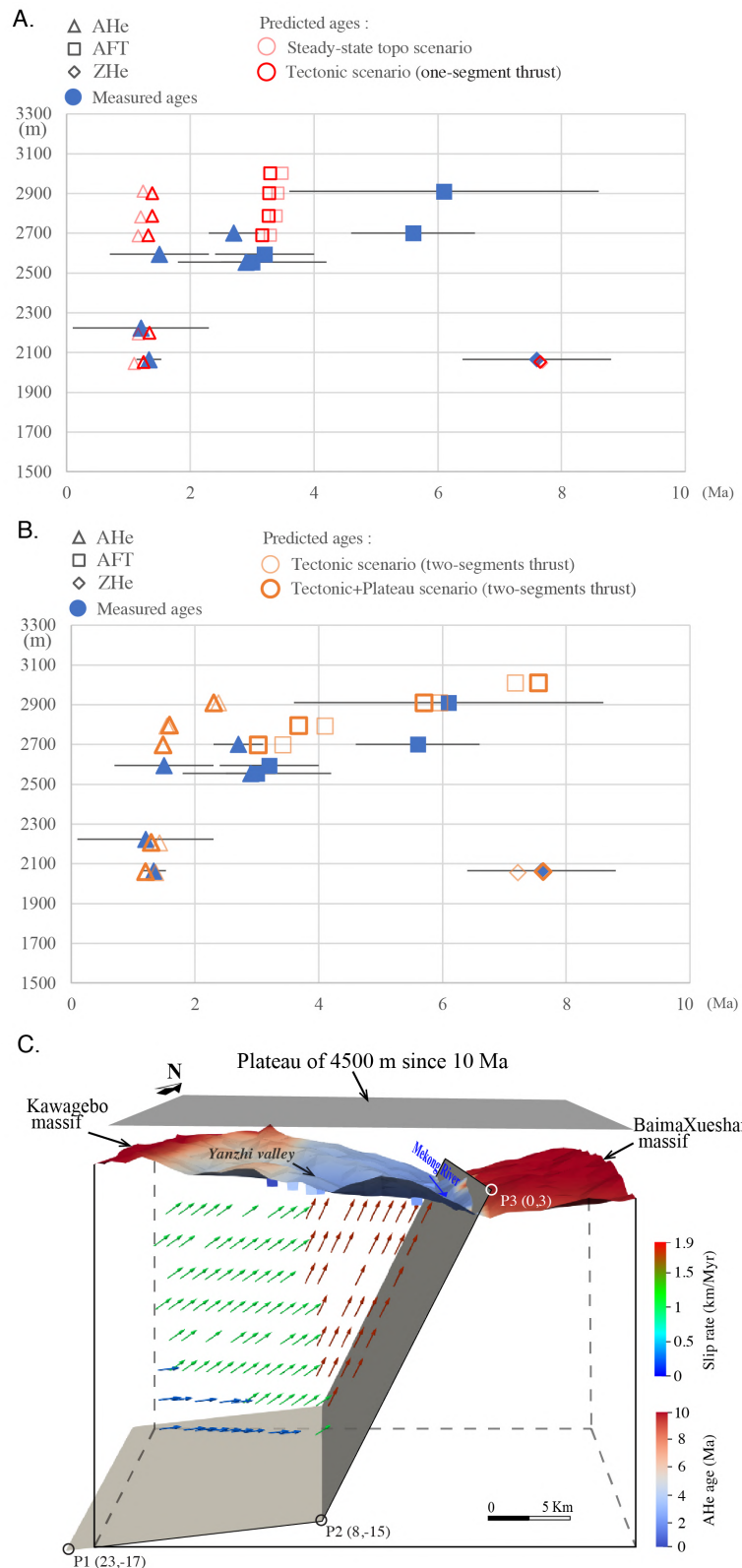


**Figure 2.7** – Modelling results for the Kawagebo massif. Age–elevation profiles of measured and predicted ages for (A) the steady–state topography scenario and the tectonic scenario with a planar (one–segment) thrust; (B) the tectonic and the tectonic+plateau scenarios, both with a kinked (two–segment) thrust. (C) 3D view of the present–day topography of the Kawagebo massif and the Mekong River valley, colored according to predicted

AHe ages of the tectonic+plateau scenario with a two-segment thrust. The geometry of the thrust and rock-particle trajectories are shown at depth; with squares indicating the sample locations. The thrust geometry is defined by P1, P2, P3 and their coordinates in distance relative to the surface trace of thrust. This scenario corresponds to the best-fit model for the Kawagebo massif (orange symbols in B). Note that the plateau is shown slightly higher than its real elevation for clarity. The arrows show the present-day velocity field generated by movement along the fault, during the recent rapid exhumation phase since 1.5 Ma; the two-segment geometry leads to spatially varying exhumation rates (shown by colors, scale on the right).

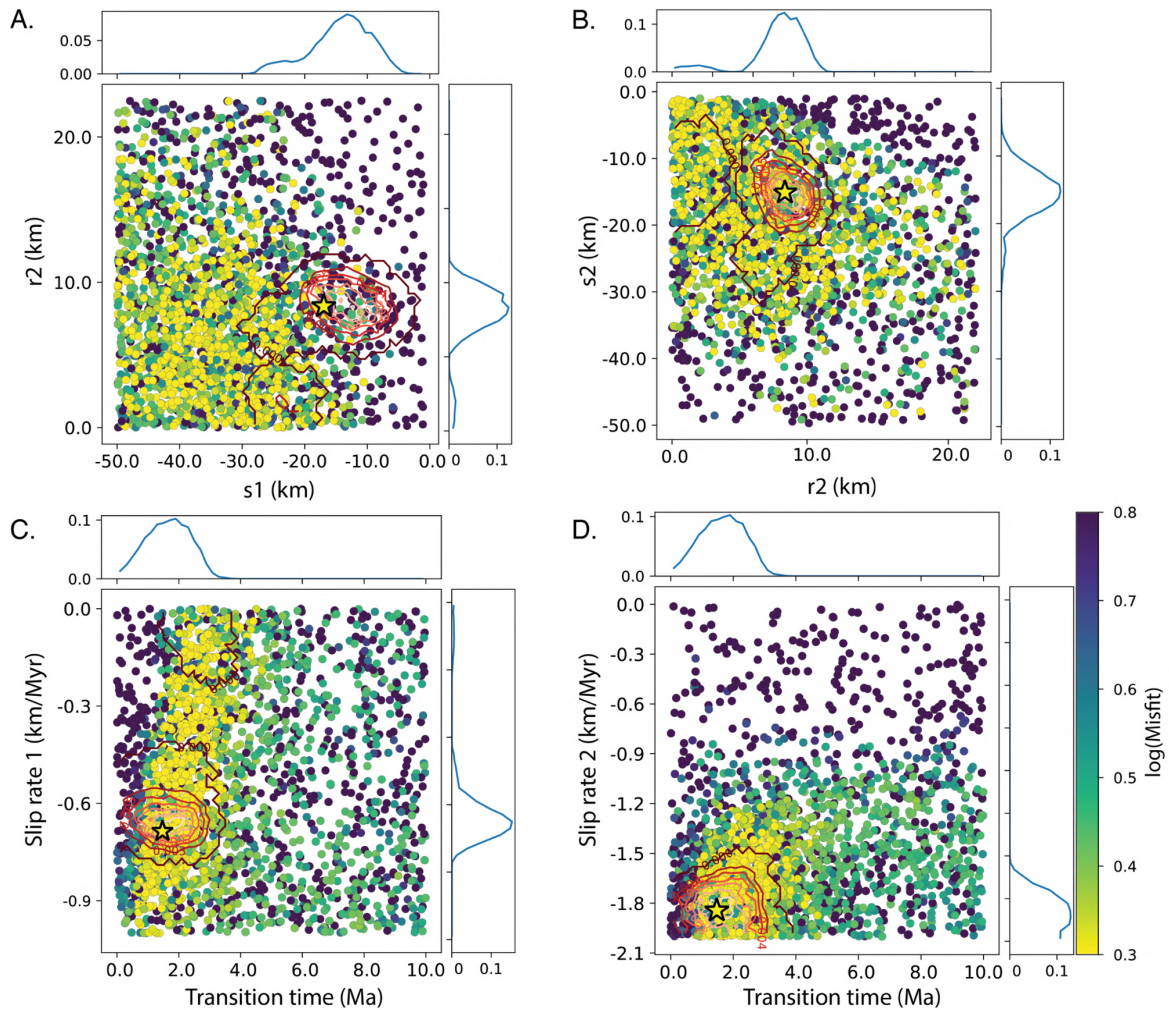


**Figure 2.8** – Scatterplots of PECUBE inversion results for two-segment thrust scenario model of the Kawagebo massif. Coloured dots represent single forward-model runs plotted in two-dimensional projections of the parameter space, with colours corresponding to misfit values, shown on a log scale. Posterior probability density functions for parameter values are plotted along the axes. The best-fit solution is represented by a star with  $2\sigma$  (dark red) and  $1\sigma$  (light red) confidence contours. (A) Depth of the base of the flat ( $s_1$ ) versus the horizontal location of the base of the ramp, relative to the surface trace of the thrust ( $r_2$ ). (B) The horizontal distance of the base of the ramp ( $r_2$ ) versus the depth of the base of the ramp ( $s_2$ ). For explanation of these parameters, see [Figure 2.7C](#). (C) Transition time versus slip rate along the fault during the first phase. (D) Transition time versus slip rate along the fault during the second phase.

## 2.1.6 Discussion: tectonic and climatic forcing on exhumation

### 2.1.6.1 Tectonic and climatic forcing on the evolution of the low-relief Baimaxueshan massif

For the Baimaxueshan massif, east of the Mekong River, our best-fit model, exploring the exhumation history since 110 Ma, shows rapid regional exhumation at a rate of 0.42 km/Myr since ~7 Ma, succeeding a phase of slow regional exhumation at a rate of 0.04 km/Myr before that. The onset of rapid exhumation occurred slightly later compared to published thermal history models using subsets of the data, which showed well-defined rapid exhumation at a rate of 0.26 km/Myr since 10 Ma (Replumaz et al., 2020<sup>[151]</sup>). Our results do not support the history inferred by Liu-Zeng et al. (2018)<sup>[157]</sup>, obtained by using pseudo-elevation profiles (Reiners and Brandon, 2006<sup>[317]</sup>), with rapid exhumation between 100 and 80 Ma at rate of 0.15 km/Myr, between 60 and 40 Ma at a rate of 0.6 km/Myr, and since ~20 Ma at a rate between 0.22 and 0.65 km/Myr. Surprisingly, both the previous 1D thermal-history modelling of Replumaz et al. (2020)<sup>[151]</sup> and the 3D thermo-kinematic modelling reported here, imply that none of the tectonic events occurring in southeast Tibet before 7 Ma have been recorded as exhumation phases in the Baimaxueshan massif. Those events include extrusion of the Indochina block between ~34 and ~17 Ma (e.g. Leloup et al., 2001<sup>[32]</sup>), significant erosion in the source region recorded by rapid sediment filling in Eocene basins downstream of the Three Rivers Region between 37–35 Ma (Gourbet et al., 2017<sup>[181]</sup>), and shortening of these basins between 28 and 20 Ma (Cao et al., 2019<sup>[309]</sup>). These results suggest that tectonic forcing in this massif has been negligible in driving its exhumation history before 7 Ma.

Our best-fit model focusing on the Neogene history of the massif since 22 Ma, implies incision of a plateau at an initial elevation of 4500 m since ~10 Ma, associated with regional exhumation at a rate of 0.25 km/Myr, succeeding a phase of slow regional exhumation at a rate of 0.01 km/Myr until 10 Ma. In this model, about 1 km of river incision (at the elevation of the samples) is added to 2.5 km of regional uplift-driven exhumation, resulting in a total exhumation of ~3.5 km since 10 Ma (Figure 2.9). Using such a simplified topographic evolution scenario mimicking the incision of a plateau, we show that differential erosion between the low-relief, mean-elevation Baimaxueshan massif and the deeply incised Mekong River valley is necessary to reproduce the break-in-slope in the AHe age-elevation profile, between samples on the plateau and samples from the Mekong River valley (Figure

2.5C). This scenario of incision of the Mekong River since ~10 Ma is compatible with the onset of incision estimated between 13 and 9 Ma for the Dadu and Yalong rivers gorges to the northeast (Clark et al., 2005a<sup>[138]</sup>; Ouimet et al., 2010<sup>[143]</sup>).

Our models show that river incision alone is not sufficient to reproduce the AHe ages at higher elevations, as well as the AFT ages from the Baimaxueshan massif (Figure 2.5A), and accounts for ~30% of the total exhumation since ~10 Ma. For the highest samples on the plateau, our results imply that ~2.5 km of overburden was removed from the plateau surface since 10 Ma, which is an order of magnitude higher than the exhumation (~0.23 km) estimated for the low-relief Daocheng plateau to the northeast during the same timespan (Clark et al., 2005a<sup>[138]</sup>). This higher exhumation is required by the much younger AHe and AFT ages in the Baimaxueshan massif (<18 Ma and <56 Ma respectively) (Liu-Zeng et al., 2018<sup>[157]</sup>) compared to the Daocheng massif (>50 Ma and >100 Ma respectively) (Clark et al., 2005a<sup>[138]</sup>). Therefore, the Baimaxueshan massif cannot be considered to represent the same relict surface as the Daocheng granite, despite the fact that both have low relief (Figure 2.2). We conclude that a relict surface *sensu-stricto*, i.e., remnant of a paleo-landscape that was barely affected by exhumation during India-Asia collision (Clark et al., 2005a<sup>[138]</sup>), should show AHe ages older than 50 Ma, and that not all low-relief surfaces in southeast Tibet can be classified as a relict surface.

The significant removal of overburden (~2.5 km) from the Baimaxueshan massif surface (currently at a mean elevation of ~4500 m and peaking at ~5400 m) since ~10 Ma implies efficient erosion processes at high elevation have generated the currently observed low-relief landscape (Figure 2.2). Glacial erosion and vigorous periglacial processes have been shown to be efficient in smoothing high-elevation regions above the glacial equilibrium line altitude (ELA) (Brozovic et al., 1997<sup>[254]</sup>; Egholm et al., 2009<sup>[269]</sup>; 2017<sup>[318]</sup>; Hales and Roering, 2009<sup>[255]</sup>). Zhang et al. (2016)<sup>[121]</sup> have proposed that these processes could be active in southeastern Tibet and could lead to seemingly continuous low-relief high-elevation surfaces despite spatially differential and diachronous tectonic exhumation of 2–4 km between the surfaces. The mean ELA across southeast Tibet during the last glacial maximum (LGM, ~20 ka) was estimated to ~4.6 km, much lower than the present-day ELA at ~5.4 km (Fu et al., 2013) (Figure 2.9). The ELA during previous glacial phases of the Quaternary would have been comparable to that of the LGM, with the average Quaternary ELA lying somewhere between these two values. Numerous cirques, moraines and U-shaped valleys are observed across the Baimaxueshan massif, providing evidence for significant glacial erosion (Figure 2.10). Based on this observation as well as the maximum elevation of the massif (5400 m), which is close to the present-day ELA (5400 m), we suggest that buzzsaw-like (peri-) glacial processes could be active in the Baimaxueshan massif, such

that any tectonic uplift bringing the elevation of the plateau above the ELA could trigger glacial processes that would erode and smooth these highlands, as previously proposed by [Zhang et al. \(2016\)](#) <sup>[121]</sup>. These glacial processes since at least ~2 Ma could thus contribute, in part, to remove the overburden of 2.5 km of materials, coupled with other erosional processes since 10 Ma.

Increasing regional rock uplift toward the eastern Himalayan Syntaxis has been inferred from relatively young thermochronological ages (AHe/AFT ages < 15 Ma, e.g., [Burg et al.; 1998](#) <sup>[319]</sup>; [Replumaz et al., 2020](#) <sup>[151]</sup>; [Ouimet et al., 2010](#) <sup>[143]</sup>) in a region between the South Tibet Detachment System–Parlung fault and the Longmucuo–Shuanghu suture ([Figure 2.11](#)), which roughly follows the Mekong River. This zone is also characterized by relatively high regional topography, with the plateau surface generally exceeding 5000 m ([Figure 2.11](#)). In contrast, the area to the east of the Longmucuo–Shuanghu suture, including the low–relief surfaces of Markam and Daocheng, show lower average elevations and older thermochronological ages (AHe/AFT > 15 Ma). This zone between the South Tibet Detachment System–Parlung fault and the Longmucuo–Shuanghu suture is thus potentially associated with regionally enhanced Late–Miocene uplift north and east of the EHS, as argued for instance by [Zeitler et al. \(2014\)](#) <sup>[160]</sup> and [Schmidt et al. \(2015\)](#) <sup>[320]</sup>, possibly due to the continuous northward advance of the eastern indenter corner of the Indian plate. In this zone, a north–south component of motion is also observed from the current GPS velocity field, which shows ongoing north–south shortening north of India ([Figure 2.11](#)) associated with surface uplift ([Liang et al., 2013](#)). The Baimaxueshan massif is located in the southeastern–most extremity of this regional uplift zone. Within the massif, N–S oriented thrusts like the Zigaishi thrust, east of and parallel to the Mekong River, are associated with a clear topographic crest bounding the massif to the west and could have been reactivated at a moderate rate (0.25 km/Myr) to accommodate shortening and thickening of the Three Rivers Region since ~10 Ma ([Figure 2.4A](#), [Figure 2.10](#)). Moderate uplift along those thrusts could be due to the distance from the EHS, with a west–to–east gradient of decreasing exhumation and erosion rates across the Three Rivers Region ([Yang et al., 2016](#) <sup>[150]</sup>).

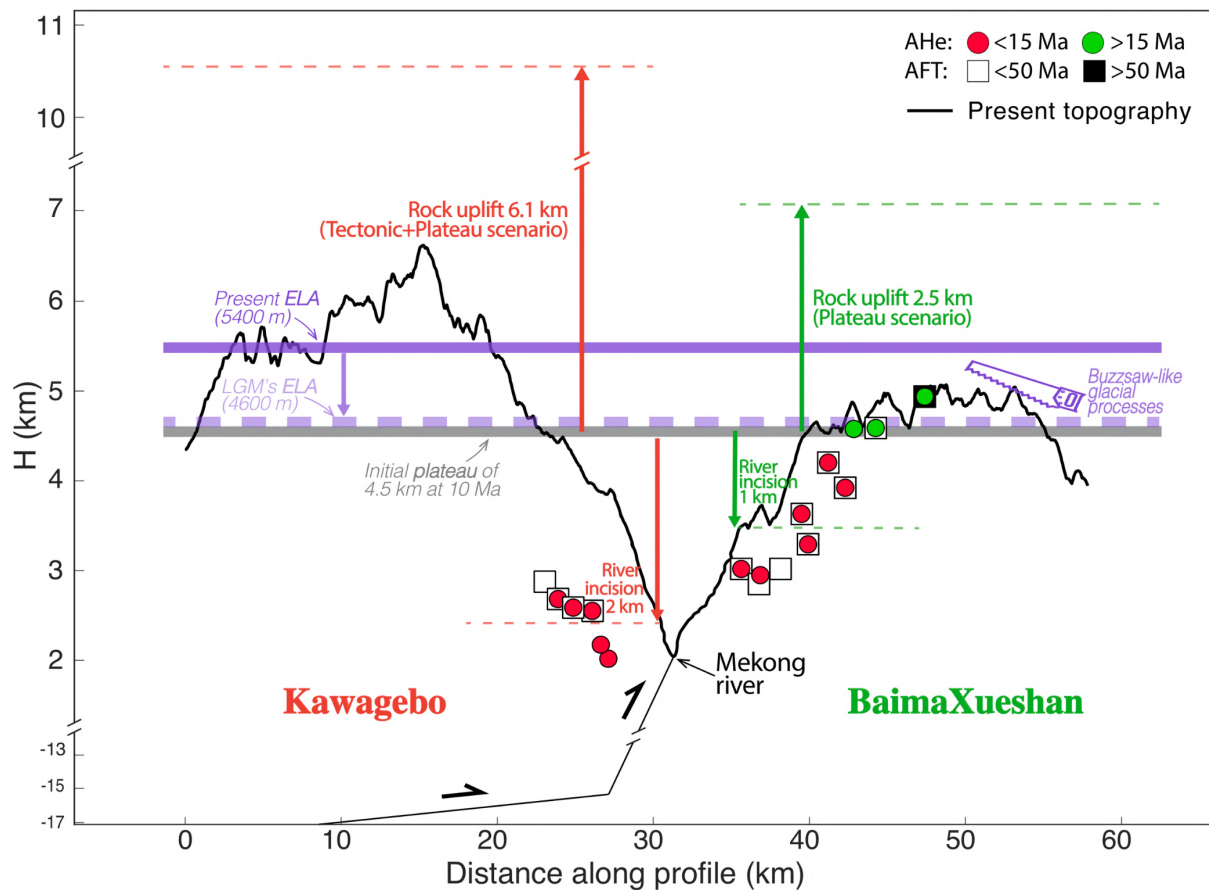


**Figure 2.9** – Exhumation since  $\sim 10$  Ma for the Kawagebo (red arrows) and Baimaxueshan (green arrows) massifs; with inferred Mekong river incision (downward red/green arrows) from scenarios with a schematic plateau at 4.5 km (horizontal grey thick line). Purple dotted thick line marks the glacial equilibrium line altitude (ELA) during the Last Glacial Maximum (LGM;  $\sim 20$  ka) (Fu et al., 2013a<sup>[250]</sup>), at which glacial erosion is most effective. Glaciation allows the formation of low-relief surfaces at high elevation through buzzsaw-like processes in Baimaxueshan, where rock exhumation is relatively low compared to the Kawagebo massif. Note that the geometry of the west-dipping thrust along Mekong river is not scaled at depth.

### 2.1.6.2 Dominant tectonic forcing on exhumation in the Kawagebo massif

Our best-fit model for the Kawagebo massif combines incision of a 4500 m high plateau and tectonically controlled rock uplift above a segmented thrust (Figure 2.7, Figure 2.9). Two phases have been modelled in this “tectonic+plateau” scenario, with an initial slip rate on the fault of 0.45 km/Myr from at least 10 Ma until 1.6 Ma, followed by rapid slip at a rate of 1.86 km/Myr, leading to 6.1 km of tectonically-driven exhumation since 10 Ma (Figure 2.9). The available dataset only covers a period since 10 Ma and cannot constrain the onset timing of the initial exhumation phase. Our model

outcomes corroborate earlier thermal-history modelling of the samples from the Yongzhi valley in the Kawagebo massif using QTQt, which suggested rapid cooling from 8 Ma and a significant acceleration from 1.5 Ma to present (Replumaz et al., 2020<sup>[151]</sup>). The average topographic lowering due to river incision at the elevation of the samples is ~2 km, accounting for ~25% of the total exhumation of the massif (Figure 2.9). This result implies that tectonic forcing has been dominant in exhuming the Kawagebo massif since at least 10 Ma. Potentially, the inferred acceleration of exhumation since 1.6 Ma could be due in part to more efficient erosion related to the onset of high-altitude glaciations and/or monsoon intensification. Efficient glacial erosion in the Kawagebo massif is attested to by deep U-shaped valleys, like the Yongzhi valley, suggesting >1 km of glacial erosion (Figure 2.10). In contrast to the Baimaxueshan massif, glacial erosion has not led to relief reduction in the Kawagebo massif; this difference could be due to the much higher rock uplift rate of up to ~1.7 km/Myr in Kawagebo versus 0.25 km/Myr in Baimaxueshan, consistent with worldwide comparisons of glacial relief in mountain belts (Pedersen et al., 2010<sup>[321]</sup>).

Combining the 3D distribution of sample ages relative to the fault trace, fault-controlled exhumation is predicted to be linked to a steep (~65°) thrust in the upper crust, which flattens at depth and strikes roughly parallel to the Mekong River (Figure 2.7C). This fault geometry reproduces the low slope in the AFT age-elevation profile as well as the observed slope break for AHe ages (Figure 2.7B, C). Replumaz et al. (2020)<sup>[151]</sup> suggested that late-Miocene uplift and exhumation of the Kawagebo massif, which peaks at ~2300 m above the mean plateau elevation of the plateau, was accommodated by such a fault. The fault was suggested to have activated at ~10 Ma in a large-scale restraining left-stepping overstep between the right-lateral Parlung and Zhongdian strike-slip faults (Figure 2.10), resulting in more pronounced local uplift compared to the regional uplift recorded in the Baimaxueshan massif. Steep to subvertical stratification and fault planes are observed along the Mekong River in the sampling area (Replumaz et al., 2020<sup>[151]</sup>), in agreement with the modelled steeply westward dipping thrust fault. However, observed striations are mostly sub-horizontal rather than dip-slip, suggesting that the active Mekong thrust is probably not outcropping in the field.

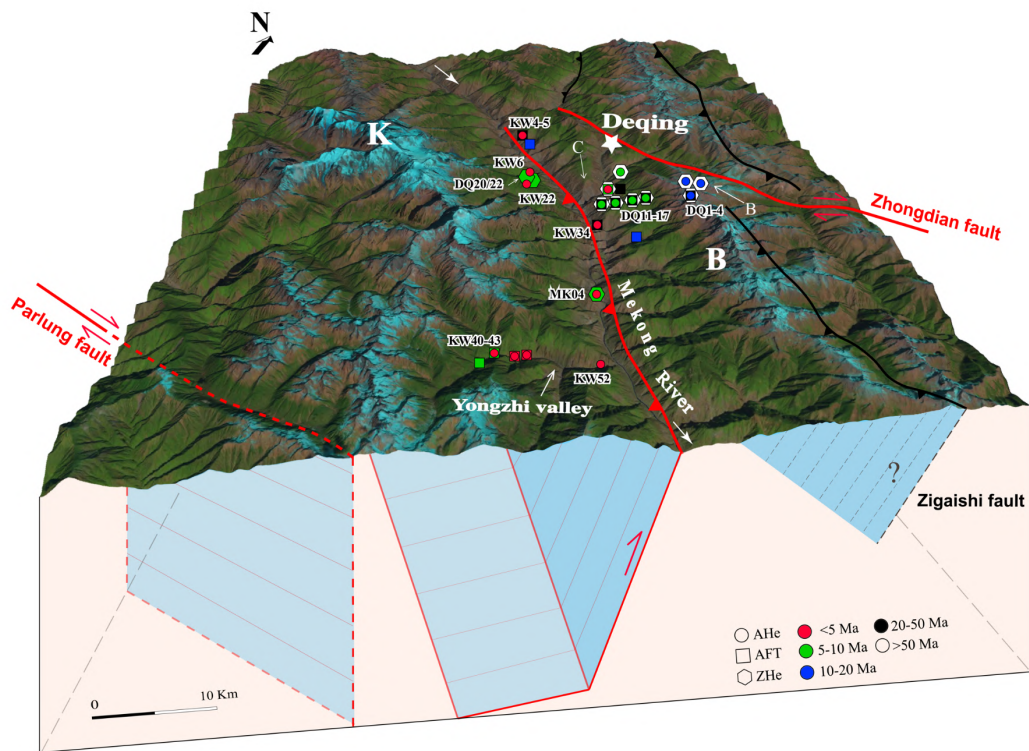


**Figure 2.10** - Three-dimensional view of the Kawagebo (K) and Baimaxueshan (B) massifs (Landsat image draped on DEM). Active faults are in red, other major faults in black. Thermo-chronological ages are shown with colour representing age and symbol representing method. MK samples are from [Yang et al. \(2016\)](#)<sup>[150]</sup>, DQ from [Liu-Zeng et al. \(2018\)](#)<sup>[157]</sup> (Baimaxueshan transect), and KW from [Replumaz et al. \(2020\)](#)<sup>[151]</sup> (Kawagebo transect). Also shown are the crustal geometries of faults (in red) active in the last 10 Myr. Arrows annotated B or C: positions of field photos shown in [Figure 2.4](#).

## 2.1.7 Conclusion

Using 3D thermo-kinematic models constrained by a relatively dense low-temperature thermochronology dataset, we have compared different exhumation scenarios for massifs along the middle reach of the Mekong River in the Three Rivers Region. We are able to discriminate between tectonically controlled rock uplift and river incision for both the Baimaxueshan and Kawagebo massifs. This method allows refining and validating the first-order conclusions on exhumation history inferred from age-elevation relationships and assessing the relative contributions of tectonic or climatic forcing to inferred phases of rapid exhumation. We show that different tectonic processes dominate the exhumation histories of the two flanks of the Mekong River. To the east, the low-relief Baimaxueshan massif is not a relict surface as defined by [Clark et al. \(2006\)](#)<sup>[126]</sup>, as it has experienced an amount of exhumation (~2.5 km since ~10 Ma) that is an order of magnitude higher than that determined for the emblematic Daocheng relict surface (~0.23 km). None of the tectonic events affecting southeast Tibet before 10 Ma has been recorded as exhumation phases in the Baimaxueshan massif, suggesting that tectonic forcing on the massif's exhumation has been negligible during that time. Moderate rock exhumation at a rate of 0.25 km/Myr since ~10 Ma was mainly triggered by the northward advance of the indenting Indian plate, leading to higher regional elevation around the EHS including the Baimaxueshan, with incision of the Mekong River contributing only ~30% of the exhumation recorded by the samples. The contrasting exhumation history of the Kawagebo massif to the west is dominated by strong local uplift driven by a segmented thrust dipping westward in a regional compressional overstep. Total tectonically driven exhumation since ~10 Ma at a rate of 0.45 km/my, with an acceleration to 1.86 km/My since 1.6 Ma, is estimated to be 6.1 km, with incision of the Mekong River contributing only ~25% of the total exhumation.

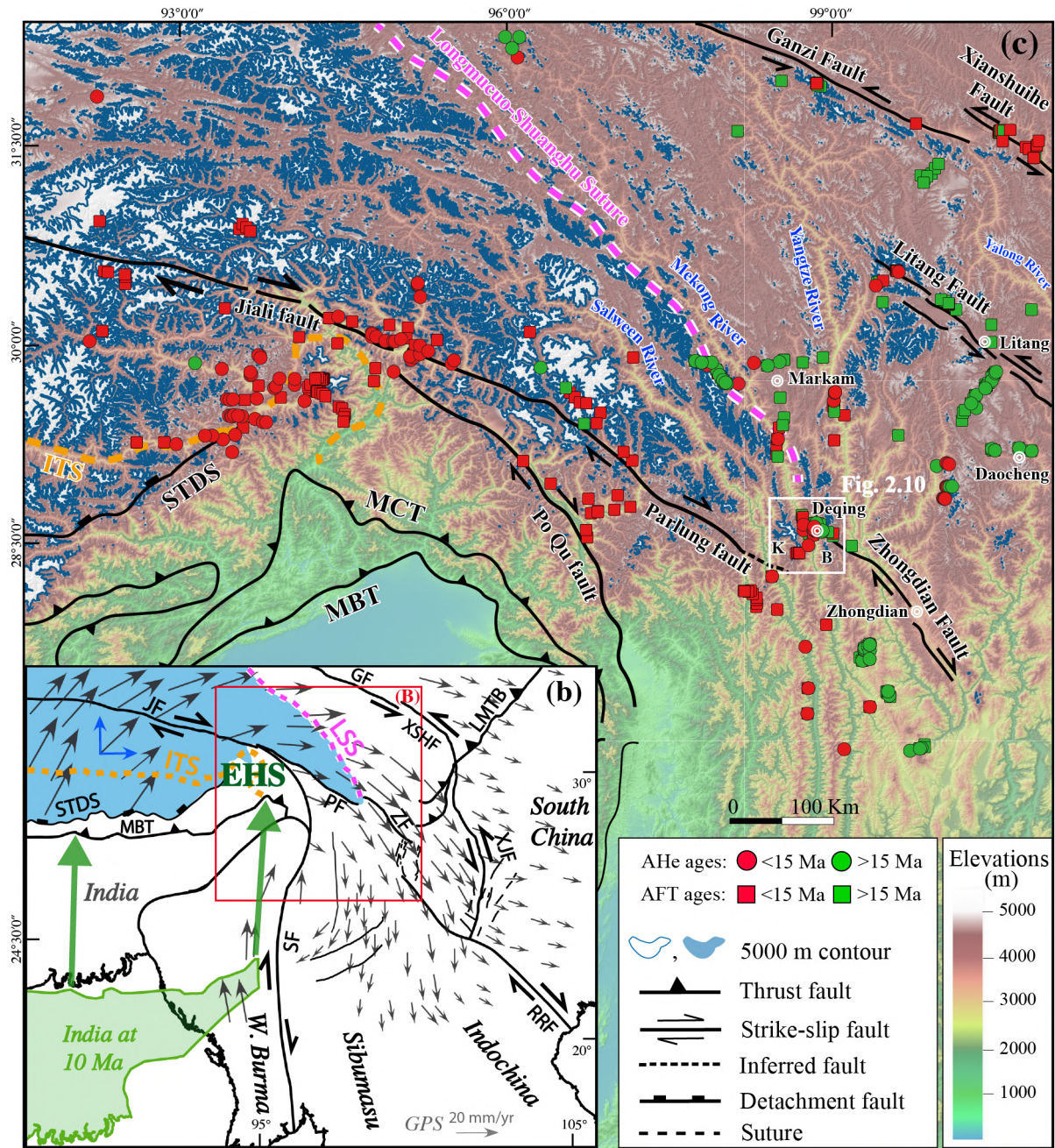


**Figure 2.11** – (A) Simplified geological structures of south-east Tibet, with GPS velocity field (modified from Wang et al., 2017<sup>[322]</sup>), showing a N–S component of motion north of India. Blue patch is the area of average elevation above 5000 m on the Tibetan Plateau. The reconstructed position of Indian continent at 10 Ma (green contour from Replumaz and Tapponnier, 2003<sup>[13]</sup>) shows continuing convergence since that time (green north-directed arrows). (B) Correlation between thermochronological (AHe and AFT) ages in south-east Tibet and topography above 5000 m (blue contour). White square represents our study area. More additional data are from Burg et al. (1998)<sup>[319]</sup>, Ding and Wang (1995)<sup>[90]</sup>, Seward and Burg (2008)<sup>[323]</sup>, Tu et al. (2015)<sup>[324]</sup>, Yu et al. (2011)<sup>[325]</sup>, and Zhang et al. (2015)<sup>[156]</sup> (see Figure 2.2, Figure 2.3 for references of other thermochronological ages). Abbreviations: GF, Ganzi Fault; ITS, Indus–Tsangpo Suture; JF, Jiali Fault; LMTB, Longmenshan Thrust Belt; LSS, Longmucuo–Shuanghu Suture; MBT, Main Boundary Thrust; MCT, Main Central Thrust; PF, Parlung Fault; RRF, Red River Fault; SF, Sagaing Fault; STDS, South Tibet Detachment System; XJF, Xiaojiang Fault; XSHF, Xianshuihe Fault; ZF, Zhongdian Fault.

## Code availability

The Pecube code for thermo-kinematic modelling to invert thermochronological data was developed by Jean Braun and is available at: <https://github.com/jeanbraun/Pecube>.

## Data availability

The compilation of data is available in the supplementary material.

## Acknowledgements

This work has been supported by the China Scholarship Council Funds. Jean Braun is warmly thanked for providing the Pecube code and constructive comments on the modelling. We thank the reviewers Paolo Ballato and Massimiliano Zattin for constructive comments that improved the manuscript.

## 2.1.8 Supplementary materials: low-temperature thermochronology data and thermo-kinematic modelling

### 2.1.8.1 Dataset

We selected a dataset composed of 11 samples from Baimaxueshan massif and 6 samples from Kawagebo massif with AHe, AFT and ZHe ages from [Yang et al. \(2016\)](#)<sup>[150]</sup>, [Liu-Zeng et al. \(2018\)](#)<sup>[157]</sup> and [Replumaz et al. \(2020\)](#)<sup>[151]</sup>, with details shown in Table S1 below. All the samples are collected from granite or granitoid intrusion or massif. To note that the altitude for each samples is re-acquired from GoogleEarth by using their original GPS coordinates because of important approximation and inaccuracy of the given altitude in references. For fission tracks analyses on apatite, a minimum of 20 grains have been counted for [Yang et al. \(2016\)](#)<sup>[150]</sup>, 29 grains for [Liu-Zeng et al. \(2018\)](#)<sup>[157]</sup> and 16 grains for [Replumaz et al. \(2020\)](#)<sup>[151]</sup>.

**Table S. 2.1** – Dataset of single-grain AHe, AFT and ZHe ages. For AHe and ZHe ages, the  $1\sigma$  error has been defined using the standard deviation of the replicate analyses divided by  $n-1$  where  $n$  represents the number of replicate. The weighted mean calculations were made using Isoplot/Ex\_ver3 (Ludwig, 2003<sup>[326]</sup>), weighted by age uncertainties of individual grains. For AFT ages from Yang et al., (2016)<sup>[150]</sup>, ages are pooled ages and were calculated using the recommended  $\zeta$  calibration approach (Hurford and Green, 1983<sup>[327]</sup>). For AFT ages from Liu-Zeng et al., (2018)<sup>[157]</sup>, ages are pooled age if  $P(\chi^2) > 5\%$  and are central age if  $P(\chi^2) < 5\%$ . For AFT age from Replumaz et al., (2020)<sup>[151]</sup>, ages are reported as central ages with  $1\sigma$  uncertainty, as well as upper and lower 95% confidence intervals.

Sample name	Longitude	Latitude	Elevation (m)	AHe age (Ma)	$1\sigma$ error (Ma)	Weighted mean age (Ma)	AFT age (Ma $\pm 1\sigma$ )	ZHe age (Ma)	$1\sigma$ error (Ma)	Weighted mean age (Ma)	Reference
<b>Baimaxueshan</b>											
DQ01-1	98.9616	28.3796	4944	19.1	0.9	18.9 $\pm$ 1.0	56.6 $\pm$ 2.8	72.9	1.0	93 $\pm$ 23	<b>Liu-Zeng et al., 2018</b>
DQ01-2				18.4	1.6			102.2	1.8		
DQ01-3				19.0	0.7			104.4	1.9		
DQ03-1	98.9687	28.3727	4553	12.0	1.2	16.4 $\pm$ 3.8	39.3 $\pm$ 2.2	97.6	1.3	97 $\pm$ 11	
DQ03-2				18.3	1.2			105.8	1.4		
DQ03-3				18.8	0.9			88.7	1.2		
DQ04-1	98.972	28.3829	4548	15.5	1.3	16.4 $\pm$ 1.5		113.0	1.7	111 $\pm$ 2	
DQ04-2				15.5	1.6			110.1	1.7		
DQ04-3				17.7	1.2			109.9	1.7		
DQ11-1	98.9263	28.3753	4228	12.1	0.4	8.75 $\pm$ 0.3	43.8 $\pm$ 2.6	97.8	1.5	93 $\pm$ 13	
DQ11-2				8.8	0.1			81.7	1.3		
DQ11-3				8.7	0.3			100.2	1.6		
DQ13-1	98.9176	28.3762	3929	9.7	0.4	9.5 $\pm$ 3.4	43.8 $\pm$ 2.1	98.0	2.0	103.9 $\pm$ 6.7	
DQ13-2				6.8	0.7			106.1	1.8		
DQ13-3				12.2	0.9			107.6	1.9		
DQ15-1	98.9091	28.3797	3641	8.9	0.4	8.6 $\pm$ 1.0	39.4 $\pm$ 2.1	90.5	1.6	85.1 $\pm$ 7.3	
DQ15-2				9.1	0.3			79.4	1.4		
DQ15-3				7.8	0.1			85.8	1.5		
DQ17-1	98.9091	28.3797	3641	4.7	0.4	6.2 $\pm$ 1.7	28.6 $\pm$ 1.5	87.0	1.5	78.6 $\pm$ 9.5	
DQ17-2				6.83	0.5			73.1	1.0		
DQ17-3				7.0	0.5			75.9	1.1		
LT18-1	98.9025	28.3482	2873								

LT18-2							15.3±1.1				
LT19-1	98.9051	28.3903	3024				21.0±1.2				
LT19-2											
MK01-1	98.9054	28.4128	2953	5.12	0.07	5.8±0.5		87.05	0.66	90.68±7.12	<b>Yang et al., 2016</b>
MK01-2				5.49	0.06			104.41	0.46		
MK01-3				5.69	0.06						
MK01-4				4.64	0.05			80.57	0.85		
MK01-5				6.76	0.07						
MK01-6				7.37	0.06						
MK08-1	98.9054	28.4128	2953	4.31	0.09	4.3±0.3	13.5±1.3	81.84	0.80	84.35±1.03	
MK08-2				4.87	0.06			83.62	0.68		
MK08-3				3.95	0.06			86.50	0.58		
MK08-4				4.26	0.05			85.43	0.34		
MK08-5				4.96	0.07						
MK08-6				3.28	0.05						
<b>Kawagebo</b>											
KW40-1	98.7660	28.2013	2911				6.1±2.5				<b>Replumaz et al., 2020</b>
KW41-2	98.7776	28.2063	2701	3.2	0.3	2.7±0.8	5.6±1.0				
KW41-4				3.1	0.3						
KW41-6				2.1	0.2						
KW42-1	98.7888	28.2022	2555	3.0	0.3	2.9±1.2	3.0±0.8				
KW42-2				2.8	0.3						
KW42-3				2.0	0.2						
KW42-4				3.8	0.3						
KW43-3	98.7776	28.2063	2701	1.2	0.11	1.5±0.4	3.2±1.2				
KW43-4				1.7	0.16						
KW43-5				1.59	0.14						
KW43-6				1.52	0.14						
KW52-1	98.8503	28.1982	2224	1.16	0.1	1.2±0.2					
KW52-2				1.09	0.1						
KW52-3				1.29	0.12						
KW52-4				1.1	0.1						
MK04-1	98.8592	28.2648	2066	1.65	0.04	1.3±0.3		8.17	0.05	7.65±0.53	<b>Yang et al., 2016</b>
MK04-2				1.01	0.02			7.12	0.07		

### 2.1.8.2 Thermo-kinematic modelling

The thermo-kinematic modelling code Pecube (Braun et al., 2012<sup>[298]</sup>) is based on a mixed Eulerian-Lagrangian approach and this finite-element model predicts the thermal structure of a crustal block and thermochronological cooling ages at the surface following an imposed kinematic and topographic histories. Pecube solves the 3D heat-transport equation during exhumation using an empirical mathematical model for fission-track annealing and analytical diffusion models for isotope-based thermochronometers (Braun et al., 2012<sup>[298]</sup>).

The upper boundary condition of the crustal block is the topography given by a global 900m resolution DEM or a user defined topography modified from the present-day one (using amplification factors or offsets) or theoretical one (constant elevation or sinusoidal etc...). Isostatic compensation is influential only in narrow river gorges and has been constrained to be less than 50 m in the SE Tibetan Plateau (Clark et al., 2006<sup>[126]</sup>). Isostatic rebound is known to be negligible on the increase of the plateau elevation and is not taken into account in our models. The block bears a thickness of 50 km as defined for the Eastern Tibetan plateau (Yao et al., 2008), with a basal temperature at 900°C (Wang Yang, 2012) corresponding to a thermal gradient of ~20°C/km. Thermal properties such as rock conductivity heat capacity density and heat production are spatially uniform and constant through time and are given by default values from Pecube code. A basic scenario is characterized by one or several exhumation phases and corresponding exhumation velocities for each phase, which are assumed to be spatially uniform but variable through time. Worthy note is that the implementation of a fault could spatially differentialize the velocity resulting in continuous motion of one part of the crustal block along the fault, the rest being tectonically quiescent. The fault trace at the surface could be fixed with two points of given coordinates in an orthonormal reference frame and the number of fault segments at depth separated by inflection points, along with the maximum depth of the fault need to be fixed too.

A two-step neighborhood algorithm inversion (Sambridge, 1999a<sup>[328]</sup>, b<sup>[329]</sup>) method is used to obtain the most suitable parameters. In the “sampling” stage, the model explores efficiently the multi-dimensional parameter space to derive optimal (best-fit) parameter values and corresponding smallest misfit through a comparison of measured and predicted thermochronological ages. In our study, an ensemble of 10,000 forward models, which is composed of 20 iterations of 500 models each, with subsequent iterations resampling the parameter space of the previous iteration, was performed. The resampling ratio from previous iteration is fixed to 90% to avoid convergence in local minima. No strict rules are applied to define the total number of forward models, but generally a more complex

scenario with more parameters to invert needs more iterations and more forward models. In the “appraisal” stage, the model ensemble generated from the first stage is resampled statistically to gain Bayesian estimates of the precision with which the different parameters are resolved. This phase yields a 1D and 2D marginal posterior probability–density function (pdf’s) of the parameter values, from which a “most likely” value and its standard deviation can be inferred (Braun et al., 2012<sup>[298]</sup>).

### 2.1.8.3 Results

For Baimaxueshan massif, we modelled some complex scenarios with three or four exhumation phases and specified transition times, in order to confirm if a rapid exhumation phase around 40 Ma, as speculated by Liu–Zeng et al. (2018)<sup>[157]</sup>. The best-fitting of these models turns to be a four–phase scenario (Table 2.2, Figure S. 2.1), with a relatively low misfit (3.13), and it shows quite well constrained parameters from pdf’s (Figure S. 2.2). However, this model is composed of protracted slow exhumation preceding an acceleration in the last few Myr, which is almost equivalent to the two–phase exhumation scenario. And no rapid exhumation phase around 40 Ma has been resolved. Its age–elevation profile resemble to that of two–phase exhumation scenario too (see in article).

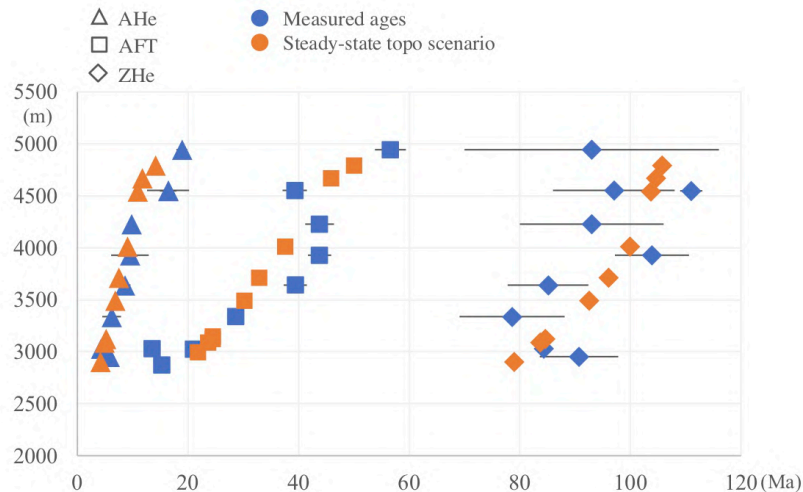
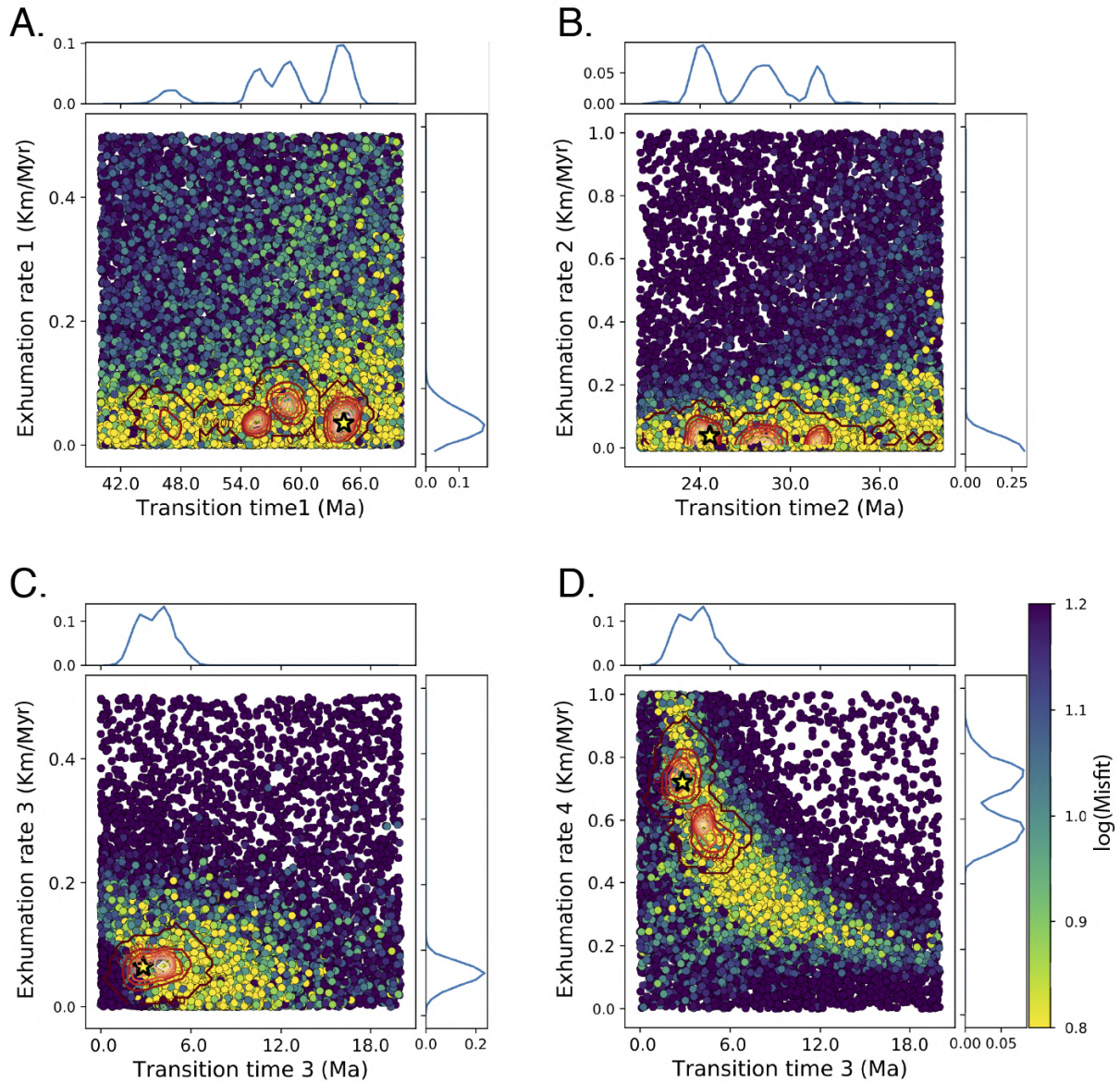


Figure S. 2.1 – Pecube modelling result for the Baimaxueshan massif, showing an age–elevation profile of measured (solid blue symbols; triangles, squares and diamonds corresponding to AHe, AFT and ZHe ages respectively) and predicted (solid orange symbols) ages for a steady–state topography scenario of four exhumation phases.



**Figure S. 2.2** – Scatterplots of Pecube inversion misfits for the steady-state scenario of four exhumation phases (orange signs in [Figure S. 2.1](#)) for the Baimaxueshan massif. Coloured dots represent individual forward-model runs plotted in 2-dimensional projections of the parameter space, with colours corresponding to misfit values, shown on a log scale. Posterior probability density functions for parameter values are plotted along the axes. The best-fit solution is represented by a yellow star with  $2\sigma$  (dark red) and  $1\sigma$  (light red) confidence contours. (A) Transition time 1 (between first and second exhumation phase) versus exhumation rate during the first phase. (B) Transition time 2 versus exhumation rate during the second phase. (C) Transition time 3 versus exhumation rate during the third phase. (D) Transition time 3 versus exhumation rate during the fourth phase.



## 2.2 Eocene–Oligocene thrusting and exhumation within the Three Rivers Region (Southeast Tibet) (in preparation)

Ou, X., Replumaz, A., van der Beek, P., Leloup, H. P., Chevalier, M. L., Pitard, P., Bai, M. K., Wang, S. G., Pan, J. W., Gautheron C., Sobel E., Balvay M.



**Figure 2.12** – Way to the location of the sample KS07 in the upstream glacial part of the Yongzhi valley, south of the Kawagebo peak, during the 2019 field mission.

The previous section, I explored the recent exhumation history since only 10 Ma under the dominant tectonic forcing and second order influence of the Mekong River incision (Ou et al., 2021<sup>[152]</sup>). I used modelling using PECUBE of the low temperature thermochronology data at low elevation of the Kawagebo Massif, allowing test of different scenario of the topography evolution and different fault geometry. The samples have been collected in 2015 by my supervisor and her team before the start of my PhD, and previously modeled using QTQt with a steady-state topography and no fault (Replumaz et al., 2020<sup>[151]</sup>). In 2019, during the first year of my PhD, we collected new samples in the high elevation part of the Kawagebo Massif to complete the existing dataset. In this section, I present the new thermochronology ages and the preliminary modelling results, attempting to constrain the tectonic history prior to 10 Ma in the Kawagebo massif. Then I compare those with published data in the nearby locations, trying to decipher the thrusting and exhumation history during the Eocene–Oligocene within the Three Rivers Region and its potential regional implication of tectonic history.

## 2.2.1 Geological setting

Present-day, the deformation of southeast Tibetan Plateau is mainly characterized by transtensional strike-slip faulting and normal faulting, as revealed by the focal mechanisms of earthquakes, which is different from the Longmenshan region, dominated by active thrusting (e.g., De Michele et al, 2010<sup>[330]</sup>; Robert et al., 2010<sup>[331]</sup>) (Figure 2.13). The northwest-southeast trending Ganzi-Xianshuihe Fault offsets the Yalong thrust belt (including the Jiulong, Muli and Jinhe-Qinghe thrusts) toward southeast from the Longmenshan thrust belt since ~12–9 Ma, (e.g., Zhang et al., 2017<sup>[140]</sup>) (Figure 2.13), and continues to the south, connecting the Anninghe and Xiaojiang faults. Adjacent to the EHS, the right-lateral Jiali strike-slip fault (active since 18 Ma) continues along the Parlung fault, jumping to the east to the dextral Zhongdian fault (activated since >10 Ma). A push-up structure in a left-stepping between these two faults contributed to the high topography of the Kawagebo massif (>6000 m) (Replumaz et al., 2020<sup>[151]</sup>). Modelling results shows a fast exhumation phase (rate of 0.45 km/Myr) above a kinked thrust since at least 10 Ma, accelerating to an exhumation rate of 1.86 km/Myr at 1.6 Ma in the massif (Ou et al., 2021<sup>[152]</sup>). Right-stepping from the dextral Zhongdian fault to the dextral Red River fault has open the Lijiang pull-apart basins, since at least 5 Ma and probably since 10 Ma (Leloup et al., 1993<sup>[332]</sup>; Replumaz et al., 2001<sup>[306]</sup>; Schoenbohm et al., 2006<sup>[333]</sup>; Fyhn and Phach, 2015<sup>[307]</sup>).

Prior to this present-day tectonic regime active since the middle Miocene, deformation in southeast Tibetan Plateau was dominated by southeastward extrusion of the Indochina block and significant thrusting. The extrusion took place either by mostly rigid block motion (Leloup et al., 1995<sup>[31]</sup>, 2001<sup>[32]</sup>; Replumaz and Tapponnier, 2003<sup>[13]</sup>) or by internally deformed crustal fragments (Wang and Burchfiel, 1997<sup>[334]</sup>). Anyhow, the extrusion was regionally accommodated along the right-lateral Gaoligong shear zone on the west and the left-lateral Ailaoshan-Red River shear zone on the east, with the Chongshan shear zone lying between them (Figure 2.13). The dextral ductile strike-slip deformation of Gaoligong shear zone is estimated to be 32–10 Ma, following a protracted pre-Oligocene transpression deformation (Wang et al., 2006<sup>[335]</sup>; Zhang et al., 2012<sup>[336]</sup>). Three episodes of deformation have been reported in the Chongshan shear zone, with transpression at 57–46 Ma, dextral ductile shearing in the northern portion of Biluoxueshan at 34–14 Ma with sinistral shearing in the southern portion during 32–22 Ma, and coeval transpressive exhumation during 19–14 Ma (Zhang et al., 2012<sup>[337]</sup>). The sinistral Ailaoshan-Red River shear zone was first proposed to be active from ~34 to 17 Ma (Leloup et al., 1995<sup>[31]</sup>, 2001<sup>[32]</sup>), while a later onset timing of sinistral shearing during ~27–17 Ma was suggested, accompanied by a rapid contemporaneous exhumation and post-extrusion

exhumation between ~14–11 Ma (Wang et al., 2016<sup>[308]</sup>). More than 700 km left-lateral offset on the Ailaoshan–Red River shear zone during its sinistral motion has been reported based on offset geological markers (suture and ultrapotassic intrusion) (Leloup et al., 1995<sup>[31]</sup>) and paleomagnetism records from the South China Sea (Briais et al., 1993<sup>[338]</sup>), providing key evidences to tectonic extrusion model (e.g., Peltzer and Tapponnier, 1988<sup>[30]</sup>). Lower estimation of ~250 km has been inferred considering other geological offsets (Searle, 2006<sup>[339]</sup>), such as gravity anomalies (Mazur et al., 2012<sup>[340]</sup>).

The Jiali–Parlung fault to the north of these large-scale shear zones first experienced a sinistral shearing during 24–18 Ma, prior to a shear sense shift to dextral at ~18 Ma (Lee et al., 2003<sup>[341]</sup>; Lin et al., 2009<sup>[342]</sup>; Zhang et al., 2020<sup>[343]</sup>). The present-day dextral Zhongdian fault potentially also experienced a shear shift at ~10 Ma (Replumaz et al., 2020<sup>[151]</sup>). These former left-lateral faults, which offset the N–S trending, highly elongated and vertically dipping Jurassic unit (Figure 2.4), are proposed to be related with a nearly east–west contraction phase accommodating large-scale thickening and surface uplift of the southeastern Tibetan Plateau prior to and/or coevally with Indochina extrusion (Liu-Zeng et al., 2008<sup>[100]</sup>). In this region, pseudo-elevation versus age plot of thermochronological data from two profiles near Deqin and Weixi recorded strong exhumation at 60–40 Ma, suggesting regional compressional deformation (Liu-Zeng et al., 2018<sup>[157]</sup>), although later thermal-kinematic modelling of the Deqin profile didn't show this cooling event (Ou et al., 2021<sup>[152]</sup>). Farther to the north, north–south to northwest–southeast trending inactive thrusts are widely documented in the Three Rivers Region (e.g., Salween, Mekong and Yangtze). Indeed, accelerating cooling at 36–34 Ma near Zuogong, in the core of the Three Rivers Region, has been recognized by recent inverse thermal history modelling of thermochronological data, revealing activation of a thrust along the Mekong River (referred as Lancangjiang thrust in Cao et al., 2022<sup>[344]</sup>) roughly following Longmucuo–Shuanghu suture during that time (Figure 2.13). These thrusts are in the continuity of the arcuate belt of Cretaceous–Paleogene intermontane basins (e.g., Hoh–Xil, Nangqian–Yushu, Gonjo, Markam and Jianchuan basins) across the Qiangtang terrane, which have been infilled and then shortened by bounding thrusts since early Paleocene until at least late Oligocene, coeval with or shortly after the onset of the India–Asia collision (e.g., Horton et al., 2002<sup>[91]</sup>; Spurlin et al., 2005<sup>[176]</sup>; Studnicki–Gizbert et al., 2008<sup>[177]</sup>; Staisch et al., 2014<sup>[175]</sup>, 2016<sup>[182]</sup>; Li et al., 2015<sup>[179]</sup>; Su et al., 2018<sup>[180]</sup>; Cao et al., 2020<sup>[122]</sup>) (Figure 1.24). To the east, development of the Mula basin and deposition of reddish clastic materials, during ~42–25 Ma, due to the local W–E thrusting, have been suggested to stem from reactivation of the Ganzi–Litang suture (eastern branch of the Jinsha suture), in response to the far-field effect of the Indian indentation (Jackson et al., 2018<sup>[345]</sup>, 2020<sup>[346]</sup>) (Figure 1.24, Figure

2.13). In Central Tibet, thrusting along the Shiquanhe–Gaize–Amdo fault due to reactivation of the Bangong–Nujiang suture during late Cretaceous and middle Tertiary, following the India–Asia collision, has also been proposed to account for the volcanoclastic sedimentation in fluvial piedmont Nima and Lunpola basins along the northern Lhasa terrane (e.g., Decelles et al., 2007<sup>[84]</sup>, Kapp et al., 2007<sup>[77]</sup>; Fang et al., 2020<sup>[347]</sup>) (Figure 2.13).

To the east of southeast Tibetan Plateau, the “Great Bends Region” consists of the lower parts of the upstream Yangtze and Yalong rivers with remarkable bends, where they cross the Yulong Thrust Belt and the Yalong Thrust Belt, respectively (Figure 2.13). These two thrust belts have northeast–southwest trend, which is perpendicular to the main river channels crossing through (Clark et al., 2004<sup>[118]</sup>). The Yulong thrust was suggested to be active roughly between 28–20 Ma (Cao et al., 2019<sup>[309]</sup>). The Yalong thrust belt consists of Jiulong thrust, which was first active during 35–30 Ma then re-activated during 9–6 Ma (Zhang et al., 2016<sup>[121]</sup>), Muli thrust with strong exhumation since  $12.5 \pm 1$  Ma (Pitard et al., 2021<sup>[123]</sup>) and Jinghe–Qinhe thrust to the south, active either during 17–5 Ma (Wang et al., 2012<sup>[348]</sup>) or during 20–16 Ma (Zhu et al., 2021<sup>[124]</sup>), generating significant topographic step, with an elevation decrease of ~2400 m over a distance of ~250 km (Liu-Zeng et al., 2008<sup>[100]</sup>). Farther to the east, in the Longmenshan Region, the activity of the Longmenshan thrust belt, during 30–25 Ma and 10–0 Ma, was roughly synchronous to that of the Yalong thrust belt (Godard et al., 2009<sup>[158]</sup>; Wang et al., 2012<sup>[120]</sup>; Tian et al., 2013<sup>[70]</sup>, 2015<sup>[145]</sup>; Tan et al., 2014<sup>[300]</sup>). Southeast to those thrusts, the Lanping, Simao and Chuxiong basins record deposits of similar ages and sedimentary environments of open, broad alluvial fan and fan delta, or large lake (Zhou et al., 2003<sup>[349]</sup>), and were proposed to act as foreland piedmont basins of the aforementioned thrusting (Liu-Zeng et al., 2008<sup>[100]</sup>).

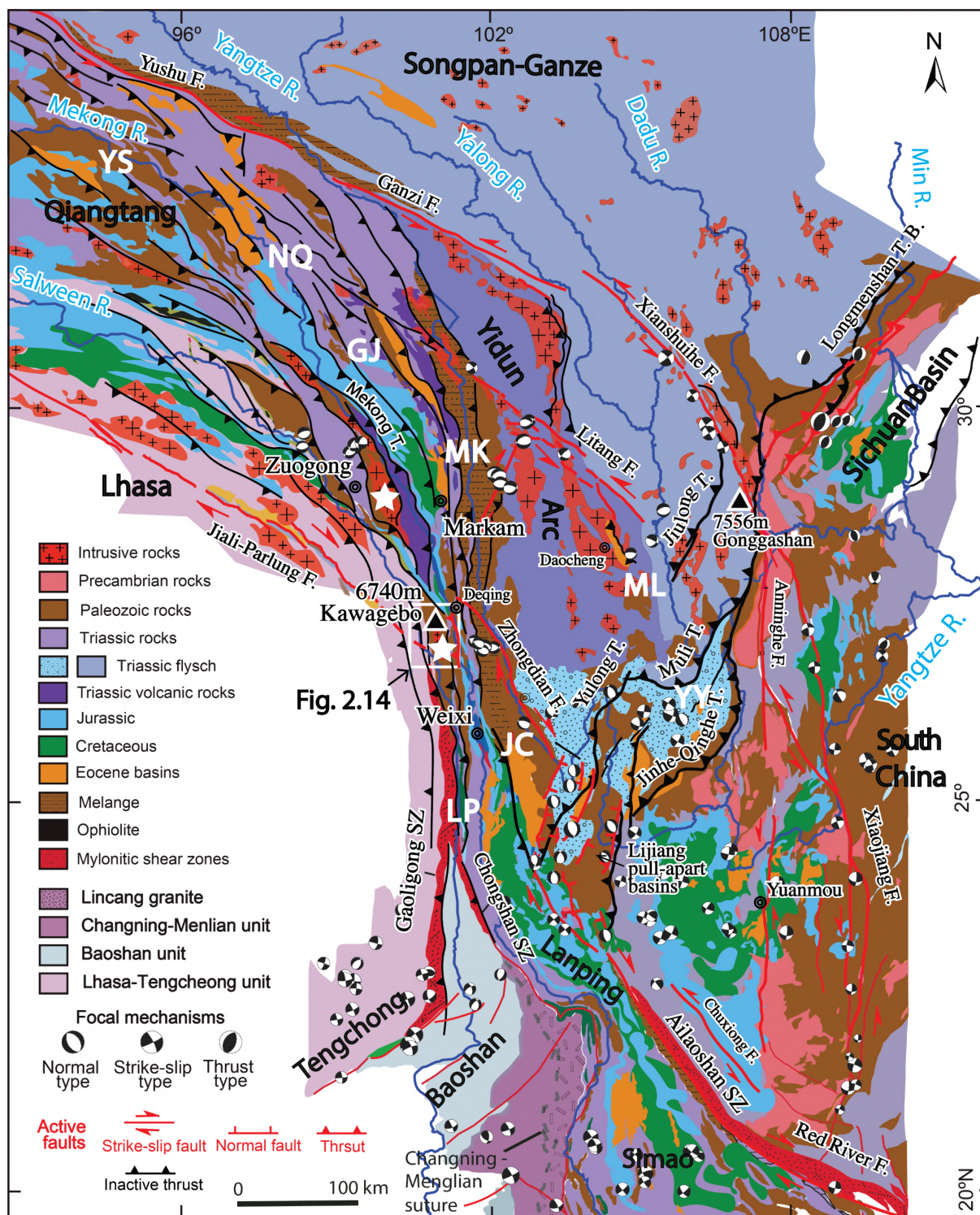


**Figure 2.13** – Geological map of southeast Tibet, centered by the Three Rivers Region, modified after [Burchfiel and Chen \(2012\)](#)<sup>[125]</sup>. The lithology of the Lhasa terrane is not described in details in this map. The main inactive faults are marked in black and active faults in red. The two white stars near Kawagebo peak and Zuogong represent locations of the newly collected low-temperature thermochronology data in this study and compiled ones from [Cao et al. \(2022\)](#)<sup>[344]</sup>, respectively. Eocene basins from north to south: YS: Yushu Basin; NQ: Nangqian Basin; GJ: Gonjo Basin; MK: Markam Basin; ML: Mula Basin; YY: Yanyuan Basin; JC: Jianchuan Basin; LP: Lanping Basin. F.: Fault, R.: River, T.: Thrust.

## 2.2.2 Low-temperature thermochronological data at high elevation in the Kawagebo Massif, sampling strategy and method

### 2.2.2.1 Sampling strategy and analysis methods

#### *Sampling Strategy*

In order to reconstruct and complete the exhumation history of the Kawagebo Massif during the India–Asia collision and to decipher a transition of tectonic regime from the regional west–east contraction to local uplift in a restraining left–stepping in the massif between the dextral Jiali–Parlung and Zhongdian faults, we collected 10 samples (KS01–KS10) from the Triassic granite along the upper Yongzhi valley and one sample (KS18) in a small diorite body near the bottom of the Mekong River valley, close to the entry of the Yongzhi valley. The lower part of the valley has been sampled (KW40–43, KW52) by [Replumaz et al. \(2020\)](#)<sup>[151]</sup>, and our new diorite sample is from the same location as MK04 of [Yang et al. \(2016\)](#)<sup>[150]</sup>. Those existing samples, together with our new samples KS01B, KS02, KS06, locate in the fluvial valley, while the rest of our new samples are from the higher glacial valley ([Figure 2.14A, B](#)). All these samples locate at elevations between 2000–4100 m.

#### *Apatite and Zircon (U–Th)/He analysis*

Apatite and zircon grains for (U–Th)/He dating were carefully selected with respect to their size, morphology and inclusions at the Institut des Sciences de la Terre (ISTerre) thermochronology laboratory. Five to six replicates were analyzed per sample for both methods. One thing to note is that all apatite grains from our samples are relatively small ([Table S. 2.2](#)), which might significantly influence the helium diffusion behaviors in the apatite crystals and the measured apparent AHe ages. The AHe dating was done at Paris Sud University (Orsay, France), following the procedures described by [Fillon et al. \(2013\)](#)<sup>[350]</sup>, and was calibrated by applying internal and external age standards of the Limberg Tuff and Durango Tuff. Similar to apatite, our zircon grains are not huge in size, but sufficiently large for dating. The ZHe dating was effectuated at the Potsdam University (Potsdam, Germany). The equivalent–sphere radius were calculated through the method of [Gautheron and Tassan–Got \(2010\)](#)<sup>[351]</sup>. Each single–grain (U–Th)/He age was corrected by its ejection factor  $F_T$ , determined by using the Monte Carlo simulation technique ([Ketcham et al., 2011](#)<sup>[352]</sup>). We adopt  $2\sigma$  error on AHe and ZHe age, which is considered to be 18%, in order to represent total errors in the age dispersion of the standards and ejection–factor correction ([Table S. 2.2](#), [Table S. 2.4](#)).

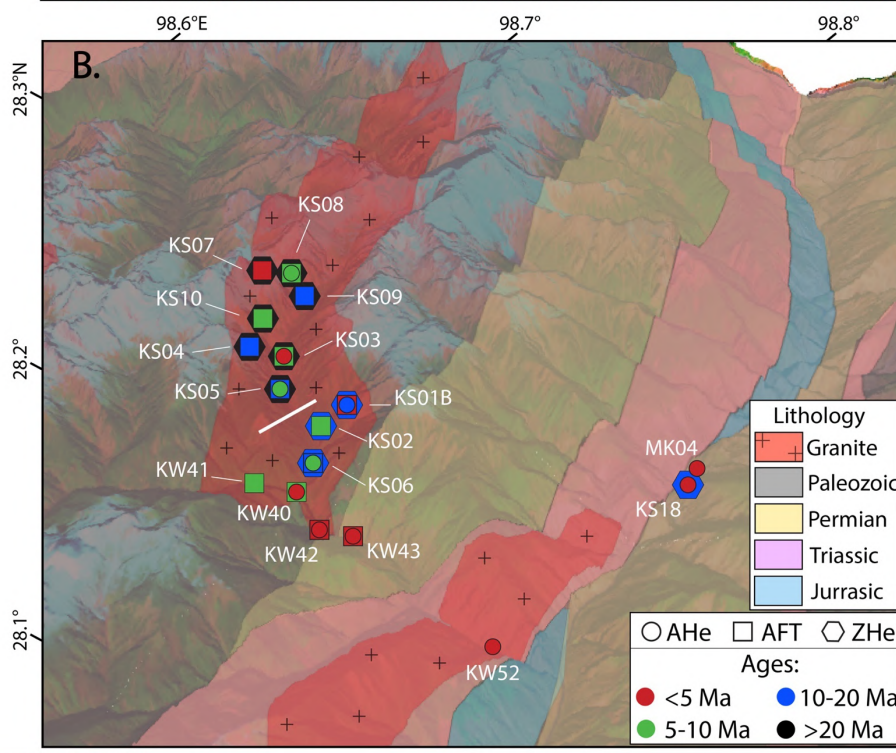
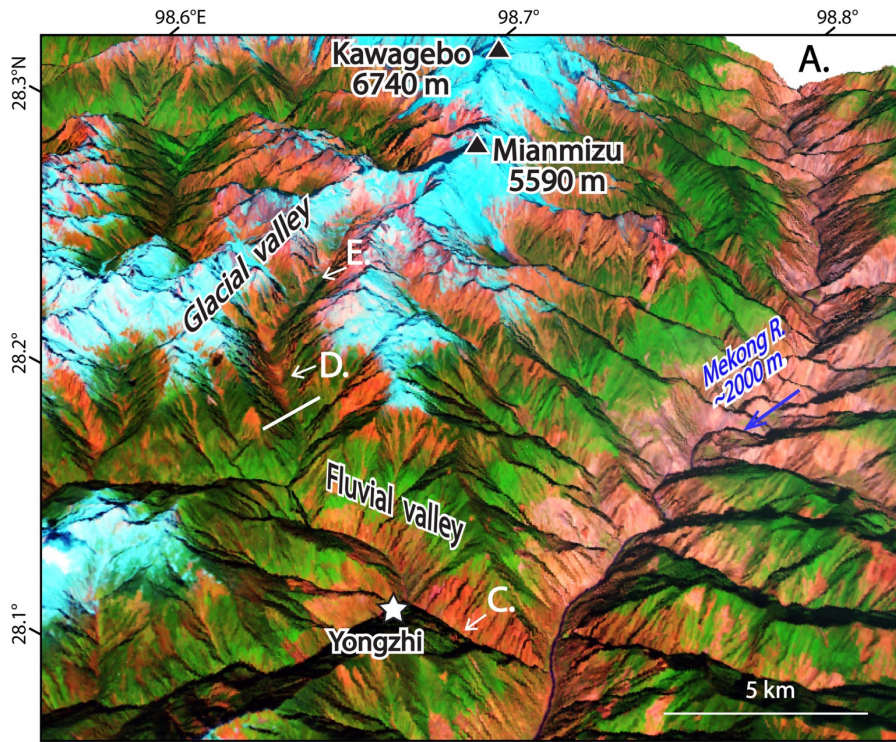


**Figure 2.14** – (A) Landsat image of the Kawagebo Massif (USGS), along which the Mekong River flows southward closely to the massif. The Yongzhi Valley is clearly divided into an upstream glacial valley and a downstream fluvial valley by the white point. (B) Simplified geological map of the Kawagebo Massif, showing the positions of newly collected low-temperature thermochronology data along the upper part of granite body in the Yongzhi Valley and compiled ones from [Yang et al. \(2016\)<sup>\[150\]</sup>](#) and [Replumaz et al. \(2020\)<sup>\[151\]</sup>](#). To note that half of samples locate in the glacial valley and the other half in the fluvial valley, separated by a white line. (C), (D), (E) Photos of valley landscapes advancing toward the Mianmizu Peak, showing a changing morphology from fluvial to glacial valley. Positions of photos are shown on A.

### ***Apatite Fission Track analysis***

Samples were selected, mounted, polished, etched and analyzed at the ISTERre thermochronology laboratory of the University of Grenoble–Alpes (Grenoble, France), using the external detector method ([Fillon et al., 2013<sup>\[350\]</sup>](#)). The irradiation of thermal neutron to generate induced fission tracks has been done by using the FRM II Research Reactor at the Technische Universität München (Germany), with IRMM540R dosimeter glasses for apatite. More than 20 grains per sample have been selected to count the spontaneous and induced fission tracks and the BINOMFIT program was used to calculate AFT ages (cf. [Ehlers et al., 2005<sup>\[353\]</sup>](#)). The  $\chi^2$ -test and age dispersion were used to assess the homogeneity of AFT ages ([Galbraith and Green, 1990<sup>\[354\]</sup>](#); [Galbraith and Laslett, 1993<sup>\[355\]</sup>](#)), which are visualized in terms of a measurement's value and precision by applying the RadialPlotter ([Vermeesch, 2009<sup>\[356\]</sup>](#)). The weighted mean apatite Zeta factor for Xiong OU is  $262.55 \pm 11.21$  (IRMM540R dosimeter glass), based on Durango and Fish Canyon Tuff age standards.

### ***Closure temperature***

The closure temperatures of AHe, AFT and ZHe thermochronometers are about 75°C, 120°C and 190°C, with partial retention zone (PRZ) or partial annealing zone (PAZ) between 50–90°C, 80–120°C and 130–200°C, respectively, depending on cooling rate ([Gallagher et al., 1998<sup>\[357\]</sup>](#); [Farley, 2002<sup>\[358\]</sup>](#); [Gautheron et al., 2009<sup>\[359\]</sup>](#)). Therefore, they could constrain exhumation and denudation histories in the shallow crust from depths between ~1.5 and ~5.5 km, depending on the local geothermal gradient ([Brandon et al., 1998<sup>\[287\]</sup>](#); [Reiners and Brandon, 2006<sup>\[317\]</sup>](#)). We obtained 38 single-grain AHe, 10 AFT and 58 single-grain ZHe ages from 11 samples ([Table S. 2.2](#), [Table S. 2.3](#), [Table S. 2.4](#)), without successfully extracting any ZFT age due to the extremely high concentration of uranium in zircon. The existing data from lower elevation of the Kawagebo Massif are detailed in [Table S. 2.5](#) and [Table S. 2.6](#).

### 2.2.2.2 Results: new low-temperature thermochronological ages of the Kawagebo Massif

The existing AHe ages at low elevation of the Yongzhi valley produce quite coherent single-grain ages. While our new samples, at elevations between 2800 and 4100 m, yield very disperse AHe ages between grains, ranging from several to several tens of millions years, except the lowest KS18 at the valley bottom of the Mekong River (Figure 2.14B, Table S. 2.2). The sample KS01A with 4 replicates shows very different ages from 8 to 73 Ma, with relatively low quantity of eU and abnormal high concentration of  $^4\text{He}$  detected. This phenomenon could be related to helium contamination from surroundings, largely increasing the helium concentration and therefore falsely yielding older AHe ages. The sample KS01B, which shows no weathering compared to KS01A at the same location, gives relatively coherent ages. All grains in KS01A and one replicate KS06-3 and are rejected due to high concentration of helium in a small grain and a much higher apparent age compared to other replicates. Also for KS06, the ages of some replicates correlate positively with the eU content (Figure 2.15A). This positive correlation is generally regarded as a proxy for the  $\alpha$ -recoil damage in the apatite grain, which increases the capacity of He retentivity in crystals and tend to yield significantly older ages when they experienced slow cooling (Flowers et al., 2009<sup>[360]</sup>; Gautheron et al., 2009<sup>[359]</sup>). The final selected replicates produce an average AHe age for each sample, as shown in Table 2.3, which shows a rough correlation with elevation (Figure 2.16A). The wide and uncoherent range in both single-grain and averaged age potentially stems from a relatively long residence in the PRZ roughly from ~15 to ~4 Ma.

Our AFT ages of new samples also present a strong age dispersion, ranging from 14–4 Ma, overlapping the AHe ages. Chi-square probabilities of most samples are >0.5%, and age dispersions are close to 0, indicating a single AFT age population (Galbraith and Laslett, 1993<sup>[355]</sup>), except the sample KS04, which is presented with a central age (Table S. 2.3). Poor age-elevation correlation is observed, which confirms a long residence in the PAZ from ~15 to ~4 Ma and suggests that elevations between 2800–4100 m of the Kawagebo massif probably represents the exhumed PRZ/PAZ. Because of the relatively low content of effective uranium and young cooling ages, no sufficient horizontally confined track-length parallel to the crystallographic c-axis have been measured. What's more, all measured etch-pit-width values ( $D_{\text{par}}$ ) are smaller than 1.3  $\mu\text{m}$ , which imply also a prolonged residence in PAZ and sufficient annealing of fission tracks (Donelick et al., 2005<sup>[361]</sup>). Although fast annealing rates could be related to F-rich apatites, which is less resistant to annealing than Cl-rich apatites

(Carlson et al., 1999 <sup>[362]</sup>; Barbarand et al., 2003 <sup>[363]</sup>), no chemical composition has been analyzed for our samples to test it.

For ZHe ages, a slighter dispersion of single-grain ages is observed, compared to the AHe ages, and no clear correlation between single-grain ZHe age and eU content is observed (Figure 2.15B), therefore no single-grain age was abandoned. The average ZHe ages show a clear positive age-elevation correlation (Table 2.3, Figure 2.16A).

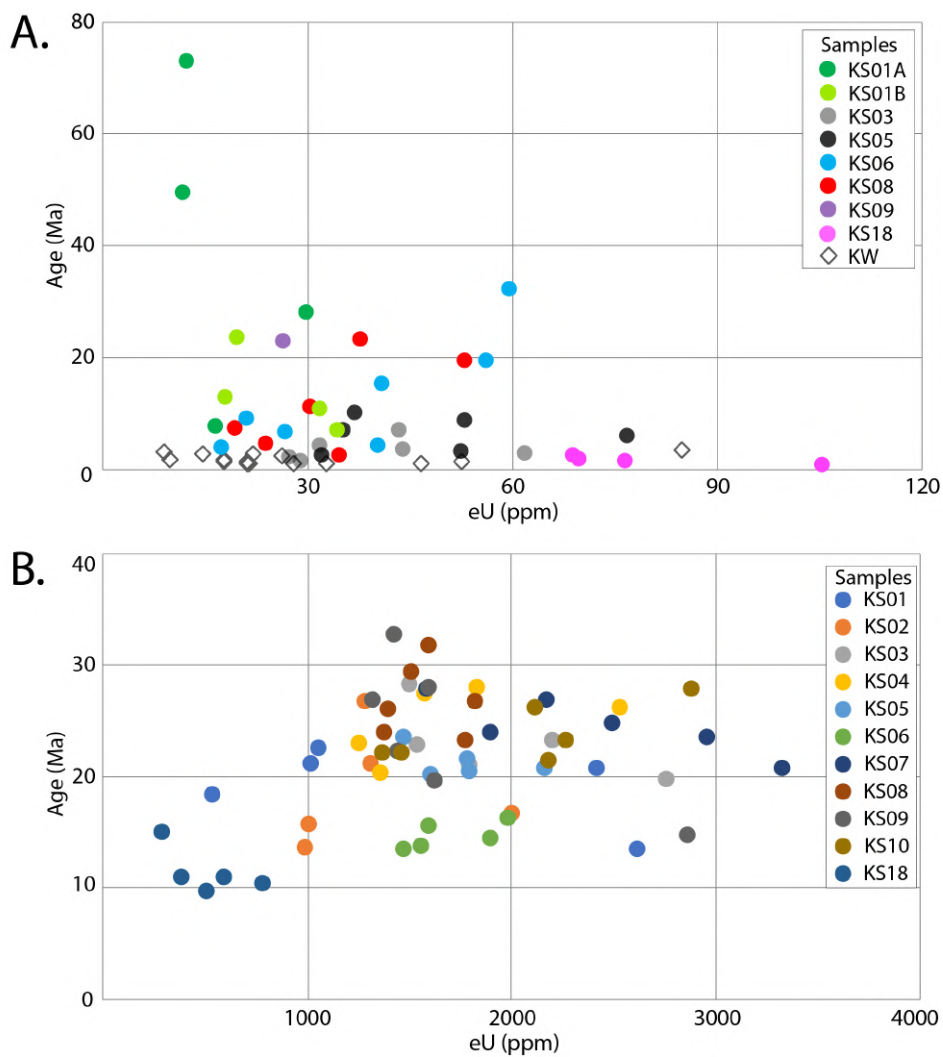


Figure 2.15 – AHe (A) and ZHe (B) ages plotted as a function of eU content.

### 2.2.2.3 Thermo-kinematic modelling method

The 3D thermal-kinematic model Pecube was used to quantify the exhumation history by combining our new dating results of low-temperature thermochronometers (Braun, 2003<sup>[297]</sup>; Braun et al., 2012<sup>[298]</sup>). Some default thermal and flexural parameters are presented in Table 2.1, of which some are optimized during the inversion. The base temperature is also fixed to 900 °C at a depth of 50 km in the crust of this region (Yao et al., 2010<sup>[313]</sup>; Wang et al., 2012<sup>[315]</sup>). A high resampling ratio of 90% during the inversion is adopted to make sure of sufficient exploration of the parameter space. For the results of inversion, a lowest misfit value  $\phi$  will be selected based on the equation (1), and the final results will be shown by scatter plots according to different parameter pairs and 1D or 2D marginal probability density functions (pdf's) of each parameter will be presented, to evaluate the credibility of inversed values (Braun et al., 2012<sup>[298]</sup>).

We first apply “steady-state topography scenarios” with only temporally varying rock exhumation rates considered, while sustaining the modern topography with no changes through time. “Tectonic scenarios” are adopted by implementing a fault (Robert et al., 2011<sup>[305]</sup>) for the Kawagebo massif, in order to model spatial variation of uplift above a crustal-scale fault rooting at a mid-crustal depth. In this scenario, the topography is also in steady state, and rock exhumation is due to slip motion along the fault.

Sample	Longitude	Latitude	Elevation (m)	AHe age (Ma)	2 $\sigma$ error (Ma)	# replicates	AFT age (Ma)	2 $\sigma$ error (Ma)	Grains	ZHe age (Ma)	2 $\sigma$ error (Ma)	# replicates
KS07	98.725	28.2584	4104	-	-	-	4.6	2.7	23	25.3	2,1	5
KS08	98.7278	28.2605	3935	6.6	3.2	4	9.7	2.1	27	26.7	3.7	6
KS09	98.7329	28.259	3697	-	-	-	11.8	3.1	28	23.9	3.6	6
KS04	98.7441	28.2354	3626	-	-	-	11	4.6	23	24.9	1.6	5
KS10	98.7343	28.2445	3504	-	-	-	7.4	3.2	26	23.7	2.9	6
KS03	98.7466	28.2355	3456	4.8	3.4	4	8.2	2.2	24	22.9	1.7	5
KS05	98.7545	28.2284	3418	8.6	5.7	3	14.2	4	24	21.2	1.9	5
KS01B	98.7705	28.2302	3368	13.1	1.9	1	3.8	2.4	30	19.1	1.3	5
KS02	98.7699	28.2255	3204	-	-	-	7.8	2	27	18.7	1.4	5
KW40	98.766	28.2013	2911	-	-	-	6.1	2.5	17	-	-	-
KS06	98.7764	28.2135	2859	6.9	3.1	3	10.5	3.1	24	14.6	1.4	5
KW41	98.7776	28.2063	2701	2.7	0.8	3	5.6	1	20	-	-	-
KW43	98.7932	28.2033	2595	1.5	0.4	4	3.2	1.2	20	-	-	-
KW42	98.7888	28.2022	2555	2.9	1.1	4	3	0.8	16	-	-	-
KW52	98.8503	28.1982	2224	1.2	0.1	4	-	-	-	-	-	-
MK04	98.8592	28.2648	2066	1.33	0.32	2	-	-	-	-	-	-
KS18	98.8598	28.2612	2076	1.7	2.3	4	-	-	-	11.3	1.4	5

Note that AHe ages reported here are averaged ages of single-grain ages of selected replicates, with details in and note that the AHe age of sample KW01B is from one replicate only. AFT ages are reported as pooled ages with 2 $\sigma$  uncertainty; see repository material for detail.

**Table 2.3** – Synthesis of low-temperature thermochronology data from the Kawagebo Massif, samples marked with KW are from the lower elevations in [Replumaz et al. \(2020\)<sup>\[151\]</sup>](#), with KS are from higher elevations in this study, and MK from [Yang et al. \(2016\)<sup>\[150\]</sup>](#).

### 2.2.3 3D thermal-kinematic modelling: timing and rate of exhumation in the Kawagebo massif

Published low temperature thermochronology data from low elevations of the Kawagebo massif, along the Yongzhi valley, show coherent young ages, with AHe ages between 1 and 4 Ma, AFT ages between 3 and 7 Ma, and a single ZHe age at ~8 Ma (Yang et al. 2016<sup>[150]</sup>; Replumaz et al., 2020<sup>[151]</sup>). Our newly collected data from higher elevation along the upstream Yongzhi valley give older more dispersed ages, with 5 AHe ages between 4.8 and 13.1 Ma, 10 AFT ages between 3.8 and 14.2 Ma and 11 ZHe ages between 11.3 and 26.7 Ma. We use all these age data together to model exhumation and related uplift histories since 32 Ma, the oldest age measured considering error bar. We first test “steady-state” scenarios and then “tectonic” scenarios for the Kawagebo massif, by implementing a thrust fault along the Mekong River, with the same fault geometry as suggested in Ou et al. (2021)<sup>[152]</sup>, aiming to determine the contribution of its activity to exhumation in the massif.

#### *“Steady-state topography” scenarios*

The steady-state topography scenario with no fault (homogenous vertical exhumation) and two exhumation phases (Model 1) since 32 Ma predicts a transition at 2.3 Ma, separating a slower exhumation (0.18 km/Myr) and a rapid exhumation (1.32 km/Myr), with a steep linear slope of the predicted ages with respect to elevation (misfit = 1.89) (Table 2.4). This scenario reproduces more or less the mean AHe ages within the error bar, but the modeled AFT ages are younger than the measured ones at high elevations >2500 m, while the ZHe ages are much older than the measured ones at low elevations <2500 m (Figure 2.16A). We then apply a steady-state topography scenario with three exhumation phases (Model 2), which predicts a first transition time at 10 Ma, separating a first fast exhumation (0.01 km/Myr) from a second phase with a moderate exhumation rate (0.47 km/Myr), and a second transition time at 2 Ma with a very fast third exhumation phase at a rate of 1.52 km/Myr (Table 2.4). In this scenario, the predicted AHe ages are similar to the ones of Model 1, the predicted AFT ages at high elevations are even younger, while the predicted ZHe ages are better reproduced (Figure 2.16A), resulting in a slightly smaller misfit with more parameters to fit (1.76). Homogenous vertical velocity field in both models is shown by the 3D representation of present-day state, exemplified by Model 3 (Figure 2.16B). In both models, a recent phase from ~2 Ma with very rapid exhumation rate (1.32 and 1.52 km/Myr) is required to reproduce the very young AHe and AFT ages at low elevations near the Mekong River.

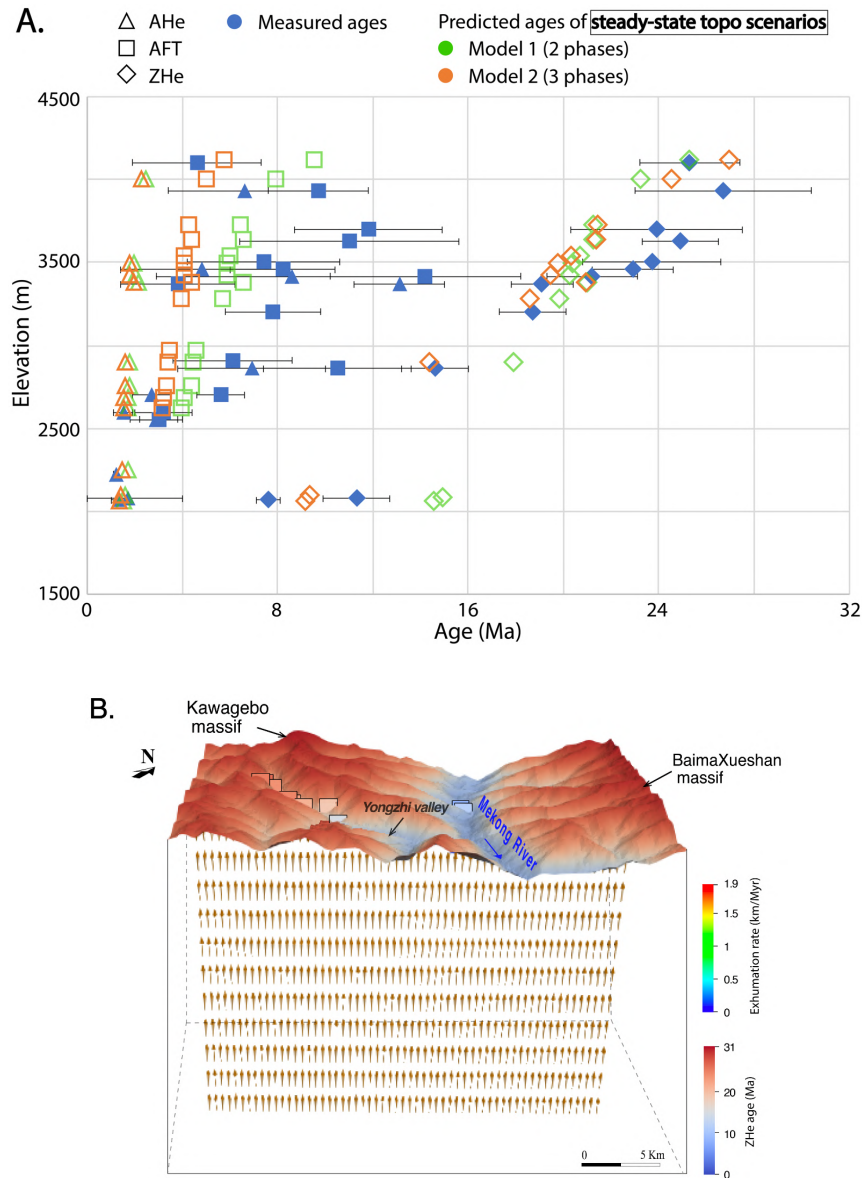


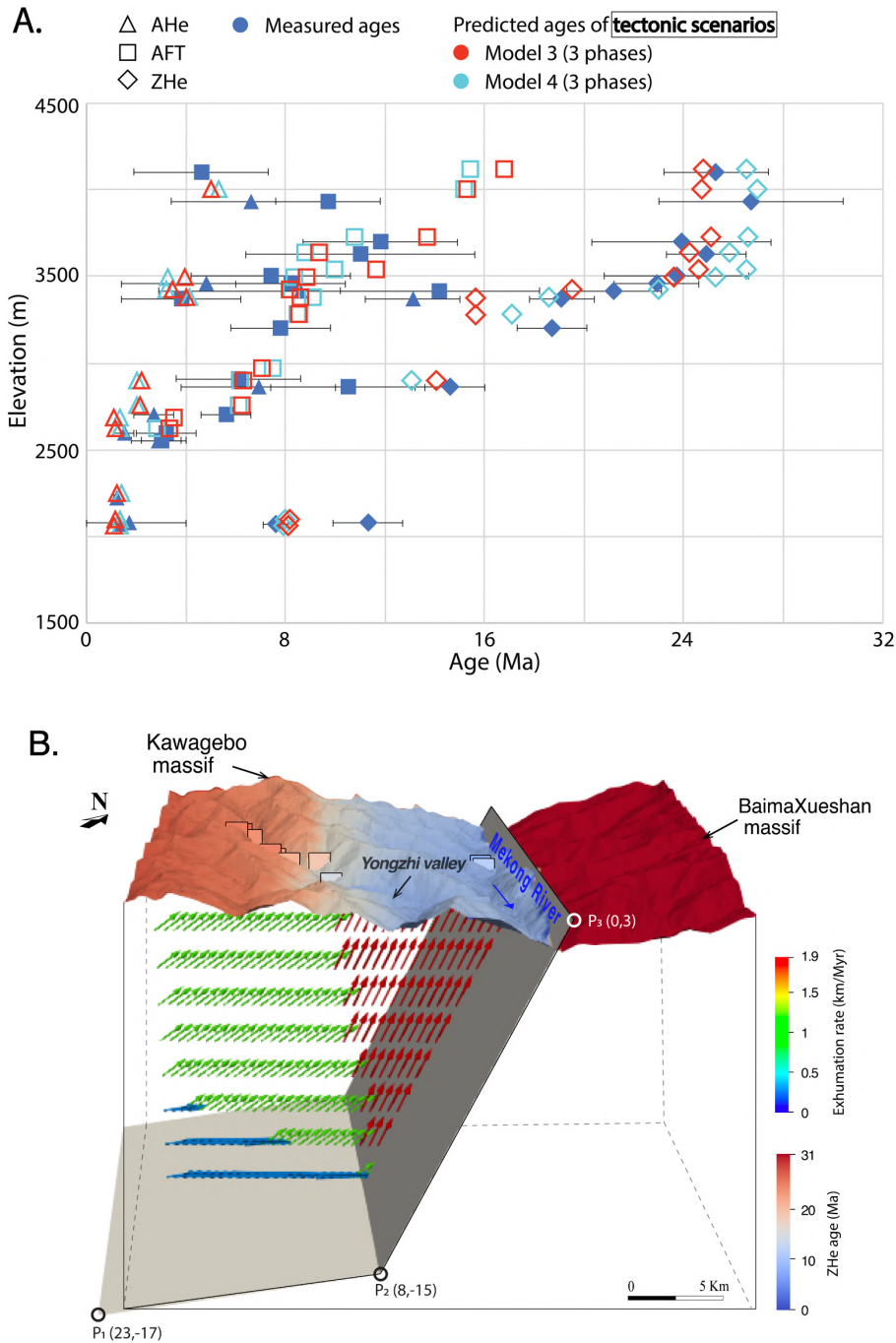
**Figure 2.16** – Modelling results of steady-state scenarios of the Kawagebo massif. (A) Age–elevation profiles of measured and predicted ages for scenarios with two and three exhumation phases. (B) 3D view of the present-day topography of the Kawagebo massif and the Mekong River valley, colored according to predicted ZHe ages of the scenario with three exhumation phases (Model 2). Squares indicates the sample locations. The arrows show the rock-particle trajectories and the present-day homogenous velocity field, generated by vertical movement during the recent rapid exhumation phase since 2 Ma.

***“Tectonic” scenarios***

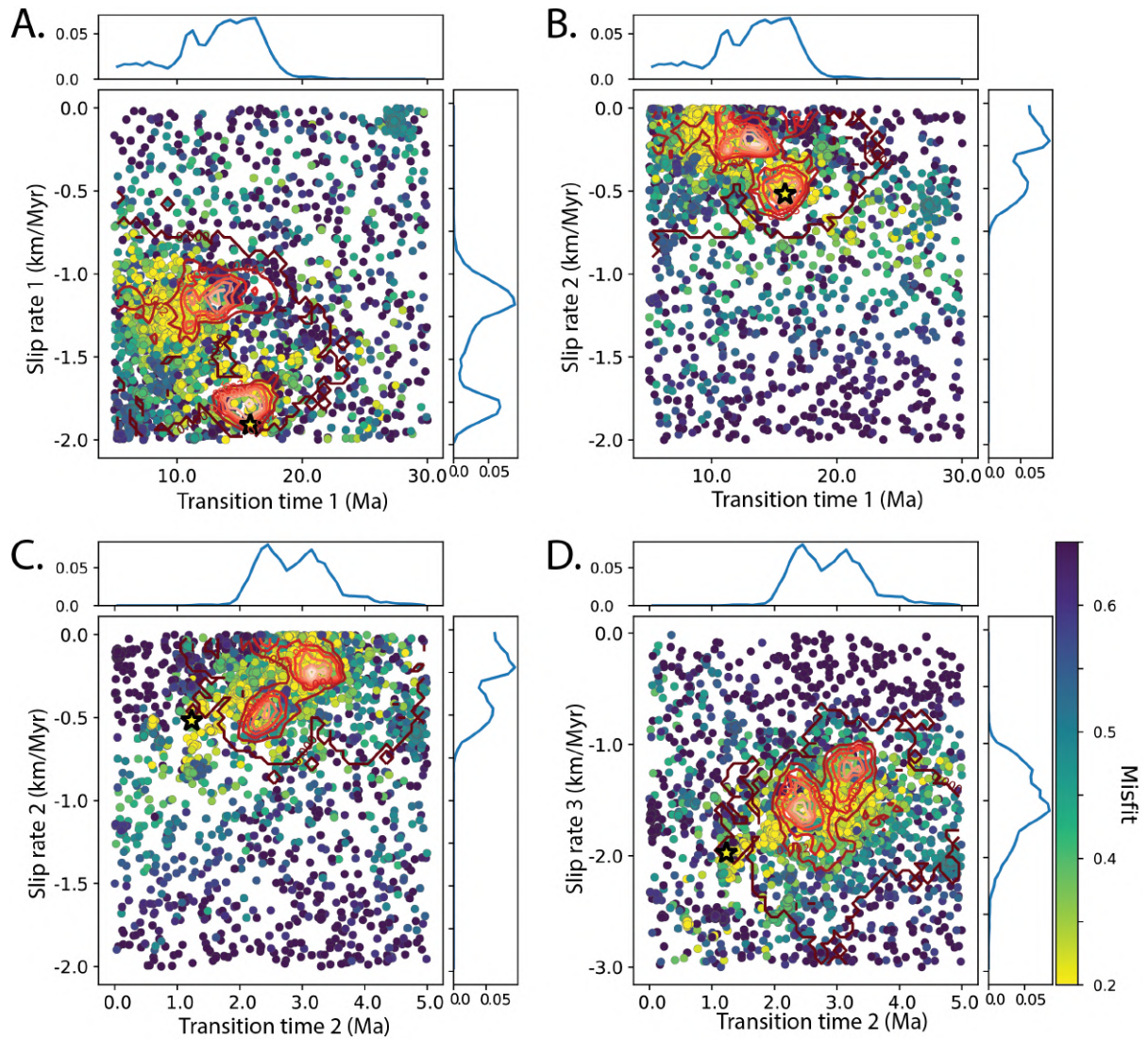
As demonstrated by the modelling results of samples at low elevations of the Kawagebo massif (section 2.1.5.2), spatially varying exhumation rates due to a curved fault at depth is needed to reproduce the age variations with respect to the distance to the fault trace and sample elevation, as

well as the slope break in age–elevation plot. We use the same fault geometry as obtained in [Ou et al. \(2021\)<sup>\[152\]</sup>](#), a kinked (two–segment) thrust with a steep shallow segment (dipping at 65° to the west) and a near–horizontal (1.5° dip) deeper segment, at a depth of 15 km, which best reproduced a simple velocity field coherent with the spatial repartition of the ages compared to the fault. A three exhumation phases (Model 3), leaving the two transition time free to be defined by the inversion, shows a slip rate of 1.91 km/Myr during the first exhumation phase between 32 Ma and 15.8 Ma, decreasing to 0.52 km/Myr until 1.3 Ma, then increasing to 1.97 km/Myr ([Table 2.4](#)). Decreasing exhumation rates are observed away from the imposed thrust roughly striking along the Mekong River, according to the velocity field produced by this model ([Figure 2.17B](#)). High exhumation rates are localized above the steep shallow segment of the thrust and much lower rates above the deep flat segment. The predicted AHe ages well reproduce the small slope break observed in the age–elevation slope above such spatial discontinuity in exhumation rates, but the young AHe ages are mainly sensitive to the fast most recent exhumation phase, and predictions are not very different from previous Model 1 and 2. In contrast, the predicted AFT and ZHe ages well reproduces the stronger slope break observed in the age–elevation slope above the discontinuity, much better than the linear one of Model 1 and 2 ([Figure 2.17A](#)). Timing and rates of this scenario are quite well constrained, as shown by the misfit scatterplots and the posterior pdf’s of parameter values ([Figure 2.18](#)).

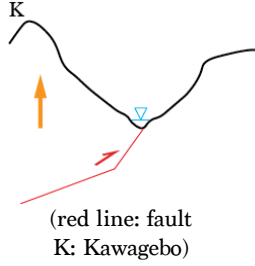
If we fix the second transition time to 2 Ma (Model 4) according to the previous modelling results from extremely young ages observed at low elevations ([Replumaz et al., 2020<sup>\[151\]</sup>](#); [Ou et al., 2021<sup>\[152\]</sup>](#)), the predicted ages are very similar, but the first transition time at 10.9 Ma is younger, with smaller exhumation rate of 1.11 km/Myr until 10.9 Ma, a second slower exhumation phase at a rate of 0.46 km/Myr until 2 Ma, and a third fast exhumation at a rate of 1.7 km/Myr ([Table 2.4](#)). This similarity in the predicted ages shows a relatively well–defined exhumation history, starting with a fast phase (32 to ~15–10 Ma), followed by a slow phase (~15–10 to 2–1.3 Ma) and an even faster phase (since 2–1.3 Ma), with some uncertainties in the transition times and related exhumation rates ([Figure 2.17A](#)).



**Figure 2.17** – Modelling results of tectonics scenarios with a two-segment thrust of the Kawagebo massif. (A) Age–elevation profiles of measured and predicted ages for scenarios with three and four exhumation phases. (B) 3D view of the present-day topography of the Kawagebo massif and the Mekong River valley, colored according to predicted ZHe ages of the Model 3, which is shown as an example, since different models predict very similar exhumations. The geometry of the thrust and rock-particle trajectories are shown at depth; with squares indicating the sample locations. The thrust geometry is defined by P1, P2, P3 and their coordinates in distance relative to the surface trace of thrust. The arrows show the present-day velocity field generated by movement along the fault, during the recent rapid exhumation phase since 1.3 Ma; the two-segment geometry leads to spatially varying exhumation rates (shown by colours, scale on the right).



**Figure 2.18** – Scatterplots of Pecube inversion results for tectonic scenario with a two-segment thrust (Model 3) of the Kawagebo massif. Coloured dots represent single forward-model runs plotted in two-dimensional projections of the parameter space, with colours corresponding to misfit values, shown on a log scale. Posterior probability density functions for parameter values are plotted along the axes. The best-fit solution is represented by a star with  $2\sigma$  (dark red) and  $1\sigma$  (light red) confidence contours. (A) Transition time 1 versus slip rate 1 along the fault during the first phase. (B) Transition time 1 versus slip rate 2 along the fault during the second phase. (C) Transition time 2 versus slip rate 2 along the fault during the second phase. (D) Transition time 2 versus slip rate 3 along the fault during the third phase.

Scenarios	Models	Inversed parameters	Misfit
<b>Steady-state topography scenario</b> 	Model 1 (2 phases)	32 Ma $\frac{-0.18 \text{ km/Myr}}{-}$ 2.3 Ma $\frac{-1.32 \text{ km/Myr}}{-}$ 0	1.89
	Model 2 (3 phases)	32 Ma $\frac{0.01 \text{ km/Myr}}{-}$ 10.0 Ma $\frac{-0.47 \text{ km/Myr}}{-}$ 1.95 Ma $\frac{-1.52 \text{ km/Myr}}{-}$ 0	1.76
<b>Tectonic scenario</b> 	Model 3 (3 phases)	32 Ma $\frac{-1.91 \text{ km/Myr}}{-}$ 15.8 Ma $\frac{-0.52 \text{ km/Myr}}{-}$ 1.3 Ma $\frac{-1.97 \text{ km/Myr}}{-}$ 0	1.54
	Model 4 (3 phases)	32 Ma $\frac{-1.11 \text{ km/Myr}}{-}$ 10.9 Ma $\frac{-0.46 \text{ km/Myr}}{-}$ 2* Ma $\frac{-1.70 \text{ km/Myr}}{-}$ 0	1.53

**Table 2.4** – Inversion parameters for the different scenarios tested for the Kawagebo massif. A range of exhumation rates is explored for different phases, separated by transition times. Note that the tectonic scenario includes a slip rate on the fault rather than a vertical exhumation velocity, and that upward slip on a thrust is indicated by negative values (see [Braun et al., 2012](#)<sup>[298]</sup> for more detail). \*: the transition times at 2 Ma in the Model 3 and 4 are fixed.

## 2.2.4 Discussion: Oligocene exhumation and tectonic deformation in the Kawagebo massif and its regional application

### 2.2.4.1 Regional exhumation patterns in the Three River Region since the Oligocene

Our new samples collected from the high elevations part (2800–4100 m) of the Kawagebo massif yield relatively young AHe (4.8–13.1 Ma), AFT (3.8–14.2 Ma) and especially young ZHe (11.3–26.7 Ma) ages (Table 2.4). We modelled this dataset of the newly acquired ages at high elevation of the Kawagebo massif, combined with published ages at lower part (Yang et al., 2016<sup>[150]</sup>; Replumaz et al., 2020<sup>[151]</sup>), by using a thermo-kinematic code. Our best-fit models is a tectonic scenario with a thrust dipping to the west, showing a first rapid exhumation phase between at least 32 to ~15–10 Ma, followed by a slower exhumation until ~2–1.3 Ma, before a new episode of acceleration in exhumation. Such thrust has not been identified in the field, but inferred to roughly follow the Mekong River in the Kawagebo region (Mekong thrust in Replumaz et al., 2020<sup>[151]</sup>), reactivating locally one of the N-S trending faults (Figure 2.13). The slip rate along the Mekong thrust during the first exhumation phase (1.11–1.91 km/Myr) related to the movement above the imposed thrust is approximately threefold as much as that deduced for the second exhumation phase (0.44–0.52 km/Myr) and is of the same order with the last recent exhumation phase (slip rate at 1.7–1.97 km/Myr).

The fault is a clear limit for low temperature thermochronology ages when comparing with the east flank of the Mekong River (Figure 2.19). Samples from similar elevations (3000–5000 m) of the Baimaxueshan massif shows slightly older AHe ages between 13.5–18.9 Ma, significantly older AFT ages of 13.5–56.6 Ma and ZHe ages of 78–104 Ma (Wilson and Fowler, 2011<sup>[144]</sup>; Liu-Zeng et al., 2018<sup>[157]</sup>). Thermal-kinematic modelling reveals a cooling phase since ~10 Ma with a nonnegligible influence of river incision rather than a pure regional tectonic forcing on exhumation (Ou et al., 2021<sup>[152]</sup>). Exhumation amount for the Kawagebo massif is estimated up to 10 km since 32 Ma, significantly higher than the exhumation (<3.5 km) on the Baimaxueshan massif. Similar differences are observed to the north, the Zuogong Plateau on the west flank of the Mekong River has a set of AHe ages from 14.9–28.7 Ma, AFT ages of 15.3–25.6 Ma with rather old ZHe ages of 37–60.2 Ma, indicating two episodes of rapid cooling at 36–34 Ma and 21–18 Ma (Xiao et al., 2015<sup>[159]</sup>; Cao et al., 2022<sup>[344]</sup>) (Table S. 2.7). Older ages (AHe, AFT >40 Ma) have been reported from the closely neighboring low-relief Markam plateau to the east of the river, suggesting a slower cooling phase between 40 and 30 Ma (Wilson and Fowler, 2011<sup>[144]</sup>; Cao et al., 2022<sup>[344]</sup>). Estimated exhumation of the Zuogong batholith reaches up to 8.0 km since 35 Ma, in contrast, the Markam plateau only experienced ~0.5 km of

exhumation since the Late Eocene (Cao et al., 2022<sup>[344]</sup>). To the south, numerous ZHe ages < 8 Ma have been also reported in valley bottom along the Salween River, younger than the ones along the Mekong River, which have been interpreted as a response to strong lateral shortening increasing toward the syntaxis due to the indentation by the northeast Indian plate corner (Yang et al., 2016<sup>[150]</sup>). While to the east, much older ages have been reported from the Weixi massif, modelled by a rapid cooling episode at 40–35 Ma (Yang et al., 2016<sup>[150]</sup>; Liu–Zeng et al., 2018<sup>[157]</sup>; Cao et al., 2022<sup>[344]</sup>).

Therefore, from the regional dataset, we clearly observe younging AFT and ZHe ages (<36 Ma) toward the syntaxis from the Salween River valley, Kawagebo and Zuogong massifs, west to the Longmucuo–Shuanghu suture, and older ages (>36 Ma) on the Markam, Baimaxueshan and Weixi massifs, east to the suture (Figure 2.19B, C). The younger ages, which have been modelled by a stronger exhumation west of the suture, makes it a prominent morphotectonic boundary, which delimits the high topography with an average elevation >5 km around the EHS (Ou et al., 2021<sup>[152]</sup>; Cao et al., 2022<sup>[344]</sup>) (Figure 2.11B, Figure 2.19, Figure 2.20A).

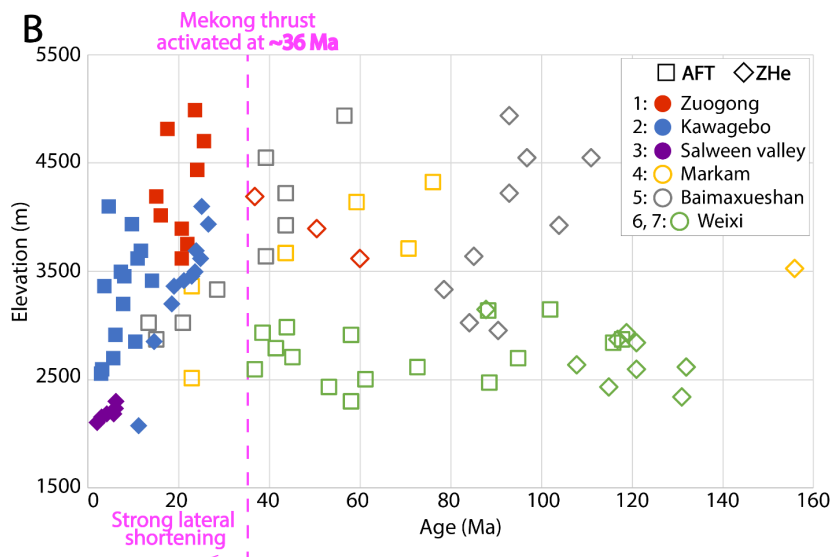
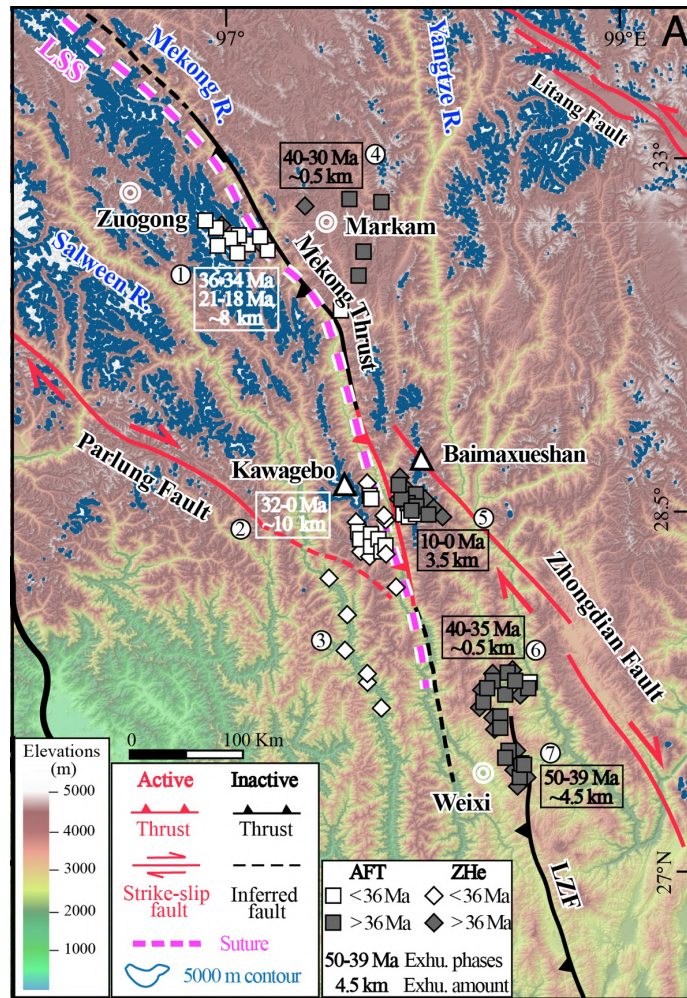


Figure 2.19 - (A) Topography and major tectonic structures of southeast Tibet, with the contour of 5000 m marked in blue. Compilation of AFT and ZHe ages in the Three Rivers Region, along vertical profiles from the

Zuogong plateau (1: [Xiao et al., 2015](#)<sup>[159]</sup>; [Cao et al., 2022](#)<sup>[344]</sup>), Markam plateau (3: [Wilson and Fowler, 2011](#)<sup>[144]</sup>; [Cao et al., 2022](#)<sup>[344]</sup>), Kawagebo (2: [Yang et al., 2016](#)<sup>[150]</sup>; [Replumaz et al., 2020](#)<sup>[151]</sup>; [this study](#)) and Baimaxueshan massifs (4: [Wilson and Fowler, 2011](#)<sup>[144]</sup>; [Liu-Zeng et al., 2018](#)<sup>[157]</sup>) and also Weixi plateau (5, 6: [Liu-Zeng et al., 2018](#)<sup>[157]</sup>; [Cao et al., 2019](#)<sup>[309]</sup>, [2022](#)<sup>[344]</sup>), from north to south in the core of the Three Rivers Region. Some very young ZHe ages (<10 Ma), reported in the Salween River valley (7: [Yang et al., 2016](#)<sup>[150]</sup>). The AHe ages of these locations are not included, since they are largely influenced by river incision. (B) Age–elevation plot of compiled ages, with young ages (<36 Ma) west of the Mekong thrust (active since ~36 Ma) ([Cao et al., 2022](#)<sup>[344]</sup>; [this study](#)), and old ages (>36 Ma) east of it. B: Baimaxueshan; K: Kawagebo; LSS: Longmucuo–Shuanghu Suture; LZP: Ludian–Zhonghejiang Thrust Fault; RRF: Red River Fault.

#### 2.2.4.2 Tectonic evolution in the Kawagebo massif: regional implication in the southeastern Tibetan Plateau

Despite the difficulty to determine the precise transition time separating each exhumation phase, the enhanced activity of the Mekong thrust, between 32 Ma and ~15–10 Ma in the Kawagebo massif (this study) or of the Lancangjiang thrust during 36–34 Ma and 21–18 Ma near the Zuogong plateau ([Cao et al., 2022](#)<sup>[344]</sup>), both roughly following the Longmucuo–Shuanghu suture, is roughly contemporaneous with the large-scale horizontal extrusion of the Indochina block during the Early Oligocene to Early Miocene in response to the India–Asia collision. The timing of this deformation phase is also difficult to determine, with different estimations depending on the shear zones studied. The block slides along the sinistral Ailaoshan–Red River shear zone from 34 Ma to 17 Ma to the east (e.g., [Leloup et al., 2001](#)<sup>[32]</sup>; [Cao et al., 2011](#)<sup>[364]</sup>; [Wang et al., 2020](#)<sup>[365]</sup>) ([Figure 2.20A, B](#)) and along the dextral Gaoligong shear zone from 32 to 10 Ma to the west ([Wang et al., 2006](#)<sup>[335]</sup>; [Zhang et al., 2012](#)<sup>[336]</sup>). In between, the dextral Chongshan shear zone has been active from 34 to 14 Ma in the north (Biluoexuehan massif), and from 32 to 22 Ma in the south ([Zhang et al., 2012](#)<sup>[337]</sup>). Nevertheless, such shear zones accommodate mostly the lateral extrusion of the Indochina block southeast of the EHS, as shown in analogue extrusion models (e.g., [Tapponnier et al., 1982](#)<sup>[29]</sup>; [Peltzer and Tapponnier, 1988](#)<sup>[30]</sup>) ([Figure 1.5](#)), while east and north of it, the prevailing deformation during this period is shortening due to strong lateral contraction of the indenting EHS ([Hallet and Molnar, 2001](#)<sup>[116]</sup>; [Yang et al., 2016](#)<sup>[150]</sup>) ([Figure 1.23](#), [Figure 2.20B](#)). Locally, as shown in this study, strong SW–NE shortening occurred west of the Longmucuo–Shuanghu suture, resulting in higher topography >5000 m around the EHS ([Figure 2.20A](#)). Furthermore, similar N–S to NW–SE trending and inactive thrusts, pervasively observed in the “Three Rivers Region”, are in the continuity of the arcuate belt of Paleogene syncontractual basins and bounding thrust belts around the EHS across the Qiangtang terrane, active between Early Eocene and Late Oligocene (e.g., [Horton et al., 2002](#)<sup>[91]</sup>; [Spurlin et al., 2005](#)<sup>[176]</sup>; [Wang et al., 2008](#)<sup>[78]</sup>; [Staisch et al., 2016](#)<sup>[182]</sup>; [Studnicki-Gizbert et al., 2008](#)<sup>[177]</sup>) ([Figure 1.24](#)).

Contemporaneous shortening in the eastern margin of Yidun terrane took place between 42 and 25 Ma along the eastern Jinsha suture (Jackson et al., 2018<sup>[345]</sup>, 2020<sup>[346]</sup>). In contrast, farther to east, early phase of shortening in the “Great Bends Region” occurred under a NW–SE compressional regime, almost perpendicular to the shortening direction in the Three Rivers Region. For instance, the Longmenshan thrust belt, bounding the South China craton, was firstly active during 30–20 Ma (Godard et al., 2009<sup>[158]</sup>; Wang et al., 2012<sup>[120]</sup>; Tian et al., 2013<sup>[70]</sup>, 2015<sup>[145]</sup>; Tan et al., 2014<sup>[300]</sup>), the Jiulong thrust was activated between 35 and 30 Ma (Zhang et al., 2016<sup>[121]</sup>), and the Yulong thrust was active during 28–20 Ma (Cao et al., 2019<sup>[309]</sup>) (Figure 2.20A). Further to the southeast of the plateau margin, similar thrusting events have been recognized for the sinistral Anninghe strike slip–fault between ~24–18 Ma (Wang et al., 2020<sup>[366]</sup>) or along the neighboring ~N–trending Yuanmou antiform between 40–28 Ma (Zhang et al., 2022<sup>[367]</sup>) as well as for NW–striking Chuxiong fault, closely parallel to the Ailaoshan–Red River shear zone between 35–26 Ma (Li et al., 2020<sup>[368]</sup>) (Figure 2.20A, B).

Such regional transpressional stress regime during the Late Eocene–Late Oligocene has played a significant role in the crustal thickening of the Southeastern and Eastern Tibetan Plateau, which is directly evidenced by surface uplift determined by paleo-elevation studies (Figure 1.29). Indeed, the uplift of the Nangqian–Yushu basin to its present-day elevation earlier than 36 Ma (Spurlin et al., 2005<sup>[176]</sup>). Consistently, the Gonjo Basin has been brought up to an elevation of ~4000 m since at least ~40 Ma (Tang et al., 2017<sup>[209]</sup>; Xiong et al., 2020<sup>[210]</sup>) and the Markam Basin reached an elevation of ~3000 m at ~34 Ma, then rising to its present elevation (~3900 m) in the early Oligocene (Li et al., 2015<sup>[179]</sup>; Su et al., 2019<sup>[97]</sup>). Further south, careful evaluation of the depositional age and paleoelevation of the Jianchuan basin (Gourbet et al., 2017<sup>[181]</sup>; Wu et al., 2018<sup>[212]</sup>) reassigned a significantly lower altitude (1200 ± 1200 m) in the late Eocene, although previous studies suggested an elevation at ~3300 m by ~35 Ma (Hoke et al., 2014<sup>[211]</sup>; Li et al., 2015<sup>[179]</sup>). The Lanping basin attained 3300 ± 450 m, higher than its present-day elevation of 2700 m, around 15 Ma (Hoke et al., 2014<sup>[211]</sup>; Li et al., 2015<sup>[179]</sup>). Such significant crustal thickening and surface uplift are consistent with the initiation of enhanced accumulation rates of clastic sediments since 34 Ma in the epicontinental marine basins in the East and Southeast Asia, interpreted as evidences of significant erosion of high topography in source region of the southeastern Tibetan Plateau (e.g., Cliff et al., 2006<sup>[167]</sup>; 2014<sup>[237]</sup>) (Figure 1.34).

Between ~17 and ~10 Ma, the extrusion along the large-scale shear zones in the Indochina terrane ceased, and the region north of the dextral Jiali–Zhongdian–Red River faults and south of the sinistral Ganzi–Xianshuihe–Xiaojiang faults began to be extruded with tectonic deformation style turning to be dominated by strike–slip shearing, except some reactivation of thrust belts (Figure 2.20C). For

example, reactivation of the Longmenshan thrust belt since 10 Ma was recognized under the continuing NW–SE compressional regime (Godard et al., 2009<sup>[158]</sup>; Wang et al., 2012<sup>[120]</sup>; Tian et al., 2013<sup>[70]</sup>, 2015<sup>[145]</sup>; Tan et al., 2014<sup>[300]</sup>) (Figure 2.20A). The Jiulong thrust was reactivated during 9–6 Ma (Zhang et al., 2016<sup>[121]</sup>) and the Muli thrust experienced strong exhumation since  $12.5 \pm 1$  Ma (Pitard et al., 2021<sup>[123]</sup>), before being offset by the sinistral Ganzi–Xianshuihe strike–slip fault toward southeast since ~9 Ma (Zhang et al., 2017<sup>[140]</sup>; Bai et al., 2018<sup>[310]</sup>). Contemporaneously, the Kawagebo massif, located in a constraining bend due to a left–stepping between dextral Jiali–Parlung and Zhongdian strike–slip faults, continues to be locally uplifted since ~15–10 Ma, but with a much slower exhumation rate (0.42–0.52 km/Myr) than the first exhumation phase, prior to a new phase of accelerated exhumation at ~2–1.3 Ma.

## 2.2.5 Conclusion

The Cenozoic tectonic deformation history in the Three Rivers Region, immediately east to the Eastern Himalayan Syntaxis (EHS), is hard to be estimated because of the superposition of successive deformation in response to the continuous indentation of Indian continent. This study presents new low temperature thermochronology data from the high–relief and high–elevation Kawagebo massif, in the core of the Three Rivers Region (Figure 2.20A). These new ages complement formerly collected dataset and thermal–kinematic modelling results reveal a first episode of rapid exhumation (amount of ~10 km) since at least 32 Ma to ~15–10 Ma, with a very rapid slip rate above the thrust (1.11–1.91 km/Myr) in the Kawagebo massif. These are consistent with recent results of strong but smaller exhumation (~8 km during 36–34 Ma and 21–18 Ma) and older ZHe ages (38–60 Ma) on the Zuogong plateau in the north, as well as strong exhumation with even younger ZHe ages (<8 Ma), along the Salween River in the south. This rapid exhumation phase is limited by the Longmucuo–Shuanghu suture zone, revealing more crustal shortening and surface uplift west of the suture, which result from strong SW–NE lateral compression increasing toward the EHS, due to the indentation of India corner. This main phase of shortening is contemporaneous with the large–scale southeastward extrusion of the Indochina block, estimated between 34 and 10 Ma depending on the shear zones considered (Figure 2.20B). The Longmucuo–Shuanghu suture delimits the high topography with an average elevation >5 km around the EHS. East of the suture, previous thermochronology dataset from the Markam, Baimaxueshan and Weixi sections all show much older ages (AFT, ZHe >36 Ma), slower and less exhumation (<3.5 km) (Figure 2.19). Less intense NW–SE compression is pervasively recorded

along main thrust belts across the eastern and southeastern Tibet east of the suture with an almost perpendicular trending, resulting in great bends in the regional rivers, bordering the South China craton.

A second slower exhumation phase (rate of 0.42–0.52 km/Myr) of the Kawagebo massif since ~15–10 Ma to ~2–1.3 Ma, due to local uplift in a left-stepping between dextral Jiali–Parlung and Zhongdian strike-slip faults, witnessed a transition of extrusion from the Indochina block to the region between the dextral Jiali–Zhongdian–Red River faults and sinistral Ganzi–Xianshuihe–Xiaojiang faults north of it (Figure 2.20C). A reactivation of Longmenshan–Yalong thrust belts occurred since Middle Miocene due to the continuing NW–SE compression related to this extrusion transition to the north. The Kawagebo massif is therefore located at a key place to record both deformation phases, making its study of great interest to understand and quantify the deformation in southeast Tibet.

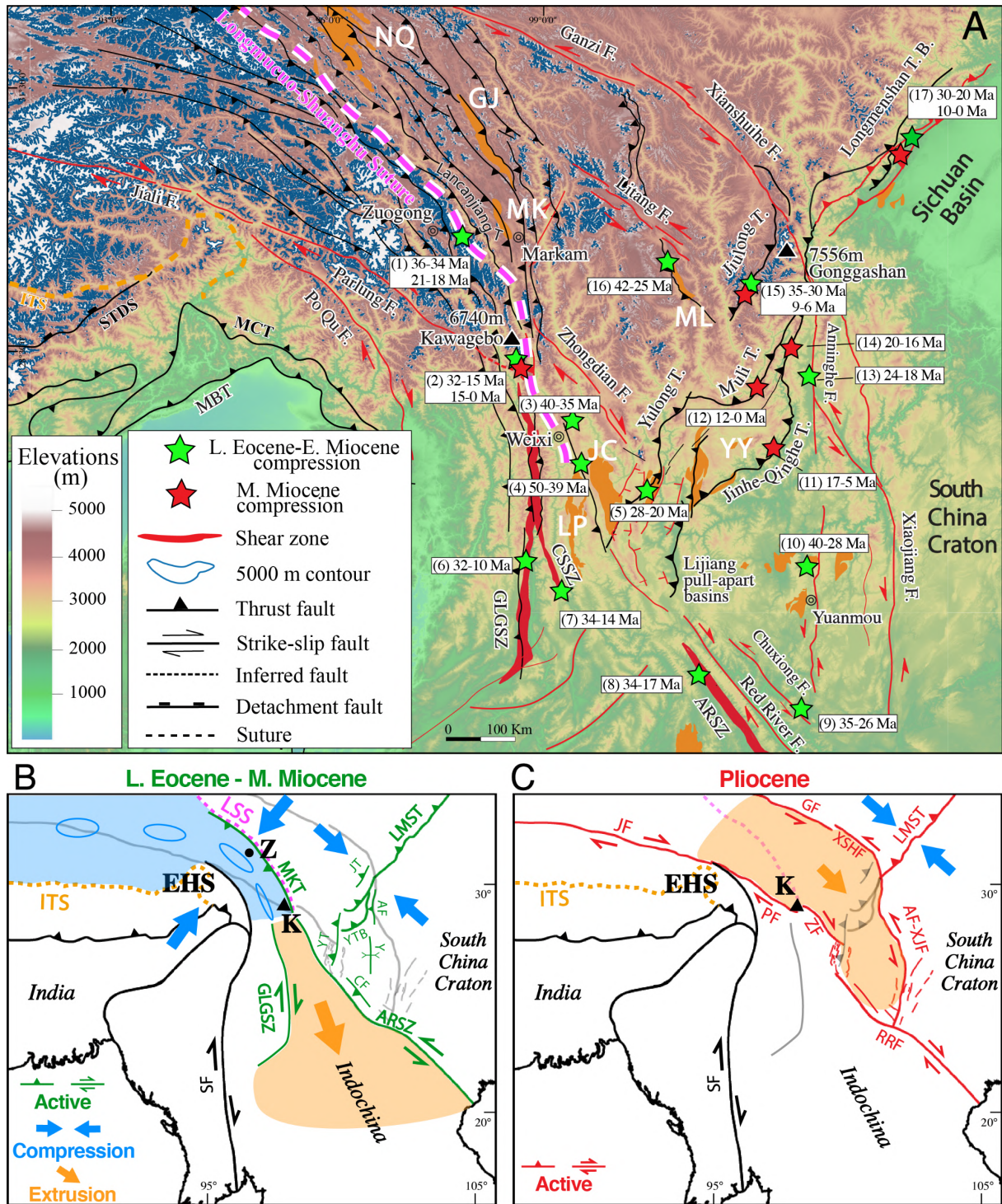


**Figure 2.20** – (A) Topography and major tectonic structures of the southeastern and eastern Tibet, with rapid exhumation related to main tectonic structures, marked in stars. The Longmucuo-Shuanghu suture delimits the extend of 5000 m contour of elevation. Thermochronology data are from (1) Xiao et al., 2015<sup>[159]</sup>; Cao et al. (2022)<sup>[344]</sup>; (2) this study; (3) Liu-Zeng et al. (2018)<sup>[157]</sup>; Cao et al. (2022)<sup>[344]</sup>; (4) Cao et al. (2020)<sup>[122]</sup>; (5) Cao et al. (2019)<sup>[309]</sup>; (6) Wang et al. (2006)<sup>[335]</sup>; Zhang et al. (2012)<sup>[336]</sup>; (7) Zhang et al. (2012)<sup>[337]</sup>; (8) Leloup et al. (2001)<sup>[32]</sup>; Cao et al. (2011)<sup>[364]</sup>; Wang et al. (2020)<sup>[365]</sup>; (9) Li et al. (2020)<sup>[368]</sup>; (10) Zhang et al. (2022)<sup>[367]</sup>; (11)

Wang et al. (2012)<sup>[348]</sup>; (12) Pitard et al. (2021)<sup>[123]</sup>; (13) Wang et al. (2020)<sup>[366]</sup>; (14) Zhu et al. (2021)<sup>[124]</sup>; (15) Zhang et al. (2016)<sup>[121]</sup>; (16) Jackson et al. (2018)<sup>[345]</sup>; (17) Godard et al., 2009<sup>[158]</sup>; Wang et al., 2012<sup>[120]</sup>; Tian et al., 2013<sup>[70]</sup>, 2015<sup>[145]</sup>; Tan et al., 2014<sup>[300]</sup>. (B) Compression took place synchronously with large-scale block extrusion during Late Eocene–Mid Miocene, shown on present-day tectonic frame. Ellipses represent the magnitude and direction of the crustal strains in response to lateral compression of the indenting EHS, with strongest shortening in the Three Rivers Region east of the EHS, modified from Hallet and Molnar, 2001<sup>[116]</sup>. (C) Region north of the ARSZ is extruded at Pliocene, with a reactivation of thrusting along the Longmenshan thrust belt. AF: Anninghe Fault; AF–XF: Anninghe–Xiaojiang Fault; ARSZ: Ailaoshan–Red River Shear Zone; CF: Chuxiong Fault; EHA: Eastern Himalayan Syntaxis; GF: Ganzi Fault; GLGSZ: Gaoligong Shear Zone; ITS: Indus–Tsangpo Suture; JT: Jiulong Thrust; K: Kawagebo Massif; LMS: Longmenshan Thrust Belt; LSS: Longmucuo–Shuanghu Suture; MT: Mekong Thrust; MBT: Main Boundary Thrust; MCT: Main Central Thrust; MT: Muli Thrust; PF: Parlung Fault; RRF: Red River Fault; SF: Sagaing Fault; STDS: Southern Tibet Detachment System; XSHF: Xianshuihe Fault; Y: Yuanmou Anticline; YT: Yulong Thrust; YTB: Yalong Thrust Belt; Z: Zuogong Plateau; ZF: Zhongdian Fault; Eocene basins from north to south: NQ: Nangqian Basin; GJ: Gonjo Basin; MK: Markam Basin; ML: Mula Basin; YY: Yanyuan Basin; JC: Jianchuan Basin; LP: Lanping Basin.

## 2.2.6 Supplementary materials: low-temperature thermochronology data and thermo-kinematic modelling

### 2.2.6.1 Dataset

I collected a new dataset of low-temperature thermochronology (details of AHe, AFT, ZHe in Table S. 2.2, Table S. 2.3, Table S. 2.4, respectively) during a field mission of 2019 in the high elevation part of the Kawagebo Massif, near the Deqin city of Yunnan Province, to complete the existing dataset in the lower elevation of the Kawagebo massif from the precedent mission in 2015 (Yang et al., 2016<sup>[150]</sup>; Replumaz et al., 2020<sup>[151]</sup>) (Table S. 2.5, Table S. 2.6). All the samples are collected from granite or granitoid intrusion body or massif. I also compiled the recently published data from the Zuogong Plateau (Cao et al., 2022<sup>[122]</sup>) (Table S. 2.7.) in the north of the Kawagebo massif in the Three Rivers Region, locations shown in the Figure 2.13. To note that the altitude for each samples is re-acquired from GoogleEarth by using their original GPS coordinates because of important approximation and inaccuracy of the measured altitude in place.

**Table S. 2.2** – Synthesis of **new AHe** data collected from high elevations of the Kawagebo Massif. To notice that several samples have 2 or 3 apatite grains in the same tube to go through the measurement process because of small size of grains. The final age, with two sigma errors, is corrected by an alpha-ejection correction parameter  $F_T$  after [Farley et al. \(2002\)](#)<sup>[358]</sup>. ESR is equivalent spherical radius from [Gautheron and Tassan-Got \(2010\)](#)<sup>[351]</sup>, the effective uranium content is defined by  $[eU] = U + 0.235 \times Th$  ppm.

Sample	Lon.	Lat.	Ele. (m)	Length ( $\mu m$ )	Width ( $\mu m$ )	Thickness ( $\mu m$ )	Grain Nb.	ESR ( $\mu m$ )	$F_T$	U	Th	eU (ppm)	4He (ppm)	Raw AHe age (Ma)	Corrected AHe age (Ma)	2 $\sigma$ error (Ma)
KS01A-5	98.7705	28.2302	3368	100	88	67	1	41.5	0.719	9.7	7.0	12	496.0	35.8	49.8	11.2
KS01A-6				109	97	70	1	37.9	0.687	9.8	8.5	12	723.9	50.3	73.2	7.2
KS01A-7				140	80	70	2	40.1	0.663	18.4	46.4	30	672.0	18.9	28.5	2.1
				73	70	69										
KS01A-8				118	98	96	2	39.3	0.734	13.2	13.4	17	115.3	5.8	7.9	1.1
				89	78	77										
KS01B-4	98.7705	28.2302	3368	117	99	99	1	48.5	0.787	16.0	7.2	18	221.3	10.3	13.1	1.9
KS01B-6				87	68	62	2	31.7	0.63	20.0	59.3	34	185.2	4.5	7.1	2.0
				69	61	61										
KS01B-7				80	61	59	2	29.5	0.62	19.1	52.2	32	265.5	7.0	11.2	4.2
				71	66	66										
KS01B-8				101	64	64	3	33.1	0.682	10.9	35.3	20	380.9	16.3	24.0	2.5
				78	77	71										
				68	62	61										
KS03-1	98.7466	28.2355	3456	115	87	87	1	42.4	0.723	24.9	28.0	32	129.7	3.4	4.7	0.8
KS03-2				111	98	98	1	47.4	0.785	53.9	33.1	62	189.1	2.5	3.2	0.4
KS03-4				130	124	124	1	54.8	0.747	37.5	26.8	44	154.4	2.9	3.9	0.7
KS03-5				110	73	73	1	37.2	0.68	38.0	21.5	43	262.7	5.0	7.4	1.5
KS03-7				121	79	74	2	40.4	0.702	24.7	17.7	29	45.0	1.3	1.8	0.6
				123	85	68										
KS03-9				147	116	107	2	57	0.807	21.6	22.3	27	68.9	2.1	2.6	0.5
				136	132	118										

KS05-1	98.7545	28.228	3418	88	64	63	1	31.6	0.632	60.7	65.4	77	365.7	4.0	6.3	2.4
KS05-2				80	76	75	1	33.6	0.67	41.8	45.8	53	386.3	6.1	9.1	1.8
KS05-6				105	96	89	1	45.4	0.777	26.4	41.8	37	357.5	8.1	10.5	1.5
<del>KS05-7</del>				87	81	69	2	35.9	0.71	22.7	38.8	32	73.2	1.9	2.7	1.0
				99	66	65										
KS05-8				69	69	65	2	38.9	0.712	24.2	44.7	35	222.5	5.3	7.4	0.9
				130	87	76										
KS05-9				96	64	61	2	34	0.671	32.6	81.6	52	142.6	2.3	3.4	1.6
				95	74	66										
KS06-1	98.7764	28.2135	2859	153	94	93	1	48.9	0.75	13.2	31.7	21	174.7	7.0	9.3	1.2
<del>KS06-2</del>				100	90	88	1	40.8	0.722	28.6	49.7	41	547.1	11.2	15.5	1.6
<del>KS06-3</del>				85	79	74	1	37.2	0.732	41.6	73.5	60	1706.3	23.9	32.6	2.9
KS06-4				123	113	104	1	50.3	0.771	17.9	91.6	40	163.5	3.4	4.4	0.5
KS06-6				122	104	87	1	46.6	0.749	18.3	33.7	27	167.3	5.3	7.0	1.3
<del>KS06-7</del>				78	78	73	2	31.2	0.647	13.1	16.6	17	57.1	2.8	4.3	1.8
				67	63	61										
KS06-8				72	66	60	2	28.7	0.612	32.4	97.8	56	816.3	12.1	19.8	1.8
				71	60	59										
KS08-1	98.7278	28.2605	3935	106	96	81	1	42.4	0.729	28.6	38.1	38	783.1	17.2	23.6	2.1
KS08-2				155	117	92	1	55.8	0.805	23.5	27.9	30	331.0	9.1	11.3	1.0
KS08-4				127	101	97	1	48.1	0.755	14.6	19.0	19	134.6	5.8	7.7	1.0
<del>KS08-5</del>				132	121	117	1	54.3	0.788	24.8	40.4	35	86.7	2.1	2.6	0.5
KS08-6				100	98	86	1	44.8	0.778	18.7	21.1	24	109.4	3.8	4.9	0.7
<del>KS08-8</del>				104	88	84	2	60	0.813	43.1	40.7	53	841.0	13.2	19.7	2.8
				162	144	116										
<del>KS09-2</del>	98.7329	28.2590	3697	177	84	80	1	46.3	0.747	19.5	27.5	26	542.4	17.2	23.0	2.6
KS18-1	98.859	28.2658	2076	117	90	80	1	43.5	0.73	51.9	69.9	69	156.0	1.9	2.6	0.4
KS18-2				109	99	99	1	44.8	0.745	52.5	70.7	70	112.2	1.3	1.8	0.5
KS18-3				82	78	70	1	36.2	0.681	82.4	94.4	105	90.0	0.7	1.0	0.9
KS18-4				100	99	86	1	45	0.7	62.1	60.3	77	98.5	1.1	1.5	0.5

**Table S. 2.3** – Synthesis of **new AFT** ages collected from high elevations of the Kawagebo Massif. All ages in the table are pooled ages, with two sigma errors, except the KS04, whose has a central age because of its  $P(\chi^2)$  smaller than 0.05.  $\rho_s$ ,  $\rho_i$ ,  $\rho_d$  represent spontaneous, induced and standard glass track densities;  $N_s$ ,  $N_i$ ,  $N_d$  are numbers of spontaneous, induced and standard glass tracks.  $N_d$ ,  $N_s$ ,  $N_i$  are corresponding number of grains counted. Due to the lack of spontaneous tracks in sample minerals, no mean confined horizontal track length was observed and measured.

Sample	Lon.	Lat.	Ele. (m)	Grain Nb.	$\rho_d \times 10^4$ (tracks/cm <sup>-2</sup> ) (Nd)	$\rho_s \times 10^4$ (tracks/cm <sup>-2</sup> ) (Ns)	$\rho_i \times 10^4$ (tracks/cm <sup>-2</sup> ) (Ni)	U $\pm 2\sigma$	P( $\chi^2$ ) %	AFT age (Ma)	2 $\sigma$ error (Ma)	Dpar $\pm 1\sigma$ error ( $\mu m$ )
KS01B	98.7705	28.2302	3368	30	160 (5366)	3.04 (15)	1.72 (848)	16 $\pm 1$	79.8	3.8	2.4	1.12
KS02	98.7699	28.2255	3204	27	160 (5366)	10.4 (90)	279 (1357)	26 $\pm 1$	29.6	7.8	2	1.30
KS03	98.7466	28.2355	3456	24	161 (5367)	9.18 (83)	236 (2134)	22 $\pm 1$	98.2	8.2	2.2	1.24
KS04	98.7441	28.2354	3626	23	161 (5367)	11.3 (95)	253 (2125)	24 $\pm 1$	0	*11	4.6	1.19
KS05	98.7545	28.228	3418	24	162 (5367)	13.8 (76)	207 (1137)	19 $\pm 1$	35.9	14.2	4.0	1.15
KS06	98.7764	28.2135	2859	24	162 (5367)	11.4 (67)	230 (1354)	21 $\pm 1$	37.3	10.5	3.1	1.14
KS07	98.725	28.2584	4104	23	162 (5367)	3.93 (18)	182 (833)	17 $\pm 1$	42.5	4.6	2.7	1.11
KS08	98.7278	28.2605	3935	27	163 (5369)	15.2 (129)	335 (2849)	31 $\pm 1$	62.2	9.7	2.1	1.19
KS09	98.7329	28.2590	3697	28	163 (5369)	11.9 (85)	215 (1543)	20 $\pm 1$	90.6	11.8	3.1	1.19
KS10	98.7343	28.2445	3504	26	164 (5368)	6.15 (29)	180 (850)	17 $\pm 1$	84.3	7.4	3.2	1.06

**Table S. 2.4** – Synthesis of **new ZHe** ages collected from high elevations of the Kawagebo Massif. The final age, with two sigma errors, is corrected by an alpha-ejection correction parameter  $F_T$  after [Farley et al. \(2002\)](#) <sup>[358]</sup>. ESR is equivalent spherical radius, the effective uranium content is defined by  $[eU] = U + 0.235 \times Th$  ppm.

Sample	Lon.	Lat.	Ele. (m)	ESR ( $\mu m$ )	$F_T$	U	Th	eU (ppm)	4He (nmol/g)	Raw AHe age (Ma)	Corrected AHe age (Ma)	2 $\sigma$ error (Ma)
KS01B-z1	98.7705	28.2302	3368	41.5	0.71	954.6	481.2	1067.7	91.5	15.9	22.4	0.3
KS01B-z2				45.9	0.74	962.3	259.8	1023.3	85.2	15.4	21.0	0.3
KS01B-z3				42.7	0.71	428.5	514.7	549.4	38.5	13.0	18.2	0.2
KS01B-z4				43.6	0.72	2240.2	776.0	2422.6	194.6	14.9	20.6	0.3
KS01B-z5				40.7	0.70	2436.2	778.7	2619.2	132.4	9.4	13.3	0.2
KS02-z1	98.7699	28.2255	3204	51.8	0.76	1273.0	183.9	1316.2	114.3	16.1	21.1	0.4
KS02-z2				51.2	0.76	926.8	368.0	1013.3	65.1	11.9	15.7	0.1
KS02-z3				55.5	0.78	926.0	302.7	997.1	56.4	10.5	13.5	0.4
KS02-z4				41.7	0.71	1856.7	664.6	2012.9	127.5	11.7	16.5	0.1
KS02-z5				48.3	0.75	1167.8	508.9	1287.4	138.7	19.9	26.7	0.4
KS03-z1	98.7466	28.2355	3456	39.6	0.70	2666.7	410.9	2763.2	203.7	13.7	19.6	0.3
KS03-z2				53.1	0.77	2068.2	582.1	2205.0	211.9	17.8	23.1	0.6
KS03-z3				42.0	0.71	1701.9	408.9	1797.9	144.4	14.9	20.9	0.2
KS03-z4				50.7	0.76	1429.7	349.4	1511.8	175.0	21.4	28.2	0.4
KS03-z5				51.2	0.76	1457.6	396.6	1550.7	144.6	17.3	22.7	0.2
KS04-z1	98.7441	28.2354	3626	38.5	0.69	1256.6	481.0	1369.7	102.4	13.9	20.1	0.2
KS04-z2				54.1	0.77	1172.9	375.9	1261.3	120.6	17.7	22.9	0.3
KS04-z3				50.5	0.76	1439.1	623.6	1585.6	177.2	20.7	27.3	0.2
KS04-z4				42.3	0.71	1673.3	719.8	1842.4	198.2	19.9	27.9	0.6
KS04-z5				40.1	0.70	2359.1	745.1	2534.2	250.2	18.3	26.1	0.3
KS05-z2	98.7545	28.2284	3418	44.7	0.73	1492.7	530.1	1617.3	128.0	14.7	20.1	0.3
KS05-z3				45.8	0.73	1371.4	477.7	1483.7	137.4	17.1	23.3	0.4
KS05-z4				45.0	0.73	1667.7	581.9	1804.4	145.0	14.9	20.4	0.3
KS05-z5				38.8	0.69	1579.7	923.7	1796.8	143.7	14.8	21.5	0.4
KS05-z7				42.8	0.72	2052.4	496.5	2169.1	173.3	14.8	20.6	0.5

KS06-z1	98.7764	28.2135	2859	47.4	0.74	1772.5	558.2	1903.6	108.8	10.6	14.3	0.3
KS06-z2				50.8	0.76	1500.6	442.5	1604.6	101.6	11.7	15.4	0.3
KS06-z3				45.0	0.73	1762.4	972.4	1990.9	126.9	11.8	16.2	0.4
KS06-z4				53.4	0.77	1476.6	364.4	1562.3	88.8	10.5	13.7	0.1
KS06-z5				40.6	0.70	1287.7	839.3	1484.9	75.1	9.4	13.3	0.2
KS07-z1	98.7250	28.2584	4104	40.7	0.70	2358.0	587.7	2496.1	234.3	17.4	24.7	0.3
KS07-z2				43.9	0.72	1468.7	523.6	1591.8	172.5	20.1	27.7	0.2
KS07-z3				44.2	0.73	1823.1	342.5	1903.6	178.3	17.3	23.9	0.5
KS07-z5				37.9	0.68	2055.2	527.8	2179.3	215.6	18.3	26.8	0.6
KS07-z6				39.1	0.69	2778.1	769.8	2959.0	259.2	16.2	23.4	0.5
KS07-z7				39.5	0.70	3206.3	539.4	3333.0	257.8	14.3	20.6	0.2
KS08-z1	98.7278	28.2605	3935	47.4	0.74	1212.6	741.7	1386.9	132.5	17.7	23.9	0.7
KS08-z2				42.0	0.71	1288.3	482.0	1401.6	139.8	18.5	25.9	0.4
KS08-z3				45.1	0.73	1715.4	479.3	1828.0	191.8	19.4	26.6	0.5
KS08-z4				43.3	0.72	1370.5	616.1	1515.3	172.4	21.0	29.2	1.0
KS08-z5				42.0	0.71	1310.1	1236.6	1600.7	193.9	22.4	31.6	0.5
KS08-z7				42.2	0.71	1652.7	560.8	1784.5	159.1	16.5	23.1	0.5
KS09-z1	98.7329	28.2590	3697	40.0	0.70	1263.9	808.9	1454.0	121.1	15.4	22.1	0.4
KS09-z2				46.2	0.74	1238.5	403.6	1333.4	141.8	19.7	26.7	0.2
KS09-z3				52.1	0.76	1473.6	533.8	1599.1	183.8	21.3	27.8	0.7
KS09-z4				54.4	0.77	1297.4	582.3	1434.2	196.0	25.3	32.7	0.8
KS09-z5				51.1	0.76	2817.4	237.8	2873.3	172.5	11.1	14.6	0.8
KS09-z6				47.3	0.74	1591.1	156.8	1628.0	127.6	14.5	19.5	0.7
KS10-z1	98.7343	28.2445	3504	48.8	0.75	1304.1	695.9	1467.6	131.0	16.5	22.1	0.2
KS10-z2				44.1	0.72	1958.7	712.0	2126.0	217.0	18.9	26.1	0.5
KS10-z3				54.0	0.77	1259.2	496.0	1375.8	126.1	17.0	22.0	0.6
KS10-z4				38.5	0.69	2690.7	830.1	2885.8	297.9	19.1	27.7	0.8
KS10-z5				42.0	0.71	2047.2	588.2	2185.5	179.1	15.2	21.3	0.3
KS10-z6				43.0	0.72	2130.4	606.1	2272.8	203.7	16.6	23.1	0.5
KS18-z1	98.8590	28.2658	2076	43.9	0.72	511.0	374.5	599.0	25.2	7.8	10.8	0.1
KS18-z2				37.9	0.68	337.2	241.5	393.9	15.6	7.3	10.8	0.4
KS18-z3				45.0	0.73	253.0	186.1	296.8	17.4	10.9	14.9	0.2
KS18-z4				47.5	0.74	452.5	258.3	513.2	19.7	7.1	9.6	0.3

---

KS18-z5	44.7	0.73	707.8	335.0	786.6	31.8	7.5	10.3	0.2
---------	------	------	-------	-------	-------	------	-----	------	-----

**Table S. 2.5** – Synthesis of **existing AHe** ages collected from low elevations of the Kawagebo Massif (KW from [Replumaz et al. \(2020\)](#) <sup>[151]</sup>, MK from [Yang et al. \(2016\)](#) <sup>[150]</sup>). To notice that several samples have 2 or 3 apatite grains in the same tube to go through the measurement process because of small size of grains. The final age, with two sigma errors, is corrected by an alpha-ejection correction parameter  $F_T$  after [Farley et al. \(2002\)](#) <sup>[358]</sup>. ESR is equivalent spherical radius from [Gautheron and Tassan-Got \(2010\)](#) <sup>[351]</sup>, the effective uranium content is defined by  $[eU] = U + 0.235 \times Th$  ppm.

Sample	Lon.	Lat.	Ele. (m)	ESR ( $\mu m$ )	$F_T$	U	Th	eU (ppm)	4He (ppm)	Raw AHe age (Ma)	Corrected AHe age (Ma)	1 $\sigma$ error (Ma)
KW41-2	98.7776	28.2063	2690	38.4	0.675	7	8	8.9	2478.7	2.2	3.2	0.3
KW41-4				44.0	0.718	16	25	21.9	5959.4	2.2	3.1	0.3
KW41-6				46.0	0.742	9	4	9.9	1859.4	1.6	2.1	0.2
KW42-1	98.7888	28.2022	2560	53.9	0.821	8	28	14.6	4303.9	2.5	3.0	0.3
KW42-2				42.5	0.712	21	22	26.2	6376.7	2.0	2.8	0.3
KW42-3				39.1	0.749	12	25	17.9	3189.5	1.5	2.0	0.2
KW42-4				37.5	0.681	46	165	84.8	26748.5	2.6	3.8	0.3
KW43-3	98.7932	28.2033	2460	34.7	0.648	12	40	21.4	2035.6	0.8	1.2	0.1
KW43-4				34.5	0.639	10	33	17.7	2355.7	1.1	1.7	0.2
KW43-5				40.1	0.688	42	46	52.6	7007.3	1.1	1.6	0.1
KW43-6				42.0	0.709	14	32	21.2	2802.5	1.1	1.5	0.1
KW52-1	98.8503	28.1982	2060	37.8	0.707	19	58	32.7	3277.9	0.8	1.2	0.1
KW52-2				35.2	0.614	30	68	46.5	3786.2	0.7	1.1	0.1
KW52-3				39.5	0.687	19	40	28.0	3031.5	0.9	1.3	0.1
KW52-4				46.5	0.706	15	24	21.2	2012.0	0.8	1.1	0.1
MK04a1	98.8592	28.2648	2066	-	0.60	24.825	30.589	45.04	4100.0	1.7	1.7	0.0
MK04a2				-	1.00	21.28	29.42	66.90	3701.2	1.0	1.0	0.0

**Table S. 2.6** – Synthesis of **existing AFT** ages collected from low elevations of the Kawagebo Massif (from [Replumaz et al. \(2020\)](#) <sup>[151]</sup>). All ages in the table are pooled ages, with two sigma errors, except the KW40, whose has a central age because of its  $P(\chi^2)$  smaller than 0.05.  $\rho_s$ ,  $\rho_i$ ,  $\rho_d$  represent spontaneous, induced and standard glass track densities;  $N_s$ ,  $N_i$ ,  $N_d$  are numbers of spontaneous, induced and standard glass tracks.  $N_d$ ,  $N_s$ ,  $N_i$  are corresponding number of grains counted.

Sample	Lon.	Lat.	Ele. (m)	Grain Nb.	$\rho_d \times 10^4$ (tracks/cm <sup>-2</sup> ) (Nd)	$\rho_s \times 10^4$ (tracks/cm <sup>-2</sup> ) (Ns)	$\rho_i \times 10^4$ (tracks/cm <sup>-2</sup> ) (Ni)	U $\pm$ 2 $\sigma$	P( $\chi^2$ ) %	AFT age (Ma)	1 $\sigma$ error (Ma)
KW40	98.766	28.2013	2911	17	117.7 (4059)	6.08 (18)	172 (509)	22 $\pm$ 1	0	*6.1	2.5
KW41	98.7776	28.2063	2701	20	117.2 (4059)	4.76 (39)	133 (1089)	17 $\pm$ 1	100	5.6	1
KW42	98.7888	28.2022	2555	16	116.7 (4059)	2.09 (15)	108 (773)	16 $\pm$ 1	77.8	0.8	2.2
KW43	98.7932	28.2033	2595	20	116.2 (4059)	0.98 (8)	47.8 (389)	6 $\pm$ 1	84.2	3.2	1.2

Sample	Longitude	Latitude	Elevation (m)	AHe age (Ma)	2 $\sigma$ error (Ma)	# replicates	AFT age (Ma)	2 $\sigma$ error (Ma)	Grains	ZHe age (Ma)	2 $\sigma$ error (Ma)	# replicates
CD280	98.0137	29.7181	4991	27.4	2.8	4	23.6	5.2	20	-	-	-
TL09-6A	98.0100	29.7200	4981	17.6	1.3	3	-	-	-	-	-	-
CD279	98.0459	29.7234	4822	12.5	0.9	4	17.7	3.9	20	-	-	-
TL09-8A	98.0900	29.7200	4724	18.6	1.1	4	-	-	-	-	-	-
CD282	97.9599	29.7323	4703	28.7	1.5	4	25.6	2.7	20	-	-	-
CD277	98.1301	29.6626	4436	18.6	0.4	4	24.2	2.4	20	-	-	-
CD276	98.1401	29.6327	4197	17	0.6	5	15.3	2	20	37	0.3	3
TL09-11A	98.1500	29.6200	4143	19.4	0.2	5	-	-	-	-	-	-
CD275	98.1663	29.5995	4020	25	2.4	4	16.2	2.8	20	-	-	-
CD274	98.1814	29.5791	3894	19.7	1.4	4	20.8	1.9	20	50.6	2.2	3
CD270	98.303	29.551	3868	14.8	1.8	4	-	-	-	-	-	-
CD273	98.1936	29.5608	3757	28.4	1.8	3	22	3.2	20	-	-	-
TL09-12A	98.1800	29.5800	3741	22.8	1.6	4	-	-	-	-	-	-
TL09-14A	98.2000	29.5600	3741	16.1	0.9	4	-	-	-	-	-	-
CD272	98.2099	29.5531	3622	24.3	2.5	5	20.9	2.5	20	60.2	5.2	4

Note that apatite (U-Th)/He (AHe) ages reported here are arithmetic means of the single-grain replicate ages; see supplementary information (repository material) for individual grain ages and note that the AHe age of sample KW22 is from one replicate only. Apatite fission-track (AFT) ages are reported as central ages with 1 $\sigma$  uncertainty; see repository material for detail.

**Table S. 2.7** – Synthesis of low-temperature thermochronology data from the profile near the Zuogong Plateau, samples marked with CD are from [Cao et al. \(2022\)](#)<sup>[344]</sup> and with TL are from [Xiao et al. \(2015\)](#)<sup>[159]</sup>.



## CHAPTER 3

# Topography and relief development in the Yalong River catchment, Southeast Tibet



# 3.1 Topography and relief development in the Yalong River catchment, Southeast Tibet (under review)

Xiong Ou<sup>1</sup> and Anne Replumaz<sup>1</sup>

<sup>1</sup> Institut des Sciences de la Terre (ISTerre). Université Grenoble Alpes. CNRS. IRD. Grenoble. 38058. France

Correspondence to: Xiong Ou (xiong.ou@univ-grenoble-alpes.fr) and Anne Replumaz (anne.replumaz@univ-grenoble-alpes.fr)

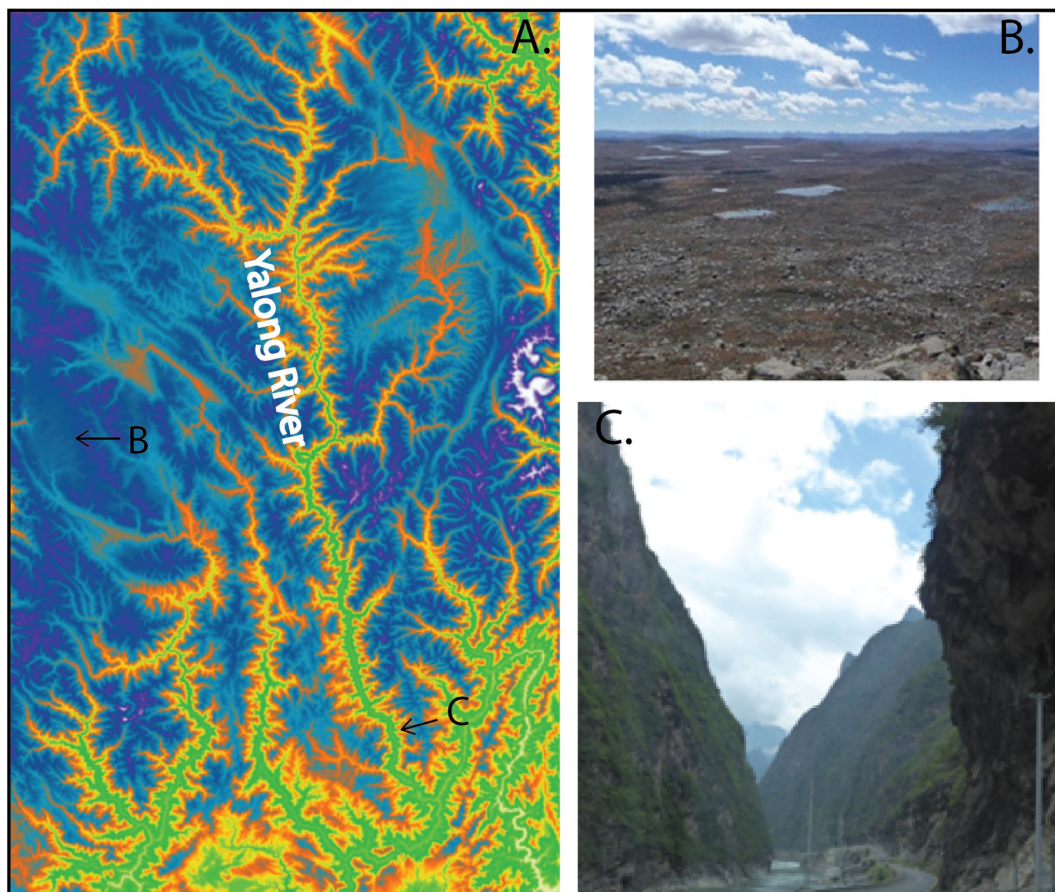


Figure 3.1 - (A) Topography of the Yalong River catchment, showing deeply entrenching middlestream river valley. (B) (C) Photos of the Daocheng massif (Fu et al., 2013a<sup>[250]</sup>) and Yalong River, respectively.



### 3.1.1 Abstract

The Southeast Tibet is characterized by low-relief surfaces at high-elevation with old thermochronological ages showing very little exhumation during the India-Asia collision, and deeply incising valleys of large rivers, such as Salween, Mekong, Yangtze and Yalong, with young thermochronological ages showing high exhumation. In what we call the “Great Bends Region”, the Yalong and Yangtze rivers cross perpendicularly northeast-trending thrust belts, generating huge river course bends with high channel slopes bracketed between these faults, which have contributed to the high plateau margin construction, including the Yalong Thrust Belt (YTB) active during ~35–25 and reactivated at ~12 Ma. In this region, the deep gorge of the Yalong River neighbors the well preserved low-relief surfaces at high-elevation, which are adjacent to the edge of the plateau and survived from regressive erosion of the river. By applying a landscape modelling (FastScape) in the Yalong River catchment with simplified scenarios of uplift deduced from fault activity, we show that strong monsoonal precipitation on the plateau (~1 m/yr) produces wide rivers and destroys the plateau edge. In contrast, a weak orographic precipitation on the plateau above 3000 m would help to preserve the constructed high plateau, but are not able to generate enough run-off in the river networks to sufficiently incise in channels. Instead, in our final model, we show that a weak net precipitation due to significant orographic effect, preserving interfluvial and headwater low-relief surfaces, has to be accompanied by imposing a large amount of inflow in then upstream and strong Miocene uniform uplift on the Muli thrust of the YTB to deeply incising downstream river valleys. Such an amount of water could be potentially collected from the flat and large upstream drainage area, inherited from capturing inland endorheic zone of the plateau. Such a model well reproduces the peculiar topography in Great Bends Region, but we also acknowledge that such landscape evolution model, combining simple stream-power law of bed rock river erosion and diffusive hillslope processes, does not allow to collect water on flat interfluvial and headwater surfaces without eroding, but requires an artificial boundary condition of increasing inflow in channels from the upstream and weak precipitation on the plateau.

**Keywords:** Southeast Tibet, Yalong River catchment, landscape evolution modelling, FastScape, low-relief surfaces, deeply incising rivers

Highlight points:

- Pure climatic forcing by strengthening monsoon will destroy the existing high plateau
- Sole orographic effect on reducing net precipitation preserves well the high plateau but can't incise deep rivers on the plateau margin
- Coupling of recent tectonic uplift, reduced orographic precipitation and imposed upstream inflow could reproduce the topography of SE Tibet
- Imposed inflow in network could inherit from capturing endorheic zone

### 3.1.2 Introduction

The immense and elevated (~5000 m on average) Tibetan Plateau is characterized by a vast low-relief endorheic zone in the west. In contrast, the eastern zone is externally drained by large rivers, such as the Salween, Mekong, Yangtze and Yalong, with low-relief upstream areas on the plateau and low-relief interfluvial surfaces perched at high elevation (~4500 m on average) along >2000 m deep gorges across the plateau edge (Clark et al., 2005b<sup>[67]</sup>; Liu-Zeng et al., 2008<sup>[100]</sup>). The pronounced topographic step on the southeastern Tibetan Plateau edge generates a strong orographic effect and results in a sharp contrast in precipitation, from more than 1 m/yr in the foreland below ~1000 m to less than 0.55 m/yr in the highland above ~3000 m (Figure 3.2). At the continental scale, it has been proposed that growth of the Tibetan Plateau under the tectonic forcing of the Indian indentation into the Asia since ~50 Ma (e.g., Tapponnier and Molnar, 1976<sup>[40]</sup>) significantly influenced climate during the Cenozoic, driving the generation and temporal/spatial evolution of the Asian monsoon system, as well as inner Asian desertification (An et al., 2001<sup>[216]</sup>; Molnar et al., 2010<sup>[369]</sup>). A ~22 Ma climatic transition from an arid environment to monsoonal wet conditions in Eastern Asia has been proposed (Guo et al., 2002<sup>[224]</sup>), contemporaneous with an enhanced monsoon since ~23 Ma according to various proxies of physical erosion and chemical weathering in marine sediments (Clift and Giosan, 2014<sup>[237]</sup>). More recent studies pushed back the establishment of the monsoon to the Eocene, based on plant fossil assemblages and fossil-leaf physiognomic signatures (Quan et al., 2012<sup>[243]</sup>; Spicer et al., 2016<sup>[370]</sup>) and corroborated by a transition from arid to wet conditions at ~41–36 Ma inferred from continental sediments (Sorrel et al., 2017<sup>[252]</sup>; Fang et al., 2021<sup>[220]</sup>; Zheng et al., 2022<sup>[251]</sup>). Sedimentation rates in epicontinental marine basins also start to increase remarkably at this time (Clift, 2006<sup>[167]</sup>). Numerous and extensive lacustrine sediments dated between ~23.5 Ma and ~13.5 Ma

suggest that the endorheic zone of the plateau extended further to the east over the upstream areas of the large external rivers in the Miocene (Wu et al., 2008<sup>[186]</sup>) (Figure 3.2B).

The southeast Tibetan Plateau has experienced extensive and intense upper crustal deformation and shortening during the India–Asia collision through large thrusting structures, such as the north–south trending thrusts in the Three Rivers Region and the northeast–striking thrust belts in the Great Bends region (Figure 3.3B). These thrust faults are building the topography of southeast Tibet in two phases, one in the Eocene/Oligocene, one during the Miocene (Godard et al., 2009<sup>[158]</sup>; Wang et al., 2012<sup>[120]</sup>; Tian et al., 2013<sup>[70]</sup>, 2015<sup>[145]</sup>; Tan et al., 2014<sup>[300]</sup>; Pitard et al., 2021<sup>[123]</sup>). A strong interaction between such tectonic and climatic forcing in the southeast Tibetan Plateau is expected to sculpt the characteristic relief and drainage network of southeast Tibet, but few quantitative models have been proposed yet at such drainage area of continental scale (Yuan et al., 2021<sup>[119]</sup>). In this paper, we focus on how the large–scale monsoonal precipitation leads to plateau destruction, while, competing with this climatic control, different uplift scenarios of this unique topography tends to preserve the high and flat surfaces in headwaters and interfluves. We also aim to study how this tectonic/climatic interaction leads to the deeply carved gorges, located on the southeast plateau edge above the thrust faults, which have been active during the building of the plateau. One of the most spectacular gorges is observed along the middlestream Yalong River, generating a great bend where it crosses the Muli thrust (Clark et al., 2004<sup>[118]</sup>) (Figure 3.3B). Here, we model the topographic evolution of the Yalong catchment in this “Great Bends region” by using FastScape (Braun and Willett, 2013<sup>[299]</sup>), testing both the influence of tectonic (uplift) and climatic (monsoon initiation, orographic precipitation) forcing, and how to simultaneously produce the deeply incised river valleys and the preservation of low–relief surfaces in the headwaters and interfluves (Figure 3.2B).

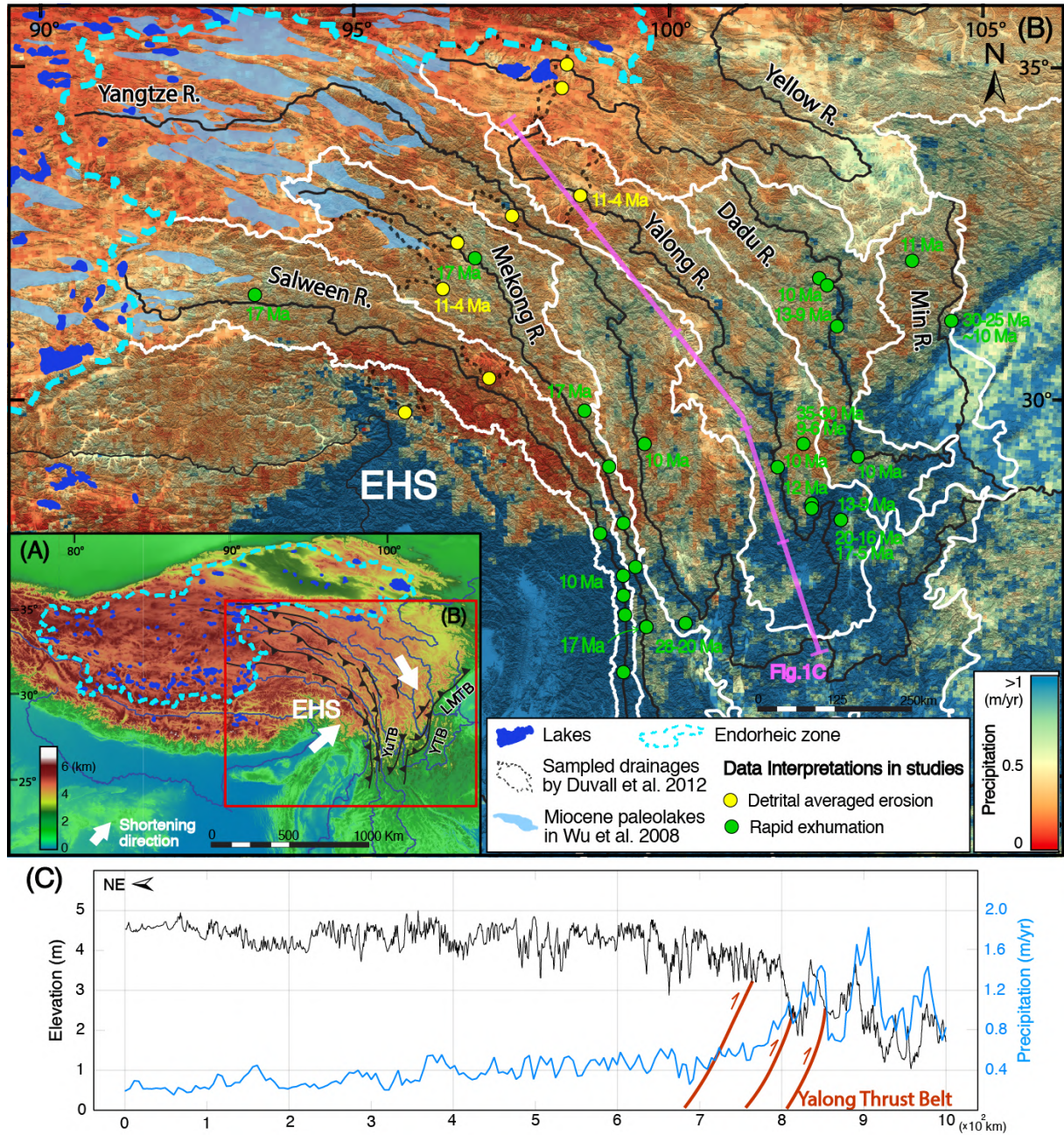


**Figure 3.2** – (A) Topography of the Tibetan Plateau with large externally drained rivers (blue lines) in the southeast region and endorheic zone delimited by cyan dashed line. EHS: Eastern Himalayan Syntaxis, LMTB: Longmenshan Thrust Belt, YTB: Yalong Thrust Belt, YuTB: Yulong Thrust Belt. White arrows roughly show the contraction direction. (B) Precipitation map of southeast Tibet based on TRMM 2B31 (1998–2009) dataset. Thick white lines delimit the different river catchments. Green circles refer to low-temperature thermochronologic studies in southeast Tibet, with numbers giving the inferred onset timing of rapid exhumation. Yellow circles are upstream basin-averaged detrital thermochronometric ages, suggesting a synchronous river incision event during ~11–4 Ma, from [Duvall et al. \(2012\)](#) [155]. (C) Precipitation and topography swath profiles across the Yalong River catchment (pink line in [Figure 3.2B](#)), showing a gradual increase of topography and a sharp decrease of precipitation toward northwest across the Yalong Thrust Belt.

### 3.1.3 Regional Cenozoic geological setting and paleoclimate

#### 3.1.3.1 Externally drained southeast Tibet: “Great Bends Region” versus “Three Rivers Region”

The externally drained southeastern Tibetan Plateau could be divided in two zones, where tectonics strongly and differently influence the drainage network. The “Great Bends Region” corresponds to the lower parts of the upstream Yangtze and Yalong rivers, displaying spectacular bends where they cross perpendicularly the northeast striking Yulong Thrust Belt and the Yalong Thrust Belt (YTB), respectively (Clark et al., 2004 <sup>[118]</sup>) (Figure 3.2B). The Yulong thrust was only active between 28–20 Ma with exhumation rates of 0.57–0.8 km/Myr (Cao et al., 2019 <sup>[309]</sup>). Within the YTB, the Jiulong thrust was active during 35–30 Ma then re-activated during 9–6 Ma, with exhumation rates of 0.5 km/Myr and 0.6 km/Myr, respectively (Zhang et al., 2016 <sup>[121]</sup>). The Muli thrust was active since 50 Ma, with an exhumation rate of  $0.2 \pm 0.06$  km/Myr, increasing to a maximum of  $0.6 \pm 0.08$  km/Myr near the fault since  $12.5 \pm 1$  Ma (Pitard et al., 2021 <sup>[123]</sup>). The Jinghe–Qinhe thrust is less-well constrained, active either during 17–5 Ma (Wang et al., 2012 <sup>[348]</sup>) or during 20–16 Ma with an exhumation rate of 0.4 km/Myr (Zhu et al., 2021 <sup>[124]</sup>). High normalized steepness index ( $K_{sn}$ ) values are observed along the downstream Yalong River where it flows across the topographic jump bracketed by the YTB, generating a large knickzone over the >100 km (Figure 3.3B, C). More to the east, in the Longmenshan Region, the Dadu and Min rivers show less pronounced bends where crossing the Longmenshan Thrust Belt (LMTB) (Figure 3.2B, Figure 3.3B). The activity of the LMTB was roughly synchronous to that of the YTB, with the first Oligocene phase (exhumation rate 0.8 km/Myr during 30–25 Ma) more intense than the second Miocene phase (exhumation rate 0.4 km/Myr during 10–0 Ma) (Godard et al., 2009 <sup>[158]</sup>; Wang et al., 2012 <sup>[120]</sup>; Tian et al., 2013 <sup>[70]</sup>, 2015 <sup>[145]</sup>; Tan et al., 2014 <sup>[300]</sup>). Furthermore, the mean elevation in the hinterland of the LMTB is lower than that of the YTB, showing a stronger erosion by the Dadu and Min rivers and well-developed dendritic river networks (Figure 3.3B).

The Three Rivers Region corresponds to the arcuate drainages of the upstream Yangtze, Mekong and Salween rivers that flow around the Eastern Himalayan Syntaxis (EHS), parallel to each other with a spacing of only a few tens of kilometers (Figure 3.2B). Such a narrow spacing between large rivers has been interpreted as indicating strong regional northeastward shortening in response to indentation of the EHS (Hallet and Molnar, 2001 <sup>[116]</sup>) (Figure 3.2A), accommodated by parallel northwest/north striking thrusts, which guide the rivers (Replumaz et al., 2020 <sup>[151]</sup>). Modelling a

dataset of multiple low temperature thermochronometers indicated a decreasing erosion rate from west (Salween River), close to the EHS, to east (Yangtze River) away from it, since at least 10 Ma, suggesting a dominant tectonic forcing of compression perpendicular to the rivers (Yang et al., 2016<sup>[150]</sup>). Modelling of the exhumation history near the Kawagebo peak, the highest summit in the Three Rivers Region, revealed that it experienced a second-order influence of river incision and has been uplifted in a restraining overstep between the Parlung and Zhongdian strike-slip faults active since at least 10 Ma, generating high  $K_{Sn}$  values in the adjacent Mekong River (Ou et al., 2021<sup>[152]</sup>) (Figure 3.3C). These findings contrast with hypothesis that suggests the erosion history along the Mekong River is either climatically forced by a strengthening summer monsoon since the Mid-Miocene Climate Optimum (~17-14 Ma) (Nie et al., 2018<sup>[154]</sup>), or by a drainage-area expansion of the large external rivers into the endorheic zone, increasing runoff and stream power (Rohrmann et al., 2018<sup>[169]</sup>). Recently, an erosion model in the Three Rivers Region (Yuan et al., 2021<sup>[119]</sup>), using FastScape (Braun and Willett, 2013<sup>[299]</sup>), has proposed that a propagating Gaussian wave of strong surface uplift toward the southeast, combined with uniform precipitation, reproduces the deep river valleys and high flat surfaces.

### 3.1.3.2 Cenozoic tectonic evolution and paleo-elevations of southeast Tibet

In southeast Tibet, the dominant deformation today is large-scale strike-slip faulting activated since ~10 Ma, suggesting that the plateau has regionally reached a threshold altitude above which its southeastward extension costs less energy than its thickening (Tapponnier and Molnar, 1976<sup>[299]</sup>). The right-lateral Jiali-Parlung fault, bypassing the EHS, jumps to the Zhongdian fault to the southeast, generating a push-up structure through locally reactivating ancient north-south thrusts and creating the high Kawagebo massif, and then jumps southeast to the Red River Fault through opening the Lijiang pull-apart basin (Replumaz et al., 2020<sup>[151]</sup>) (Figure 3.3B). To the northeast, the left-lateral Xianshuihe fault system offsets the YTB from LMTB since ~9 Ma (e.g., Zhang et al., 2015<sup>[156]</sup>). The transtensive left-lateral Litang fault activated since ~7 Ma to accommodate internal deformation in between these major faults (Zhang et al., 2017). Nowadays, those strike-slip faults together accommodate an overall clockwise rotation around the EHS and southeastward extrusion of blocks (Gan et al., 2007<sup>[21]</sup>; Bai et al., 2018<sup>[310]</sup>).

In the Three Rivers Region, the uplift phase started probably soon after the onset of the collision at ~50 Ma, as shown by the infilling and uplift of the Fenghuoshan basin from Mid–Eocene to 34 Ma or even 27 Ma (e.g., [Staisch et al., 2014<sup>\[175\]</sup>](#), [2016<sup>\[182\]</sup>](#)), the Nangqian–Yushu basin from ~51 Ma to 36 Ma, and the Jianchuan basin from ~51 Ma to 22 Ma (e.g., [Horton et al., 2002<sup>\[91\]</sup>](#); [Spurlin et al., 2005<sup>\[176\]</sup>](#); [Gourbet et al., 2017<sup>\[181\]</sup>](#); [Cao et al., 2020<sup>\[122\]</sup>](#)) ([Figure 3.3A, B](#)). Consistently, paleoaltimetric data show that the Gonjo Basin reached an elevation of ~4000 m since at least ~40 Ma ([Tang et al., 2017<sup>\[209\]</sup>](#); [Xiong et al., 2020<sup>\[210\]</sup>](#)) and the Markam Basin was at an elevation of ~3000 m at ~34 Ma, rising to its present elevation (~3900 m) in the early Oligocene ([Li et al., 2015<sup>\[179\]</sup>](#); [Su et al., 2019<sup>\[97\]</sup>](#)). Further south, the Jianchuan basin was first reported to rise to its present elevation at ~3300 m by ~35 Ma ([Hoke et al., 2014<sup>\[211\]</sup>](#); [Li et al., 2015<sup>\[179\]</sup>](#)). However, a later careful revising of the depositional age and paleoelevation of the Jianchuan basin ([Gourbet et al., 2017<sup>\[181\]</sup>](#); [Wu et al., 2018<sup>\[212\]</sup>](#)) reassigned a significantly lower altitude ( $1200 \pm 1200$  m) in the late Eocene. The Lanping basin attained  $3300 \pm 450$  m, higher than its present–day elevation of 2700 m, around 15 Ma ([Hoke et al., 2014<sup>\[211\]</sup>](#); [Li et al., 2015<sup>\[179\]</sup>](#)). Furthermore, such a regional phase of uplift starting since ~35 Ma agrees with a strong increase of sedimentation rates in epicontinental seas of east and southeast Asia ([Clift, 2006<sup>\[167\]</sup>](#)) ([Figure 3.3D](#)). Decrease of sedimentation rates between ~10 Ma to the Pliocene has been linked to a drawdown of precipitation until a reinforcement of summer precipitation and intensifying seasonality at ~5 Ma (e.g., [Clift, 2006<sup>\[167\]</sup>](#)). Modelled erosion rates from detrital thermochronometry, averaged over the upstream catchments of major rivers ([Figure 3.3B](#)), showed rapid erosion between 11 and 4 Ma, in concert with the rapid downstream incision phase and interpreted as deriving from uniform regional surface uplift ([Duvall et al., 2012<sup>\[155\]</sup>](#)).

The Great Bends Region, prior to the southeastward extrusion, experienced a phase of topography building along numerous thrusts (e.g., the YTB) since at most 35 Ma, with enhanced activity since ~15 Ma. However, no paleo–elevation data shows when the plateau had reached its present–day elevation in this region. Nevertheless, in the piedmont of the region, the Eryuan and Yanyuan basins reached their present elevation of ~2300 m around 5 Ma, and the Chake Basin to the south was uplifted to ~2000 m at ~11 Ma ([Hoke et al., 2014<sup>\[211\]</sup>](#); [Li et al., 2015<sup>\[179\]</sup>](#)) ([Figure 3.3A, B](#)), suggesting that the main uplift phase started probably since ~15 Ma, in agreement with the tectonics activity. The mechanism of thickening of southeast Tibet in link with the observed thrust faults is still highly debated, driven either by the upper crustal faults (e.g., [Cao et al., 2019<sup>\[309\]</sup>](#); [Pitard et al., 2021<sup>\[123\]</sup>](#)), or by lower–

crust channel flow, with minor upper crustal shortening (e.g., [Clark et al., 2005b](#)<sup>[138]</sup>; [Godard et al., 2010](#)<sup>[142]</sup>; [Ouimet et al., 2010](#)<sup>[143]</sup>). While, it is beyond the scope of this paper to resolve this controversy, and only schematic regional uplift scenarios will be considered in our models.

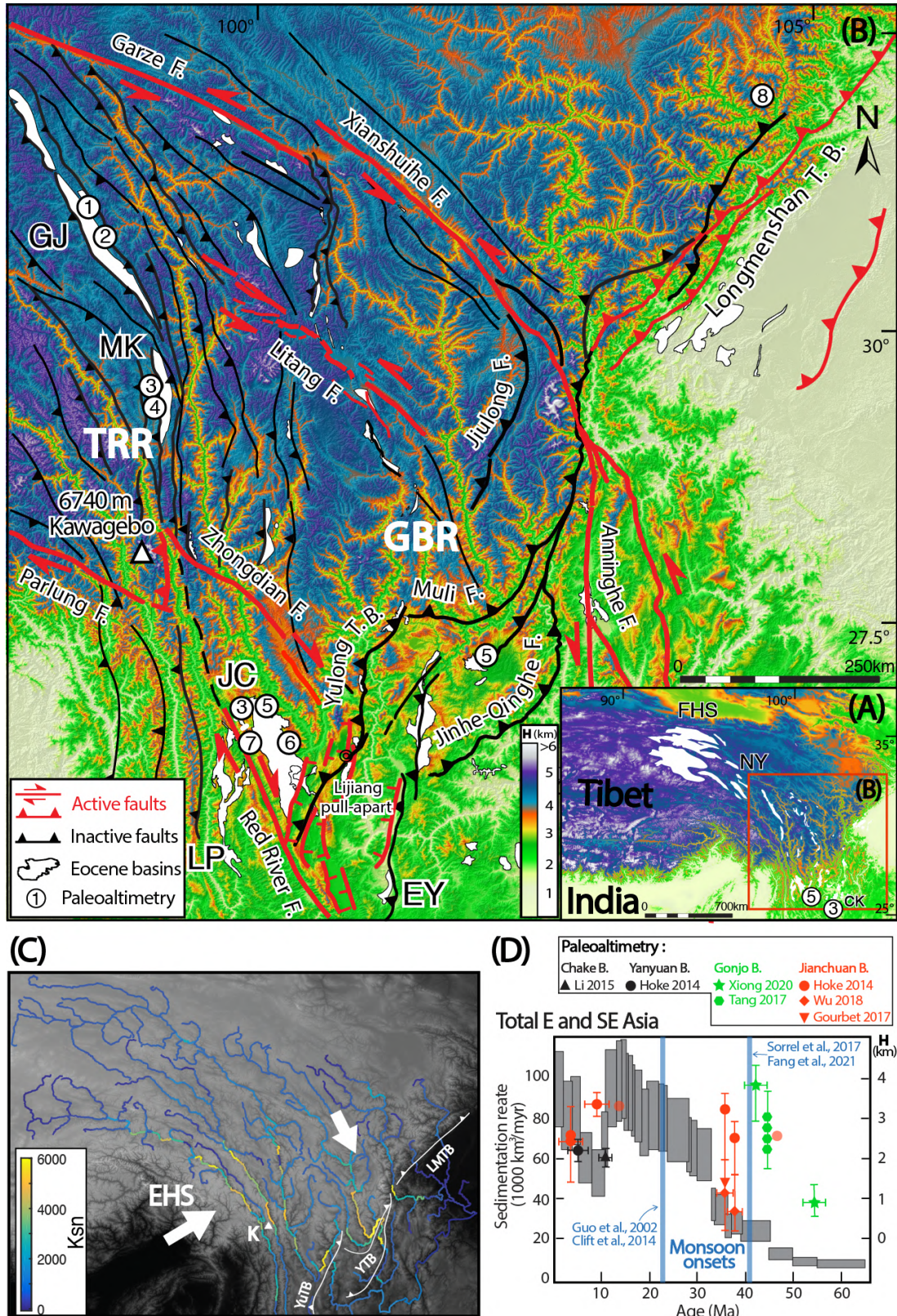


**Figure 3.3** – (A) Topography of the central and eastern Tibetan Plateau. White shading represents Eocene intermontane basins. CK: Chake Basin, FHS: Fenghuoshan Basin, NY: Nangqian–Yushu Basin. (B) Topography of southeast Tibet, with active faults in red, mainly strike–slip faults, accommodating an overall

clockwise rotation around the EHS, and inactive faults in black, mainly thrust faults, accommodating the building of the topography. GBR: Great Bends Region, TRR: Three Rivers Region. Basins: EY: Eryuan Basin, GJ: Gonjo Basin, JC: Jianchuan Basin, LP: Lanping Basin, MK: Markam Basin. The circled numbers denote locations of paleoaltimetric studies, as follows: 1: Tang et al., 2017<sup>[209]</sup>; 2: Xiong et al., 2020<sup>[210]</sup>; 3: Li et al., 2015<sup>[179]</sup>; 4: Su et al., 2019<sup>[97]</sup>; 5: Hoke et al., 2014<sup>[211]</sup>; 6: Gourbet et al., 2017<sup>[181]</sup>; 7: Wu et al., 2018<sup>[212]</sup>. (C)  $k_{sn}$  map of large rivers of southeast Tibet. EHS: Eastern Himalayan Syntaxis; LMTB: Longmenshan Thrust Belt; K: Kawagebo peak; YTB: Yalong Thrust Belt; YuTB: Yulong Thrust Belt. White arrows roughly show the contraction direction. (D) Synthesis of sedimentation rate in epicontinental seas of east and southeast Asia, based on Clift (2006)<sup>[167]</sup>. The selected paleoaltimetric data are from the Gonjo and Jianchuan basins, showing the Tibetan orography has expanded southeastward since the Eocene in the Three Rivers Region; from the Yanyuan and Chake basins, showing no conclusion of paleoaltimetry evolution in the Great Bends Region.

### 3.1.4 Method: Landscape evolution model (FastScape) and parametric studies

#### 3.1.4.1 Landscape evolution modelling

In tectonically active regions, landscape evolution rate is principally set by the efficiency of bedrock river incision, with the steep slopes of such regions responding rapidly to river incision (Clark et al., 2004<sup>[118v]</sup>). We used FastScape (Braun and Willett, 2013<sup>[299]</sup>), to solve the stream power law for bedrock river incision (Whipple and Tucker, 1999<sup>[277]</sup>) and predict landscape evolution by imposing tectonic forcing (uplift), climatic forcing (precipitation/erosion coefficient), initial topography and boundary conditions. According to the stream power law, the height evolution of fluvial channels ( $\frac{\partial h}{\partial t}$ ) depends on the difference between the rock uplift rate ( $U$ ) and the surface erosion rate ( $E$ ), which is proportional to the local slope ( $S$ ) and to the drainage area ( $A$ ), a proxy for river discharge (Howard and Kerby, 1983<sup>[371]</sup>). Fluvial erosion is also interdependent with hillslope processes, which are subject to mass transport at a rate that is commonly represented by linear diffusion, proportional to the curvature of topography (Ahnert, 1967<sup>[372]</sup>), by assuming mass conservation. The basic equation solved by FastScape is:

$$\frac{\partial h}{\partial t} = U - K_f p^m A^n S^n + K_d \left( \frac{\partial^2 h}{\partial x^2} + \frac{\partial^2 h}{\partial y^2} \right) \quad (2)$$

where  $h$  is elevation ( $m$ ),  $t$  is time ( $yr$ ),  $U$  is uplift rate ( $m/yr$ ),  $K_f$  is the erodibility coefficient ( $m^{1-2m}/yr$ ),  $p$  is net precipitation rate ( $m/yr$ ),  $A$  is drainage area ( $m^2$ ),  $S$  is local slope in the flow direction, namely the steepest descent between a point and any among its eight neighbors, and  $m$ ,  $n$

are exponents.  $K_f$ ,  $m$  and  $n$  depend on lithology, mean precipitation, channel width, flood frequency and channel hydraulics (Whipple and Tucker, 1999<sup>[277]</sup>). Empirical values for  $K_f$  range from  $10^{-6}$  to  $10^{-2} m^{1-2m}/yr$  (Stock and Montgomery, 1999<sup>[373]</sup>). The ratio  $m/n$  typically varies in a range of 0.3–0.7 (Kirby and Whipple, 2001<sup>[374]</sup>; Wobus et al., 2006<sup>[375]</sup>), as recommended in (Croissant and Braun, 2014<sup>[376]</sup>),  $m = 0.4$ ,  $n = 1$  will be adopted in our study, assuming a linear slope dependence.  $K_d$  is a hillslope sediment transport coefficient or diffusivity ( $m^2/yr$ ), ranging from  $10^{-4}$  and  $10^{-1} m^2/yr$  (Martin, 2000). A constant value of  $K_d = 10^{-2} m^2/yr$  will be used here as proposed in Densmore et al. (2007)<sup>[377]</sup>, as shown in Table 3.1.

### 3.1.4.2 Model setup

The model setup is based on a rectangle of 1250 km in length and 200 km in width, similar to the Yalong River catchment, discretized by  $1250 \times 200$  regularly spaced nodes (Figure 3.4A). All models in our study were run during a period of 50 Ma, the approximative onset timing of Asian–Indian collision. The time step is set to be 200 ka, so that models run for 250 time steps. The initial topography is set to be 1000 m, with the lower boundary being a fixed *basel\_level*, which is the only outlet of the model domain. The upper boundary is a symmetrical or reflecting boundary; no water can flow out through this limit and is reflected in the opposite direction. The left and right boundaries are periodic boundaries with water flowing across one boundary and ‘re-appearing’ on the other side, so that nodes on one boundary will have nodes on the other boundary as neighbors (Braun and Willett, 2013<sup>[299]</sup>). Uplift rate and precipitation, the two principal parameters in our models, can vary in time and in space. A small initial canal is emplaced in the middle of the foreland to avoid too many random outlets on the fixed lower boundary (Figure 3.4A).

We treat the model outputs of FastScape with the open-source topographic analysis tool Topotoolbox2 (Schwanghart and Scherler, 2014<sup>[378]</sup>). For the chosen time-steps in outputs, we first plot channel elevation versus an upstream integral of drainage area,  $\chi$  (Perron and Royden, 2013<sup>[379]</sup>) and the upstream distance, for a comparison between modeled and observed river profiles. Cross-sections of the river valleys and 20-km wide swath profiles along the river channel are extracted to compare the geometry of modeled river valleys to the deeply incised river gorges in the southeast

Tibet. The normalized channel steepness index ( $k_{sn}$ ), representing the gradient of channel elevation with respect to  $\chi$ , is also calculated for the river profiles (e.g., [Wobus et al., 2006](#) <sup>[375]</sup>).

**Table 3.1**

*Parameters for model setup*

Notation	Definition	Value/Range	Unit
<b><math>h</math></b>	topography elevation		<b><math>m</math></b>
<b><math>\Delta t</math></b>	incremental time	<b>200000</b>	<b><math>yr</math></b>
<b><math>n_{steps}</math></b>	Total run steps	<b>250</b>	–
<b><math>x</math></b>	width	<b>200</b>	<b><math>km</math></b>
<b><math>y</math></b>	length	<b>1250</b>	<b><math>km</math></b>
<b><math>\Delta x, \Delta y</math></b>	pixel size	<b>1</b>	<b><math>km</math></b>
<b><math>U</math></b>	rock uplift rate		<b><math>m/yr</math></b>
<b><math>p</math></b>	net precipitation rate		<b><math>m/yr</math></b>
<b><math>A</math></b>	drainage area		<b><math>m^2</math></b>
<b><math>S</math></b>	slope in flow direction		–
<b><math>m</math></b>	stream power law exponent	<b>0.4<sup>a</sup></b>	–
<b><math>n</math></b>	stream power law exponent	<b>1<sup>a</sup></b>	–
<b><math>K_f</math></b>	erosion coefficient	<b><math>4 \times 10^{-6}</math></b>	<b><math>m^{1-2m}/yr</math></b>
<b><math>K_d</math></b>	hillslope diffusion coefficient	<b><math>1 \times 10^{-2}</math></b>	<b><math>m^2/yr</math></b>
<b><math>base\_level</math></b>	fixed height boundary	<b>1000</b>	<b><math>m</math></b>

*Note.*

<sup>a</sup>Parameters from [Croissant and Braun, 2014](#) <sup>[376]</sup>,

<sup>b</sup>Parameters from [Densmore et al., 2017](#) <sup>[377]</sup>.

### 3.1.4.3 Basic parameter study

The upstream low-relief area of the Yalong River catchment lies at an average elevation of ~4500 m, gradually decreasing southeastward to ~2000 m ([Figure 3.2C](#), [Figure 3.4B](#)). The YTB delimits a knickzone with a high value of  $k_{sn}$ , where the river has downcut narrow and deep valley, with a local relief >2500 m, shown on the valley cross-section and the swath profile of the Yalong River ([Figure 3.4B inset, C](#)). Our initial simple models are applied to test different values of  $K_f$  and  $p$ , with a constant uplift rate of  $0.1 \times 10^{-3} m/yr$  in the upstream hinterland to reach a maximum total surface uplift of 5000 m during 50 Ma, and a slow uplift rate of  $0.01 \times 10^{-3} m/yr$  in the zone downstream of 150 km, representing the footwall of the YTB ([Figure 3.4A](#)). Results show that increasing  $K_f$  and/or  $p$  strengthens regressive erosion, with the slope of the main river channel varying from nearly linear

to convex-up (Figure 3.4D, E). Precipitation of  $0.1\text{ m/yr}$  and a small value of  $K_f$  of  $2 \times 10^{-6}\text{ m}^{1-2m}/\text{yr}$  are insufficient to propagate river erosion to the plateau interior, producing a short linear river and  $\chi$  profiles, with low-relief interfluvial surfaces at high elevations and intact flat surfaces in the high headwaters. In contrast, a  $K_f$  value of  $6 \times 10^{-6}\text{ m}^{1-2m}/\text{yr}$  erodes the whole region even with low precipitation ( $0.1\text{ m/yr}$ ), creating a strongly convex-up river and  $\chi$  profiles and leaving almost no high channels or surfaces preserved along the river (Figure 3.4D, E). Both cases are not consistent with the characteristics of the Yalong River catchment. With a medium value of  $K_f$  of  $4 \times 10^{-6}\text{ m}^{1-2m}/\text{yr}$ , the model relatively well reproduces the river channel convexity and some preserved high topography, but not the narrow valley of the Yalong River. The width of the modeled river valleys increases, shifting from a narrow and deeply incised valley to a broad one, when increasing the  $K_f$  value (Figure 3.4E insets). In all these models, high  $k_{sn}$  values are propagated upstream, showing localized intense erosion in the upstream-most part, contrasting with the knickzone observed at the edge of the plateau when crossing the YTB (Figure 3.4C).

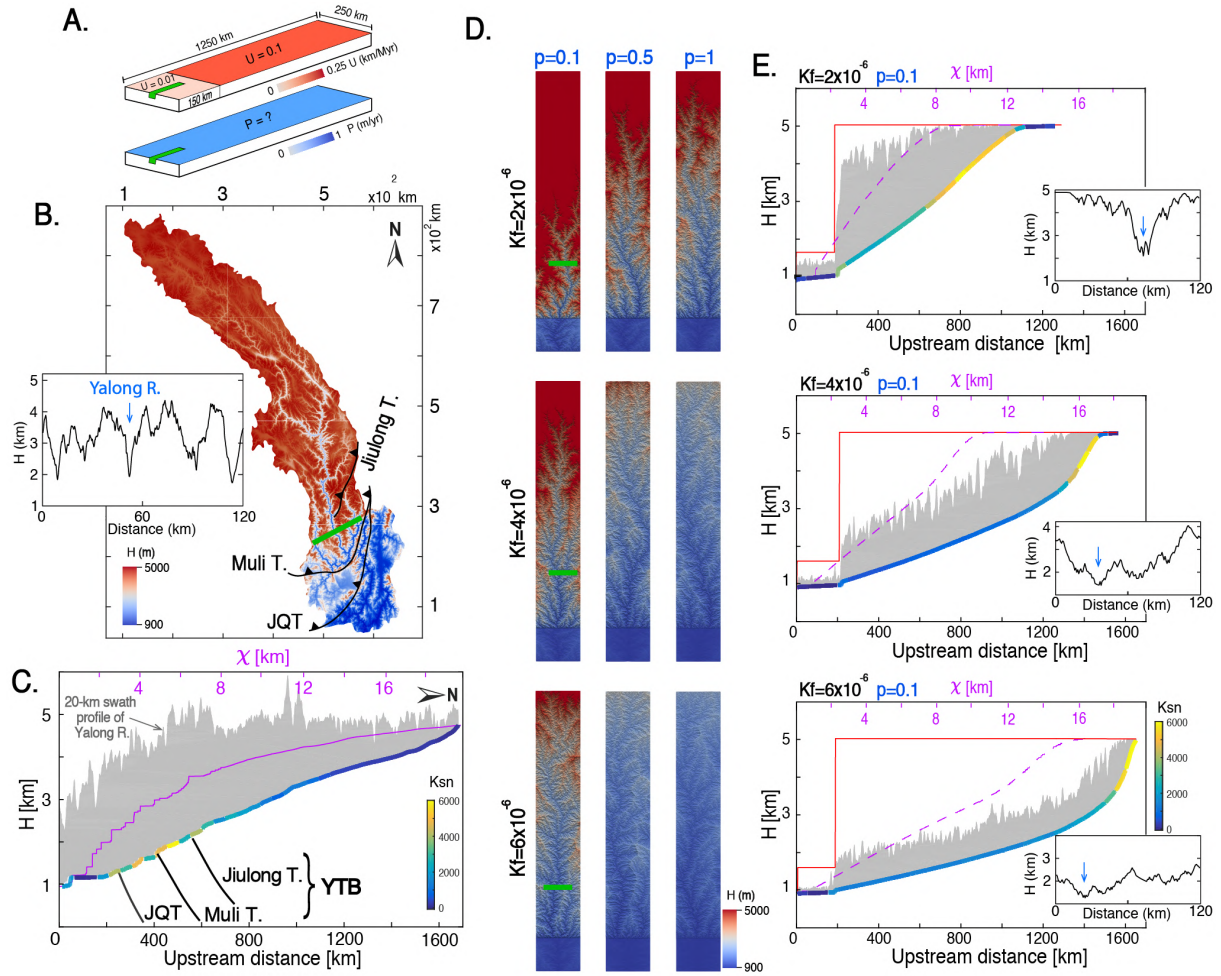


**Figure 3.4** – (A) Setting of simple models testing the erosional parameters. The  $1250 \times 200$  km box with spatially variable uplift rate ( $u$ ) in red and constant precipitation ( $p$ ) in blue. (B) The topography of the Yalong River catchment and its valley cross-section (inset) at an upstream distance of 450 km (green line). JQT: Jinghe–Qinhe thrusts. (C) The 20-km wide swath profile (with  $k_{sn}$  values) and  $\chi$  profile (in purple) of Yalong river. YTB: Yalong Thrust Belt, including Jiulong, Muli and Jinghe–Qinhe thrusts. (D) Topography of the final state of models with different  $K_f$  and  $p$ . (E) The 20-km wide swath and  $\chi$  profile (in dashed purple) of modeled rivers with  $k_{sn}$  values, under  $p = 0.1$  m/yr but different  $K_f$ . The red line stands for the maximum surface uplift attained. The spaces between the maximum surface uplift (red thick lines) and the maximum topography of the final state (upper limit of light grey shadows) represent the minimum erosion on the creeks or plateau. Inset figures are the cross-sections of river valleys at an upstream distance of 450 km (green line in D).

## 3.1.5 Landscape evolution under different climatic and tectonic scenarios

### 3.1.5.1 Climatic scenarios

We first test a scenario that includes monsoonal strengthening since the Mid-Miocene Climate Optimum (~17-14 Ma) on an existing high plateau of present-day elevation, suggested to explain the enhanced exhumation in the Mekong River valley during that period (Nie et al., 2018<sup>[154]</sup>). We denote this scenario as the “Mid-Miocene Monsoon scenario”. Uplift at a rate of 0.13 km/Myr from 50–20 Ma creates a high plateau under arid conditions ( $p = 0.2$  m/yr,  $K_f = 4 \times 10^{-6} m^{1-2m}/yr$ ), before shifting to a wet monsoonal condition, with a higher precipitation of 1 m/yr (Figure 3.5A). The final state of the model shows that the plateau is strongly eroded by efficient regressive erosion due to enhanced monsoonal precipitation (Figure 3.5C), with a drastic decrease of the maximum topography between 17 Ma and 0 Ma (Figure 3.5E). Only a few high surfaces and channels at ~5000 m are preserved upstream, with a ubiquitously flat foreland. The river and  $\chi$  profiles are strongly concave-up with a significant knickzone and highest  $k_{sn}$  values on the edge of the residual plateau. We also test enhanced runoff and stream power in channels through an upstream drainage capture from the endorheic zone on the high plateau near ~15 Ma (Rohrmann et al., 2018<sup>[169]</sup>), denoted as the “Top-down incision scenario”. Similar uplift at a rate of 0.13 km/Myr from 50–20 Ma produces a high endorheic plateau, considering no precipitation for the upstream half of the model. Capture of the endorheic zone takes place at 15 Ma, incarnated by an upstream expansion of strong rainfall ( $p = 1$  m/yr,  $K_f = 4 \times 10^{-6} m^{1-2m}/yr$ ). Such a remarkable amount of runoff flowing into the external river network destroys the high topography by “escarpment-retreat” like regression of the maximum topography since 15 Ma, with a final concave-up river and  $\chi$  profiles and  $k_{sn}$  distribution similar to the “Mid-Miocene Monsoon scenario” (Figure 3.5F).

### “Mid-Miocene Monsoon scenario”

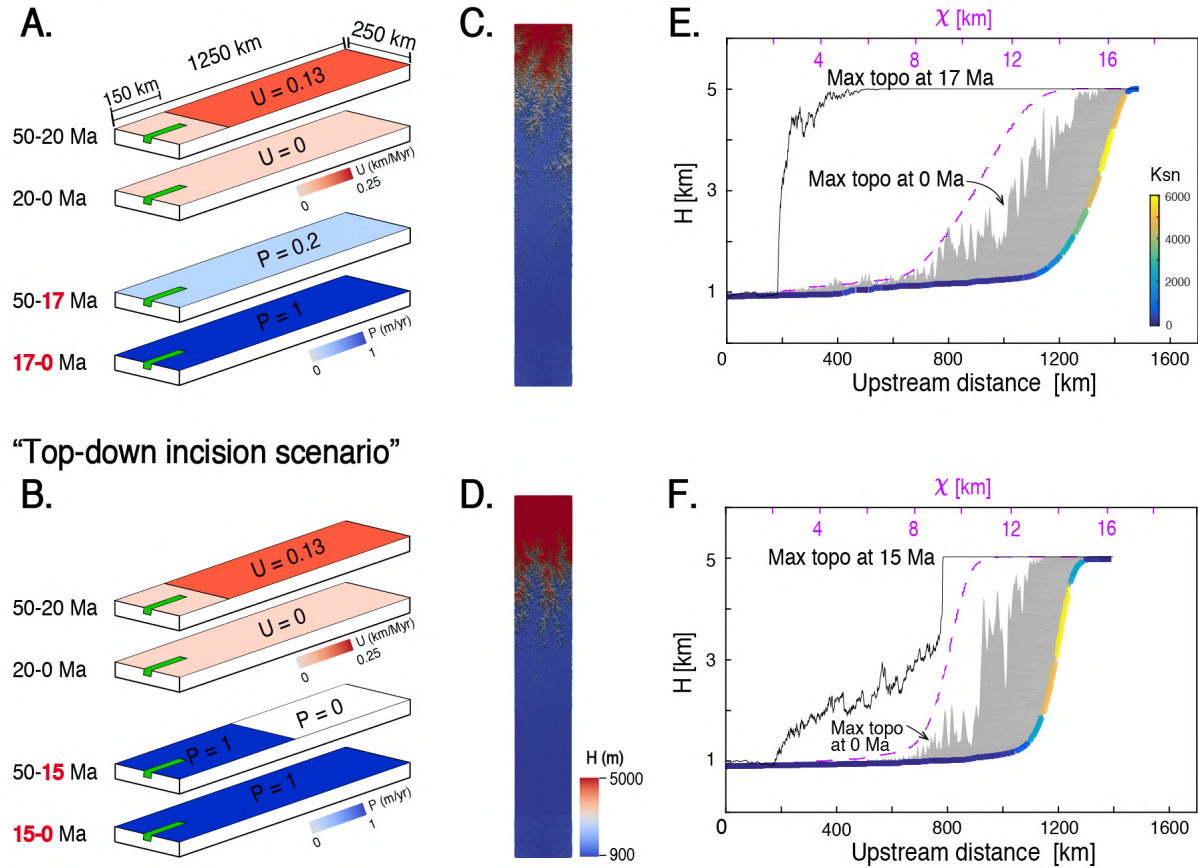


**Figure 3.5** – (A), (B) Model setting with different phases of uplift and precipitation, corresponding to the hypothesis of [Nie et al. \(2018\)](#)<sup>[154]</sup> and [Rohrmann et al. \(2018\)](#)<sup>[169]</sup>, respectively. “Mid-Miocene Monsoon scenario” has an enhanced rainfall since 17 Ma. “Top-down incision scenario” shows an expansion of a drainage area since 15 Ma. (C), (D) are the final topographic states of model, showing a complete erosion of the most of high topography. (E), (F) are the 20–km wide swath and  $\chi$  profiles (in dashed purple) of the modeled rivers, showing extremely upward convexity, with little high topography preserved. The thin black lines represent the maximum topography in the y direction at 17 or 15 Ma before a climatic transition.

#### 3.1.5.2 Tectonic scenarios

We first test a scenario with an uplift phase during 30–0 Ma with a rate of 0.13 *km/Myr*, representing exhumation since the Late Eocene–Oligocene observed on the Jiulong thrust ([Zhang et al., 2016](#)<sup>[121]</sup>), named “Jiulong uplift scenario”. Then we test a strong uplift rate of 0.24 *km/Myr* since 15 Ma, representing the middle Miocene exhumation phase revealed for the Muli thrust ([Pitard et al., 2021](#)<sup>[123]</sup>), named “Muli uplift scenario”. Prior to the onset of thrust activity, a protracted phase with

low uplift rate of  $0.01 \text{ km/Myr}$  is applied everywhere in the models. A constant strong precipitation of  $1 \text{ m/yr}$  since  $50 \text{ Ma}$  is employed in both scenarios considering a middle Eocene onset of the ITCZ-induced monsoon (e.g., Sorrel et al., 2017<sup>[252]</sup>; Spicer et al., 2016<sup>[370]</sup>). Results show that a long uplift phase since  $30 \text{ Ma}$  with a relatively small uplift rate favors strong regressive erosion in the channels, creating always strongly concave-up rivers, no matter which  $K_f$  value is applied (Figure 3.6E). However, a higher uplift rate during a shorter period of  $15 \text{ Ma}$  roughly reproduces river and  $\chi$  profiles similar to the Yalong River, when applying a  $K_f$  of  $4 \times 10^{-6} \text{ m}^{1-2m}/\text{yr}$ , but not the  $k_{sn}$ , which shows high values along the entire modeled profile (Figure 3.6F). When using a lower  $K_f$  of  $2 \times 10^{-6} \text{ m}^{1-2m}/\text{yr}$ , the high values of  $k_{sn}$  are located close to the plateau edge, but the propagation of the rivers into the hinterland is limited and the river profile is placed much higher than the Yalong River. When using a higher  $K_f$  of  $6 \times 10^{-6} \text{ m}^{1-2m}/\text{yr}$ , the modeled river incises more deeply than the Yalong River, with generally lower  $k_{sn}$  values (Figure 3.6C).

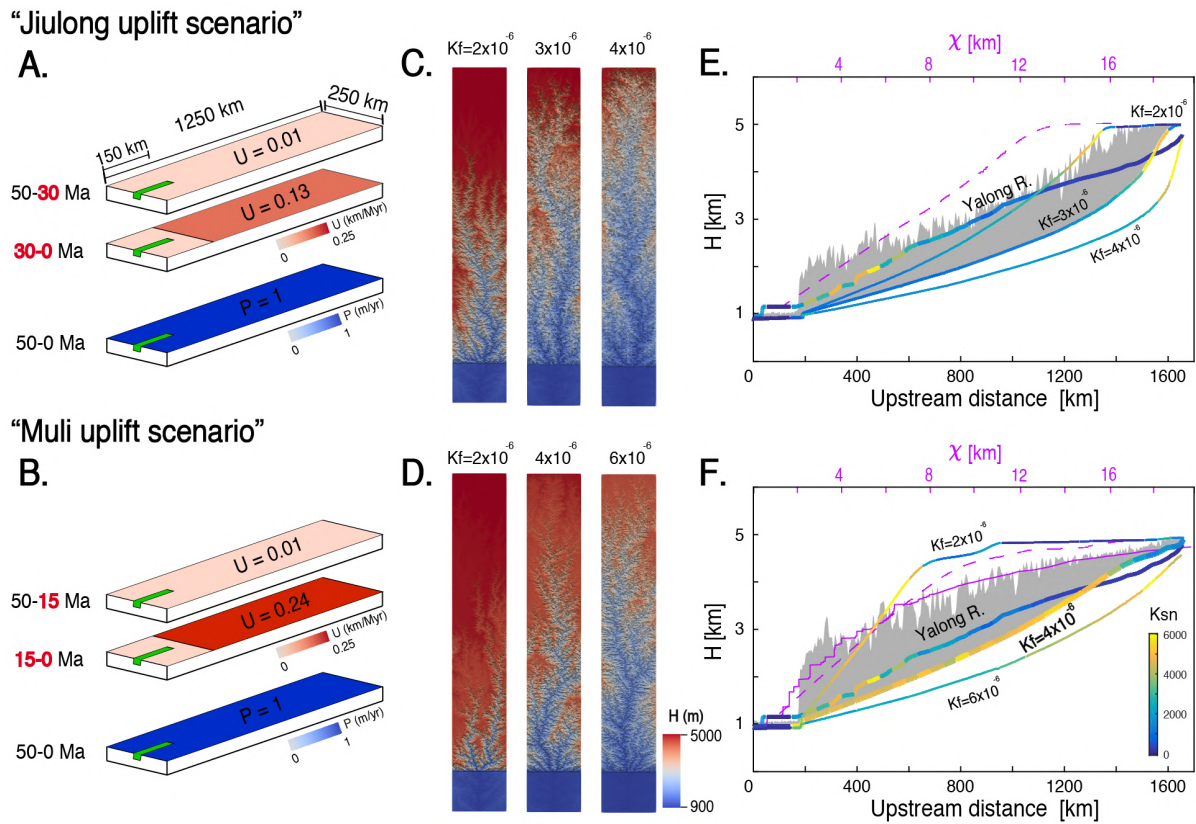


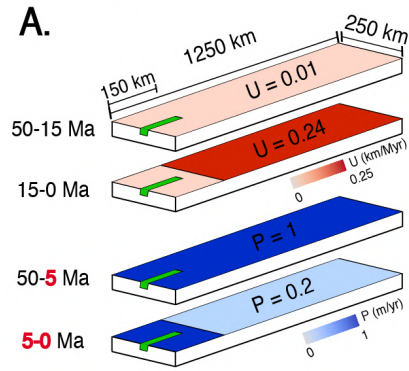
**Figure 3.6** - (A), (B) Model settings with different phases of uplift and constant precipitation ( $p = 1 \text{ m/yr}$ ) of the “Jiulong/Muli uplift scenario”. Constant strong uplift takes place in hinterland since  $30$  or  $15 \text{ Ma}$ ,

respectively. (C), (D) show the final topographic states of models with different  $K_f$ . (E), (F) present the 20-km wide swath profiles of the modeled rivers, revealing that a  $K_f$  of  $4 \times 10^{-6} m^{1-2m}/yr$  with a strong uplift since 15 Ma is most favorable to reproduce a proper river profile. The solid purple line is the x profile of the Yalong River and the dashed purple lines are the modeled rivers'  $\chi$  profiles, when  $K_f = 2 \times 10^{-6} m^{1-2m}/yr$  in E, and  $K_f = 4 \times 10^{-6} m^{1-2m}/yr$  in F.

### 3.1.5.3 Scenarios with orographic effect and/or reduced monsoon

Due to strong evapotranspiration of  $\sim 0.35 m/yr$  on the high plateau (average precipitation of  $\sim 0.55 m/yr$ ), the effective precipitation collected in the river network on the high plateau is of  $< \sim 0.2 m/yr$  (e.g., Lin et al., 2021;<sup>[230]</sup> Ma and Zhang, 2022<sup>[231]</sup>). We test an “Orographic effect scenario” with a dramatic drawdown of rainfall once the elevation of the hinterland reaches 3000 m (Figure 3.2), from  $1 m/yr$  in the foreland to  $0.2 m/yr$  of net precipitation on the plateau. With an uplift regime of  $0.24 km/Myr$  since 15 Ma and a  $K_f$  of  $4 \times 10^{-6} m^{1-2m}/yr$ , similar to the “Muli uplift scenario”, the elevation of the hinterland reaches 3000 m at 5 Ma (Figure 3.7A). Results show that a drier condition at high altitude contributes pronouncedly to preserve high topography along the modeled river and in the headwaters, with river and  $\chi$  profiles roughly similar to the Yalong River, but less incised (Figure 3.7C). Two knickzones with one at the plateau edge and another in the upstream—most part with high  $k_{sn}$  values identified (Figure 3.7E). Considering that the Asian monsoonal precipitation could have sharply dampened during 10–5 Ma, before an intensification and high seasonality of rainfall since 5 Ma (Clift, 2006<sup>[167]</sup>; Clift and Giosan, 2014)<sup>[237]</sup>, we test a scenario with the onset of aridification on the southeast Tibetan Plateau back to 10 Ma (Figure 3.7B), denoted as “Reduced monsoon scenario”. Such an earlier arid condition on the plateau preserves more efficiently the high interfluves and headwaters, but with a much more limited propagation of the river incision in the hinterland and a peculiar strongly convex-down river and  $\chi$  profile, including a greatly flat upstream part (Figure 3.7D, F). Remarkable flat surfaces are well preserved at high elevation in the interfluves of tributaries, which are rather shallow and wide (Figure 3.7F inset).

### “Orographic effect scenario”



### “Reduced monsoon scenario”

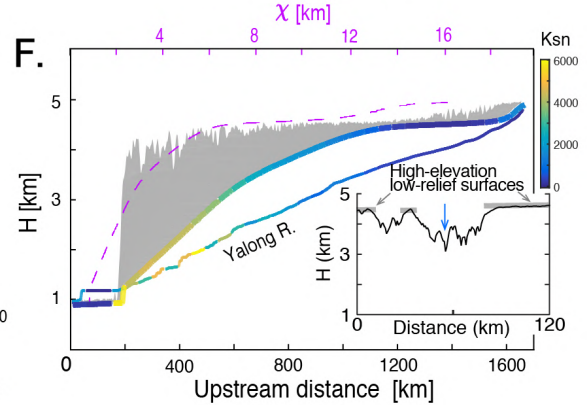
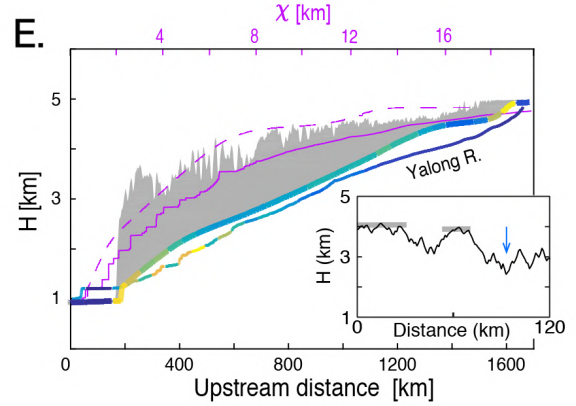
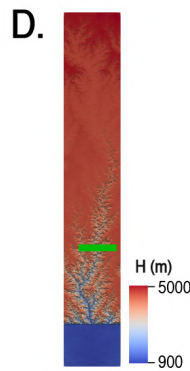
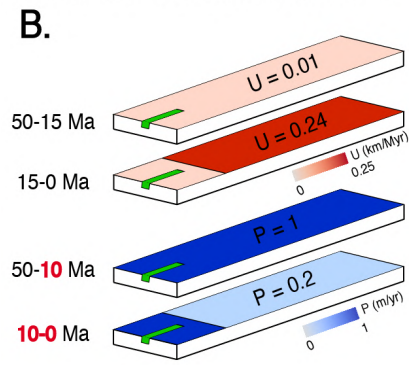


**Figure 3.7** - (A), (B) Model setting with different phases of uplift and precipitation of the “Orographic effect scenario” and “Reduced monsoon scenario”. Constant strong uplift takes place in hinterland since 15 Ma. Precipitation drops to  $0.2\text{ m/yr}$  after 5 or 10 Ma, due to a strong orographic effect on precipitation or a dramatic drop of monsoonal rainfall, respectively. (C), (D) are the final topographic states of model. (E), (F) show the 20-km wide swath profiles of modeled rivers, which incise insufficiently and inset figures are the cross-sections of river valleys (green lines in C, D). The solid purple line shows the  $\chi$  profile of the Yalong River and the dashed purple lines are the modeled rivers’  $\chi$  profiles.

#### 3.1.5.4 Increasing upstream inflow scenario

The former models reveal that a contradiction between the deep incision of river channels due to abundant runoff collected in the river network and the preservation of flat high topography for which little upstream precipitation is mandatory. We test a combination of a slight precipitation ( $p = 0.2\text{ m/yr}$ ) on the most part of plateau since 10 Ma due to orographic effect on precipitation and a weakened monsoon, and plentiful runoff in the channels, by incorporating a strong inflow in the river network with an enhanced precipitation ( $p = 1\text{ m/yr}$ ) in the uppermost 450 km of the model (Figure

3.8A). Such a combination well reconstructs a river channel similar to the Yalong River, with high-elevation and low-relief surfaces in the interfluves and headwaters and a more deeply and narrowly incised valleys down to a depth of  $\sim 2500$  m (Figure 3.8C insets). One thing worthy note is that the upstream-most section of the Yalong River profile (1/3 of all) shows a headward flattening of channel slope, marked by a slope rupture, this is not reproduced in our model. And the 20-km wide swath profile along the Yalong River envelopes tightly the swath profile of modeled river, except several local topographic peaks (Figure 3.8C), which are associated to the activity of Jiulong thrust and Ganzi thrust, branching to the Ganzi strike-slip fault (Zhang et al., 2016<sup>[121]</sup>) (Figure 3.3B) and are not reproduced in our model. The highest  $k_{sn}$  values in this scenario occur near the thrust belt, similar to the knickzone across the YTB in the Yalong River catchment.

### “Increasing upstream inflow scenario”

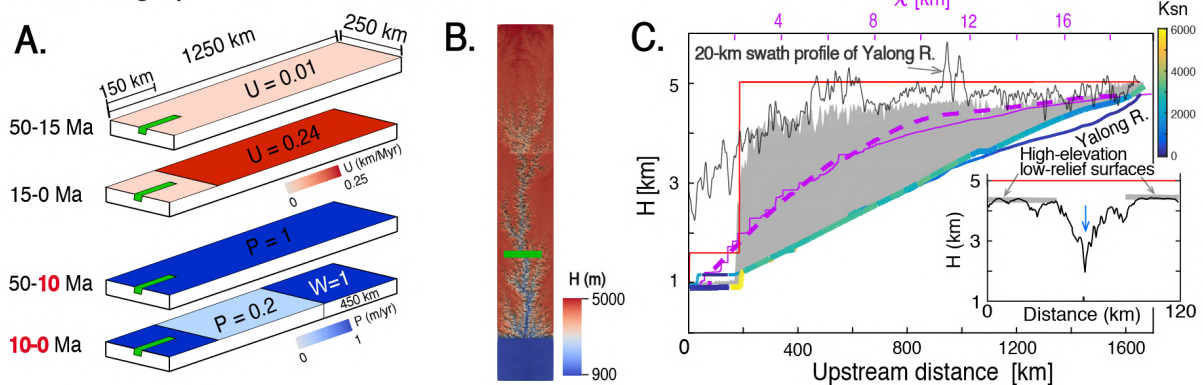


Figure 3.8 - (A) Model setting with different phases of uplift and precipitation. Constant strong uplift takes place in hinterland since 15 Ma. Precipitation drops to  $0.2 \text{ m/yr}$  since 10 Ma, due to a combination of strong orographic effect on precipitation and dramatic drop of monsoonal rainfall. Strong imposed runoff in the river networks is incarnated by an enhanced precipitation of  $1 \text{ m/yr}$  ( $W=1$ ) in the uppermost 450 km part. (B) is the final topographic state of model. (C) gives the rivers’ 20-km wide swath profile, showing deeply incised valley and preservation of a high plateau. Inset figures are the cross-sections of modeled river valleys (green lines in B). The red line represents the maximum surface uplift attained. The solid purple line represents the  $\chi$  profile of the Yalong River and the dashed purple line shows the modeled river’s  $\chi$  profile.

## 3.1.6 Discussion

### 3.1.6.1 Effect of the monsoon on the topographic evolution of southeast Tibet

In southeast Tibet, the juxtaposition of high-elevation, low-relief interfluvial surfaces (~4500 m high) close to the plateau edge and deeply-incised river valleys (>2500 m deep) in the middle reaches of the large rivers has drawn attentions to how the interaction between climate and tectonics generates this peculiar landscape (e.g., Clark et al., 2005b<sup>[67]</sup>; Liu-Zeng et al., 2008<sup>[100]</sup>). But modelling such an interaction on a large zone has been rarely done yet. Using FastScape allows us to predict landscape evolution, where surface erosion rate depends mainly on river discharge and hillslope processes (Braun and Willett, 2013<sup>[299]</sup>), by imposing simplified scenarios of uplift (tectonic forcing) and precipitation (climatic forcing). Employing a protracted and constant uplift rate of  $0.1 \times 10^{-3} \text{ m/yr}$ , our basic parameter study results for the Yalong River catchment in the Great Bends Region demonstrate that any increase of the erosion coefficient  $K_f$  and/or precipitation  $p$  in the stream power law favors regressive erosion throughout the river network, destroying the uplifted high topography and enlarging the valley widths. In contrast, decreasing  $K_f$  and/or  $p$  will contribute to preserving high topography and/or flat surfaces and generating strongly incising and narrow river valleys, but not propagating fluvial incision into the plateau interior (Figure 3.4D, E). Furthermore, any model with strong precipitation (1 m/yr) on an existing high plateau of present-day elevation, for example caused by monsoonal strengthening since the Mid-Miocene Climate Optimum (~17–14 Ma, Nie et al., 2018<sup>[154]</sup>), could not maintain the already established high topography and leads to a significant topographic decay in a relatively short time (Figure 3.5E, F). At last, such regressive erosion leads to the formation of steep escarpments upstream, similar to the one observed in passive continental margins with a relatively dry climate along the coasts of southwest Africa and southeast of South America, interpreted as a long-existing “escarpment-retreat” primarily controlled by flexural isostatic rebound (Braun, 2018<sup>[380]</sup>). But such an upstream escarpment topography is not observed in the tectonically active southeast Tibet.

A recent modelling study of topographic evolution in the Three Rivers Region employed a wave of maximum surface uplift of  $0.24 \text{ km/Myr}$  propagating toward the southeast (Yuan et al., 2021<sup>[119]</sup>). This model well reproduced the deeply incised river valleys and high flat surfaces in the headwater and interfluvial, persisting for tens of millions of years, and resembles the hypothesis of lower crustal channel flow propagating from central Tibet (Clark and Royden, 2000<sup>[18]</sup>; Royden et al., 1997<sup>[59]</sup>). The

combination of a strong  $p$  of  $1\text{ m/yr}$  and a small  $K_f$  of  $1.2 \times 10^{-6}\text{ m}^{1-2m}/\text{yr}$  in their model helped to avoid extensive erosion of uplifted high topography, meanwhile the propagating uplift imposed a localized strong river incision on the plateau edge, which traveled along the uplift wave toward downstream. Paleoaltimetry studies from the Gonjo and Markam basins on the plateau edge showed that this part has been at present day's elevation since  $\sim 40\text{ Ma}$  or  $\sim 30\text{ Ma}$ , respectively (Li et al., 2015<sup>[179]</sup>; Su et al., 2019<sup>[97]</sup>; Tang et al., 2017<sup>[209]</sup>; Xiong et al., 2020<sup>[210]</sup>), and the foreland Jianchuan basin was uplifted since  $\sim 28\text{ Ma}$  to reach the modern height at  $\sim 20\text{ Ma}$  (Cao et al., 2020<sup>[122]</sup>; Gourbet et al., 2017<sup>[181]</sup>). Indeed, this shows, to the first order, a southeastward propagation of the growing plateau edge since  $50\text{ Ma}$  in the Three Rivers Region. However, abundant low temperature thermochronological data show decreasing erosion rates from west to east in the Three Rivers Region (Yang et al., 2016), in agreement with a strong northeastward shortening perpendicular to the river channels due to the indenting EHS, revealed by the narrow spacing between large rivers and the arcuate belt of Paleogene intramountainous basins (e.g., Hallet and Molnar, 2001<sup>[116]</sup>; Horton et al., 2002<sup>[91]</sup>). Such shortening has been accommodated by parallel northwest/north striking thrusts guiding the large rivers (Replumaz et al., 2020<sup>[151]</sup>), which have a stable channel since the onset of the collision (Lacassin et al., 1998<sup>[311]</sup>). This lateral advection has to be the main tectonic forcing to form the elongate shape of drainage basins and the unique characteristics of landscape. Nevertheless, the propagating uplift wave model (Yuan et al., 2021<sup>[119]</sup>) shows that this lateral advection is only slightly contributive, but not necessarily needed. To the east, this propagating uplift wave is not evidenced in the Great Bends Region by either paleoaltimetric or thermochronological data, while similar river profiles among the Yalong, Yangtze, Mekong and Salween rivers (Yang et al., 2016<sup>[150]</sup>) suggest that other potential processes could sculpt the similar landscapes.

### **3.1.6.2 Implication of Oligocene (LMTB) versus Miocene (YTB) uplift on the resulting topography of the Yalong catchment**

Based on low temperature thermochronological data, the Oligocene to Miocene activity of YTB has been invoked to explain the uplift history of the Yalong margin of the southeast Tibetan Plateau, with strong activity since  $\sim 12.5\text{ Ma}$  (Clark et al., 2005a<sup>[138]</sup>; Pitard et al., 2021<sup>[123]</sup>), or since  $\sim 35\text{ Ma}$  (Wang et al., 2012<sup>[120]</sup>; Zhang et al., 2016<sup>[121]</sup>). We use these results to build two simplified tectonic scenarios, the “Muli uplift scenario”, and the “Jiulong uplift scenario”, with uniform uplift starting at  $15$  or  $30\text{ Ma}$ , respectively. Our such scenarios only use these onset timing of regional surface uplift,

without attempting to explore the mechanism of regional crustal thickening. We show that the “Muli uplift scenario” best reproduces the river profile morphology, while the longer uplift phase of the “Jiulong uplift scenario” with reduced uplift rate would result in an enhancement of erosion, as in the basic parameter study models (Figure 3.4, Figure 3.6A, E). Therefore, we conclude that a predominant strong exhumation phase since the middle Miocene as estimated for the Muli thrust (Pitard et al., 2021<sup>[123]</sup>) is mandatory to build a strong topographic step in the southeast Tibet, while earlier crustal thickening phases made a less important contribution to the building of the plateau margin (Zhang et al., 2016<sup>[121]</sup>). Similar to the “Jiulong uplift scenario”, the activity of the LMTB may have been more intense during 30–25 Ma (exhumation rate 0.8 km/Myr) than since 10 Ma (exhumation rate 0.4 km/Myr) (Godard et al., 2009<sup>[158]</sup>; Wang et al., 2012<sup>[120]</sup>; Tian et al., 2013<sup>[70]</sup>, 2015<sup>[145]</sup>; Tan et al., 2014<sup>[300]</sup>), such a longer tectonic phase would reinforce a regional fluvial erosion. Indeed, we observed a lower mean elevation for the Longmenshan range, stronger erosion imposed by the Dadu and Min rivers, and more developed dendritic drainage networks in the hinterland of the range, compared to the Yalong river catchment (Figure 3.3B, Figure 3.9).

### **3.1.6.3 Competition between deeply incising rivers and interfluvial surfaces preservation of southeast Tibet**

The modelling results of a weak effective precipitation ( $0.2\text{ m/yr}$ ) at high elevation since 5 Ma (“Orographic effect scenario”) or 10 Ma (“Reduced monsoon scenario”) illustrate an efficient protection of high interfluvial/headwater creeks or flat surfaces (Figure 3.7E, F). Indeed, the “Reduced monsoon scenario” shows a strongly convex-up river profile without efficiently dissecting the high topography due to a significant deficiency of runoff in the network, compared to the uplift scenarios with strong precipitation. It illustrates the competition between deeply incising rivers which needs plentiful stream power in the rivers (strong precipitation on the plateau) and preserving high and flat interfluvial/headwater surfaces which needs limited large-scale fluvial erosion (low precipitation on the plateau).

To combine these two effects, we choose to make a model of “Increasing upstream inflow scenario”, with artificial boundary conditions by applying an orographically reduced precipitation ( $0.2\text{ m/yr}$ ) on the high plateau since 10 Ma as well as an artificial water inflow by maintaining a strong precipitation ( $1\text{ m/yr}$ ) in the uppermost part of plateau. This artificial combination reproduces well a coexistence

of deep river gorges adjacent to high and low-relief surfaces, through laterally hampering a wave of upstream-propagating river incision in the tributaries, while sustaining a strong downward dissection in the stem river (Figure 3.8B, C). Such a topography characteristic is very similar to the high and low-relief Daocheng and Jaggai massifs along the middlestream Yalong river gorge (Figure 3.9). Those two low-relief surfaces, located very close to the plateau edge and to the deeply incised Yalong River, have rarely been affected by regressive erosion, with very old apatite (U-Th)/He ages of 50–110 Ma (Daocheng massif) and ~60 Ma (Jaggai massif), showing little denudation during the India-Asia collision (e.g., Clark et al., 2005a<sup>[138]</sup>; Tian et al., 2014<sup>[139]</sup>). This is also in concert with our model showing little erosion/exhumation (~500 m) on those flat surfaces, which is calculated as the space between the maximum surface uplift (red thick lines) and the maximum topography of the final state (upper limit of light grey shadows) (Figure 3.8C). The absence of such flat surfaces in the hinterland of the Longmenshan is probably due to stronger precipitation related to weaker orographic effect across lower average elevation, while the endorheic plateau north of the range was also captured and drained to north by the Yellow River since Quaternary (e.g., Craddock et al., 2010<sup>[189]</sup>).

#### 3.1.6.4 Potential gradual capture of upstream endorheic zone

The endorheic zone of the Tibetan Plateau has been proposed to be more extensive to the east, where evasive lacustrine sediments were deposited between ~23.5 Ma and ~13.5 Ma in numerous immense interconnected paleo-lakes, before being captured during the expansion of externally drained rivers from the southeast (Wu et al., 2008<sup>[212]</sup>) (Figure 3.2B). The basin-averaged detrital low temperature thermochronological ages from the upstream drainage of large rivers in southeast Tibet illustrate a roughly synchronous river incision event at ~11 Ma, which potentially reveals the onset of capturing the endorheic zone (Duvall et al., 2012<sup>[155]</sup>). The strong artificial inflow water in our “Increasing upstream inflow scenario”, which contributes to deeply dissect the plateau edge, could be explained by a long-lasting and gradual capture and integration of upstream endorheic zone, bringing more runoff into the external river networks. This mechanism of excessive water due to a drainage integration has been convocated to explain a reinforced fluvial incision since Quaternary in the Yellow River, through lake spillover and capture events of the upstream basins (e.g., Zoige Basin, Figure 3.9), occurring substantially later than the mountain building onset during 14–8 Ma (Craddock et al., 2010<sup>[189]</sup>). Similarly, in the northwest Iranian Plateau, a coexistence of high lake level in wet condition and subdued topography at the plateau margin enabled lake overflow to cut ~1 km deep gorge downstream

since ~4 Ma (Heidarzadeh et al., 2017<sup>[381]</sup>). In the central Apennines, sufficient sediments were generated by reliefs formed through fault-block uplift to fill the extensional basins, leading to successive overspill of individual small basins, which resulted in strong fluvial incision since the early Pleistocene (Geurts et al., 2018<sup>[382]</sup>). Even though only an Eocene basin has been reported and no large Miocene paleo-lakes was observed in the upstream Yalong River (Zhang et al., 2010<sup>[383]</sup>), a possible capture event of a vast endorheic zone, since the capture onset at ~11 Ma determined for the upstream Yalong River catchment, could have sufficiently increased the runoff and stream power in the river network to entrench the middlestream Yalong River into deep gorges, while flat surfaces are also preserved close to the edge of the plateau by the orographic effect (Figure 3.9).

### 3.1.6.5 Inefficiency of simple Stream Power Law to model plateau scale topography of southeast Tibet

The upstream-most section of the Yalong river (~1/3) is much flatter, showing a slope rupture marked by an inflection point on the channel profile (Figure 3.8C), which has also been observed for the Yangtze, Mekong and Salween rivers (Yang et al., 2016<sup>[150]</sup>). We consider that the upstream drainage area of those large rivers was part of the low-relief endorheic zone of the Tibetan Plateau before captured (Figure 3.2), and is not yet affected by the strong fluvial incision (Figure 3.9), which allows a significant amount of water to be collected in a single river without eroding the flat upstream plateau. This has been integrated in our model (section 3.1.5.4) with a strong artificial water inflow in the uppermost part. Such extra stream power in the channel and an aridification on the plateau are needed to carve deep gorges in downstream and also avoid eroding the high and flat topography between the large rivers. However, our “Increasing upstream inflow scenario” model result shows only a simple linear river profile and could not reproduce the relatively flat slope of the upstream-most section. For us, it shows that the landscape evolution model FastScape, combining simple stream-power law of bed rock river erosion and simple diffusive hillslope processes, requires some unrealistic boundary conditions to reproduce the present-day topography in southeast Tibet. A previous study using FastScape to jointly reconstruct the topographic and exhumational history has imposed a threshold parameter of critical shear stress ( $\tau_c$ ) to successfully avoid excessive erosion of the post-orogenic in the Pyrenees range since ~20 Ma (Curry et al., 2019<sup>[384]</sup>). While applying such a threshold parameter in modelling the topography evolution on the Tibetan Plateau scale had eventually prohibited the erosion into the plateau (Maret, master thesis, 2018), similar to our

parameter study model with precipitation of  $0.1\text{ m/yr}$  and  $K_f$  of  $2 \times 10^{-6}\text{ m}^{1-2m}/\text{yr}$  (Figure 3.4D, E).

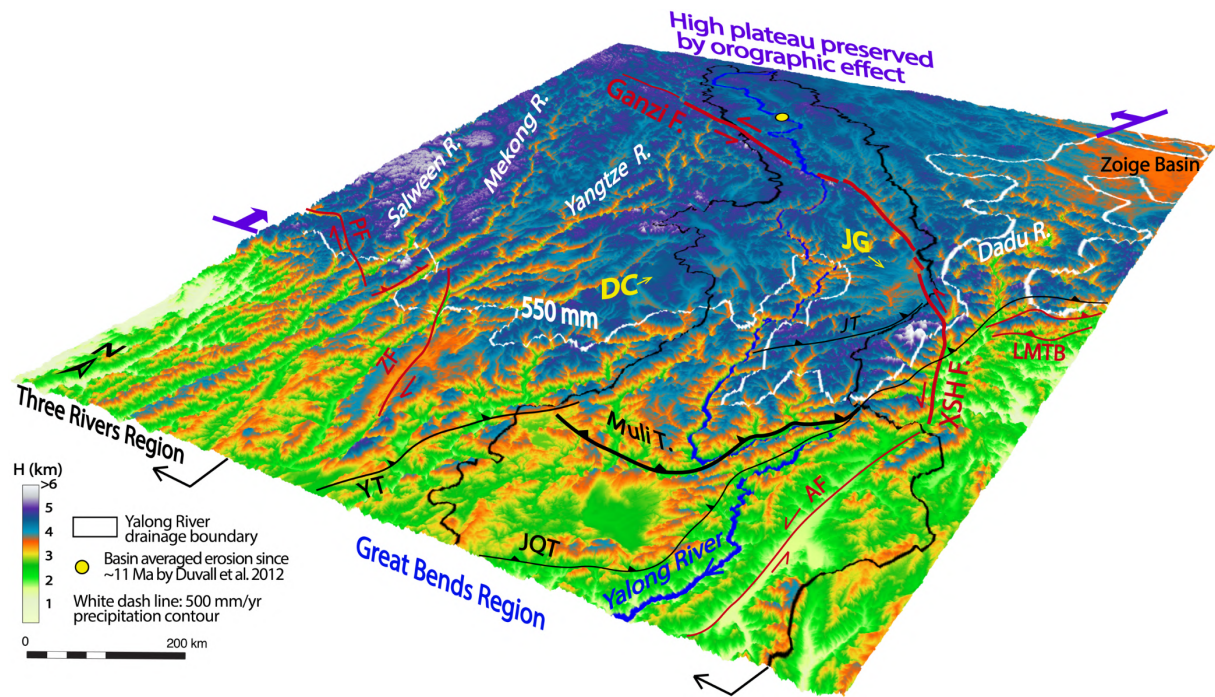


**Figure 3.9** – Topography of southeast Tibet, divided into two zones, the Three Rivers Region to the west and the Great Bends Region to the east, delimited by black arrows on the southern border. The outlined Yalong River catchment (in black) is separated into three zones from north to south, a flat upstream zone with a low slope river channel collecting water without eroding, a deeply incised middlestream zone with a strong channel slope and the foreland zone with strong monsoonal precipitation but a low channel slope. The Gaussian-filtered precipitation contour of  $550\text{ mm/yr}$  (in white) roughly outlines the southeast Tibetan Plateau edge, showing a strong orographic effect, above which the plateau is preserved from regressive erosion. This is exemplified by the low-relief and high-elevation Daocheng (DC) and Jaggai (JG) surfaces (in yellow) near the plateau edge, bordering the deep Yalong middlestream gorge. The yellow circle shows the study of basin-averaged river erosion during  $\sim 11\text{--}4\text{ Ma}$  of the upstream Yalong River. Mains active faults from west to east are in red thick line: Parlung Fault (PF), Zhongdian Fault (ZF), Ganzi fault, Xianshuihe Fault (XSHF), Anninghe Fault (AF) and Longmenshan Thrust Belt (LMTB). Main thrusts of the Yulong and Yalong Thrust Belts are in black thick line: Yulong Thrust (YT), Jinghe-Qinghe Thrust (JQT), Jiulong Thrust (JT) and Muli Thrust.

### 3.1.7 Conclusion

The southeast Tibet, externally drained by the large Salween, Mekong, Yangtze and Yalong rivers, is characterized by flat upstream areas on the inland plateau and low-relief interfluvial surfaces at high

elevation, bordering deep gorges across the plateau edge. Our modelling results show that the previously suggested intensified monsoon since the Mid-Miocene Climate Optimum (~17-14 Ma) on the already-existing pre-Neogene high plateau, could destroy the high plateau. Similarly, a simple expansion of drainage area by capturing the upstream endorheic zone of a high plateau since 15 Ma without considering a potential spatial variation in precipitation would also destroy the pre-existing high topography. A long uplift phase (since ~30 Ma) would also result in strong erosion of the topography, with large and wide rivers and no interfluvial low-relief surfaces preserved at high elevation, while a shorter uplift phase (since ~15 Ma), such as the Miocene activity revealed from the Muli thrust, is essential to preserve the interfluvial elevated surfaces. While, considering only the orographic effect on reducing precipitation on the plateau would result in a weak net precipitation, which could not generate enough runoff to sufficiently incise in river channels. Conclusively, we propose that, in the Great Bends Region, a combination of strong Miocene uplift, as suggested by the strong tectonic exhumation on the Muli thrust, weak net precipitation on the high plateau above 3000 m, together with an increasing channel inflow, due to large amount of water collected from capturing a formerly larger endorheic zone of inland plateau, could well reproduce the headwater and interfluvial low-relief surfaces and deeply incising rivers in the Yalong River catchment. Nevertheless, the simple Stream Power Law used here is not completely efficient to model catchment-scale topography of southeast Tibet, and it cannot collect sufficient amount of water on the high and flat inland plateau without eroding, which needs to be artificially reproduced by increasing inflow in channels from the upstream and weak precipitation on the plateau.

## **Code availability**

The FastScape code for landscape evolution modelling was developed by Jean Braun and is available at: <https://github.com/fastescape-lem>.

## **Acknowledgements**

This work has been supported by the China Scholarship Council Funds and Agence Nationale de Recherche (ANR “Tibetan Orchestra”). Jean Braun is warmly thanked for providing the FastScape code and constructive comments on the modelling. Thanks for Peter van der Beek for very helpful discussion and correction of manuscript.

## **Author contribution**

X. OU and A. Replumaz have worked together through this manuscript.

Xiong OU: Conceptualization, Methodology, Code, Visualization, Writing-Original draft preparation

Anne Replumaz: Conceptualization, Supervision, Writing-Reviewing and Editing

## **Declaration of competing interest**

The authors declare that there are no known competing financial interests or personal relationships that could have influenced this paper.

# Conclusions and outlook

The main results obtained during my PhD work allow to better understand, to the first order, how the unique landscapes of the southeast Tibetan Plateau, significantly different from flat plateau interior and other highly mountainous plateau rims with abrupt topographic steps, evolves into today's physiography. Here I will present the synthesized conclusions and their implications with respect to the principle questions developed in the Chapter 1, concerning the major roles undertaken by the temporally and spatially varying tectonic and climatic forcing during the topographic evolution, first in a local scale of the Kawagebo and Baimaxueshan massifs, and then extend our vision to a regional scale. Whereafter, some unsolved questions arising from our results will be discussed and some perspectives will be given to illustrate some guidelines for the future works, in order to complete and enrich this thesis work.

### **4.1 Contrasting exhumation and topography development histories in the core of the Three Rivers Region**

Southeast Tibet is characterized by extensive low-relief high-elevation surfaces in the interfluvies and headwaters, which have been interpreted as “relict surfaces” (Clark et al., 2006 <sup>[126]</sup>), where thermochronological data generally show old ages and very little exhumation during the India-Asia

collision (e.g., Clark et al., 2005a<sup>[138]</sup>; Wilson and Fowler, 2011<sup>[144]</sup>; Tian et al., 2014<sup>[139]</sup>; Liu-Zeng et al., 2018<sup>[157]</sup>; Cao et al., 2022<sup>[344]</sup>). Meanwhile, in the neighbouring deep valleys, high local relief are prevailing and strong exhumation are generally reported in the river valleys, giving young thermochronological ages (e.g., Clark et al., 2005 a<sup>[138]</sup>; Godard et al., 2010<sup>[142]</sup>; Ouimet et al., 2010<sup>[143]</sup>; Yang et al., 2016<sup>[150]</sup>; Nie et al., 2018<sup>[154]</sup>; Replumaz et al., 2020<sup>[151]</sup>). Those relict surfaces are proposed to be formed at low elevation and then uplifted and dissected by large rivers, based on a regional interpolation and combination of such surfaces and young thermochronological data (<15 Ma), interpreted as reflecting a regional regressive river erosion into these surfaces since middle Miocene (Clark et al., 2005a<sup>[138]</sup>).

The first part of my work pays attention to the relief/topography evolution of such relict surface and the development of deep river incision in a local scale, through careful interpretation of an abundant low temperature thermochronological data and thermo-kinematic modelling (Pecube). One of relict surfaces, the Baimaxueshan massif with low relief (<600 m) and moderate elevation (~4500 m) and the high-relief (~3500 m) and high-elevation (~6500 m) Kawagebo massif across the Mekong river were selected to illustrate contrasting exhumation and relief development. The Baimaxueshan massif is the closest relict surface to the Eastern Himalayan Syntaxis (EHS) in the Three Rivers Region, where Salween, Mekong and Yangtze rivers flow southward parallelly and closely, showing large-scale shortening during the collision. This region represents a transition between the strongly deformed zone around EHS and the less deformed southeast Tibetan plateau margin in Yunnan and Sichuan, and is an appropriate zone to examine the relief development and the interaction between pre-existing structures, Cenozoic regional/local tectonics and river incision during the landscape evolution of southeast Tibet.

I compiled and modelled published thermochronometric ages for Baimaxueshan massif (Liu-Zeng et al., 2018<sup>[157]</sup>), east of the Mekong River. Modelling results show regional rock uplift at a rate of 0.25 km/Myr since ~10 Ma, following slow exhumation at a rate of 0.01 km/Myr since at least 22 Ma. Estimated Mekong River incision accounts for a maximum of 30% of the total exhumation since 10 Ma. I interpret moderate exhumation of the Baimaxueshan massif since 10 Ma as a response to a regional uplift due to the continuous northward indentation of NE India in a zone around the Eastern Himalayan Syntaxis (EHS) and delimited by Longmucuo-Shuanghu suture in the north. Thus my results show that the Baimaxueshan massif with significant exhumation due to strong regional uplift could not be classified as “relict surface” and not all low-relief surfaces are formed at low. I speculate that its low relief results from in part glacial “buzzsaw-like” processes at high elevation, enhancing

since ~2 Ma, consistent with the previous proposition of in-situ formation of low-relief landscape enhanced glacial erosion (Zhang et al., 2016<sup>[121]</sup>). Therefore, any application of such a regional “relict surface” should bear more attention, when investigating such low-relief surfaces in different regions, characterized by various tectonic and climatic regimes.

In contrast, by modelling the thermochronological data from last filed mission in 2015 (Replumaz et al., 2020<sup>[151]</sup>) and Yang et al. (2016)<sup>[150]</sup>, I determine that the high-relief, high-elevation Kawagebo massif to the west of the Mekong River, facing the Baimaxueshan massif, show much stronger local rock uplift at a rate of 0.45 km/Myr since at least 10 Ma, accelerating to 1.86 km/Myr since 1.6 Ma. I show that the thermochronometric ages are best reproduced by local rock uplift related to late Miocene reactivation of a kinked westward-dipping thrust, striking roughly parallel to the Mekong River, with a steep shallow segment flattening out at depth. The reactivation of such thrust results from a constraining bend due to a left-stepping between dextral Jiali-Parlung and Zhongdian strike-slip faults. Such strong local uplift above the reactivated thrust is part of a large-scale knickzone around the EHS in the core of the Three Rivers Region. My results also imply a similar contribution of Mekong River incision (25%) to exhumation, indicating that the formerly proposed dominance of river incision due to strengthened monsoonal precipitation since the Mid-Miocene Climatic Optimum (MMCO) is, at least, not applicable in this large knickzone. To conclude this part, the strong differences in elevation and relief that characterize both massifs are linked to variable exhumation histories due to a strongly differing tectonic imprint.

## **4.2 Regional crustal deformation and surface uplift in the Three Rivers Region during Cenozoic**

Since the first part of my PhD work only looks into a local scale of tectonic deformation and topography development by using thermochronology data from low elevations, I was interested to investigate more into the longer complex tectonic evolution of the Kawagebo massif, as well as the tectonic responses of the whole Three Rivers Region, Eastern Qiangtang terrane, to the continuous indentation of the EHS since the India-Asia collision, by combing the previously reported data in the neighboring locations of Baimaxueshan (Liu-Zeng et al., 2018<sup>[157]</sup>), Zuogong (Xiao et al., 2015<sup>[159]</sup>; Cao

et al., 2022 <sup>[344]</sup>), Markam (Wilson and Fowler, 2011 <sup>[144]</sup>; Cao et al., 2022 <sup>[344]</sup>) and Weixi massifs (Liu-Zeng et al., 2018 <sup>[157]</sup>; Cao et al., 2020 <sup>[122]</sup>, 2022 <sup>[344]</sup>).

The exceptionally narrow spacing among the large parallel rivers (e.g., Salween, Mekong, Yangtze), ubiquitous inactive NW-SE to N-S thrusts, together with the prevailing vertical dip of Jurassic-Cretaceous sedimentary layers, all reflect the large crustal strains and enhanced NE-SW shortening oriented radially from the EHS (e.g., Hallet and Molnar, 2001 <sup>[116]</sup>; Replumaz et al., 2020 <sup>[151]</sup>). While the Cenozoic tectonic deformation history in the Three Rivers Region remains ambiguous and far away from being determined. My second part of work brings new of low temperature thermochronology data from the high-relief and high-elevation Kawagebo massif, enriching the regional dataset and contributing to the general tectonic evolution.

My new samples from elevations between 2800–4100 m of massif yield relatively young AHe (4.8–13.1 Ma), AFT (3.8–14.2 Ma) and especially young ZHe (11.3–26.7 Ma) ages. My thermo-kinematic modelling results determine a first episode of rapid exhumation since at least 32 Ma to ~15–10 Ma, with an exhumation amount up ~10 km and a very rapid slip rate above the Mekong thrust (1.11–1.91 km/Myr). This is consistent with recent results of strong exhumation (~8 km) during 36–34 Ma and 21–18 Ma in the Zuogong plateau, located north of the massif (Cao et al., 2022 <sup>[122]</sup>). Therefore, both sections demonstrate a rapid exhumation, which is roughly contemporaneous, above the activated Mekong thrust along the mechanically weak Longmucuo-Shuanghu suture. I compared new thermochronology data with datasets from the massifs east to the suture (Markam, Baimaxueshan and Weixi massifs) and it clearly illustrates less exhumation (<3.5 km) since the collision and much older ages (AFT, ZHe >36 Ma), revealing weaker tectonic activity on these massifs since ~36 Ma. Therefore, significant crustal shortening and surface uplift occurs principally during the Late Eocene and Early Miocene to the west of the Longmucuo-Shuanghu suture and results in a remarkable topography excess, with an average elevation >5 km in the region around the EHS, comparing to the massifs east to the suture. This strong compression overlaps the continuous or episodic activity of thrust belts since ~50 Ma to ~25 Ma, bounding the syncontractional intermontane basins with Eocene to Early Oligocene ages and uplifting those basins to elevations of ~3.5 to 4 km at Early Oligocene, slightly lower than their present-day elevations at ~4500 m (e.g., Horton et al., 2002 <sup>[91]</sup>; Spurlin et al., 2005 <sup>[176]</sup>; Wang et al., 2008 <sup>[78]</sup>; Studnicki-Gizbert et al., 2008 <sup>[177]</sup>; Staisch et al., 2016 <sup>[182]</sup>).

Activation or reactivation along main thrust belts across the eastern and southeastern Tibet also pervasively record this compressional event, such as the Longmenshan thrust belt during 30–20 Ma (Godard et al., 2009 <sup>[158]</sup>; Wang et al., 2012 <sup>[120]</sup>; Tian et al., 2013 <sup>[70]</sup>, 2015 <sup>[145]</sup>; Tan et al., 2014 <sup>[300]</sup>), the

Jiulong thrust during 35–30 Ma (Zhang et al., 2016<sup>[121]</sup>), and the Anninghe fault during 24–18 Ma (Wang et al., 2020<sup>[366]</sup>) and Yulong thrust during 28–20 Ma (Cao et al., 2019). Southeast to the EHS, large-scale southeastward extrusion of the Indochina block occurs during 34–17 Ma in response to the indenting EHS (e.g., Leloup et al., 2001<sup>[32]</sup>; Cao et al., 2011<sup>[364]</sup>; Wang et al., 2020<sup>[365]</sup>). Since ~15–10 Ma, a second slower exhumation phase (rate of 0.42–0.52 km/Myr) of the Kawagebo massif is also determined, after the regional cessation of the Mekong thrust. A left-stepping between dextral Jiali–Parlung and Zhongdian strike-slip faults causes relatively weaker local uplift in the massif. This second uplift phase witnesses a transition of block extrusion from the Indochina to the region between the dextral Jiali–Zhongdian–Red River faults and sinistral Ganzi–Xianshuihe–Xiaojiang faults north of it in southeast Tibet. Reactivation of Longmenshan–Yalong thrust belts also took place since Middle Miocene due to compression related to this extrusion transition to the north.

Our study zone of the Kawagebo massif, locating between the compressed Three Rivers Region and the extruded Indochina block, remains a key place to have recorded these two important tectonic phases, making its study of great interest to understand and quantify the evolution of the deformation in southeast Tibet.

### **4.3 Cenozoic topographic evolution in the southeastern Tibetan Plateau: exemplified by the Yalong River catchment**

The topographic characteristic of the first order in southeast Tibet consists of a coexistence of deeply incising rivers valleys (Salween, Mekong, Yangtze, Yalong, etc.) and neighboring low-relief surfaces in interfluvial and headwaters of these large rivers. The first part of my work illustrates, on a local scale, the different contribution of tectonic forcing and river incision to the exhumation and topography evolution in the rugged and high Kawagebo massif and the Baimaxueshan massif, one of the low-relief “relict surfaces” at moderate elevation. In order to obtain a better understanding of the regional landscape evolution of southeast Tibet, I needed to apply a method which deals with the tectonic uplift and erosion processes on a large scale. I effectuated different models with the landscape evolution model FastScape (Braun and Willett, 2013<sup>[299]</sup>) by implementing compiled tectonic and

climate information since the India–Asia collision. In the “Three Rivers Region” around the EHS, a southeastward propagating uplift wave from central Tibet has recently been used to generate the peculiar topography of this region, combined with strong precipitation but small erosion coefficient (Yuan et al., 2021<sup>[119]</sup>). I focus only on the Yalong River catchment in the “Great Bends Region” to the east, which is more influenced by NW–SE contraction.

By modelling the previously suggested intensified monsoon since the Mid–Miocene Climate Optimum (~17–14 Ma) on the already-existing pre–Neogene high plateau (Nie et al., 2018<sup>[154]</sup>), I firstly show that this strong monsoonal precipitation could completely destroy the high plateau and this is consistent with our conclusion of the first section, indicating no dominant role of fluvial erosion in, at least, the large knickzone along the Mekong River. Then, I modelled a simple expansion of drainage area by capturing the upstream endorheic zone of a high plateau since 15 Ma (Rohrmann et al., 2018<sup>[169]</sup>), but without considering any spatial variation in precipitation, similarly, the pre-existing high topography would be destroyed, creating an “escarpment–retreat” like topography, which is obviously not the case of southeast Tibet.

In the following, I explored the different tectonic scenarios (with a constant high precipitation of 1 m/yr), based on the existing regional thermochronology data, giving the timing of exhumation and related fault activity. I used a long uplift phase (since ~30 Ma) since the Yulong and Longmenshan thrust belts both experienced such a exhumation phase. This model would also lead to enhanced erosion of the topography, generating large and wide rivers and no interfluvial low-relief surfaces preserved at high elevation. I also used a shorter uplift phase (since ~15 Ma) based on the Miocene activity revealed from the Muli thrust, showing that this recent uplift is essential to preserve the interfluvial elevated surfaces, but the river morphologies are still significantly different from the observation.

High topography would largely reduce the precipitation on the plateau over a certain elevation. I therefore took into consideration the orographic effect on reducing precipitation on the plateau in my model. Modelling shows that such a resulting weak net precipitation could not generate enough runoff to sufficiently incise in river channels. Until here, my models clearly illustrate a strong competition between deeply incising rivers, which needs plentiful stream power in the rivers (strong precipitation on the plateau), and preserving high and flat interfluvial/headwater surfaces, which needs limited large-scale fluvial erosion (low precipitation on the plateau).

Attempting to resolve this dilemma, I combined strong Miocene uniform uplift on the Muli thrust of the YBT, strong orographic effect on precipitation on the high plateau edge above 3000 m and supplementary increase of channel inflow to simulate capturing of upstream endorheic zone of inland plateau in my final model. This model could well reproduce the headwater and interfluvial low-relief surfaces and deeply incising rivers in the Yalong River catchment in the “Great Bends Region”.

In summary, I provided new low temperature thermochronology data in the core of the Three Rivers Region, enriching the regional dataset, which allows for a regional evaluation of regional tectonic deformation and topographic building. My PhD work tried to resolve the control of tectonic forcing and climatic forcing/river incision on the topographic evolution on a local scale first and then a regional scale by using different methods. I succeeded to show a collaboration between these factors is essential to sculpt the present-day landscape of the tectonically active southeast Tibet, under careful evaluation of existing data with respect to fault activities and climatic evolution since the India-Asia collision.

## 4.4 Perspectives for future works

Our new data from the high elevations of the Kawagebo massif show relatively large dispersion in AHe and AFT ages, it should be related to a long residency in the PRZ or PAZ during ~15–5 Ma. Our primitive thermo-kinematic modelling clearly could not reproduce such a age dispersion. Detailed analysis the helium diffusion dynamics and fission tracks annealing behaviours with respect to grain sizes, effective uranium concentration and thermal histories, should be conducted with the help of diffusion or annealing models to investigate this age dispersion. Our data only cover an exhumation history up to 32 Ma, which makes it impossible to investigate the complete exhumation since the India-Asia collision. Fortunately, we have collected sufficient amount of biotite and muscovite mineral grains from several samples, which have higher closure temperatures for the  $^{40}\text{Ar}/^{39}\text{Ar}$  dating in coming future and allows us to explore into history prior to 32 Ma. QTQt modelling which inverts thermochronological ages for multiple samples with a known elevation relationship (Gallagher, 2012<sup>[312]</sup>), by using an alpha-damage-dependent kinetic model of helium diffusion in apatite (Flowers et al., 2009<sup>[360]</sup>), helium diffusion parameters from Reiners and Brandon, (2006)<sup>[317]</sup> for zircon and a multi-kinetic AFT annealing model (Ketchum et al., 2007)<sup>[352]</sup>, probably allows us for a better

investigation of the temperature–time relationship for explaining disperse our AHe and AFT ages and sheds light on determining the precise transition time between different exhumation phase and their corresponding exhumation rates. Thereafter, the temperature path could serve as inputs in Pecube to help us to better reconstruct the thermal history of the Kawagebo massif in 3 dimensions. Regionally speaking, although our modelling yielded a similar exhumation history with the existing data from the Zuogong massif, north of the Kawagebo massif in the Three Rivers Region, indicating a regional compression regime during the Late Eocene–Early Miocene, data are still rather scarce in the region at high elevation west to the Longmucuo–Shuanghu suture. Collection of more data will definitely help us to better resolve the deformation history in this highly deformed region, adjacent to the continuously indenting EHS.

For the modelling of regional topographic evolution, I recognized that the simple Stream Power Law and simplified hillslope processes used in FastScape are not completely efficient to model catchment–scale topography of southeast Tibet. In our final model, the simple Stream Power Law cannot collect sufficient amount of water on the high and flat inland plateau without eroding, which was eventually reproduced by artificially increasing inflow in channels from the upstream and imposing weak precipitation on the plateau. A simplified orographic effect on precipitation was adopted in our models, the new Python version of FastScape provides an opportunity to investigate this effect by implementing a global climatic system. This could potentially help us to simulate the spatial distribution of precipitation on the plateau, but the evolution of paleo–precipitation still remains a huge challenge for the geoscience community, although more and more paleoclimate data have been reported, while converting these data into reconstruction of paleo–precipitation is still not apparent. This region’s landscape could also have been largely regulated and smoothed by efficient glacial and periglacial erosion since Quaternary, which is not taken into consideration yet in the FastScape code.

Abundant thermochronology data have been yielded across the southeast Tibet, an implementation of these data into the FastScape would better constrain the denudation, even though such a work has not yet been done in such a large scale. In the beginning of our project, we divided the southeast Tibet into three regions: the “Three Rivers Region” close to the EHS, which experienced strong lateral shortening as shown in the second part of my work, the “Great Bends Region” and the Longmenshan region farther away from the EHS, where the NW–SE contraction plays an important role in the regional deformation. While, the tectonic reconstruction of the Three Rivers Region needs a coupling with a geodynamic model to resolve the crustal shortening, because the uplift implemented in

FastScape today is more like the surface uplift without calling any deep processes. In the Great Bends Region, the lower part of upper Yangtze and downstream Yalong rivers both show huge bends of the river course over >100 kilometers, when they flow across the NE-SE striking Yalong and Yulong thrust belts, respectively. Our attempt to model this feature always failed by simply mimicking a thrust fault through implementing two blocks of different uplift. Probably a combination of spatially varying thrusting rates and minor strike-slip motion along the thrust is necessary to reproduce such huge river bends, while strike-slip motion is not permitted yet in FastScape. As for the Longmenshan region, stronger net precipitation into the hinterland plateau results in more water collected into the river and the generation of dendritic river networks with relatively wide and large valleys, compared to other large rivers in southeast Tibet. Another intriguing problematic is how the endorheic zone closely located in the northern hinterland of the Longmenshan range remains un-attacked by the strong erosive Dadu and Min rivers from the south, while the hydraulically weaker Yellow River captured this vast endorheic zone from north since only Quaternary. These could be interesting topics for future work.



# CHAPTER 5

## Annexes

### 5.1 AFT age data by sample

Here are the radial plot of the AFT ages of our samples. The  $\chi^2$ -test and age dispersion are used to assess the homogeneity of AFT ages (Galbraith and Green, 1990<sup>[354]</sup>; Galbraith and Laslett, 1993<sup>[355]</sup>), which are visualized in terms of a measurement's value and precision by applying the RadialPlotter (Vermeesch, 2009<sup>[356]</sup>). The weighted mean apatite Zeta factor for Xiong OU is  $262.55 \pm 11.21$  (IRMM540R dosimeter glass), based on Durango and Fish Canyon Tuff age standards. Details of AFT ages could be found in Table S. 2.3.

Figure S. 5.1 – Radial plot of the AFT age of sample KS01B

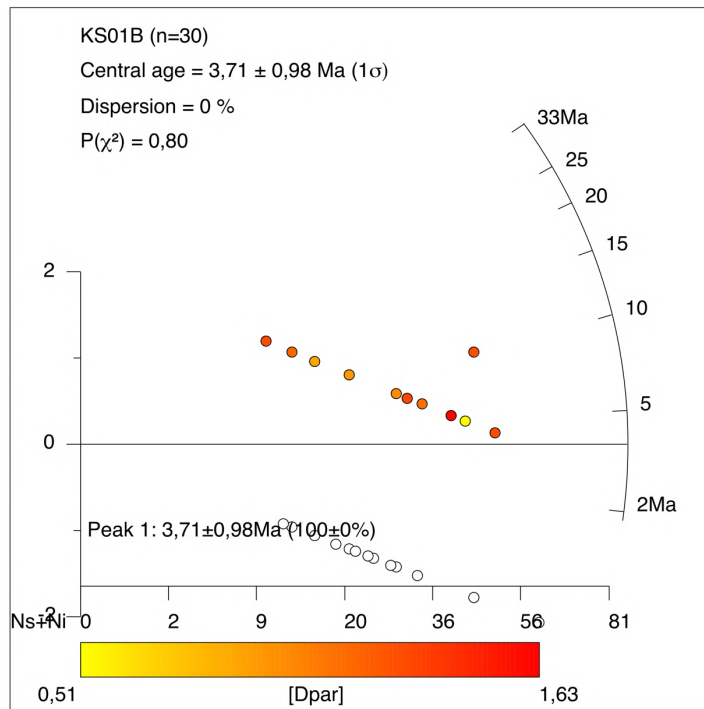


Figure S. 5.2 – Radial plot of the AFT age of sample KS02:

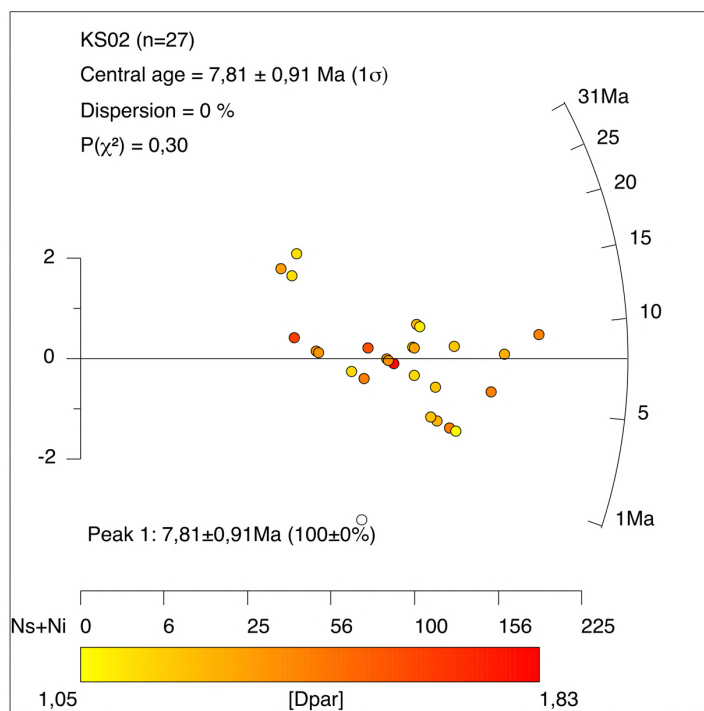


Figure S. 5.3 - Radial plot of the AFT age of sample KS03:

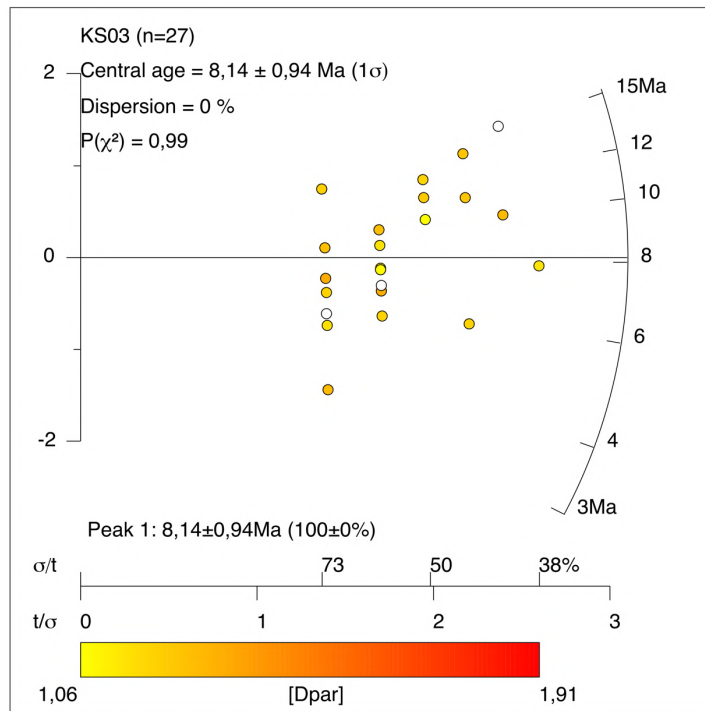


Figure S. 5.4 - Radial plot of the AFT age of sample KS04:

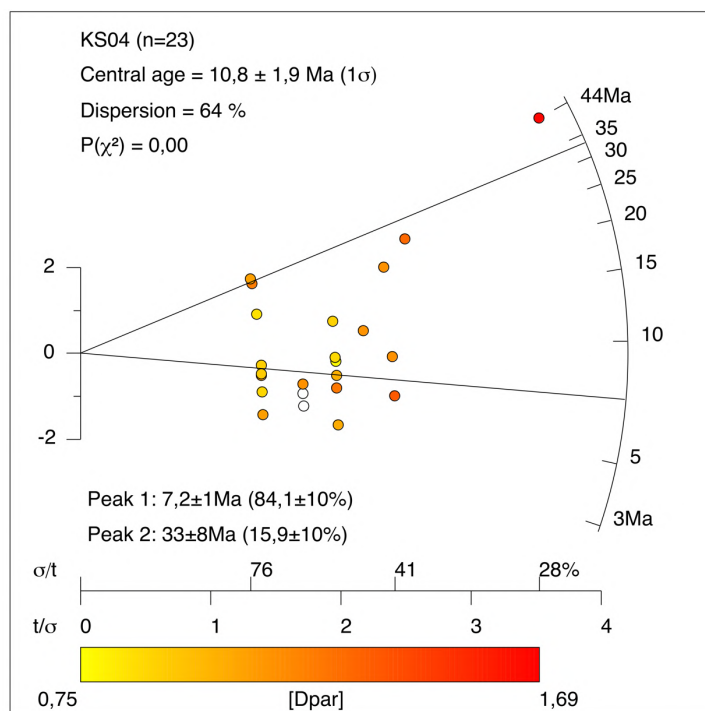


Figure S. 5.5 - Radial plot of the AFT age of sample KS05:

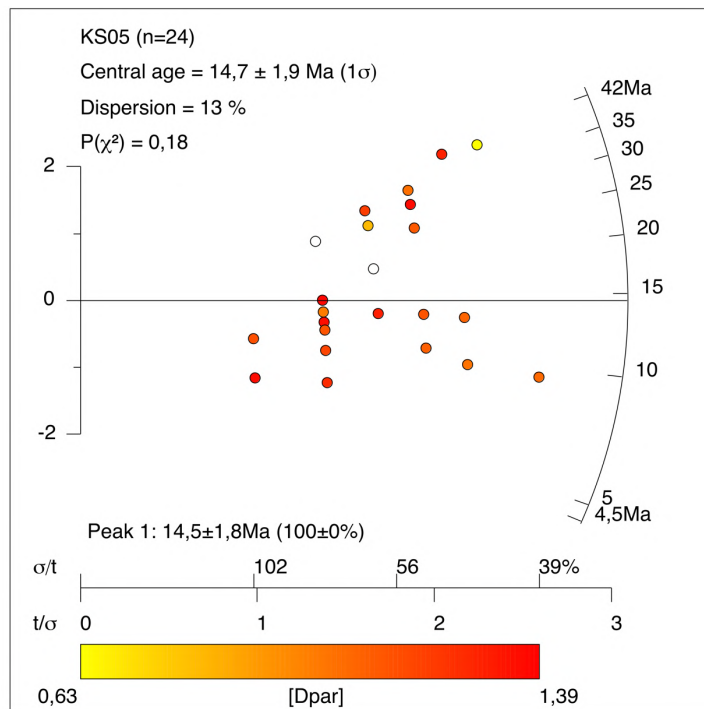


Figure S. 5.6 - Radial plot of the AFT age of sample KS06:

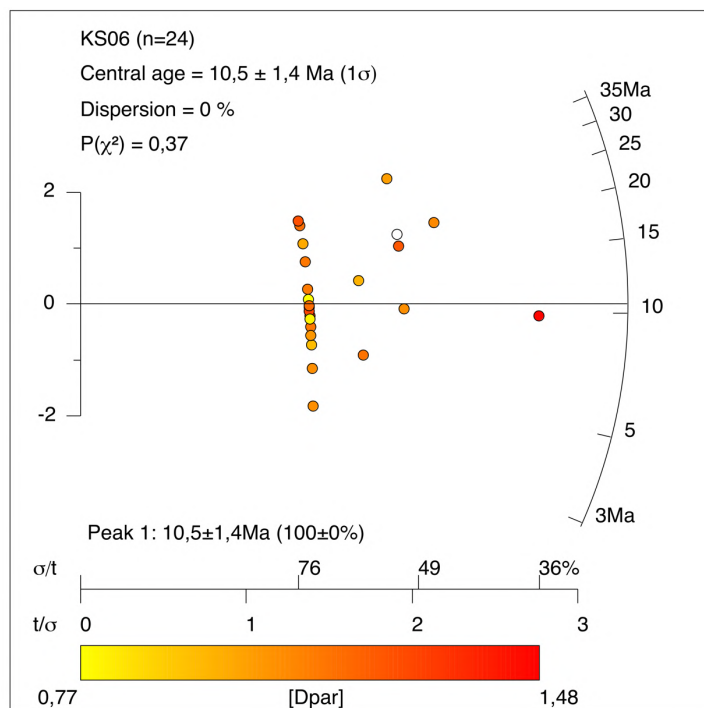


Figure S. 5.7 – Radial plot of the AFT age of sample KS07:

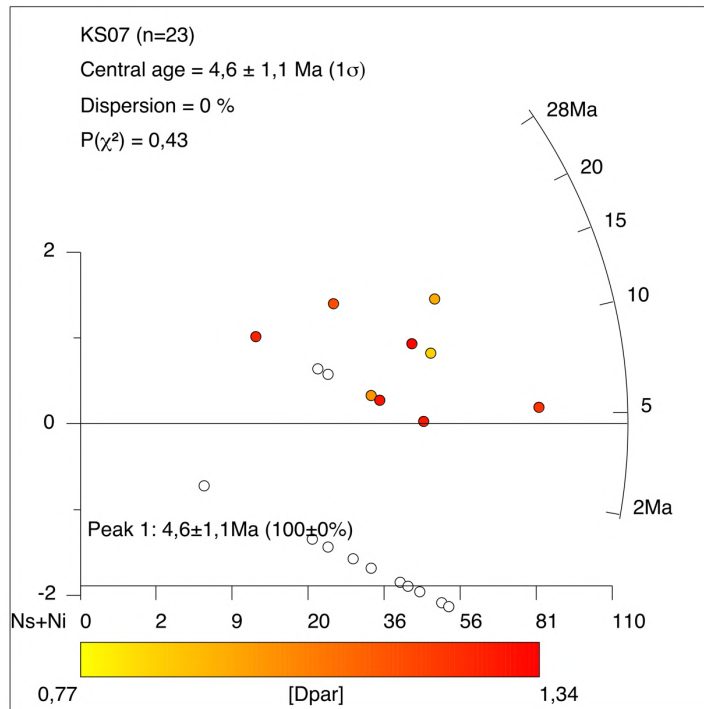


Figure S. 5.8 – Radial plot of the AFT age of sample KS08:

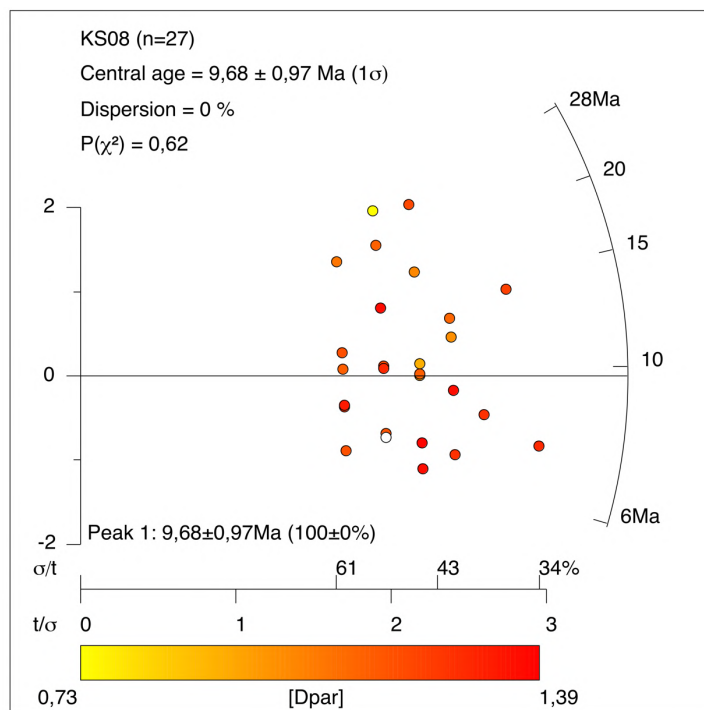


Figure S. 5.9 - Radial plot of the AFT age of sample KS09:

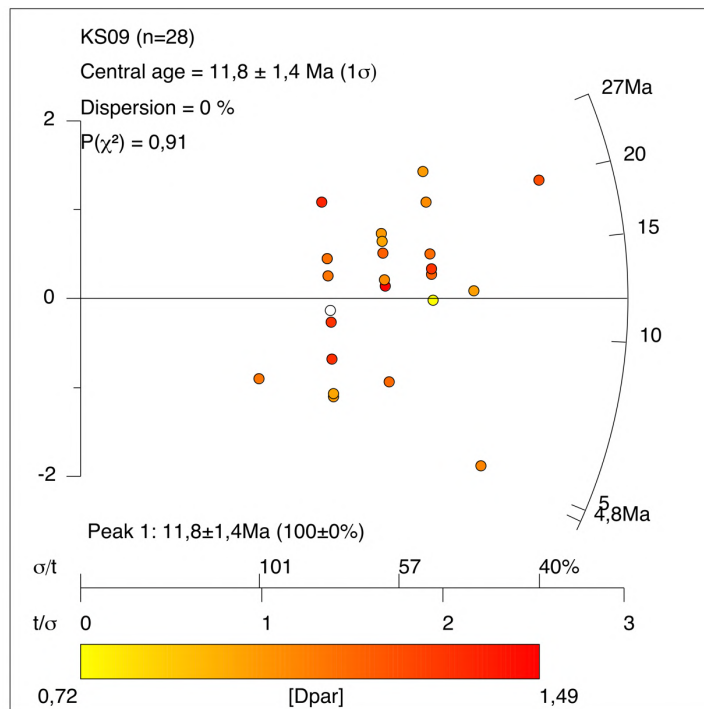
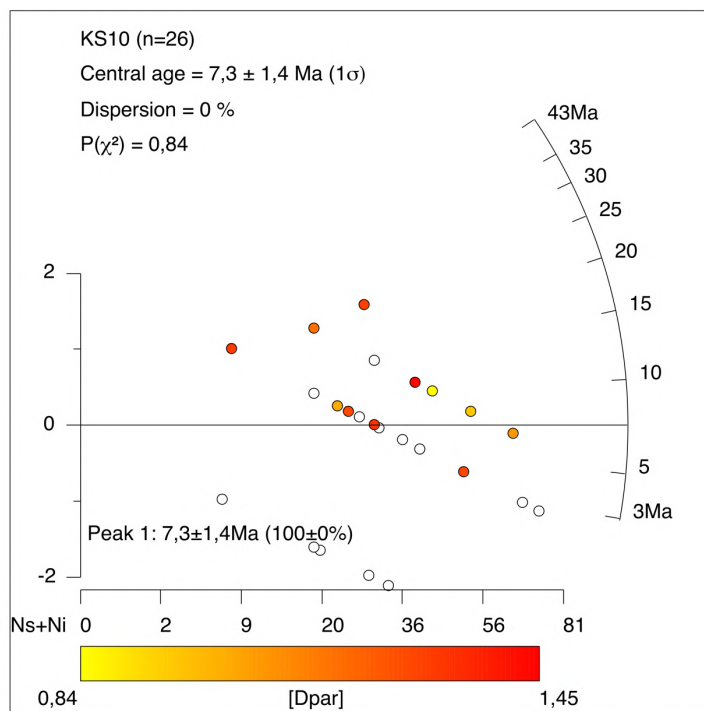


Figure S. 5.10 - Radial plot of the AFT age of sample KS10:



# References

- [1] Fielding, E., Isacks, B., Barazangi, M., Duncan, C., 1994. How flat is Tibet? *Geology* 22, 163-167.
- [2] Dewey, J.F., Shackleton, R.M., Chengfa, C., Yiyin, S., 1988. The tectonic evolution of the Tibetan Plateau. *Philosophical Transactions of the Royal Society of London. Series A, Mathematical and Physical Sciences* 327, 379-413.
- [3] Yin, A., Harrison, T.M., 2000. Geologic evolution of the Himalayan-Tibetan orogen. *Annual review of earth and planetary sciences* 28, 211-280.
- [4] Metcalfe, I., 2021. Multiple Tethyan ocean basins and orogenic belts in Asia. *Gondwana Research* 100, 87-130.
- [5] Roger, F., Tapponnier, P., Arnaud, N., SchaÈrer, U., Brunel, M., Zhiqin, X., Jingsui, Y., 2000. An Eocene magmatic belt across central Tibet: mantle subduction triggered by the Indian collision? *Terra Nova* 12, 102-108.
- [6] Molnar, P., Tapponnier, P., 1975. Cenozoic Tectonics of Asia: Effects of a Continental Collision: Features of recent continental tectonics in Asia can be interpreted as results of the India-Eurasia collision. *Science* 189, 419-426.
- [7] England, P., Searle, M., 1986. The Cretaceous-tertiary deformation of the Lhasa Block and its implications for crustal thickening in Tibet. *Tectonics* 5, 1-14.
- [8] Tapponnier, P., Zhiqin, X., Roger, F., Meyer, B., Arnaud, N., Wittlinger, G., Jingsui, Y., 2001. Oblique stepwise rise and growth of the Tibet Plateau. *science* 294, 1671-1677.
- [9] Royden, L.H., Burchfiel, B.C., van der Hilst, R.D., 2008. The Geological Evolution of the Tibetan Plateau. *Science* 321, 1054-1058.
- [10] Tapponnier, P., Peltzer, G., Armijo, R., 1986. On the mechanics of the collision between India and Asia. *Geological Society, London, Special Publications* 19, 113-157.
- [11] Replumaz, A., Capitanio, F.A., Guillot, S., Negredo, A.M., Villaseñor, A., 2014. The coupling of Indian subduction and Asian continental tectonics. *Gondwana Research* 26, 608-626.
- [12] Replumaz, A., Guillot, S., Villaseñor, A., Negredo, A.M., 2013. Amount of Asian lithospheric mantle subducted during the India/Asia collision. *Gondwana Research* 24, 936-945.

- [13] Replumaz, A., Tapponnier, P., 2003. Reconstruction of the deformed collision zone Between India and Asia by backward motion of lithospheric blocks. *Journal of Geophysical Research: Solid Earth* 108.
- [14] Replumaz, A., Negredo, A.M., Villaseñor, A., Guillot, S., 2010. Indian continental subduction and slab break-off during Tertiary collision. *Terra Nova* 22, 290-296.
- [15] Lippert, P.C., van Hinsbergen, D.J., Dupont-Nivet, G., 2014. Early Cretaceous to present latitude of the central proto-Tibetan Plateau: A paleomagnetic synthesis with implications for Cenozoic tectonics, paleogeography, and climate of Asia. *Geological Society of America Special Papers* 507, 1-21.
- [16] Van Hinsbergen, D.J.J., Kapp, P., Dupont-Nivet, G., Lippert, P.C., DeCelles, P.G., Torsvik, T.H., 2011. Restoration of Cenozoic deformation in Asia and the size of Greater India. *Tectonics* 30.
- [17] Van Hinsbergen, D.J., Lippert, P.C., Dupont-Nivet, G., McQuarrie, N., Doubrovine, P.V., Spakman, W., Torsvik, T.H., 2012. Greater India Basin hypothesis and a two-stage Cenozoic collision between India and Asia. *Proceedings of the National Academy of Sciences* 109, 7659-7664.
- [18] Clark, M.K., Royden, L.H., 2000. Topographic ooze: Building the eastern margin of Tibet by lower crustal flow. *Geology* 28, 703-706.
- [19] Zhang, P.-Z., Shen, Z., Wang, M., Gan, W., Bürgmann, R., Molnar, P., Wang, Q., Niu, Z., Sun, J., Wu, J., 2004. Continuous deformation of the Tibetan Plateau from global positioning system data. *Geology* 32, 809-812.
- [20] Wang, Q., Zhang, P.-Z., Freymueller, J.T., Bilham, R., Larson, K.M., Lai, X.a., You, X., Niu, Z., Wu, J., Li, Y., Liu, J., Yang, Z., Chen, Q., 2001. Present-Day Crustal Deformation in China Constrained by Global Positioning System Measurements. *Science* 294, 574-577.
- [21] Gan, W., Zhang, P., Shen, Z.-K., Niu, Z., Wang, M., Wan, Y., Zhou, D., Cheng, J., 2007. Present-day crustal motion within the Tibetan Plateau inferred from GPS measurements. *Journal of Geophysical Research: Solid Earth* 112.
- [22] Gan, W., Molnar, P., Zhang, P., Xiao, G., Liang, S., Zhang, K., Li, Z., Xu, K., Zhang, L., 2021. Initiation of Clockwise Rotation and Eastward Transport of Southeastern Tibet Inferred from Deflected Fault Traces and GPS Observations. *GSA Bulletin* 134, 1129-1142.
- [23] Molnar, P., Tapponnier, P., 1978. Active tectonics of Tibet. *Journal of Geophysical Research: Solid Earth* 83, 5361-5375.

- [24] Armijo, R., Tapponnier, P., Mercier, J.L., Han, T.-L., 1986. Quaternary extension in southern Tibet: Field observations and tectonic implications. *Journal of Geophysical Research: Solid Earth* 91, 13803-13872.
- [25] Lyon-Caen, H., Molnar, P., 1989. Constraints on the deep structure and dynamic processes beneath the Alps and adjacent regions from an analysis of gravity anomalies. *Geophysical Journal International* 99, 19-32.
- [26] Elliott, J., Walters, R., England, P., Jackson, J., Li, Z., Parsons, B., 2010. Extension on the Tibetan plateau: recent normal faulting measured by InSAR and body wave seismology. *Geophysical Journal International* 183, 503-535.
- [27] Ge, W.-P., Molnar, P., Shen, Z.-K., Li, Q., 2015. Present-day crustal thinning in the southern and northern Tibetan Plateau revealed by GPS measurements. *Geophysical Research Letters* 42, 5227-5235.
- [28] Wang, C., Dai, J., Zhao, X., Li, Y., Graham, S.A., He, D., Ran, B., Meng, J., 2014. Outward-growth of the Tibetan Plateau during the Cenozoic: A review. *Tectonophysics* 621, 1-43.
- [29] Tapponnier, P., Peltzer, G., Le Dain, A.Y., Armijo, R., Cobbold, P., 1982. Propagating extrusion tectonics in Asia: New insights from simple experiments with plasticine. *Geology* 10, 611-616.
- [30] Peltzer, G., Tapponnier, P., 1988. Formation and evolution of strike-slip faults, rifts, and basins during the India-Asia Collision: An experimental approach. *Journal of Geophysical Research: Solid Earth* 93, 15085-15117.
- [31] Leloup, P.H., Lacassin, R., Tapponnier, P., Schärer, U., Zhong, D., Liu, X., Zhang, L., Ji, S., Trinh, P.T., 1995. The Ailao Shan-Red River shear zone (Yunnan, China), Tertiary transform boundary of Indochina. *Tectonophysics* 251, 3-84.
- [32] Leloup, P.H., Arnaud, N., Lacassin, R., Kienast, J.R., Harrison, T.M., Trong, T.T.P., Replumaz, A., Tapponnier, P., 2001. New constraints on the structure, thermochronology, and timing of the Ailao Shan-Red River shear zone, SE Asia. *Journal of Geophysical Research: Solid Earth* 106, 6683-6732.
- [33] Guillot, S., Replumaz, A., 2013. Importance of continental subductions for the growth of the Tibetan plateau. *Bulletin de la Société Géologique de France* 184, 199-223.
- [34] Mattauer, M., 1986. Intracontinental subduction, crust-mantle décollement and crustal-stacking wedge in the Himalayas and other collision belts. *Geological Society, London, Special Publications* 19, 37-50.

- [35] Tapponnier, P., Meyer, B., Avouac, J.P., Peltzer, G., Gaudemer, Y., Guo, S., Xiang, H., Yin, K., Chen, Z., Cai, S., Dai, H., 1990. Active thrusting and folding in the Qilian Shan, and decoupling between upper crust and mantle in northeastern Tibet. *Earth and Planetary Science Letters* 97, 382-403.
- [36] Replumaz, A., Funicello, F., Reitano, R., Faccenna, C., Balon, M., 2016. Asian collisional subduction: A key process driving formation of the Tibetan Plateau. *Geology* 44, 943-946.
- [37] Pitard, P., Replumaz, A., Funicello, F., Husson, L., Faccenna, C., 2018. Mantle kinematics driving collisional subduction: Insights from analogue modeling. *Earth and Planetary Science Letters* 502, 96-103.
- [38] Goussin, F., Riel, N., Cordier, C., Guillot, S., Boulvais, P., Roperch, P., Replumaz, A., Schulmann, K., Dupont-Nivet, G., Rosas, F., 2020. Carbonated inheritance in the Eastern Tibetan lithospheric mantle: Petrological evidences and geodynamic implications. *Geochemistry, Geophysics, Geosystems* 21, e2019GC008495.
- [39] Meyer, B., Tapponnier, P., Bourjot, L., Metivier, F., Gaudemer, Y., Peltzer, G., Shunmin, G., Zhitai, C., 1998. Crustal thickening in Gansu-Qinghai, lithospheric mantle subduction, and oblique, strike-slip controlled growth of the Tibet plateau. *Geophysical Journal International* 135, 1-47.
- [40] Tapponnier, P., Molnar, P., 1976. Slip-line field theory and large-scale continental tectonics. *Nature* 264, 319-324.
- [41] Molnar, P., Tapponnier, P., 1977. Relation of the tectonics of eastern China to the India-Eurasia collision: Application of slip-line field theory to large-scale continental tectonics. *Geology* 5, 212-216.
- [42] Richter, F., McKenzie, D., 1977. Simple plate models of mantle convection. *Journal of Geophysics* 44, 441-471.
- [43] England, P., McKenzie, D., 1982. A thin viscous sheet model for continental deformation. *Geophysical Journal International* 70, 295-321.
- [44] England, P., Houseman, G., 1986. Finite strain calculations of continental deformation: 2. Comparison with the India-Asia collision zone. *Journal of Geophysical Research: Solid Earth* 91, 3664-3676.
- [45] Houseman, G., England, P., 1986. Finite strain calculations of continental deformation: 1. Method and general results for convergent zones. *Journal of Geophysical Research: Solid Earth* 91, 3651-3663.

- [46] Jiménez-Munt, I., Platt, J.P., 2006. Influence of mantle dynamics on the topographic evolution of the Tibetan Plateau: Results from numerical modeling. *Tectonics* 25.
- [47] England, P., Houseman, G., 1989. Extension during continental convergence, with application to the Tibetan Plateau. *Journal of Geophysical Research: Solid Earth* 94, 17561-17579.
- [48] Molnar, P., England, P., Martinod, J., 1993. Mantle dynamics, uplift of the Tibetan Plateau, and the Indian monsoon. *Reviews of Geophysics* 31, 357-396.
- [49] England, P.C., Houseman, G.A., Osmaston, M.F., Ghosh, S., Shackleton, R.M., Dewey, J.F., Windley, B.F., 1988. The mechanics of the Tibetan Plateau. *Philosophical Transactions of the Royal Society of London. Series A, Mathematical and Physical Sciences* 326, 301-320.
- [50] Platt, J., England, P., 1994. Convective removal of lithosphere beneath mountain belts-Thermal and mechanical consequences. *American Journal of Science* 294.
- [51] [Bibliography Number] Kroon, D., Steens, T., Troelstra, S.R., 1991. 13. Onset of monsoonal related upwelling in the western Arabian Sea as revealed by planktonic foraminifers1, *Proceedings of the ocean drilling program, scientific results*, pp. 257-263.
- [52] Kuhn, T.S., 1997. The structure of scientific revolutions. *Computers & Mathematics with Applications* 33, 129-129.
- [53] Burke, K., Dewey, J.F., 1973. Plume-generated triple junctions: key indicators in applying plate tectonics to old rocks. *The Journal of Geology* 81, 406-433.
- [54] Zhao, W.L., Morgan, W.J., 1985. Uplift of Tibetan plateau. *Tectonics* 4, 359-369.
- [55] Jin, Y., McNutt, M.K., Zhu, Y.-s., 1996. Mapping the descent of Indian and Eurasian plates beneath the Tibetan Plateau from gravity anomalies. *Journal of Geophysical Research: Solid Earth* 101, 11275-11290.
- [56] Nelson, K.D., Zhao, W., Brown, L.D., Kuo, J., Che, J., Liu, X., Klempner, S.L., Makovsky, Y., Meissner, R., Mechie, J., Kind, R., Wenzel, F., Ni, J., Nabelek, J., Leshou, C., Tan, H., Wei, W., Jones, A.G., Booker, J., Unsworth, M., Kidd, W.S.F., Hauck, M., Alsdorf, D., Ross, A., Cogan, M., Wu, C., Sandvol, E., Edwards, M., 1996. Partially Molten Middle Crust Beneath Southern Tibet: Synthesis of Project INDEPTH Results. *Science* 274, 1684-1688.
- [57] Wei, W., Unsworth, M., Jones, A., Booker, J., Tan, H., Nelson, D., Chen, L., Li, S., Solon, K., Bedrosian, P., Jin, S., Deng, M., Ledo, J., Kay, D., Roberts, B., 2001. Detection of Widespread Fluids in the Tibetan Crust by Magnetotelluric Studies. *Science* 292, 716-719.

- [58] Royden, L., 1996. Coupling and decoupling of crust and mantle in convergent orogens: Implications for strain partitioning in the crust. *Journal of Geophysical Research: Solid Earth* 101, 17679-17705.
- [59] Royden, L.H., Burchfiel, B.C., King, R.W., Wang, E., Chen, Z., Shen, F., Liu, Y., 1997. Surface Deformation and Lower Crustal Flow in Eastern Tibet. *Science* 276, 788-790.
- [60] Medvedev, S., Beaumont, C., 2006. Growth of continental plateaus by channel injection: models designed to address constraints and thermomechanical consistency. Geological Society, London, Special Publications 268, 147-164.
- [61] Mancktelow, N.S., 1995. Nonlithostatic pressure during sediment subduction and the development and exhumation of high pressure metamorphic rocks. *Journal of Geophysical Research: Solid Earth* 100, 571-583.
- [62] Godin, L., Grujic, D., Law, R.D., Searle, M.P., 2006. Channel flow, ductile extrusion and exhumation in continental collision zones: an introduction. Geological Society, London, Special Publications 268, 1-23.
- [63] Klemperer, S.L., 2006. Crustal flow in Tibet: geophysical evidence for the physical state of Tibetan lithosphere, and inferred patterns of active flow. Geological Society, London, Special Publications 268, 39-70.
- [64] Burchfiel, B., Royden, L., van der Hilst, R., Hager, B., Chen, Z.L., King, R., Li, C., L'u, J., Yao, H., Kirby, E., 2008. A geological and geophysical context for the Wenchuan earthquake of 12 May 2008, Sichuan, People's Republic of China. *GSA today* 18, 4-11.
- [65] Zhang, Z., Wang, Y., Chen, Y., Houseman, G.A., Tian, X., Wang, E., Teng, J., 2009. Crustal structure across Longmenshan fault belt from passive source seismic profiling. *Geophysical Research Letters* 36.
- [66] Zhao, G., Unsworth, M.J., Zhan, Y., Wang, L., Chen, X., Jones, A.G., Tang, J., Xiao, Q., Wang, J., Cai, J., Li, T., Wang, Y., Zhang, J., 2012. Crustal structure and rheology of the Longmenshan and Wenchuan Mw 7.9 earthquake epicentral area from magnetotelluric data. *Geology* 40, 1139-1142.
- [67] Clark, M.K., Bush, J.W.M., Royden, L.H., 2005. Dynamic topography produced by lower crustal flow against rheological strength heterogeneities bordering the Tibetan Plateau. *Geophysical Journal International* 162, 575-590.
- [68] Hubbard, J., Shaw, J.H., 2009. Uplift of the Longmen Shan and Tibetan plateau, and the 2008 Wenchuan (M = 7.9) earthquake. *Nature* 458, 194-197.

- [69] Liu-Zeng, J., Zhang, Z., Wen, L., Tapponnier, P., Sun, J., Xing, X., Hu, G., Xu, Q., Zeng, L., Ding, L., Ji, C., Hudnut, K.W., van der Woerd, J., 2009. Co-seismic ruptures of the 12 May 2008, Ms 8.0 Wenchuan earthquake, Sichuan: East-west crustal shortening on oblique, parallel thrusts along the eastern edge of Tibet. *Earth and Planetary Science Letters* 286, 355-370.
- [70] Tian, Y., Kohn, B.P., Gleadow, A.J.W., Hu, S., 2013. Constructing the Longmen Shan eastern Tibetan Plateau margin: Insights from low-temperature thermochronology. *Tectonics* 32, 576-592.
- [71] Tian, Y., Kohn, B.P., Phillips, D., Hu, S., Gleadow, A.J.W., Carter, A., 2016. Late Cretaceous-earliest Paleogene deformation in the Longmen Shan fold-and-thrust belt, eastern Tibetan Plateau margin: Pre-Cenozoic thickened crust? *Tectonics* 35, 2293-2312.
- [72] Xu, X., Wen, X., Han, Z., Chen, G., Li, C., Zheng, W., Zhnag, S., Ren, Z., Xu, C., Tan, X., Wei, Z., Wang, M., Ren, J., He, Z., Liang, M., 2013. Lushan MS7.0 earthquake: A blind reserve-fault event. *Chinese Science Bulletin* 58, 3437-3443.
- [73] Kind, R., Yuan, X., Saul, J., Nelson, D., Sobolev, S.V., Mechie, J., Zhao, W., Kosarev, G., Ni, J., Achauer, U., Jiang, M., 2002. Seismic Images of Crust and Upper Mantle Beneath Tibet: Evidence for Eurasian Plate Subduction. *Science* 298, 1219-1221.
- [74] Vergne, J., Wittlinger, G., Hui, Q., Tapponnier, P., Poupinet, G., Mei, J., Herquel, G., Paul, A., 2002. Seismic evidence for stepwise thickening of the crust across the NE Tibetan plateau. *Earth and Planetary Science Letters* 203, 25-33.
- [75] Wittlinger, G., Farra, V., Vergne, J., 2004. Lithospheric and upper mantle stratifications beneath Tibet: New insights from Sp conversions. *Geophysical Research Letters* 31.
- [76] Murphy, M.A., Yin, A., Harrison, T.M., Dürr, S.B., Z, C., Ryerson, F.J., Kidd, W.S.F., X, W., X, Z., 1997. Did the Indo-Asian collision alone create the Tibetan plateau? *Geology* 25, 719-722.
- [77] Kapp, P., DeCelles, P.G., Gehrels, G.E., Heizler, M., Ding, L., 2007. Geological records of the Lhasa-Qiangtang and Indo-Asian collisions in the Nima area of central Tibet. *GSA Bulletin* 119, 917-933.
- [78] Wang, C., Zhao, X., Liu, Z., Lippert, P.C., Graham, S.A., Coe, R.S., Yi, H., Zhu, L., Liu, S., Li, Y., 2008. Constraints on the early uplift history of the Tibetan Plateau. *Proceedings of the National Academy of Sciences* 105, 4987-4992.
- [79] Searle, M.P., Elliott, J.R., Phillips, R.J., Chung, S.-L., 2011. Crustal-lithospheric structure and continental extrusion of Tibet. *Journal of the Geological Society* 168, 633-672.
- [80] Mulch, A., Chamberlain, C.P., 2006. The rise and growth of Tibet. *Nature* 439, 670-671.

- [81] Fielding, E.J., 1996. Tibet uplift and erosion. *Tectonophysics* 260, 55-84.
- [82] Burg, J.P., Chen, G.M., 1984. Tectonics and structural zonation of southern Tibet, China. *Nature* 311, 219-223.
- [83] Rowley, D.B., Currie, B.S., 2006. Palaeo-altimetry of the late Eocene to Miocene Lunpola basin, central Tibet. *Nature* 439, 677-681.
- [84] DeCelles, P.G., Kapp, P., Ding, L., Gehrels, G.E., 2007. Late Cretaceous to middle Tertiary basin evolution in the central Tibetan Plateau: Changing environments in response to tectonic partitioning, aridification, and regional elevation gain. *GSA Bulletin* 119, 654-680.
- [85] Polissar, P.J., Freeman, K.H., Rowley, D.B., McInerney, F.A., Currie, B.S., 2009. Paleoelevation of the Tibetan Plateau from D/H ratios of lipid biomarkers. *Earth and Planetary Science Letters* 287, 64-76.
- [86] Deng, T., Ding, L., 2015. Paleoelevation reconstructions of the Tibetan Plateau: progress and contradictions. *National Science Review* 2, 417-437.
- [87] Kapp, P., Yin, A., Harrison, T.M., Ding, L., 2005. Cretaceous-Tertiary shortening, basin development, and volcanism in central Tibet. *GSA Bulletin* 117, 865-878.
- [88] Rohrmann, A., Kapp, P., Carrapa, B., Reiners, P.W., Guynn, J., Ding, L., Heizler, M., 2012. Thermochronologic evidence for plateau formation in central Tibet by 45 Ma. *Geology* 40, 187-190.
- [89] Allégre, C.J., Courtillot, V., Tapponnier, P., Hirn, A., Mattauer, M., Coulon, C., Jaeger, J.J., Achache, J., Schärer, U., Marcoux, J., Burg, J.P., Girardeau, J., Armijo, R., Gariépy, C., Göpel, C., Tindong, L., Xuchang, X., Chenfa, C., Guangqin, L., Baoyu, L., Jiwen, T., Naiwen, W., Guoming, C., Tonglin, H., Xibin, W., Wanming, D., Huaibin, S., Yougong, C., Ji, Z., Hongrong, Q., Peisheng, B., Songchan, W., Bixiang, W., Yaoxiu, Z., Xu, R., 1984. Structure and evolution of the Himalaya-Tibet orogenic belt. *Nature* 307, 17-22.
- [90] Ding, L., Xu, Q., Yue, Y., Wang, H., Cai, F., Li, S., 2014. The Andean-type Gangdese Mountains: Paleoelevation record from the Paleocene-Eocene Linzhou Basin. *Earth and Planetary Science Letters* 392, 250-264.
- [91] Horton, B.K., Yin, A., Spurlin, M.S., Zhou, J., Wang, J., 2002. Paleocene-Eocene syncontractional sedimentation in narrow, lacustrine-dominated basins of east-central Tibet. *GSA Bulletin* 114, 771-786.
- [92] Dai, J., Zhao, X., Wang, C., Zhu, L., Li, Y., Finn, D., 2012. The vast proto-Tibetan Plateau: New constraints from Paleogene Hoh Xil Basin. *Gondwana Research* 22, 434-446.

- [93] Molnar, P., Stock, J.M., 2009. Slowing of India's convergence with Eurasia since 20 Ma and its implications for Tibetan mantle dynamics. *Tectonics* 28.
- [94] G ebel, A., Mulch, A., Teyssier, C., Jessup, M.J., Law, R.D., Brunel, M., 2013. The Miocene elevation of Mount Everest. *Geology* 41, 799-802.
- [95] Wu, F., Miao, D., Chang, M.-m., Shi, G., Wang, N., 2017. Fossil climbing perch and associated plant megafossils indicate a warm and wet central Tibet during the late Oligocene. *Scientific Reports* 7, 878.
- [96] Liu, J., Su, T., Spicer, R.A., Tang, H., Deng, W.-Y.-D., Wu, F.-X., Srivastava, G., Spicer, T., Van Do, T., Deng, T., Zhou, Z.-K., 2019. Biotic interchange through lowlands of Tibetan Plateau suture zones during Paleogene. *Palaeogeography, Palaeoclimatology, Palaeoecology* 524, 33-40.
- [97] Su, T., Farnsworth, A., Spicer, R.A., Huang, J., Wu, F.-X., Liu, J., Li, S.-F., Xing, Y.-W., Huang, Y.-J., Deng, W.-Y.-D., Tang, H., Xu, C.-L., Zhao, F., Srivastava, G., Valdes, P.J., Deng, T., Zhou, Z.-K., 2019. No high Tibetan Plateau until the Neogene. *Science Advances* 5, eaav2189.
- [98] Tang, H., Liu, J., Wu, F.-X., Spicer, T., Spicer, R.A., Deng, W.-Y.-D., Xu, C.-L., Zhao, F., Huang, J., Li, S.-F., Su, T., Zhou, Z.-K., 2019. Extinct genus *Lagokarpos* reveals a biogeographic connection between Tibet and other regions in the Northern Hemisphere during the Paleogene. *Journal of Systematics and Evolution* 57, 670-677.
- [99] Xiong, Z., Liu, X., Ding, L., Farnsworth, A., Spicer, R.A., Xu, Q., Valdes, P., He, S., Zeng, D., Wang, C., Li, Z., Guo, X., Su, T., Zhao, C., Wang, H., Yue, Y., 2022. The rise and demise of the Paleogene Central Tibetan Valley. *Science Advances* 8, eabj0944.
- [100] Liu-Zeng, J., Tapponnier, P., Gaudemer, Y., Ding, L., 2008. Quantifying landscape differences across the Tibetan plateau: Implications for topographic relief evolution. *Journal of Geophysical Research: Earth Surface* 113.
- [101] Viviroli, D., D urr, H.H., Messerli, B., Meybeck, M., Weingartner, R., 2007. Mountains of the world, water towers for humanity: Typology, mapping, and global significance. *Water Resources Research* 43.
- [102] Immerzeel, W.W., Lutz, A.F., Andrade, M., Bahl, A., Biemans, H., Bolch, T., Hyde, S., Brumby, S., Davies, B.J., Elmore, A.C., Emmer, A., Feng, M., Fern andez, A., Haritashya, U., Kargel, J.S., Koppes, M., Kraaijenbrink, P.D.A., Kulkarni, A.V., Mayewski, P.A., Nepal, S., Pacheco, P., Painter, T.H., Pellicciotti, F., Rajaram, H., Rupper, S., Sinisalo, A., Shrestha, A.B., Viviroli, D., Wada, Y., Xiao, C., Yao, T., Baillie, J.E.M., 2020. Importance and vulnerability of the world's water towers. *Nature* 577, 364-369.

- [103] Van der Woerd, J., Xu, X., Li, H., Tapponnier, P., Meyer, B., Ryerson, F.J., Meriaux, A.-S., Xu, Z., 2001. Rapid active thrusting along the northwestern range front of the Tanghe Nan Shan (western Gansu, China). *Journal of Geophysical Research: Solid Earth* 106, 30475-30504.
- [104] Métivier, F., Gaudemer, Y., Tapponnier, P., Meyer, B., 1998. Northeastward growth of the Tibet plateau deduced from balanced reconstruction of two depositional areas: The Qaidam and Hexi Corridor basins, China. *Tectonics* 17, 823-842.
- [105] Sobel, E.R., Hilley, G.E., Strecker, M.R., 2003. Formation of internally drained contractional basins by aridity-limited bedrock incision. *Journal of Geophysical Research: Solid Earth* 108.
- [106] Babault, J., Bonnet, S.p., Crave, A., Van Den Driessche, J., 2005. Influence of piedmont sedimentation on erosion dynamics of an uplifting landscape: An experimental approach. *Geology* 33, 301-304.
- [107] Babault, J., Bonnet, S., Driessche, J.V.D., Crave, A., 2007. High elevation of low-relief surfaces in mountain belts: does it equate to post-orogenic surface uplift? *Terra Nova* 19, 272-277.
- [108] Garcia-Castellanos, D., 2007. The role of climate during high plateau formation. Insights from numerical experiments. *Earth and Planetary Science Letters* 257, 372-390.
- [109] Bird, P., 1991. Lateral extrusion of lower crust from under high topography in the isostatic limit. *Journal of Geophysical Research: Solid Earth* 96, 10275-10286.
- [110] Shen, F., Royden, L.H., Burchfiel, B.C., 2001. Large-scale crustal deformation of the Tibetan Plateau. *Journal of Geophysical Research: Solid Earth* 106, 6793-6816.
- [111] McKenzie, D., Jackson, J., 2002. Conditions for flow in the continental crust. *Tectonics* 21, 5-1-5-7.
- [112] Lamb, S., Hoke, L., 1997. Origin of the high plateau in the central Andes, Bolivia, South America. *Tectonics* 16, 623-649.
- [113] Wittlinger, G., Vergne, J., Tapponnier, P., Farra, V., Poupinet, G., Jiang, M., Su, H., Herquel, G., Paul, A., 2004. Teleseismic imaging of subducting lithosphere and Moho offsets beneath western Tibet. *Earth and Planetary Science Letters* 221, 117-130.
- [114] Koons, P.O., 1995. Modeling the Topographic Evolution of Collisional Belts. *Annual Review of Earth and Planetary Sciences* 23, 375-408.
- [115] Brookfield, M.E., 1998. The evolution of the great river systems of southern Asia during the Cenozoic India-Asia collision: rivers draining southwards. *Geomorphology* 22, 285-312.

- [116] Hallet, B., Molnar, P., 2001. Distorted drainage basins as markers of crustal strain east of the Himalaya. *Journal of Geophysical Research: Solid Earth* 106, 13697-13709.
- [117] Yang, R., Willett, S.D., Goren, L., 2015. In situ low-relief landscape formation as a result of river network disruption. *Nature* 520, 526-529.
- [118] Clark, M.K., Schoenbohm, L.M., Royden, L.H., Whipple, K.X., Burchfiel, B.C., Zhang, X., Tang, W., Wang, E., Chen, L., 2004. Surface uplift, tectonics, and erosion of eastern Tibet from large-scale drainage patterns. *Tectonics* 23.
- [119] Yuan, X.P., Huppert, K.L., Braun, J., Shen, X., Liu-Zeng, J., Guerit, L., Wolf, S.G., Zhang, J.F., Jolivet, M., 2021. Propagating uplift controls on high-elevation, low-relief landscape formation in the southeast Tibetan Plateau. *Geology* 50, 60-65.
- [120] Wang, E., Kirby, E., Furlong, K.P., van Soest, M., Xu, G., Shi, X., Kamp, P.J.J., Hodges, K.V., 2012. Two-phase growth of high topography in eastern Tibet during the Cenozoic. *Nature Geoscience* 5, 640-645.
- [121] Zhang, H., Oskin, M.E., Liu-Zeng, J., Zhang, P., Reiners, P.W., Xiao, P., 2016. Pulsed exhumation of interior eastern Tibet: Implications for relief generation mechanisms and the origin of high-elevation planation surfaces. *Earth and Planetary Science Letters* 449, 176-185.
- [122] Cao, K., Leloup, P.H., Wang, G., Liu, W., Mahéo, G., Shen, T., Xu, Y., Sorrel, P., Zhang, K., 2020. Thrusting, exhumation, and basin fill on the western margin of the South China block during the India-Asia collision. *GSA Bulletin* 133, 74-90.
- [123] Pitard, P., Replumaz, A., Chevalier, M.-L., Leloup, P.-H., Bai, M., Doin, M.-P., Thieulot, C., Ou, X., Balvay, M., Li, H., 2021. Exhumation History Along the Muli Thrust—Implication for Crustal Thickening Mechanism in Eastern Tibet. *Geophysical Research Letters* 48, e2021GL093677.
- [124] Zhu, C., Wang, G., Leloup, P.H., Cao, K., Mahéo, G., Chen, Y., Zhang, P., Shen, T., Wu, G., Sotiriou, P., Wu, B., 2021. Role of the Early Miocene Jinhe-Qinghe Thrust Belt in the building of the Southeastern Tibetan Plateau topography. *Tectonophysics* 811, 228871.
- [125] Burchfiel, B.C., Zhiliang, C., 2013. *Tectonics of the Southeastern Tibetan Plateau and Its Adjacent Foreland*. Geological Society of America.
- [126] Clark, M.K., Royden, L.H., Whipple, K.X., Burchfiel, B.C., Zhang, X., Tang, W., 2006. Use of a regional, relict landscape to measure vertical deformation of the eastern Tibetan Plateau. *Journal of Geophysical Research: Earth Surface* 111.

- [127] Fox, M., Carter, A., Dai, J.-G., 2020. How Continuous Are the “Relict” Landscapes of Southeastern Tibet? *Frontiers in Earth Science* 8.
- [128] Burchfiel, B.C., Zhiliang, C., Yupinc, L., Royden, L.H., 1995. Tectonics of the Longmen Shan and Adjacent Regions, Central China. *International Geology Review* 37, 661-735.
- [129] HUANG, M.-H., BUICK, I.S., HOU, L.W., 2003. Tectonometamorphic Evolution of the Eastern Tibet Plateau: Evidence from the Central Songpan-Garzê Orogenic Belt, Western China. *Journal of Petrology* 44, 255-278.
- [130] Harrowfield, M.J., Wilson, C.J.L., 2005. Indosinian deformation of the Songpan Garzê Fold Belt, northeast Tibetan Plateau. *Journal of Structural Geology* 27, 101-117.
- [131] de Sigoyer, J., Vanderhaeghe, O., Duchêne, S., Billerot, A., 2014. Generation and emplacement of Triassic granitoids within the Songpan Ganze accretionary-orogenic wedge in a context of slab retreat accommodated by tear faulting, Eastern Tibetan plateau, China. *Journal of Asian Earth Sciences* 88, 192-216.
- [132] Liu, M., Mooney, W.D., Li, S., Okaya, N., Detweiler, S., 2006. Crustal structure of the northeastern margin of the Tibetan plateau from the Songpan-Ganzi terrane to the Ordos basin. *Tectonophysics* 420, 253-266.
- [133] Reid, A., Wilson, C.J.L., Shun, L., Pearson, N., Belousova, E., 2007. Mesozoic plutons of the Yidun Arc, SW China: U/Pb geochronology and Hf isotopic signature. *Ore Geology Reviews* 31, 88-106.
- [134] Bureau of Geology and Mineral Resources of Sichuan Province (BGMRS) (1991), *Regional Geology of Sichuan Province*, 730 pp., Geol. Publ. House, Beijing.
- [135] Xu, G., Kamp, P.J.J., 2000. Tectonics and denudation adjacent to the Xianshuihe Fault, eastern Tibetan Plateau: Constraints from fission track thermochronology. *Journal of Geophysical Research: Solid Earth* 105, 19231-19251.
- [136] Kirby, E., Reiners, P.W., Krol, M.A., Whipple, K.X., Hodges, K.V., Farley, K.A., Tang, W., Chen, Z., 2002. Late Cenozoic evolution of the eastern margin of the Tibetan Plateau: Inferences from  $^{40}\text{Ar}/^{39}\text{Ar}$  and (U-Th)/He thermochronology. *Tectonics* 21, 1-1-1-20.
- [137] Reid, A.J., Wilson, C.J.L., Phillips, D., Liu, S., 2005. Mesozoic cooling across the Yidun Arc, central-eastern Tibetan Plateau: A reconnaissance  $^{40}\text{Ar}/^{39}\text{Ar}$  study. *Tectonophysics* 398, 45-66.
- [138] Clark, M.K., House, M., Royden, L., Whipple, K., Burchfiel, B., Zhang, X., Tang, W., 2005. Late Cenozoic uplift of southeastern Tibet. *Geology* 33, 525-528.

- [139] Tian, Y., Kohn, B.P., Gleadow, A.J.W., Hu, S., 2014. A thermochronological perspective on the morphotectonic evolution of the southeastern Tibetan Plateau. *Journal of Geophysical Research: Solid Earth* 119, 676-698.
- [140] Zhang, Y.-Z., Replumaz, A., Leloup, P.H., Wang, G.-C., Bernet, M., van der Beek, P., Paquette, J.L., Chevalier, M.-L., 2017. Cooling history of the Gongga batholith: Implications for the Xianshuihe Fault and Miocene kinematics of SE Tibet. *Earth and Planetary Science Letters* 465, 1-15.
- [141] Wang, E., Burchfiel, B.C., Royden, L.H., Liangzhong, C., Jishen, C., Wenxin, L., Zhiliang, C., 1998. Late Cenozoic Xianshuihe-Xiaojiang, Red River, and Dali Fault Systems of Southwestern Sichuan and Central Yunnan, China. *Geological Society of America*.
- [142] Godard, V., Lavé, J., Carcaillet, J., Cattin, R., Bourlès, D., Zhu, J., 2010. Spatial distribution of denudation in Eastern Tibet and regressive erosion of plateau margins. *Tectonophysics* 491, 253-274.
- [143] Ouimet, W., Whipple, K., Royden, L., Reiners, P., Hodges, K., Pringle, M., 2010. Regional incision of the eastern margin of the Tibetan Plateau. *Lithosphere* 2, 50-63.
- [144] Wilson, C.J.L., Fowler, A.P., 2011. Denudational response to surface uplift in east Tibet: Evidence from apatite fission-track thermochronology. *GSA Bulletin* 123, 1966-1987.
- [145] Tian, Y., Kohn, B.P., Hu, S., Gleadow, A.J.W., 2015. Synchronous fluvial response to surface uplift in the eastern Tibetan Plateau: Implications for crustal dynamics. *Geophysical Research Letters* 42, 29-35.
- [146] Yang, R., Suhail, H.A., Gourbet, L., Willett, S.D., Fellin, M.G., Lin, X., Gong, J., Wei, X., Maden, C., Jiao, R., Chen, H., 2020. Early Pleistocene drainage pattern changes in Eastern Tibet: Constraints from provenance analysis, thermochronometry, and numerical modeling. *Earth and Planetary Science Letters* 531, 115955.
- [147] McPhillips, D., Hoke, G.D., Liu-Zeng, J., Bierman, P.R., Rood, D.H., Niedermann, S., 2016. Dating the incision of the Yangtze River gorge at the First Bend using three-nuclide burial ages. *Geophysical Research Letters* 43, 101-110.
- [148] Lacassin, R., Schärer, U., Leloup, P.H., Arnaud, N., Tapponnier, P., Liu, X., Zhang, L., 1996. Tertiary deformation and metamorphism SE of Tibet: The folded Tiger-leap décollement of NW Yunnan, China. *Tectonics* 15, 605-622.
- [149] Shen, X., Tian, Y., Li, D., Qin, S., Vermeesch, P., Schwanethal, J., 2016. Oligocene-Early Miocene river incision near the first bend of the Yangze River: Insights from apatite (U-Th-Sm)/He thermochronology. *Tectonophysics* 687, 223-231.

- [150] Yang, R., Fellin, M.G., Herman, F., Willett, S.D., Wang, W., Maden, C., 2016. Spatial and temporal pattern of erosion in the Three Rivers Region, southeastern Tibet. *Earth and Planetary Science Letters* 433, 10-20.
- [151] Replumaz, A., San José, M., Margirier, A., van der Beek, P., Gautheron, C., Leloup, P.H., Ou, X., Kai, C., Wang, G.-C., Zhang, Y.-Z., Valla, P.G., Balvay, M., 2020. Tectonic Control on Rapid Late Miocene—Quaternary Incision of the Mekong River Knickzone, Southeast Tibetan Plateau. *Tectonics* 39, e2019TC005782.
- [152] Ou, X., Replumaz, A., van der Beek, P., 2021. Contrasting exhumation histories and relief development within the Three Rivers Region (south-east Tibet). *Solid Earth* 12, 563-580.
- [153] Dai, J., Wang, C., Hourigan, J., Santosh, M., 2013. Multi-stage tectono-magmatic events of the Eastern Kunlun Range, northern Tibet: Insights from U–Pb geochronology and (U–Th)/He thermochronology. *Tectonophysics* 599, 97-106.
- [154] Nie, J., Ruetenik, G., Gallagher, K., Hoke, G., Garzzone, C.N., Wang, W., Stockli, D., Hu, X., Wang, Z., Wang, Y., Stevens, T., Danišik, M., Liu, S., 2018. Rapid incision of the Mekong River in the middle Miocene linked to monsoonal precipitation. *Nature Geoscience* 11, 944-948.
- [155] Duvall, A.R., Clark, M.K., Avdeev, B., Farley, K.A., Chen, Z., 2012. Widespread late Cenozoic increase in erosion rates across the interior of eastern Tibet constrained by detrital low-temperature thermochronometry. *Tectonics* 31.
- [156] Zhang, Y.-Z., Replumaz, A., Wang, G.-C., Leloup, P.H., Gautheron, C., Bernet, M., van der Beek, P., Paquette, J.L., Wang, A., Zhang, K.-X., Chevalier, M.-L., Li, H.-B., 2015. Timing and rate of exhumation along the Litang fault system, implication for fault reorganization in Southeast Tibet. *Tectonics* 34, 1219-1243.
- [157] Liu-Zeng, J., Zhang, J., McPhillips, D., Reiners, P., Wang, W., Pik, R., Zeng, L., Hoke, G., Xie, K., Xiao, P., 2018. Multiple episodes of fast exhumation since Cretaceous in southeast Tibet, revealed by low-temperature thermochronology. *Earth and Planetary Science Letters* 490, 62-76.
- [158] Godard, V., Pik, R., Lavé, J., Cattin, R., Tibari, B., de Sigoyer, J., Pubellier, M., Zhu, J., 2009. Late Cenozoic evolution of the central Longmen Shan, eastern Tibet: Insight from (U–Th)/He thermochronometry. *Tectonics* 28.
- [159] Xiao, P., Liu, J., Wang, W., Zhong, N., Zeng, L., Raphaël, P., Xie, K., 2015. The thermal history of the Baimaxueshan pluton in Deqin area and its implications for the tectonic-geomorphic evolution in the Three River Region of Tibetan Plateau. *Acta Petrologica Sinica*,31(5): 1348-1360 (in Chinese with English abstract).

- [160] Zeitler, P.K., Meltzer, A.S., Brown, L., Kidd, W.S.F., Lim, C., Enkelmann, E., Nie, J., Horton, B.K., Hoke, G.D., 2014. Tectonics and topographic evolution of Namche Barwa and the easternmost Lhasa block, Tibet, Toward an Improved Understanding of Uplift Mechanisms and the Elevation History of the Tibetan Plateau. *Geological Society of America*, p. 0.
- [161] Gourbet, L., Yang, R., Fellin, M.G., Paquette, J.-L., Willett, S.D., Gong, J., Maden, C., 2019. Evolution of the Yangtze River network, southeastern Tibet: Insights from thermochronology and sedimentology. *Lithosphere* 12, 3-18.
- [162] Wang, Y., Zhang, P., Schoenbohm, L.M., Zheng, W., Zhang, B., Zhang, J., Zheng, D., Zhou, R., Tian, Y., 2018. Two-phase exhumation along major shear zones in the SE Tibetan Plateau in the late Cenozoic. *Tectonics* 37, 2675-2694.
- [163] Reid, A.J., Fowler, A.P., Phillips, D., Wilson, C.J., 2005. Thermochronology of the Yidun Arc, central eastern Tibetan Plateau: constraints from  $^{40}\text{Ar}/^{39}\text{Ar}$  K-feldspar and apatite fission track data. *Journal of Asian Earth Sciences* 25, 915-935.
- [164] Lai, Q., Ding, L., Wang, H., Yue, Y., Cai, F., 2007. Constraining the stepwise migration of the eastern Tibetan Plateau margin by apatite fission track thermochronology. *Science in China Series D: Earth Sciences* 50, 172-183.
- [165] Lei, Y.L., Ji, J., Gong, D.H., Zhong, D.L., Wang, X.S., Zhang, J., Wang, X.M., 2006. Thermal and denudational history of granitoid batholith recorded by apatite fission track in the Dulong River region in northwestern Yunnan, since Late Miocene. *Acta Petrologica Sinica* 22, 938-948.
- [166] Métivier, F., Gaudemer, Y., Tapponnier, P., Klein, M., 1999. Mass accumulation rates in Asia during the Cenozoic. *Geophysical Journal International* 137, 280-318.
- [167] Clift, P.D., 2006. Controls on the erosion of Cenozoic Asia and the flux of clastic sediment to the ocean. *Earth and Planetary Science Letters* 241, 571-580.
- [168] Clift, P.D., Sun, Z., 2006. The sedimentary and tectonic evolution of the Yinggehai–Song Hong basin and the southern Hainan margin, South China Sea: Implications for Tibetan uplift and monsoon intensification. *Journal of Geophysical Research: Solid Earth* 111.
- [169] Rohrmann, A., Schwanghart, W., Kirby, E., 2018. Yangtze upstream-river network expansion reveals potential top-down incision, pp. EP53A-03.
- [170] Willett, S.D., McCoy, S.W., Perron, J.T., Goren, L., Chen, C.-Y., 2014. Dynamic Reorganization of River Basins. *Science* 343, 1248765.

- [171] Whipple, K.X., Forte, A.M., DiBiase, R.A., Gasparini, N.M., Ouimet, W.B., 2017. Timescales of landscape response to divide migration and drainage capture: Implications for the role of divide mobility in landscape evolution. *Journal of Geophysical Research: Earth Surface* 122, 248-273.
- [172] Li, S., van Hinsbergen, D.J.J., Shen, Z., Najman, Y., Deng, C., Zhu, R., 2020. Anisotropy of Magnetic Susceptibility (AMS) Analysis of the Gonjo Basin as an Independent Constraint to Date Tibetan Shortening Pulses. *Geophysical Research Letters* 47, e2020GL087531.
- [173] Leeder, M.R., Smith, A.B., Jixiang, Y., Chengfa, C., Shackleton, R.M., Dewey, J.F., Jixiang, Y., 1988. Sedimentology, palaeoecology and palaeoenvironmental evolution of the 1985 Lhasa to Golmud Geotraverse. *Philosophical Transactions of the Royal Society of London. Series A, Mathematical and Physical Sciences* 327, 107-143.
- [174] Li, Y., Wang, C., Zhao, X., Yin, A., Ma, C., 2012. Cenozoic thrust system, basin evolution, and uplift of the Tanggula Range in the Tuotuohe region, central Tibet. *Gondwana Research* 22, 482-492.
- [175] Staisch, L.M., Niemi, N.A., Hong, C., Clark, M.K., Rowley, D.B., Currie, B., 2014. A Cretaceous-Eocene depositional age for the Fenghuoshan Group, Hoh Xil Basin: Implications for the tectonic evolution of the northern Tibet Plateau. *Tectonics* 33, 281-301.
- [176] Spurlin, M.S., Yin, A., Horton, B.K., Zhou, J., Wang, J., 2005. Structural evolution of the Yushu-Nangqian region and its relationship to syncollisional igneous activity, east-central Tibet. *GSA Bulletin* 117, 1293-1317.
- [177] Studnicki-Gizbert, C., Burchfiel, B.C., Li, Z., Chen, Z., 2008. Early Tertiary Gonjo basin, eastern Tibet: Sedimentary and structural record of the early history of India-Asia collision. *Geosphere* 4, 713-735.
- [178] Zhang, Y., Huang, W., Huang, B., van Hinsbergen, D.J.J., Yang, T., Dupont-Nivet, G., Guo, Z., 2018. 53–43 Ma Deformation of Eastern Tibet Revealed by Three Stages of Tectonic Rotation in the Gongjue Basin. *Journal of Geophysical Research: Solid Earth* 123, 3320-3338.
- [179] Li, S., Currie, B.S., Rowley, D.B., Ingalls, M., 2015. Cenozoic paleoaltimetry of the SE margin of the Tibetan Plateau: Constraints on the tectonic evolution of the region. *Earth and Planetary Science Letters* 432, 415-424.
- [180] Su, T., Spicer, R.A., Li, S.-H., Xu, H., Huang, J., Sherlock, S., Huang, Y.-J., Li, S.-F., Wang, L., Jia, L.-B., Deng, W.-Y.-D., Liu, J., Deng, C.-L., Zhang, S.-T., Valdes, P.J., Zhou, Z.-K., 2018. Uplift, climate and biotic changes at the Eocene–Oligocene transition in south-eastern Tibet. *National Science Review* 6, 495-504.
- [181] Gourbet, L., Leloup, P.H., Paquette, J.-L., Sorrel, P., Maheo, G., Wang, G., Yadong, X., Cao, K., Antoine, P.-O., Eymard, I., Liu, W., Lu, H., Replumaz, A., Chevalier, M.-L., Kexin, Z.,

- Jing, W., Shen, T., 2017. Reappraisal of the Jianchuan Cenozoic basin stratigraphy and its implications on the SE Tibetan plateau evolution. *Tectonophysics* 700-701, 162-179.
- [182] Staisch, L.M., Niemi, N.A., Clark, M.K., Chang, H., 2016. Eocene to late Oligocene history of crustal shortening within the Hoh Xil Basin and implications for the uplift history of the northern Tibetan Plateau. *Tectonics* 35, 862-895.
- [183] Yi, H., Wang, C., Liu, S., Liu, Z., Wang, S., 2000. Sedimentary Record of the Planation Surface in the Hoh Xil Region of the Northern Tibet Plateau. *Acta Geologica Sinica - English Edition* 74, 827-835.
- [184] Liu, Z., Wang, C., 2001. Facies analysis and depositional systems of Cenozoic sediments in the Hoh Xil basin, northern Tibet. *Sedimentary Geology* 140, 251-270.
- [185] Liu, Z., Wang, C., Yi, H., 2001. Evolution and Mass Accumulation of the Cenozoic Hoh Xil Basin, Northern Tibet. *Journal of Sedimentary Research* 71, 971-984.
- [186] Wu, Z., Barosh, P.J., Zhonghai, W., Daogong, H., Xun, Z., Peisheng, Y., 2008. Vast early Miocene lakes of the central Tibetan Plateau. *GSA Bulletin* 120, 1326-1337.
- [187] Zhao, J., Li, S., Farnsworth, A., Valdes, P.J., Reichgelt, T., Chen, L., Zhou, Z., Su, T., 2022. The Paleogene to Neogene climate evolution and driving factors on the Qinghai-Tibetan Plateau. *Science China Earth Sciences* 65, 1339-1352.
- [188] Harkins, N., Kirby, E., Heimsath, A., Robinson, R., Reiser, U., 2007. Transient fluvial incision in the headwaters of the Yellow River, northeastern Tibet, China. *Journal of Geophysical Research: Earth Surface* 112.
- [189] Craddock, W.H., Kirby, E., Harkins, N.W., Zhang, H., Shi, X., Liu, J., 2010. Rapid fluvial incision along the Yellow River during headward basin integration. *Nature Geoscience* 3, 209-213.
- [190] Perrineau, A., Van Der Woerd, J., Gaudemer, Y., Liu-Zeng, J., Pik, R., Tapponnier, P., Thuitat, R., Zheng, R., 2011. Incision rate of the Yellow River in Northeastern Tibet constrained by <sup>10</sup>Be and <sup>26</sup>Al cosmogenic isotope dating of fluvial terraces: implications for catchment evolution and plateau building. *Geological Society, London, Special Publications* 353, 189-219.
- [191] Li, Z., Wang, X., Vandenberghe, J., Lu, H., 2021. Extension of the Upper Yellow River into the Tibet Plateau: Review and New Data. *Quaternary* 4, 14.
- [192] Garzzone, C.N., Ikari, M.J., Basu, A.R., 2005. Source of Oligocene to Pliocene sedimentary rocks in the Linxia basin in northeastern Tibet from Nd isotopes: Implications for tectonic forcing of climate. *GSA Bulletin* 117, 1156-1166.

- [193] Lease, R.O., Burbank, D.W., Gehrels, G.E., Wang, Z., Yuan, D., 2007. Signatures of mountain building: Detrital zircon U/Pb ages from northeastern Tibet. *Geology* 35, 239-242.
- [194] Molnar, P., 2004. LATE CENOZOIC INCREASE IN ACCUMULATION RATES OF TERRESTRIAL SEDIMENT: How Might Climate Change Have Affected Erosion Rates? *Annual Review of Earth and Planetary Sciences* 32, 67-89.
- [195] Hu, Z., Li, M., Dong, Z., Guo, L., Bridgland, D., Pan, B., Li, X., Liu, X., 2019. Fluvial entrenchment and integration of the Sanmen Gorge, the Lower Yellow River. *Global and Planetary Change* 178, 129-138.
- [196] Bridgland, D.R., Hu, Z., Vandenberghe, J., Wang, X., 2020. Late Cenozoic fluvial history worldwide: A context for the Yellow River record. *Global and Planetary Change* 193, 103274.
- [197] Jackson, J., Leeder, M., 1994. Drainage systems and the development of normal faults: an example from Pleasant Valley, Nevada. *Journal of Structural Geology* 16, 1041-1059.
- [198] Wang, C., Liang, X., Foster, D.A., Liang, X., Zhang, L., Su, M., 2019. Provenance and Drainage Evolution of the Red River Revealed by Pb Isotopic Analysis of Detrital K-Feldspar. *Geophysical Research Letters* 46, 6415-6424.
- [199] Clift, P.D., Long, H.V., Hinton, R., Ellam, R.M., Hannigan, R., Tan, M.T., Blusztajn, J., Duc, N.A., 2008. Evolving east Asian river systems reconstructed by trace element and Pb and Nd isotope variations in modern and ancient Red River-Song Hong sediments. *Geochemistry, Geophysics, Geosystems* 9.
- [200] Clift, P.D., Carter, A., Wysocka, A., Van Hoang, L., Zheng, H., Neubeck, N., 2020. A Late Eocene-Oligocene Through-Flowing River Between the Upper Yangtze and South China Sea. *Geochemistry, Geophysics, Geosystems* 21, e2020GC009046.
- [201] Deng, B., Chew, D., Jiang, L., Mark, C., Cogné, N., Wang, Z., Liu, S., 2018. Heavy mineral analysis and detrital U-Pb ages of the intracontinental Paleo-Yangtze basin: Implications for a transcontinental source-to-sink system during Late Cretaceous time. *GSA Bulletin* 130, 2087-2109.
- [202] Zhao, X., Zhang, H., Hetzel, R., Kirby, E., Duvall, A.R., Whipple, K.X., Xiong, J., Li, Y., Pang, J., Wang, Y., Wang, P., Liu, K., Ma, P., Zhang, B., Li, X., Zhang, J., Zhang, P., 2021. Existence of a continental-scale river system in eastern Tibet during the late Cretaceous–early Palaeogene. *Nature Communications* 12, 7231.
- [203] Wissink, G.K., Hoke, G.D., Garzzone, C.N., Liu-Zeng, J., 2016. Temporal and spatial patterns of sediment routing across the southeast margin of the Tibetan Plateau: Insights from detrital zircon. *Tectonics* 35, 2538-2563.

- [204] Zhang, Z., Daly, J.S., Li, C.a., Tyrrell, S., Sun, X., Yan, Y., 2017. Sedimentary provenance constraints on drainage evolution models for SE Tibet: Evidence from detrital K-feldspar. *Geophysical Research Letters* 44, 4064-4073.
- [205] Quade, J., Breecker, D.O., Daëron, M., Eiler, J., 2011. The paleoaltimetry of Tibet: An isotopic perspective. *American Journal of Science* 311, 77-115.
- [206] Rowley, D.B., Pierrehumbert, R.T., Currie, B.S., 2001. A new approach to stable isotope-based paleoaltimetry: implications for paleoaltimetry and paleohypsometry of the High Himalaya since the Late Miocene. *Earth and Planetary Science Letters* 188, 253-268.
- [207] Cyr, A.J., Currie, B.S., Rowley, D.B., 2005. Geochemical evaluation of Fenghuoshan Group lacustrine carbonates, north-central Tibet: Implications for the paleoaltimetry of the Eocene Tibetan Plateau. *The Journal of Geology* 113, 517-533.
- [208] Li, X., Zhang, R., Zhang, Z., Yan, Q., 2018. Do climate simulations support the existence of East Asian monsoon climate in the Late Eocene? *Palaeogeography, Palaeoclimatology, Palaeoecology* 509, 47-57.
- [209] Tang, M., Liu-Zeng, J., Hoke, G.D., Xu, Q., Wang, W., Li, Z., Zhang, J., Wang, W., 2017. Paleoelevation reconstruction of the Paleocene-Eocene Gonjo basin, SE-central Tibet. *Tectonophysics* 712-713, 170-181.
- [210] Xiong, Z., Ding, L., Spicer, R.A., Farnsworth, A., Wang, X., Valdes, P.J., Su, T., Zhang, Q., Zhang, L., Cai, F., Wang, H., Li, Z., Song, P., Guo, X., Yue, Y., 2020. The early Eocene rise of the Gonjo Basin, SE Tibet: From low desert to high forest. *Earth and Planetary Science Letters* 543, 116312.
- [211] Hoke, G.D., Liu-Zeng, J., Hren, M.T., Wissink, G.K., Garziona, C.N., 2014. Stable isotopes reveal high southeast Tibetan Plateau margin since the Paleogene. *Earth and Planetary Science Letters* 394, 270-278.
- [212] Wu, J., Zhang, K., Xu, Y., Wang, G., Garziona, C.N., Eiler, J., Leloup, P.H., Sorrel, P., Mahéo, G., 2018. Paleoelevations in the Jianchuan Basin of the southeastern Tibetan Plateau based on stable isotope and pollen grain analyses. *Palaeogeography, Palaeoclimatology, Palaeoecology* 510, 93-108.
- [213] Xu, Q., Liu, X., Ding, L., 2016. Miocene high-elevation landscape of the eastern Tibetan Plateau. *Geochemistry, Geophysics, Geosystems* 17, 4254-4267.
- [214] Allen, M.B., Armstrong, H.A., 2012. Reconciling the Intertropical Convergence Zone, Himalayan/Tibetan tectonics, and the onset of the Asian monsoon system. *Journal of Asian Earth Sciences* 44, 36-47.

- [215] Webster, P.J., Chou, L.C., 1980. Seasonal structure of a simple monsoon system. *Journal of Atmospheric Sciences* 37, 354-367.
- [216] An, Z., Kutzbach, J.E., Prell, W.L., Porter, S.C., 2001. Evolution of Asian monsoons and phased uplift of the Himalaya-Tibetan plateau since Late Miocene times. *Nature* 411, 62-66.
- [217] Boos, W.R., Kuang, Z., 2010. Dominant control of the South Asian monsoon by orographic insulation versus plateau heating. *Nature* 463, 218-222.
- [218] Wang, B., 2006. *The asian monsoon*. Springer Science & Business Media.
- [219] Kitoh, A., Endo, H., Krishna Kumar, K., Cavalcanti, I.F., Goswami, P., Zhou, T., 2013. Monsoons in a changing world: A regional perspective in a global context. *Journal of Geophysical Research: Atmospheres* 118, 3053-3065.
- [220] Fang, X., Yan, M., Zhang, W., Nie, J., Han, W., Wu, F., Song, C., Zhang, T., Zan, J., Yang, Y., 2021. Paleogeography control of Indian monsoon intensification and expansion at 41 Ma. *Science Bulletin* 66, 2320-2328.
- [221] Bookhagen, B., Thiede, R.C., Strecker, M.R., 2005. Late Quaternary intensified monsoon phases control landscape evolution in the northwest Himalaya. *Geology* 33, 149-152.
- [222] Barros, A.P., Chiao, S., Lang, T.J., Burbank, D., Putkonen, J., 2006. From weather to climate-seasonal and interannual variability of storms and implications for erosion processes in the Himalaya. *Special Papers-Geological Society of America* 398, 17.
- [223] Ramstein, G., Fluteau, F., Besse, J., Jousaume, S., 1997. Effect of orogeny, plate motion and land-sea distribution on Eurasian climate change over the past 30 million years. *Nature* 386, 788-795.
- [224] Guo, Z.T., Ruddiman, W.F., Hao, Q.Z., Wu, H.B., Qiao, Y.S., Zhu, R.X., Peng, S.Z., Wei, J.J., Yuan, B.Y., Liu, T.S., 2002. Onset of Asian desertification by 22 Myr ago inferred from loess deposits in China. *Nature* 416, 159-163.
- [225] Guo, Z.T., Sun, B., Zhang, Z.S., Peng, S.Z., Xiao, G.Q., Ge, J.Y., Hao, Q.Z., Qiao, Y.S., Liang, M.Y., Liu, J.F., 2008. A major reorganization of Asian climate by the early Miocene. *Climate of the Past* 4, 153-174.
- [226] Roe, G.H., Montgomery, D.R., Hallet, B., 2003. Orographic precipitation and the relief of mountain ranges. *Journal of Geophysical Research: Solid Earth* 108.
- [227] Roe, G.H., 2005. Orographic precipitation. *Annual Review of earth and planetary sciences* 33, 645-671.

- [228] Smith, R.B., 2006. Progress on the theory of orographic precipitation.
- [229] Bookhagen, B., Burbank, D.W., 2010. Toward a complete Himalayan hydrological budget: Spatiotemporal distribution of snowmelt and rainfall and their impact on river discharge. *Journal of Geophysical Research: Earth Surface* 115.
- [230] Lin, S., Wang, G., Hu, Z., Huang, K., Sun, X., Sun, J., Luo, M., Xiao, X., 2021. Dynamics of Evapotranspiration and Variations in Different Land-Cover Regions over the Tibetan Plateau during 1961–2014. *Journal of Hydrometeorology* 22, 955-969.
- [231] Ma, N., Zhang, Y., 2022. Increasing Tibetan Plateau terrestrial evapotranspiration primarily driven by precipitation. *Agricultural and Forest Meteorology* 317, 108887.
- [232] Quade, J., Cerling, T.E., Bowman, J.R., 1989. Development of Asian monsoon revealed by marked ecological shift during the latest Miocene in northern Pakistan. *Nature* 342, 163-166.
- [233] Prell, W.L., Murray, D.W., Clemens, S.C., Anderson, D.M., 1992. Evolution and variability of the Indian Ocean summer monsoon: evidence from the western Arabian Sea drilling program. Washington DC American Geophysical Union Geophysical Monograph Series 70, 447-469.
- [234] Rea, D.K., Snoeckx, H., Joseph, L.H., 1998. Late Cenozoic eolian deposition in the North Pacific: Asian drying, Tibetan uplift, and cooling of the northern hemisphere. *Paleoceanography* 13, 215-224.
- [235] Qiang, X., Li, Z.-X., Powell, C.M., Zheng, H., 2001. Magnetostratigraphic record of the Late Miocene onset of the East Asian monsoon, and Pliocene uplift of northern Tibet. *Earth and Planetary Science Letters* 187, 83-93.
- [236] Sun, X., Wang, P., 2005. How old is the Asian monsoon system?—Palaeobotanical records from China. *Palaeogeography, Palaeoclimatology, Palaeoecology* 222, 181-222.
- [237] Clift, P.D., Giosan, L., 2014. Sediment fluxes and buffering in the post-glacial Indus Basin. *Basin Research* 26, 369-386.
- [238] Xu, J., Ma, Y., 2009. Response of the hydrological regime of the Yellow River to the changing monsoon intensity and human activity. *Hydrological Sciences Journal* 54, 90-100.
- [239] Harrison, T.M., Copeland, P., Hall, S.A., Quade, J., Burner, S., Ojha, T.P., Kidd, W., 1993. Isotopic preservation of Himalayan/Tibetan uplift, denudation, and climatic histories of two molasse deposits. *The Journal of Geology* 101, 157-175.

- [240] Quade, J., Cater, J.M., Ojha, T.P., Adam, J., Mark Harrison, T., 1995. Late Miocene environmental change in Nepal and the northern Indian subcontinent: Stable isotopic evidence from paleosols. *Geological Society of America Bulletin* 107, 1381-1397.
- [241] Sanyal, J., Lu, X.X., 2004. Application of remote sensing in flood management with special reference to monsoon Asia: a review. *Natural Hazards* 33, 283-301.
- [242] Galy, V., France-Lanord, C., Peucker-Ehrenbrink, B., Huyghe, P., 2010. Sr-Nd-Os evidence for a stable erosion regime in the Himalaya during the past 12 Myr. *Earth and Planetary Science Letters* 290, 474-480.
- [243] Quan, C., Liu, Y.-S., Utescher, T., 2012. Eocene monsoon prevalence over China: A paleobotanical perspective. *Palaeogeography, Palaeoclimatology, Palaeoecology* 365-366, 302-311.
- [244] Quan, C., Liu, Z., Utescher, T., Jin, J., Shu, J., Li, Y., Liu, Y.-S.C., 2014. Revisiting the Paleogene climate pattern of East Asia: a synthetic review. *Earth-Science Reviews* 139, 213-230.
- [245] Clift, P.D., Layne, G.D., Blusztajn, J., 2004. Marine sedimentary evidence for monsoon strengthening, Tibetan uplift and drainage evolution in East Asia. *Continent-Ocean Interactions in the East Asian Marginal Seas, Geophys. Monogr. Ser* 149, 255-282.
- [246] Clift, P., Gaedicke, C., 2002. Accelerated mass flux to the Arabian Sea during the middle to late Miocene. *Geology* 30, 207-210.
- [247] Kent-Corson, M.L., Ritts, B.D., Zhuang, G., Bovet, P.M., Graham, S.A., Chamberlain, C.P., 2009. Stable isotopic constraints on the tectonic, topographic, and climatic evolution of the northern margin of the Tibetan Plateau. *Earth and Planetary Science Letters* 282, 158-166.
- [248] Jiang, H., Ding, Z., 2009. Spatial and temporal characteristics of Neogene palynoflora in China and its implication for the spread of steppe vegetation. *Journal of Arid Environments* 73, 765-772.
- [249] Owen, L.A., Robinson, R., Benn, D.I., Finkel, R.C., Davis, N.K., Yi, C., Putkonen, J., Li, D., Murray, A.S., 2009. Quaternary glaciation of mount everest. *Quaternary Science Reviews* 28, 1412-1433.
- [250] Fu, P., Harbor, J.M., Stroeven, A.P., Hättestrand, C., Heyman, J., Zhou, L., 2013. Glacial geomorphology and paleoglaciation patterns in Shaluli Shan, the southeastern Tibetan Plateau – Evidence for polythermal ice cap glaciation. *Geomorphology* 182, 66-78.

- [251] Zheng, H., Yang, Q., Cao, S., Clift, P.D., He, M., Kano, A., Sakuma, A., Xu, H., Tada, R., Jourdan, F., 2022. From desert to monsoon: irreversible climatic transition at ~ 36 Ma in southeastern Tibetan Plateau. *Progress in Earth and Planetary Science* 9, 12.
- [252] Sorrel, P., Eymard, I., Leloup, P.-H., Maheo, G., Olivier, N., Sterb, M., Gourbet, L., Wang, G., Jing, W., Lu, H., Li, H., Yadong, X., Zhang, K., Cao, K., Chevalier, M.-L., Replumaz, A., 2017. Wet tropical climate in SE Tibet during the Late Eocene. *Scientific Reports* 7, 7809.
- [253] Licht, A., van Cappelle, M., Abels, H.A., Ladant, J.B., Trabucho-Alexandre, J., France-Lanord, C., Donnadiou, Y., Vandenberghe, J., Rigaudier, T., Lécuyer, C., Terry Jr, D., Adriaens, R., Boura, A., Guo, Z., Soe, A.N., Quade, J., Dupont-Nivet, G., Jaeger, J.J., 2014. Asian monsoons in a late Eocene greenhouse world. *Nature* 513, 501-506.
- [254] Brozovic, N., Burbank, D.W., Meigs, A.J., 1997. Climatic limits on landscape development in the northwestern Himalaya. *Science* 276, 571-574.
- [255] Hales, T., Roering, J., 2009. A frost “buzzsaw” mechanism for erosion of the eastern Southern Alps, New Zealand. *Geomorphology* 107, 241-253.
- [256] Heyman, J., Stroeven, A.P., Alexanderson, H., Hättestrand, C., Harbor, J., Li, Y., Caffee, M.W., Zhou, L., Veres, D., Liu, F., 2009. Palaeoglaciation of Bayan Har Shan, northeastern Tibetan Plateau: glacial geology indicates maximum extents limited to ice cap and ice field scales. *Journal of Quaternary Science: Published for the Quaternary Research Association* 24, 710-727.
- [257] Fu, P., Heyman, J., Hättestrand, C., Stroeven, A.P., Harbor, J.M., 2012. Glacial geomorphology of the Shaluli Shan area, southeastern Tibetan Plateau. *Journal of Maps* 8, 48-55.
- [258] Menzies, J., 2018. *Glacial Geomorphology* ☆ , Reference Module in Earth Systems and Environmental Sciences. Elsevier.
- [259] Shi, Y., Ren, B., Wang, J., Derbyshire, E., 1986. Quaternary glaciation in China. *Quaternary Science Reviews* 5, 503-507.
- [260] Owen, L.A., Finkel, R.C., Caffee, M.W., 2002. A note on the extent of glaciation throughout the Himalaya during the global Last Glacial Maximum. *Quaternary Science Reviews* 21, 147-157.
- [261] Owen, L.A., Benn, D.I., 2005. Equilibrium-line altitudes of the Last Glacial Maximum for the Himalaya and Tibet: an assessment and evaluation of results. *Quaternary International* 138, 55-78.

- [262] Zheng, B., Xu, Q., Shen, Y., 2002. The relationship between climate change and Quaternary glacial cycles on the Qinghai-Tibetan Plateau: review and speculation. *Quaternary international* 97, 93-101.
- [263] Heyman, J., Stroeven, A.P., Caffee, M.W., Hättestrand, C., Harbor, J.M., Li, Y., Alexanderson, H., Zhou, L., Hubbard, A., 2011. Palaeoglaciology of Bayan Har Shan, NE Tibetan Plateau: exposure ages reveal a missing LGM expansion. *Quaternary Science Reviews* 30, 1988-2001.
- [264] Heyman, J., Stroeven, A.P., Harbor, J.M., Caffee, M.W., 2011. Too young or too old: evaluating cosmogenic exposure dating based on an analysis of compiled boulder exposure ages. *Earth and Planetary Science Letters* 302, 71-80.
- [265] Morén, B., Heyman, J., Stroeven, A.P., 2011. Glacial geomorphology of the central Tibetan Plateau. *Journal of Maps* 7, 115-125.
- [266] Fu, P., Stroeven, A.P., Harbor, J.M., Hättestrand, C., Heyman, J., Caffee, M.W., Zhou, L., 2013. Paleoglaciation of Shaluli Shan, southeastern Tibetan Plateau. *Quaternary Science Reviews* 64, 121-135.
- [267] Li, J., Feng, Z., Zhou, S., 1996. Quaternary glacial remnants in Hengduan Shan. *Glaciers in Hengduan Shan*. Science Press, Beijing, pp. 157e173 (in Chinese).
- [268] Kessler, M.A., Anderson, R.S., Stock, G.M., 2006. Modeling topographic and climatic control of east-west asymmetry in Sierra Nevada glacier length during the Last Glacial Maximum. *Journal of Geophysical Research: Earth Surface* 111.
- [269] Egholm, D., Nielsen, S., Pedersen, V., Lesemann, J.-E., 2009. Glacial effects limiting mountain height. *Nature* 460, 884-887.
- [270] Oskin, M., Burbank, D.W., 2005. Alpine landscape evolution dominated by cirque retreat. *Geology* 33, 933-936.
- [271] Willett, S.D., 1999. Orogeny and orography: The effects of erosion on the structure of mountain belts. *Journal of Geophysical Research: Solid Earth* 104, 28957-28981.
- [272] Willett, S.D., Hovius, N., Brandon, M.T., Fisher, D.M., 2006. Tectonics, climate, and landscape evolution.
- [273] Reiners, P.W., Ehlers, T.A., Mitchell, S.G., Montgomery, D.R., 2003. Coupled spatial variations in precipitation and long-term erosion rates across the Washington Cascades. *Nature* 426, 645-647.

- [274] Whipple, K.X., 2009. The influence of climate on the tectonic evolution of mountain belts. *Nature Geoscience* 2, 97-104.
- [275] Barry, A.H., 1983. Book reviews : Barry, R.G. 1981: *Mountain weather and climate*. London: Methuen. 313 pp. £17.50. *Progress in Physical Geography: Earth and Environment* 7, 301-302.
- [276] Howard, A.D., Dietrich, W.E., Seidl, M.A., 1994. Modeling fluvial erosion on regional to continental scales. *Journal of Geophysical Research: Solid Earth* 99, 13971-13986.
- [277] Whipple, K.X., Tucker, G.E., 1999. Dynamics of the stream-power river incision model: Implications for height limits of mountain ranges, landscape response timescales, and research needs. *Journal of Geophysical Research: Solid Earth* 104, 17661-17674.
- [278] Sklar, L.S., Dietrich, W.E., 2001. Sediment and rock strength controls on river incision into bedrock. *Geology* 29, 1087-1090.
- [279] Hartshorn, K., Hovius, N., Dade, W.B., Slingerland, R.L., 2002. Climate-Driven Bedrock Incision in an Active Mountain Belt. *Science* 297, 2036-2038.
- [280] Burbank, D.W., Leland, J., Fielding, E., Anderson, R.S., Brozovic, N., Reid, M.R., Duncan, C., 1996. Bedrock incision, rock uplift and threshold hillslopes in the northwestern Himalayas. *Nature* 379, 505-510.
- [281] Hovius, N., Stark, C.P., Allen, P.A., 1997. Sediment flux from a mountain belt derived by landslide mapping. *Geology* 25, 231-234.
- [282] Suppe, J., 1980. A retrodeformable cross section of northern Taiwan, *Proc. Geol. Soc. China*, pp. 46-55.
- [283] Barr, T.D., Dahlen, F.A., McPhail, D.C., 1991. Brittle frictional mountain building 3. Low-grade metamorphism. *Journal of Geophysical Research: Solid Earth* 96, 10319-10338.
- [284] Adams, J., 1980. Contemporary Uplift and Erosion of the Southern Alps, New Zealand. *GSA Bulletin* 91, 1-114.
- [285] Norris, R.J., Koons, P.O., Cooper, A.F., 1990. The obliquely-convergent plate boundary in the South Island of New Zealand: implications for ancient collision zones. *Journal of Structural Geology* 12, 715-725.
- [286] Koons, P.O., 1989. The topographic evolution of collisional mountain belts; a numerical look at the Southern Alps, New Zealand. *American Journal of Science* 289, 1041.

- [287] Brandon, M.T., Roden-Tice, M.K., Garver, J.I., 1998. Late Cenozoic exhumation of the Cascadia accretionary wedge in the Olympic Mountains, northwest Washington State. *GSA Bulletin* 110, 985-1009.
- [288] Molnar, P., England, P., 1990. Late Cenozoic uplift of mountain ranges and global climate change: chicken or egg? *nature* 346, 29-34.
- [289] Farnsworth, A., Lunt, D.J., Robinson, S.A., Valdes, P.J., Roberts, W.H., Clift, P.D., Markwick, P., Su, T., Wrobel, N., Bragg, F., 2019. Past East Asian monsoon evolution controlled by paleogeography, not CO<sub>2</sub>. *Science Advances* 5, eaax1697.
- [290] Tardif, D., Fluteau, F., Donnadieu, Y., Le Hir, G., Ladant, J.B., Sepulchre, P., Licht, A., Poblete, F., Dupont-Nivet, G., 2020. The origin of Asian monsoons: a modelling perspective. *Clim. Past* 16, 847-865.
- [291] Pagani, M., Zachos, J.C., Freeman, K.H., Tipple, B., Bohaty, S., 2005. Marked decline in atmospheric carbon dioxide concentrations during the Paleogene. *Science* 309, 600-603.
- [292] Maher, K., Chamberlain, C., 2014. Hydrologic regulation of chemical weathering and the geologic carbon cycle. *science* 343, 1502-1504.
- [293] Torres, M.A., West, A.J., Li, G., 2014. Sulphide oxidation and carbonate dissolution as a source of CO<sub>2</sub> over geological timescales. *Nature* 507, 346-349.
- [294] Lavé, J., Avouac, J.-P., 2001. Fluvial incision and tectonic uplift across the Himalayas of central Nepal. *Journal of Geophysical Research: Solid Earth* 106, 26561-26591.
- [295] Bettinelli, P., Avouac, J.-P., Flouzat, M., Jouanne, F., Bollinger, L., Willis, P., Chitrakar, G.R., 2006. Plate motion of India and interseismic strain in the Nepal Himalaya from GPS and DORIS measurements. *Journal of Geodesy* 80, 567-589.
- [296] Blythe, A., Burbank, D., Carter, A., Schmidt, K., Putkonen, J., 2007. Plio - Quaternary exhumation history of the central Nepalese Himalaya: 1. Apatite and zircon fission track and apatite [U-Th]/He analyses. *Tectonics* 26.
- [297] Braun, J., 2003. Pecube: a new finite-element code to solve the 3D heat transport equation including the effects of a time-varying, finite amplitude surface topography. *Computers & Geosciences* 29, 787-794.
- [298] Braun, J., van der Beek, P., Valla, P., Robert, X., Herman, F., Glotzbach, C., Pedersen, V., Perry, C., Simon-Labric, T., Prigent, C., 2012. Quantifying rates of landscape evolution and tectonic processes by thermochronology and numerical modeling of crustal heat transport using PECUBE. *Tectonophysics* 524-525, 1-28.

- [299] Braun, J., Willett, S.D., 2013. A very efficient  $O(n)$ , implicit and parallel method to solve the stream power equation governing fluvial incision and landscape evolution. *Geomorphology* 180-181, 170-179.
- [300] Tan, X.-B., Lee, Y.-H., Chen, W.-Y., Cook, K.L., Xu, X.-W., 2014. Exhumation history and faulting activity of the southern segment of the Longmen Shan, eastern Tibet. *Journal of Asian Earth Sciences* 81, 91-104.
- [301] Reiners, P.W., 2007. Thermochronologic Approaches to Paleotopography. *Reviews in Mineralogy and Geochemistry* 66, 243-267.
- [302] Braun, J., 2002. Quantifying the effect of recent relief changes on age–elevation relationships. *Earth and Planetary Science Letters* 200, 331-343.
- [303] Valla, P.G., Herman, F., van der Beek, P.A., Braun, J., 2010. Inversion of thermochronological age-elevation profiles to extract independent estimates of denudation and relief history – I: Theory and conceptual model. *Earth and Planetary Science Letters* 295, 511-522.
- [304] Valla, P.G., van der Beek, P.A., Braun, J., 2011. Rethinking low-temperature thermochronology data sampling strategies for quantification of denudation and relief histories: A case study in the French western Alps. *Earth and Planetary Science Letters* 307, 309-322.
- [305] Robert, X., van der Beek, P., Braun, J., Perry, C., Mugnier, J.-L., 2011. Control of detachment geometry on lateral variations in exhumation rates in the Himalaya: Insights from low-temperature thermochronology and numerical modeling. *Journal of Geophysical Research: Solid Earth* 116.
- [306] Replumaz, A., Lacassin, R., Tapponnier, P., Leloup, P., 2001. Large river offsets and Plio-Quaternary dextral slip rate on the Red River fault (Yunnan, China). *Journal of Geophysical Research: Solid Earth* 106, 819-836.
- [307] Fyhn, M.B.W., Phach, P.V., 2015. Late Neogene structural inversion around the northern Gulf of Tonkin, Vietnam: Effects from right-lateral displacement across the Red River fault zone. *Tectonics* 34, 290-312.
- [308] Wang, Y., Zhang, B., Schoenbohm, L.M., Zhang, J., Zhou, R., Hou, J., Ai, S., 2016. Late Cenozoic tectonic evolution of the Ailao Shan-Red River fault (SE Tibet): Implications for kinematic change during plateau growth. *Tectonics* 35, 1969-1988.
- [309] Cao, K., Wang, G., Leloup, P.H., Mahéo, G., Xu, Y., van der Beek, P.A., Replumaz, A., Zhang, K., 2019. Oligocene-Early Miocene Topographic Relief Generation of Southeastern Tibet Triggered by Thrusting. *Tectonics* 38, 374-391.

- [310] Bai, M., Chevalier, M.-L., Pan, J., Replumaz, A., Leloup, P.H., Métois, M., Li, H., 2018. Southeastward increase of the late Quaternary slip-rate of the Xianshuihe fault, eastern Tibet. Geodynamic and seismic hazard implications. *Earth and Planetary Science Letters* 485, 19-31.
- [311] Lacassin, R., Replumaz, A., Hervé Leloup, P., 1998. Hairpin river loops and slip-sense inversion on southeast Asian strike-slip faults. *Geology* 26, 703-706.
- [312] Gallagher, K., 2012. Transdimensional inverse thermal history modeling for quantitative thermochronology. *Journal of Geophysical Research: Solid Earth* 117.
- [313] Yao, H., van der Hilst, R.D., Montagner, J.-P., 2010. Heterogeneity and anisotropy of the lithosphere of SE Tibet from surface wave array tomography. *Journal of Geophysical Research: Solid Earth* 115.
- [314] Bermúdez, M.A., van der Beek, P., Bernet, M., 2011. Asynchronous Miocene–Pliocene exhumation of the central Venezuelan Andes. *Geology* 39, 139-142.
- [315] Wang, Y., 2012. A preliminary study on the lithospheric thermal structure and rheology of the Tibetan plateau. *Earthquake Science* 25, 399-408.
- [316] Chen, B., Liu, J., Kaban, M.K., Sun, Y., Chen, C., Du, J., 2014. Elastic thickness, mechanical anisotropy and deformation of the southeastern Tibetan Plateau. *Tectonophysics* 637, 45-56.
- [317] Reiners, P.W., Brandon, M.T., 2006. USING THERMOCHRONOLOGY TO UNDERSTAND OROGENIC EROSION. *Annual Review of Earth and Planetary Sciences* 34, 419-466.
- [318] Egholm, D.L., Jansen, J.D., Brædstrup, C.F., Pedersen, V.K., Andersen, J.L., Ugelvig, S.V., Larsen, N.K., Knudsen, M.F., 2017. Formation of plateau landscapes on glaciated continental margins. *Nature Geoscience* 10, 592-597.
- [319] Burg, J.-P., Nievergelt, P., Oberli, F., Seward, D., Davy, P., Maurin, J.-C., Diao, Z., Meier, M., 1998. The Namche Barwa syntaxis: evidence for exhumation related to compressional crustal folding. *Journal of Asian Earth Sciences* 16, 239-252.
- [320] Schmidt, J.L., Zeitler, P.K., Pazzaglia, F.J., Tremblay, M.M., Shuster, D.L., Fox, M., 2015. Knickpoint evolution on the Yarlung river: Evidence for late Cenozoic uplift of the southeastern Tibetan plateau margin. *Earth and Planetary Science Letters* 430, 448-457.
- [321] Pedersen, V.K., Egholm, D.L., Nielsen, S.B., 2010. Alpine glacial topography and the rate of rock column uplift: a global perspective. *Geomorphology* 122, 129-139.
- [322] Wang, W., Qiao, X., Yang, S., Wang, D., 2017. Present-day velocity field and block kinematics of Tibetan Plateau from GPS measurements. *Geophysical Journal International* 208, 1088-1102.

- [323] Seward, D., Burg, J.-P., 2008. Growth of the Namche Barwa Syntaxis and associated evolution of the Tsangpo Gorge: Constraints from structural and thermochronological data. *Tectonophysics* 451, 282-289.
- [324] Tu, J.-Y., Ji, J.-Q., Sun, D.-X., Gong, J.-F., Zhong, D.-L., Han, B.-F., 2015. Thermal structure, rock exhumation, and glacial erosion of the Namche Barwa Peak, constraints from thermochronological data. *Journal of Asian Earth Sciences* 105, 223-233.
- [325] Yu, X., Ji, J., Gong, J., Sun, D., Qing, J., Wang, L., Zhong, D., Zhang, Z., 2011. Evidences of rapid erosion driven by climate in the Yarlung Zangbo (Tsangpo) Great Canyon, the eastern Himalayan syntaxis. *Chinese Science Bulletin* 56, 1123-1130.
- [326] Ludwig, K.R., 2003. *Isoplot 3.00: A geochronological toolkit for Microsoft Excel*. Berkeley Geochronology Center Special Publication 4, 70.
- [327] Hurford, A.J., Green, P.F., 1983. The zeta age calibration of fission-track dating. *Chemical Geology* 41, 285-317.
- [328] Sambridge, M., 1999. Geophysical inversion with a neighbourhood algorithm—I. Searching a parameter space. *Geophysical Journal International* 138, 479-494.
- [329] Sambridge, M., 1999. Geophysical inversion with a neighbourhood algorithm—II. Appraising the ensemble. *Geophysical Journal International* 138, 727-746.
- [330] de Michele, M., Raucoules, D., de Sigoyer, J., Pubellier, M., Chamot-Rooke, N., 2010. Three-dimensional surface displacement of the 2008 May 12 Sichuan earthquake (China) derived from Synthetic Aperture Radar: evidence for rupture on a blind thrust. *Geophysical Journal International* 183, 1097-1103.
- [331] Robert, A., Pubellier, M., de Sigoyer, J., Vergne, J., Lahfid, A., Cattin, R., Findling, N., Zhu, J., 2010. Structural and thermal characters of the Longmen Shan (Sichuan, China). *Tectonophysics* 491, 165-173.
- [332] Leloup, P.H., Harrison, T.M., Ryerson, F., Wenji, C., Qi, L., Tapponnier, P., Lacassin, R., 1993. Structural, petrological and thermal evolution of a Tertiary ductile strike-slip shear zone, Diancang Shan, Yunnan. *Journal of Geophysical Research: Solid Earth* 98, 6715-6743.
- [333] Schoenbohm, L.M., Burchfiel, B.C., Liangzhong, C., Jiyun, Y., 2006. Miocene to present activity along the Red River fault, China, in the context of continental extrusion, upper-crustal rotation, and lower-crustal flow. *GSA Bulletin* 118, 672-688.

- [334] Wang, E., Burchfiel, B., 1997. Interpretation of Cenozoic tectonics in the right-lateral accommodation zone between the Ailao Shan shear zone and the eastern Himalayan syntaxis. *International Geology Review* 39, 191-219.
- [335] Wang, Y., Fan, W., Zhang, Y., Peng, T., Chen, X., Xu, Y., 2006. Kinematics and  $^{40}\text{Ar}/^{39}\text{Ar}$  geochronology of the Gaoligong and Chongshan shear systems, western Yunnan, China: Implications for early Oligocene tectonic extrusion of SE Asia. *Tectonophysics* 418, 235-254.
- [336] Zhang, B., Zhang, J., Zhong, D., Yang, L., Yue, Y., Yan, S., 2012. Polystage deformation of the Gaoligong metamorphic zone: Structures,  $^{40}\text{Ar}/^{39}\text{Ar}$  mica ages, and tectonic implications. *Journal of Structural Geology* 37, 1-18.
- [337] Zhang, B., Zhang, J., Chang, Z., Wang, X., Cai, F., Lai, Q., 2012. The Biluoxueshan transpressive deformation zone monitored by synkinematic plutons, around the Eastern Himalayan Syntaxis. *Tectonophysics* 574-575, 158-180.
- [338] Briais, A., Patriat, P., Tapponnier, P., 1993. Updated interpretation of magnetic anomalies and seafloor spreading stages in the South China Sea: Implications for the Tertiary tectonics of Southeast Asia. *Journal of Geophysical Research: Solid Earth* 98, 6299-6328.
- [339] Searle, M.P., 2006. Role of the Red River Shear zone, Yunnan and Vietnam, in the continental extrusion of SE Asia. *Journal of the Geological Society* 163, 1025-1036.
- [340] Mazur, S., Green, C., Stewart, M.G., Whittaker, J.M., Williams, S., Bouatmani, R., 2012. Displacement along the Red River Fault constrained by extension estimates and plate reconstructions. *Tectonics* 31.
- [341] Lee, H.-Y., Chung, S.-L., Wang, J.-R., Wen, D.-J., Lo, C.-H., Yang, T.F., Zhang, Y., Xie, Y., Lee, T.-Y., Wu, G., Ji, J., 2003. Miocene Jiali faulting and its implications for Tibetan tectonic evolution. *Earth and Planetary Science Letters* 205, 185-194.
- [342] Lin, T.-H., Lo, C.-H., Chung, S.-L., Hsu, F.-J., Yeh, M.-W., Lee, T.-Y., Ji, J.-Q., Wang, Y.-Z., Liu, D., 2009.  $^{40}\text{Ar}/^{39}\text{Ar}$  dating of the Jiali and Gaoligong shear zones: Implications for crustal deformation around the Eastern Himalayan Syntaxis. *Journal of Asian Earth Sciences* 34, 674-685.
- [343] Zhang, B., Cai, F., Chen, S., Li, X., Zhang, L., 2020. Sinistral strike-slip shearing along the Jiali shear zone around the Eastern Himalaya syntaxis region: Evidences for oligocene eastward limited translation of Tibet. *Journal of Structural Geology* 139, 104136.
- [344] Cao, K., Tian, Y., van der Beek, P., Wang, G., Shen, T., Reiners, P., Bernet, M., Husson, L., 2022. Southwestward growth of plateau surfaces in eastern Tibet. *Earth-Science Reviews* 232, 104160.

- [345] Jackson Jr., W.T., Robinson, D.M., Weislogel, A.L., Jian, X., McKay, M.P., 2018. Cenozoic Development of the Nonmarine Mula Basin in the Southern Yidun Terrane: Deposition and Deformation in the Eastern Tibetan Plateau Associated with the India-Asia Collision. *Tectonics* 37, 2446-2465.
- [346] Jackson, W.T., Robinson, D.M., Weislogel, A.L., Jian, X., 2020. Cenozoic reactivation along the Late Triassic Ganzi-Litang suture, eastern Tibetan Plateau. *Geoscience Frontiers* 11, 1069-1080.
- [347] Fang, X., Dupont-Nivet, G., Wang, C., Song, C., Meng, Q., Zhang, W., Nie, J., Zhang, T., Mao, Z., Chen, Y., 2020. Revised chronology of central Tibet uplift (Lunpola Basin). *Sci Adv* 6.
- [348] Wang, S., Jiang, G., Xu, T., Tian, Y., Zheng, D., Fang, X., 2012. The Jinhe-Qinghe fault—An inactive branch of the Xianshuihe-Xiaojiang fault zone, Eastern Tibet. *Tectonophysics* 544-545, 93-102.
- [349] Zhou, J., Wang, J., Yin, A., Horton, B., Spurlin, M., 2003. Sedimentology and tectonic significance of Paleogene coarse clastic rocks in eastern Tibet. *Acta Geologica Sinica* 77, 262-271.
- [350] Fillon, C., Gautheron, C., van der Beek, P., 2013. Oligocene–Miocene burial and exhumation of the Southern Pyrenean foreland quantified by low-temperature thermochronology. *Journal of the Geological Society* 170, 67-77.
- [351] Gautheron, C., Tassan-Got, L., 2010. A Monte Carlo approach to diffusion applied to noble gas/helium thermochronology. *Chemical Geology* 273, 212-224.
- [352] Ketcham, R.A., Gautheron, C., Tassan-Got, L., 2011. Accounting for long alpha-particle stopping distances in (U–Th–Sm)/He geochronology: Refinement of the baseline case. *Geochimica et Cosmochimica Acta* 75, 7779-7791.
- [353] Ehlers, T.A., 2005. Crustal Thermal Processes and the Interpretation of Thermochronometer Data. *Reviews in Mineralogy and Geochemistry* 58, 315-350.
- [354] Galbraith, R.F., Green, P.F., 1990. Estimating the component ages in a finite mixture. *International Journal of Radiation Applications and Instrumentation. Part D. Nuclear Tracks and Radiation Measurements* 17, 197-206.
- [355] Galbraith, R.F., Laslett, G.M., 1993. Statistical models for mixed fission track ages. *Nuclear Tracks and Radiation Measurements* 21, 459-470.
- [356] Vermeesch, P., 2009. RadialPlotter: A Java application for fission track, luminescence and other radial plots. *Radiation Measurements - RADIAT MEAS* 44, 409-410.

- [357] Gallagher, K., Brown, R., Johnson, C., 1998. FISSION TRACK ANALYSIS AND ITS APPLICATIONS TO GEOLOGICAL PROBLEMS. *Annual Review of Earth and Planetary Sciences* 26, 519-572.
- [358] Farley, K.A., 2002. (U-Th)/He Dating: Techniques, Calibrations, and Applications. *Reviews in Mineralogy and Geochemistry* 47, 819-844.
- [359] Gautheron, C., Tassan-Got, L., Barbarand, J., Pagel, M., 2009. Effect of alpha-damage annealing on apatite (U-Th)/He thermochronology. *Chemical Geology* 266, 157-170.
- [360] Flowers, R.M., Ketcham, R.A., Shuster, D.L., Farley, K.A., 2009. Apatite (U-Th)/He thermochronometry using a radiation damage accumulation and annealing model. *Geochimica et Cosmochimica Acta* 73, 2347-2365.
- [361] Donelick, R.A., O'Sullivan, P.B., Ketcham, R.A., 2005. Apatite Fission-Track Analysis. *Reviews in Mineralogy and Geochemistry* 58, 49-94.
- [362] Carlson, W.D., Donelick, R.A., Ketcham, R.A., 1999. Variability of apatite fission-track annealing kinetics; I, Experimental results. *American Mineralogist* 84, 1213-1223.
- [363] Barbarand, J., Carter, A., Wood, I., Hurford, T., 2003. Compositional and structural control of fission-track annealing in apatite. *Chemical Geology* 198, 107-137.
- [364] Cao, S., Liu, J., Leiss, B., Neubauer, F., Genser, J., Zhao, C., 2011. Oligo-Miocene shearing along the Ailao Shan-Red River shear zone: Constraints from structural analysis and zircon U/Pb geochronology of magmatic rocks in the Diancang Shan massif, SE Tibet, China. *Gondwana Research* 19, 975-993.
- [365] Wang, Y., Wang, Y., Schoenbohm, L.M., Zhang, P., Zhang, B., Sobel, E.R., Zhou, R., Shi, X., Zhang, J., Stockli, D.F., Guo, X., 2020. Cenozoic Exhumation of the Ailaoshan-Red River Shear Zone: New Insights From Low-Temperature Thermochronology. *Tectonics* 39, e2020TC006151.
- [366] Wang, H., Li, K., Tian, Y., Zhang, G., 2022. Oligocene-Early Miocene exhumation and shortening along the Anninghe fault in the southeastern Tibetan Plateau: insights from zircon and apatite (U-Th)/He thermochronology. *International Geology Review* 64, 390-404.
- [367] Zhang, G., Tian, Y., Li, R., Shen, X., Zhang, Z., Sun, X., Chen, D., 2022. Progressive tectonic evolution from crustal shortening to mid-lower crustal expansion in the southeast Tibetan Plateau: A synthesis of structural and thermochronological insights. *Earth-Science Reviews* 226, 103951.
- [368] Li, S., Su, T., Spicer, R.A., Xu, C., Sherlock, S., Halton, A., Hoke, G., Tian, Y., Zhang, S., Zhou, Z., Deng, C., Zhu, R., 2020. Oligocene Deformation of the Chuandian Terrane in the SE

Margin of the Tibetan Plateau Related to the Extrusion of Indochina. *Tectonics* 39, e2019TC005974.

- [369] Molnar, P., Boos, W.R., Battisti, D.S., 2010. Orographic Controls on Climate and Paleoclimate of Asia: Thermal and Mechanical Roles for the Tibetan Plateau. *Annual Review of Earth and Planetary Sciences* 38, 77-102.
- [370] Spicer, R.A., Yang, J., Herman, A.B., Kodrul, T., Maslova, N., Spicer, T.E.V., Aleksandrova, G., Jin, J., 2016. Asian Eocene monsoons as revealed by leaf architectural signatures. *Earth and Planetary Science Letters* 449, 61-68.
- [371] Howard, A.D., Kerby, G., 1983. Channel changes in badlands. *GSA Bulletin* 94, 739-752.
- [372] Ahnert, F., 1967. The Role of the Equilibrium Concept in the Interpretation of Landforms of Fluvial Erosion and Deposition.
- [373] Stock, J.D., Montgomery, D.R., 1999. Geologic constraints on bedrock river incision using the stream power law. *Journal of Geophysical Research: Solid Earth* 104, 4983-4993.
- [374] Kirby, E., Whipple, K., 2001. Quantifying differential rock-uplift rates via stream profile analysis. *Geology* 29, 415-418.
- [375] Wobus, C., Whipple, K.X., Kirby, E., Snyder, N., Johnson, J., Spyropolou, K., Crosby, B., Sheehan, D., Willett, S.D., Hovius, N., Brandon, M.T., Fisher, D.M., 2006. Tectonics from topography: Procedures, promise, and pitfalls, *Tectonics, Climate, and Landscape Evolution*. Geological Society of America, p. 0.
- [376] Croissant, T., Braun, J., 2014. Constraining the stream power law: a novel approach combining a landscape evolution model and an inversion method. *Earth Surf. Dynam.* 2, 155-166.
- [377] Densmore, A.L., Gupta, S., Allen, P.A., Dawers, N.H., 2007. Transient landscapes at fault tips. *Journal of Geophysical Research: Earth Surface* 112.
- [378] Schwanghart, W., Scherler, D., 2014. Short Communication: TopoToolbox 2 – MATLAB-based software for topographic analysis and modeling in Earth surface sciences. *Earth Surf. Dynam.* 2, 1-7.
- [379] Perron, J.T., Royden, L., 2013. An integral approach to bedrock river profile analysis. *Earth Surface Processes and Landforms* 38, 570-576.
- [380] Braun, J., 2018. A review of numerical modeling studies of passive margin escarpments leading to a new analytical expression for the rate of escarpment migration velocity. *Gondwana Research* 53, 209-224.

- [381] Heidarzadeh, G., Ballato, P., Hassanzadeh, J., Ghassemi, M.R., Strecker, M.R., 2017. Lake overflow and onset of fluvial incision in the Iranian Plateau: Insights from the Mianeh Basin. *Earth and Planetary Science Letters* 469, 135-147.
- [382] Geurts, A.H., Cowie, P.A., Duclaux, G., Gawthorpe, R.L., Huismans, R.S., Pedersen, V.K., Wedmore, L.N.J., 2018. Drainage integration and sediment dispersal in active continental rifts: A numerical modelling study of the central Italian Apennines. *Basin Research* 30, 965-989.
- [383] Zhang, K., Wang, G., Ji, J., Luo, M., Kou, X., Wang, Y., Xu, Y., Chen, F., Chen, R., Song, B., Zhang, J., Liang, Y., 2010. Paleogene-Neogene stratigraphic realm and sedimentary sequence of the Qinghai-Tibet Plateau and their response to uplift of the plateau. *Science China Earth Sciences* 53, 1271-1294.
- [384] Curry, M.E., van der Beek, P., Huismans, R.S., Wolf, S., Muñoz, J.A., 2019. Peak- to post-orogenic landscape evolution of the Pyrenees Mountains from numerical modeling and thermochronology, pp. T41G-0339.